UNIVERSITÀ DEGLI STUDI DI TRIESTE

XXIX CICLO DEL DOTTORATO DI RICERCA IN

Scienze della Terra e Meccanica dei Fluidi

Reconstructing with numerical Ice Sheet Models the post-LGM decay of the Eurasian Ice Sheets: data-model comparison and focus on the Storfjorden (Svalbard) ice stream dynamics history

Specific subject area: **FIS/06**
FISICA PER IL SISTEMA TERRA E IL MEZZO CIRCUMTERRESTRE

Ph.D. student
Michele Petrini

Ph.D. program Coordinator
Prof. Pierpaolo Omari

Thesis Supervisor
Dr. Emanuele Forte

Thesis co-Supervisors
Dr. Angelo Camerlenghi
Dr. Michele Rebesco
Prof. Nina Kirchner
Dr. Florence Colleoni
Dr. Renato R. Colucci
Dr. Renata G. Lucchi

ANNO ACCADEMICO 2015/2016

Abstract

The challenge of reconstructing the growth and decay of *palaeo*-ice sheets represents a critical task to better understand mechanisms of global climate change and associated sea-level fluctuations in the present and future. The Eurasian *palaeo*-Ice Sheet (EIS) at its maximum volume and extent (between 21,000 and 20,000 years ago) comprised the Scandinavian (SIS), Svalbard/Barents/Kara seas (SBKSIS), and British-Irish (BIIS) *palaeo*-ice sheets. The SBKSIS was a so called marine based ice sheet, as it rested several hundreds of meters below the sea level in the Barents and Kara seas. From a bathymetric and topographic point of view, there is a strong similarity between the SBKSIS and the *present-day* West Antarctic Ice Sheet (WAIS). Consequently, to reconstruct the dynamic processes driving the last deglaciation of the SBKSIS may represent an important task to better understand the WAIS present and future evolution. In this study, the evolution of the EIS during the last deglaciation is reconstructed with two hybrid Shallow-Ice/Shallow-Shelf-Approximation numerical Ice Sheet Models (ISMs), namely PSU and GRISLI. These two ISMs differ mainly in the ice stream parametrization and in the complexity with which grounding line migration is treated. A particular focus in this study is given to the Storfjorden glacial system in the north-western Barents Sea. In fact, several *palaeo*-data from this area furnish insights on the Storfjorden ice stream dynamics history, providing a good testing ground for ISMs. The ISMs are forced with macro-regional indexes representative of the climate evolution over Siberia/Kara Sea, Svalbard/Barents Sea and Fennoscandia during the last deglaciation. The climate indexes are based on TraCE-21ka, a transient climate simulation of the last 21,000 years carried out with the Atmosphere-Ocean General Circulation Model CCSM3. Two different ocean basal melting parametrizations based on ice-ocean heat fluxes are tested. The ocean basal melting parametrizations are forced with time-varying ocean temperature and salinity from TraCE-21ka transient climate simulation. Ocean temperature and salinity representative of Arctic Ocean, Norwegian Sea, north-western and south-western Barents Sea are employed. In order to deal with ISMs poorly constrained model parameters, a statistical approach is adopted. A Latin Hypercube Sampling (LHS) of five GRISLI parameters is performed. Due to large computational costs it is not possible to perform such a statistical approach with PSU ISM. Therefore, a restricted number of simulations performed with PSU ISM employ model parameter values from GRISLI significant simulations. GRISLI-simulated ice streams dynamics has a strong control on the deglaciation of the EIS, in particular in the Southern SIS and in the Western SBKSIS. In terms of total ice volume there is a good agreement between GRISLI simulations, ICE-5G reconstruction and global Eustatic Sea Level data. In contrast, GRISLI-simulated ice sheet extent evolution presents discrepancies with geological observation in the Southern SIS and in the Eastern SBKSIS. The use of different basal melting parametrizations in GRISLI has a strong impact both on the deglaciation of the SBKSIS and on the retreat of Storfjorden ice stream. The Storfjorden ice stream dynamics history in GRISLI simulations is in good agreement with *palaeo*-data in terms of timing of the ice stream retreat, Grounding Zone Wedges formation and response to Meltwater Pulse 1A. The different treatment in PSU of ice streams and Grounding Line migration has a remarkable effect on the EIS deglaciation. In particular, in PSU the Grounding Line dynamics plays a primary role with respect to ocean basal melting, thus exerting a strong control on the decay of the marine-based SBKSIS. Finally, an inverse-type approach is adopted to match PSU simulations with ICE-5G reconstruction and the other *palaeo*-data.

Contents

CHAPTER 1

Introduction

In this chapter the research carried out within this Ph.D. project is addressed. First of all, the main scientific questions motivating this research are illustrated and discussed. In the second section, the last deglaciation of the Eurasian *palaeo*-Ice Sheet is put into a larger context. A brief introduction on the atmosphere/ocean/ice-sheet feedbacks and interaction is provided. It follows a synthesis of the previous modeling studies on past glacial/interglacial cycles and of the Cenozoic history of the Eurasian *palaeo*-Ice Sheet, with particular interest in the Late Quaternary period. In the second section, a detailed analysis of the last deglaciation of the Eurasian *palaeo*-Ice Sheet is undertaken. Ice sheet extent empirical reconstructions that will be used in this study as "global" constraints for the Ice Sheet Models results are presented, along with previous numerical modeling studies. *Palaeo*-data relevant for this research from Storfjorden and Kveithola Trough Mouth Fans in the north-western Barents Sea are presented. The insights provided by such *palaeo*-data that will be used as "local" constraints on the simulated Storfjorden ice stream dynamics history results are summarized.

1.1 Scientific motivation for this study

The challenge of reconstructing *palaeo*-ice sheets growth and decay represents a critical task to better understand mechanisms of global climate change and the associated sea-level fluctuations in the present and future. *Palaeo*-ice sheets constitute in fact analogues for assessing recent changes observed in present-day ice sheets, Stokes et al. 2015. Moreover, the observations of changes in present-day ice sheets are restricted to a few decades and a better understanding of their impact in a long term context is needed. A larger degree of confidence can be placed in predictions of future Sea Level Rise (SLR) and ice sheet mass balance from those Ice Sheet Models (ISMs) that have been rigorously tested against *palaeo*-data, Stokes et al. 2015. In this sense, the Last Glacial Maximum (LGM, around 21,000 years ago) and the subsequent deglaciation represent an excellent testing ground for ISMs, due to the relatively abundant data available that can be used in an ISM as boundary conditions, forcings or constraints to test the ISMs results. Several terrestrial and marine geological data have been collected during field studies to improve the understanding of the dimension and chronology of the Eurasian *palaeo*-Ice Sheet (EIS) during the LGM and throughout the subsequent deglaciation, such as QUEEN programme (Svendsen et al. 1999) and the DATED-1 project (Hughes et al. 2016). Such dataset provides reliable sources to constrain and evaluate numerical ISMs investigations of the EIS in the last glacial cycle in terms of ice sheet extent.

In this study, numerical reconstructions of the evolution of the EIS throughout the post-LGM deglaciation are carried out with two hybrid Shallow-Ice/Shallow-Shelf-Approximation (SIA/SSA) numerical ISMs, namely GRISLI (Ritz et al. 2001) and PSU (Pollard & DeConto 2012). These two ISMs differ mainly in the ice stream parametrization and in the complexity with which GL migration is treated (see Subsection 2.2.2). Particular interest is given to the deglaciation of the Svalbard/Barents/Kara Sea *palaeo*-Ice Sheet (SBKSIS). The SBKSIS was a so-called marine-based ice sheet, as its largest portion rested several hundreds of meters below the sea level in the Barents and Kara seas. From a bathymetric and topographic point of view, there is a strong similarity

between the SBKSIS at the LGM and the *present-day* West Antarctic Ice Sheet (WAIS), as pointed out first by Mercer 1970 (see Figure 1.1). In fact, both these polar regions contain a wide continental shelf few hundred meters deep.

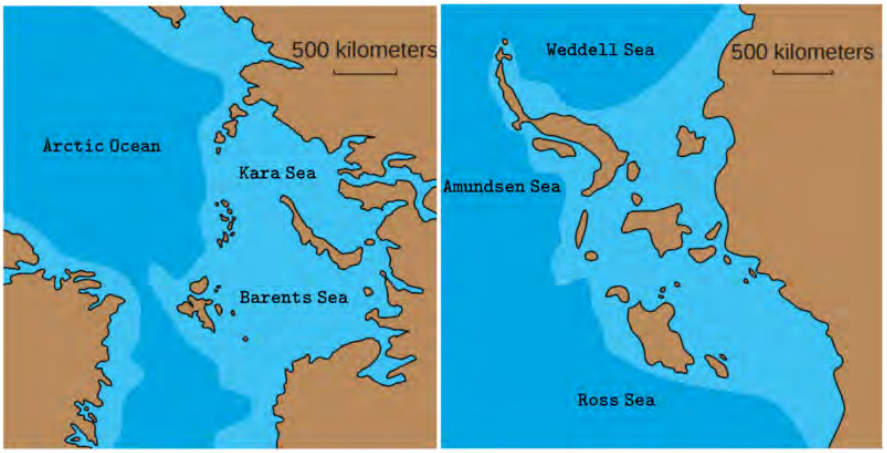

Figure 1.1: After Siegert et al. 2002: bathymetric similarity between the Barents Sea (*left*) and western Antarctica (*right*). The shallow continental shelf is represented in light blue.

Therefore to identify, reconstruct and analyze with ISMs the dynamical processes driving the deglaciation of the SBKSIS may be important to understand the present and the future evolution of the WAIS. In particular, in order to better capture such dynamical processes, the simulated evolution of the Storfjorden glacial system in the north-western Barents Sea is carefully analyzed. *Palaeo*-data from this area provide in fact precious insights into the dynamics history of Storfjorden and Kveithola ice streams, allowing for a thorough model-data comparison for the Storfjorden ice stream evolution in the last 21 thousand years (ka).

The main scientific questions that this study aims to answer are the following:

- What component of the climate-ice sheet system primarily drives the simulated Eurasian *palaeo*-Ice Sheet last deglaciation both in its marine and terrestrial portion?

- To what extent do the different parametrization of ice stream dynamics and Grounding Line migration in the Ice Sheet Models impacts the simulated deglaciation of the Eurasian *palaeo*-Ice Sheet?

- To what extent do the use of different ocean basal melting parametrizations in the Ice Sheet Models impacts the simulated deglaciation of the marine-based Svalbard/Barents/Kara Sea *palaeo*-Ice Sheet and the Storfjorden ice stream retreat?

- Is the simulated Eurasian *palaeo*-Ice Sheet evolution during the last deglaciation in agreement with the observations in terms of ice sheet volume and extent through time?

- Is the timing of the simulated Storfjorden ice stream deglaciation in agreement with the field observations?

- Sediment cores data from Storfjorden and Kveithola troughs suggest rapid Storfjorden ice stream melting and retreat in response to the Meltwater Pulse-1A between 14.7 and 13.5 thousand years ago (ka BP); are the numerical Ice Sheet Models able to reproduce such an event?

- The presence of Grounding Zone Wedges in Storfjorden and Kveithola troughs suggests that during the ice streams retreat the Grounding Line experienced several still-stands lasting hundreds of years; is this dynamic behaviour reproduced by the Ice Sheet Models employed?

1.2 Climate and Ice Sheets in the past: a general overview

1.2.1 Atmosphere/ocean/ice-sheet feedbacks and interaction

Climate and ice sheet interactions are a two-way coupling; on the one hand, ice sheets respond nonlinearly to climate changes. On the other hand, the growth and decay of ice sheets affects the global climate system on several time scales, Stocker et al. 2013. In Figure 1.2, a synthesis of the climate system-ice sheets interactions is shown. A very important example of this mutual interaction is represented by the so-called ice-albedo positive feedback, which is recognised to play an important role in polar amplification in climate change, Masson-Delmotte et al. 2006, Perovich et al. 2007. The albedo is the fraction of solar radiation that is reflected. A reduction (increase) of the area of snow-covered land, ice sheets, glaciers or sea ice results in lower (larger) albedo. Consequently, cooling tends to increase the ice cover and hence the albedo, which causes a reduction in the amount of solar energy absorbed and thus leads to a further drop in surface air temperatures. Conversely, warming tends to decrease the ice cover and consequently the albedo, which leads to an increase in the amount of solar energy absorbed resulting in turn to larger surface air temperatures, Deser et al. 2000. Moreover, as ice sheet height increases, air surface temperatures drop down as a result of the lapse-rate effect. The lapse-rate effect accounts for the decrease in air temperature with altitude in the troposphere. The environmental lapse rate value measures the rate of such air temperature cooling with altitude. According to the International Civil Aviation Organization (ICAO), the average value for the Earth's environmental lapse rate is 6.49 ^{o}C/km, ICAO 2002. The increase in ice sheet height and the consequent air temperature decrease also affects snow accumulation because of the so-called elevation-desert effect, Oerlemans 1980. In fact, as the air cools down its ability to hold moisture decreases. A typical vertical profile of the air temperature and moisture in the troposphere is shown inlay in Figure 1.2. Lapse-rate and elevation-desert effects represent a crucial negative feedback for ice sheets in limitating their growth, Stocker et al. 2013. The presence of large ice sheets at middle to high latitudes in the northern Hemisphere (NH) also causes a deviation in the path of the extratropical NH Westerlies, which are winds predominantly

from the South-West toward the North-East in middle latitudes between 30° and 60°, Cook & Held 1988. Large ice sheets act as topographic barriers for such warm air masses coming from the South and as a consequence only the western side of the ice sheets will be warmed, whilst the remainder part of the ice sheets will remain cool, *e.g.*, Roe & Lindzen 2001. More in general, a reorganization of the global atmosphere circulation is led by the orographic effect of large ice sheets, thus allowing for a fast transmission of ice sheet signals to remote regions, Stocker et al. 2013. Isostatic depression of the solid Earth as a result of the enormous ice sheets surface loading can reach values of up to 1 km, causing a drop in ice sheet height, which in turn leads to a surface warming as a result of the lapse-rate effect, Van den Berg et al. 2008, Stocker et al. 2013. Moreover, the isostatic adjustment of the Earth affects changes in relative sea level and so influences the amount of calving and Grounding Line (GL) dynamics, Van den Berg et al. 2008. Studies depict the isostatic adjustment as an internal feedback mechanism to generate the 100-ka cycle evident in observational records in response to orbital forcing, *e.g.*, Birchfield et al. 1981.

As concerns the *so-called* marine-based ice sheets, *i.e.*, ice sheets whose bed lies below sea level, interaction with the ocean plays an important role in regulating ice shelves mass balance and consequently ice sheets and GL dynamics, as shown in several recent studies in the WAIS, *e.g.*, Pollard & DeConto 2009, Hellmer et al. 2012, Golledge et al. 2015, Li et al. 2015, Feldmann & Levermann 2015, Alley et al. 2016, Sato & Greve 2012. Loss of ice shelf mass is observed, especially in West Antarctica, where warm sea water reaches ocean cavities beneath ice shelves, Rignot et al. 2013, Pritchard et al. 2012. Increased submarine melting is also acknowledged to have triggered the retreat of outlet glaciers in the Greenland Ice Sheet (GIS), Joughin & Alley 2011, Straneo & Heimbach 2013. Ice shelves provide resistance to the flow of grounded ice towards the ocean, a mechanism referred to as buttressing effect. If this resistance is decreased as a result of ice shelf thinning or disintegration, acceleration of grounded ice can occur, increasing rates of sea-level rise, Alley et al. 2016. Advection of warmer waters below ice shelves can also induce GL retreat. Theoretical boundary layer studies such as Weertman 1974 and Schoof 2012 show that marine ice sheets volume and extent changes can be abrupt because of the GL instability that can occur in coastal regions where bedrock is retrograde, *i.e.*, sloping towards the interior of the ice sheet (marine ice sheet instability), Stocker et al. 2013. On orbital and millennial time scales such processes may have played a relevant role in driving ice volume changes in all the marine-based portions of ice sheets, such as the WAIS over the last five million years (Pollard & DeConto 2009, Naish et al. 2009). Pliocene ISMs simulations of the Antarctic Ice Sheet (AIS) from the international Pliocene Ice Sheet Modeling Intercomparison Project (PLISMIP-ANT) demonstrate that high ocean temperatures are able to induce a retreat of the WAIS from its present-day configuration, de Boer et al. 2015. ISM simulations of the AIS evolution over the last 25 kyr show that changes in Southern Ocean temperature foster episodes of accelerated ice sheet retreat due to warm subsurface water thermally eroding grounded marine-based ice, Golledge et al. 2012. Concerning the NH, conceptual ISM simulations demonstrate that North Atlantic ocean temperature oscillations generate periodic pulses of iceberg discharge in an ice-sheet/ice-shelf system, thus suggesting a link between millennial-scale North Atlantic ocean temperature variability and cold Heinrich events during the last glacial period, Alvarez-Solas et al. 2010. In particular, combined coupled climate model

and ISM simulations show that that the penetration of the North Atlantic intermediate water in the Labrador Sea has strong impacts on the Laurentide *palaeo*-Ice Sheet (LIS) dynamics during Heinrich event 1 (18 to 15 ka BP), Álvarez Solás et al. 2011. Simulations of the NH last glacial inception with a three-dimensional thermomecanical ISM, forced with a coupled climate model, suggest that high oceanic heat transport into the Nordic Seas is able to prevent large scale ice growth over Scandinavia, Born et al. 2010.

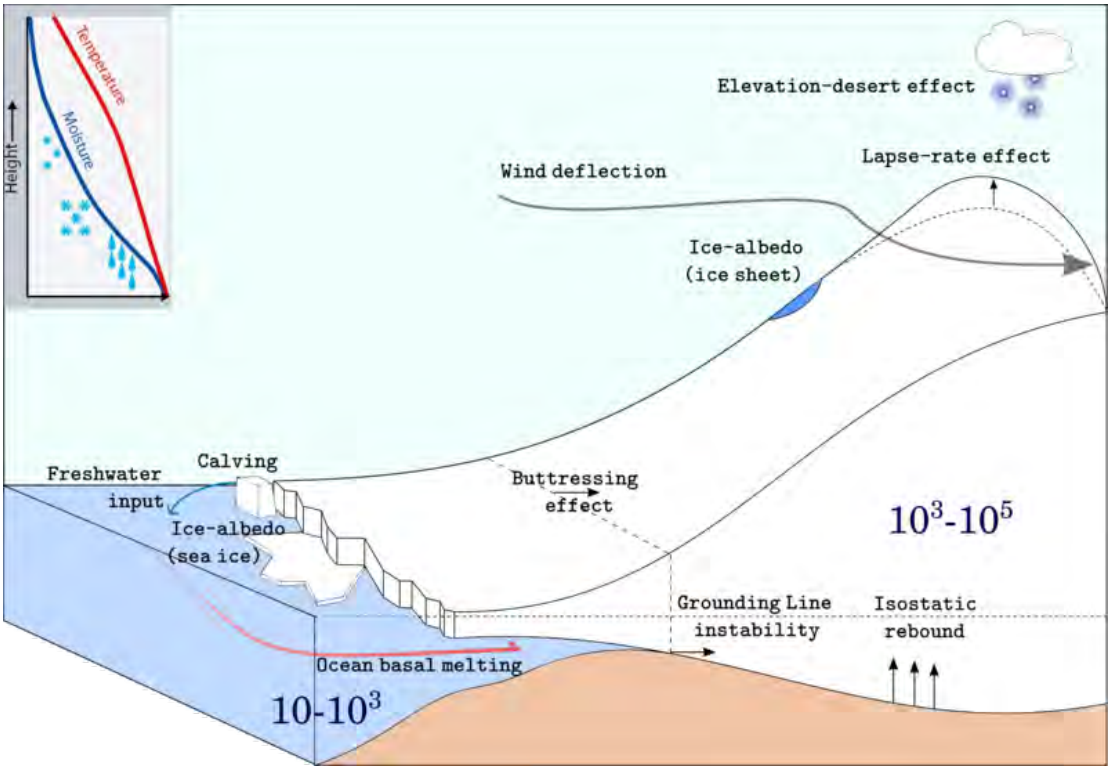

Figure 1.2: Schematic illustration of multiple interactions and feedbacks between ice sheets and the climate system discussed in this subsection. The inlay figure from Solomon et al. 2007 represents a typical height profile of atmospheric temperature and moisture in the troposphere.

Massive freshwater inputs to the ocean resulting from large ice sheets melting affect the climate system by altering sea level, oceanic deep convection, ocean circulation, heat transport, sea ice and the global atmospheric circulation, Stocker et al. 2013. Sediment data and model simulations show that some of the past changes occurring in the northern Hemisphere could have been triggered by instabilities in the ice sheets surrounding the Atlantic at the time and by the associated release of freshwater into the ocean. If on the one hand the initial response of ice sheets to climate forcings can be quite fast, involving for instance ice shelf processes and outlet glaciers (10 to 10^3 years), on the other hand their long-term adjustment can take much longer (10^4 to 10^5 years), which implies that climate and ice sheets are not even in full equilibrium with the orbital forcing. Feedback-derived abrupt climate change events do not necessarily involve large changes in global mean temperature and are usually not synchronous in the northern-southern Hemisphere, Solomon et al. 2007.

1.2.2 Previous modeling studies of the last glacial/interglacial cycle

Milanković theory (Milanković 1941) suggests that conditions for cooler (glacial) and warmer (interglacial) cycles are driven by temporal variations in the Earth's orbit, which affect the amount of solar radiation arriving at the top of the Earth's atmosphere (*i.e.*, the insolation) during the summer. Nevertheless, both intensity and duration of cold and warm cycles are strongly influenced by non-linear amplification mechanisms involving the atmospheric carbon dioxide (CO_2) concentration (*e.g.*, Berger et al. 1999), alterations in the thermohaline circulation (*e.g.*, Kageyama et al. 2006) and in the vegetation cover (*e.g.*, Claussen 2009), as well as the atmosphere/ocean/ice-sheet set of feedbacks described in the previous Subsection. During the last glacial cycle, major ice sheets experienced alternating phases of expansion and regression (Bonelli et al. 2009 and references therein). Ice sheet extent and thickness reconstructions based on refined models of glacial isostatic adjustments, constrained by relative sea-level (Yokoyama et al. 2001, Lambeck & Chappell 2001; Lambeck et al. 2002) and geological observations (Peltier et al. 1994, Peltier 2004) have been proposed. Although such reconstructions show a good match with individual estimates in each corresponding region, the reconstructed ice thickness is often underestimated in regions in which no data are available, Bonelli et al. 2009. Moreover, glacial isostatic adjustment models do not include atmosphere/ocean/ice-sheet physical processes and are not able to reconstruct the dynamical evolution of the ice sheets through time. In this sense, modeling ice sheet dynamics represents an important challenge to improve our knowledge of the Earth's glacial and climatic history.

Several numerical ice sheet modeling studies aimed at reconstructing the volume and extent of the NH major ice sheets over the last glacial cycle or during specific periods such as the last glacial inception or the last deglaciation, Bonelli et al. 2009. Different approaches have been undertaken in such studies. A widely used approach consists in using palaeoclimatic data to force the ISM. For instance, Siegert & Dowdeswell 2004 simulated the EIS evolution between 30 and 12 ka BP by forcing an ISM with an near-surface air temperature change matched to the CO_2 signal, assumed to represent a proxy for global ice volume. Other studies employ outputs from climate simulations with General Circulation Models (GCMs). For instance, Yamagishi et al. 2005 reconstructed the NH major ice sheets at the LGM by forcing the ISM with a steady-state LGM climatology previously simulated with a high-resolution atmospheric GCM. However, steady-state ISMs simulations allow to reconstruct the ice sheet extent and volume during a specific time period, in order to investigate whether the simulated ice sheets are in equilibrium with the forcing climate, Bonelli et al. 2009. In order to reconstruct the ice sheet evolution through glacial cycles, glacial inceptions or deglaciations a widely used approach is to force ISMs with GCM time-slices experiments interpolated through time using near-surface air temperature and precipitation indexes derived from isotopic records from ice cores. For instance, Zweck & Huybrechts 2005 reconstructed the NH major ice sheets during the last glacial cycle by forcing an ISM with temperature and precipitation anomalies from the United Kingdom Meteorological Office GCM scaled to the oxygen isotope record. Charbit et al. 2007 simulated the evolution of the NH major ice sheets through the last deglaciation by forcing an ISM with a time-evolving climatology provided by the linear interpolation through time of climate snapshots (at 21, 15, 9, 6 and 0 kyr BP) simulated by the LMD5.3 atmospheric GCM, driven by insolation,

atmospheric CO_2 content, ice-sheet configuration and sea surface temperatures. In a more recent work, Patton et al. 2016 employed an ISM to perform transient simulations of the EIS throughout its build-up from 37 ka BP to 19 ka BP. The model is forced with Mid-Weichselian (MIS4) and LGM climatologies from GCM experiments scaled with the oxygen isotope record. Other numerical ISM studies employing a similar approach are for instance Marshall et al. 2000; Marshall 2002, Charbit et al. 2002, Tarasov & Peltier 2004, Clason et al. 2014. However, although such method successfully provides consistent reconstructions of NH major ice sheets, the ice evolution does not feed back on climate, Bonelli et al. 2009. An alternative approach consists in employing ISMs fully coupled with climate models. For instance, Berger et al. 1999 employed a two-dimensional ISM coupled with a simplified climate model driven by insolationand atmospheric CO_2 concentration to simulate the evolution of the NH major ice sheets over the last glacial cycle. Tarasov & Peltier 1999 simulated the NH major ice sheets evolution in the last 100 kyrs by using an energy balance model coupled with a three-dimensional ISM. Transient simulations with a three-dimensional thermo-mechanical ISM coupled with a climate model of intermediate complexity (atmosphere/ocean/vegetation) have been performed to simulate the evolution of the NH major ice sheets during the last glacial cycle, in order to investigate the ice sheets response to both insolation and atmospheric CO_2 concentration (Bonelli et al. 2009, Ganopolski et al. 2010). Heinemann et al. 2014 employed a three-dimensional thermo-mechanical ISM coupled with a climate model of intermediate complexity (atmosphere/ocean/sea-ice/land) to simulate the evolution of the NH major ice sheets between 78 and 0 ka BP. Similarly as in Bonelli et al. 2009 and Ganopolski et al. 2010, the study demonstrated the role of changes in the orbital parameters as main driver mechanisms for glacial inception, as well as the important role played by atmospheric CO_2 concentration in determining a simulated glacial history consistent with geomorphological data.

1.2.3 Cenozoic history of the Eurasian Palaeo-Ice Sheet

Since around 55 million years ago (Ma), Earth's climate has undergone a profound cooling at both poles and across the lower latitudes of both hemispheres (see Figure 1.3b), Ruddiman 2001. CO_2 concentrations have been low and the poles glaciated (see Figure 1.3a), Zachos et al. 2008. In the southern Hemisphere (SH), Ice-Rafted Debris (IRD) dating back to $\sim$35 Ma found in ocean sediment on the continental margin of Antarctica represents the first evidence for ice, whilst in the NH the earliest recorded appearance of IRD in the Norwegian-Greenland Sea dates between 44 and 30 Ma, Eldrett et al. 2007, Tripati et al. 2008. During the first part of the Oligocene (around 33.55 Ma) a large AIS is suggested to have formed, causing a 55-70 m eustatic sea level fall and a 1% increase in the ratio of stable isotopes oxygen-18 ^{18}O and oxygen-16 ^{16}O (see Figure 1.3b), Francis et al. 2008. Such a ratio, commonly denoted with $\delta^{18}O$, is known to be an excellent proxy for surface air temperature and, based on the assumption that the variation in $\delta^{18}O$ can be attributed to the temperature change alone, Epstein & Mayeda 1953 estimated that a $\delta^{18}O$ increase of 0.22% is equivalent to a cooling of $1^{o}C$. Sudden and widespread glaciation in Antarctica around 33.55 Ma appears to have been caused primarily by low atmospheric CO_2 concentrations (see Figure 1.3a), orbital forcing and ice-climate feedbacks rather than by the opening of southern Ocean gateways, Pollard

& De Conto 2003. Following the ice-free Middle Miocene Climate Optimum (MMCO, 17-15 Ma) the expansion of the EAIS resulted in a global cooling (Pekar & DeConto 2006) and a reduction in atmospheric CO_2 concentrations from ∼500 ppmv to ∼300 ppmv (see Figure 1.3), Kürschner et al. 2008. During the Late Pliocene continental-sized ice sheets likely began to develop in the NH, between 3.6 and 2.4 Ma, with a long term increase of ice volume (0.4%) leading to a sea level lowering of ∼43 m, Mudelsee & Raymo 2005, Knies et al. 2009, Matthiessen et al. 2009. Due to the slow ice build-up, a slow, tectonic mechanism has been proposed as the main driver of the northern Hemisphere glaciation (NHG), Mudelsee & Raymo 2005.

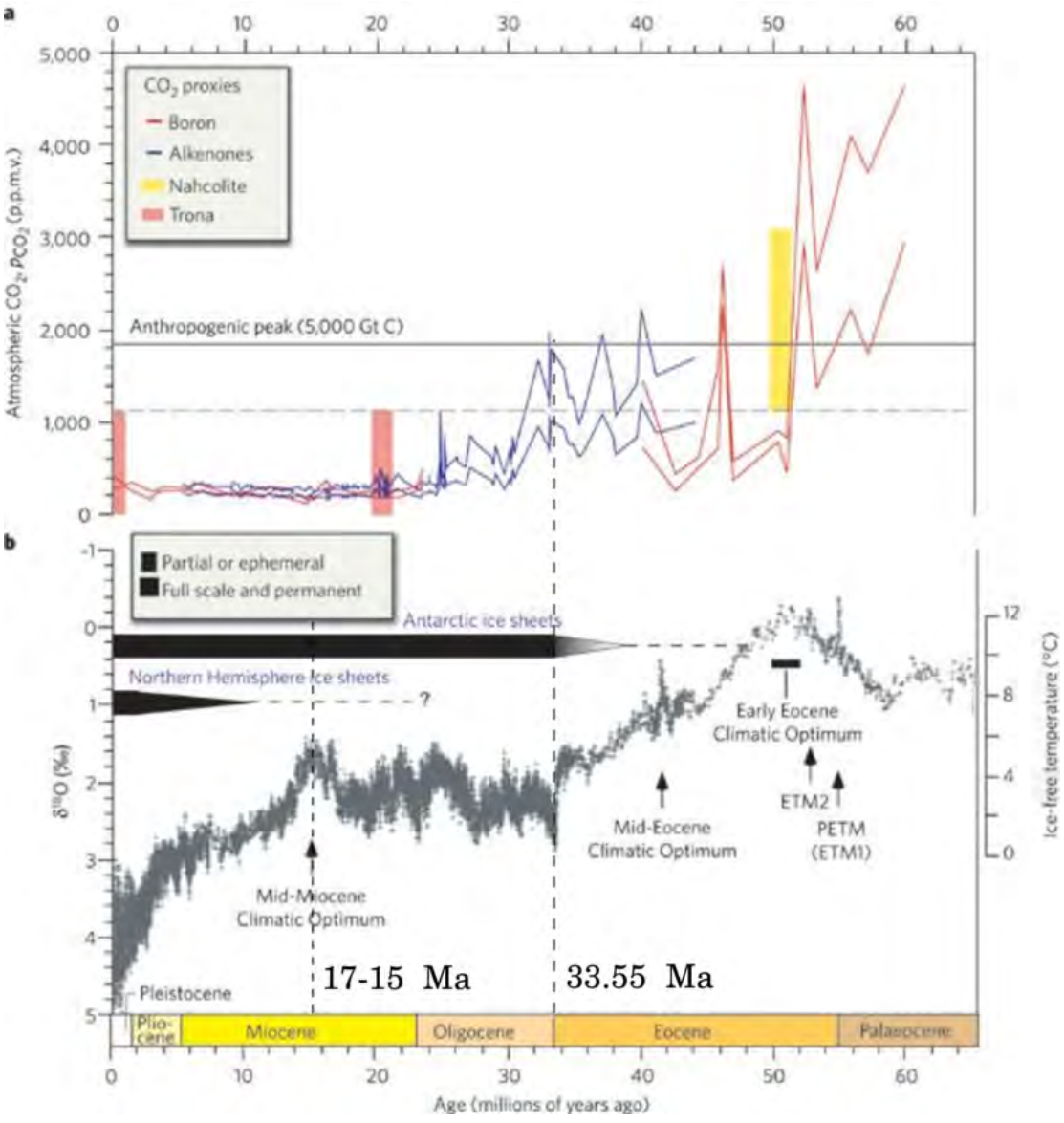

Figure 1.3: After Zachos et al. 2008; (a) Cenozoic CO_2 concentration for the period 0-65 Ma, according to a compilation of marine and lacustrine proxy records (see Zachos et al. 2008 and reference therein). The dashed horizontal line represents the maximum CO_2 concentration for the Neogene (Miocene to present) and the minimum CO_2 concentration for the early Eocene (1,125 ppmv). (b) Climate evolution for the same period (0-65 Ma) deduced from the variation of the $\delta^{18}O$. The $\delta^{18}O$ temperature scale, on the right axis, was computed on the assumption of an ice-free ocean; it therefore applies only to the time preceding the onset of large-scale glaciation on Antarctica (about 35 Ma).

Many other hypotheses have been suggested in order to explain the NHG, as for instance the shoaling of the Central American Seaway during the Pliocene, which may have resulted in an intensified Gulf Stream and consequently to an increase in moisture transport to high northern latitudes, Keigwin 1982. Raymo et al. 1988 proposed the Tibetan uplift to have led to chemical weathering-induced atmospheric carbon dioxide removal; moreover, Tibetan uplift could also have resulted in a tenfold increase in atmospheric dust load, due to aridification effect, and a strengthening of the East Asian monsoon resulting in a more powerful weathering process, Mudelsee & Raymo 2005. Also, the restriction of the Indonesian Seaway could have reduced the amount of atmospheric heat transported from the tropics to higher northern latitudes in the Pacific region, Cane & Molnar 2001. Around 1.1 Ma large-scale intensification of glaciation in the northern Hemisphere started, with a significant increase in global ice volume during the mid-Pleistocene transition around 0.94 Ma (Mudelsee & Stattegger 1997) associated with a distinct sea level drop of 20-30 m, Kitamura & Kawagoe 2006.

In the Barents Sea, IRD and mineralogical data suggest the prevalence of mountainous to coastal-style glaciations on the exposed lands in the initial ice growth phase between 3.6 and 2.4 Ma (see Figure 1.4a), Knies et al. 2009. According to Rebesco et al. 2013, ice expanded in this age beyond the coast North of Svalbard. Concomitant with the ∼2.7 Ma global ice volume increase, short-term glacial expansion beyond the coastline is documented in the north-western Barents Sea in response to Late Pliocene climate deterioration. Between 2.4 and 1.0 Ma the SBKSIS developed to a moderate size (see Figure 1.4b), Knies et al. 2009. Data collected by Rebesco et al. 2013 suggest that the SBKSIS extended to the continental shelf edge in Bjørnøyrenna around 1.5 Ma and in Storfjorden/southern Spitsbergen around 1.2 Ma respectively. The intensification of glaciation in the Barents Sea around 1.0 Ma coincides with glacial expansions in the circum-Atlantic region and over the entire Barents Sea (Knies et al. 2009), as shown in Figure 1.4c.

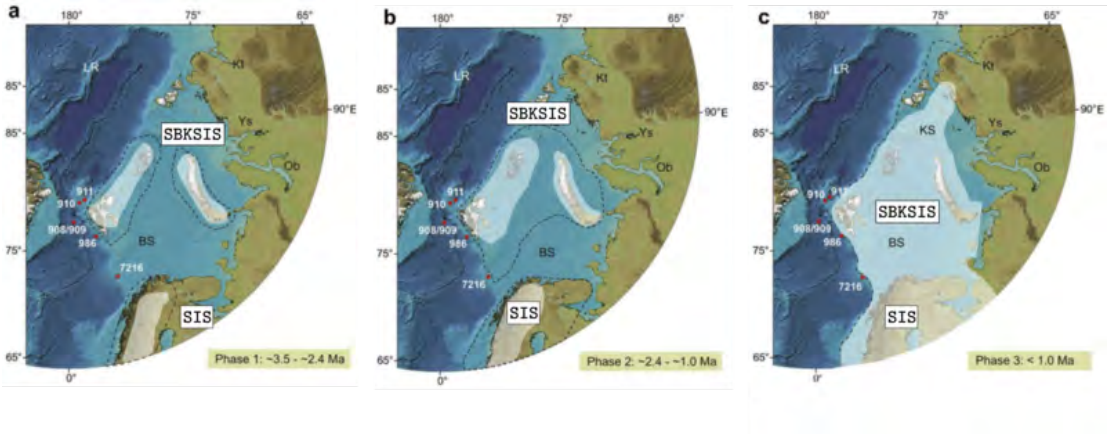

Figure 1.4: After Knies et al. 2009; Schematic (min./max.) model of ice extension in the Barents Sea region during the Late Plio-Pleistocene time period (black stippled lines = maximum; white transparent polygons = minimum): (a) Phase 1 (∼3.5–2.4 Ma), (b) Phase 2 (∼2.4–1.0 Ma) (c) Phase 3 (<1.0 Ma) is represented by the reconstructed Saalian (maximum) and LGM (minimum) glaciations (Svendsen et al. 2004).

The SBKSIS reached the shelf edge during glacial maxima and massive meltwater pulses during major terminations of the ice sheet suggests that at least five or six shelf edge glaciations have taken place in the Barents Sea over the past 800 ka, Knies et al. 2009. In Eurasia, four major glaciations have been recorded during the last 160 ka although the majority of this time the ice cover was only limited, Mangerud et al. 2001.

The terrestrial and marine geological data collected in the Eurasian Arctic within the Quaternary Environments of the Eurasian North (QUEEN) programme consistently improved the understanding of the dimension and chronology of the EIS during the last four glacial cycles, Svendsen et al. 1999, Svendsen et al. 2004. Based on QUEEN geological records, such major glaciations occurred during the Late Saalian (before 130 ka BP) and three times in the Weichselian: during the Early Weichselian (90-80 ka BP), the early Middle Weichselian (60-50 ka BP) and the Late Weichselian (20-15 ka BP). Limits showing the maximum ice sheet extent for each of these glaciations are drawn in Figure 1.5, although the maximum extent during the various glaciations was not necessary attained at the same time in various regions. Late Saalian glaciation (160-130 ka BP) was one of the most extensive Quaternary glaciations in Eurasia and at this time a huge ice sheet complex formed over northern Eurasia (see Figure 1.5a). A large ice shelf possibly fringed the SBKSIS and may have reached into the central Arctic Ocean, Svendsen et al. 2004. During the Early Weichselian a major ice dome was located on the continental shelf in the northern Kara Sea, whereas only a restricted ice sheet existed over Fennoscandia, as shown in Figure 1.5b).

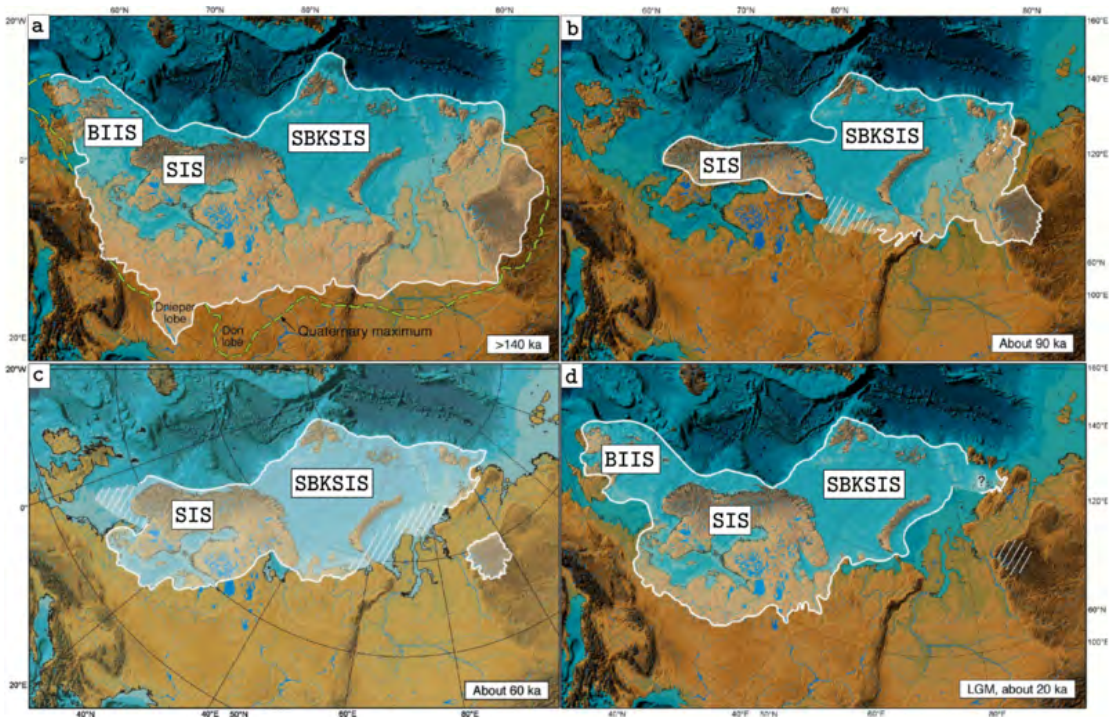

Figure 1.5: After Svendsen et al. 2004; limits showing the maximum ice sheet extent during (a) the Late Saalian (before 130 ka BP), (b) the Early Weichselian (90-80 ka BP), (c) the early Middle Weichselian (60-50 ka BP) and (d) the Late Weichselian (20-15 ka BP) glaciations; notice that the maximum extent during the various glaciations was not necessary attained at the same time in various regions.

A warm interstadial (MIS5a, between 85-75 ka BP) followed the Early Weichselian, causing a major deglaciation in particular in the central Taimyr region due to a marine inundation of the glacioisostatic depressed area, Svendsen et al. 2004. During the early Middle Weichselian, the SBKSIS advanced onto the northern margin of the Eurasian mainland at around 60-50 ka BP, while the southern margin of the Scandinavian *palaeo*-Ice Sheet (SIS) reached Denmark and the eastern flank covered the whole of Finland (see Figure 1.5c), Svendsen et al. 2004. The glaciation around 60-50 ka BP was followed by a major Middle Weichselian deglaciation and most likely the entire Barents-Kara Sea shelves were ice free during the interval 50-30 ka BP. During this interval, evidence from Svalbard suggests that the ice-covered area was not larger than present-day, whilst relative sea levels were lower than present, Mangerud et al. 1998, Ingólfsson & Landvik 2013. Also the early Middle Weichselian SIS likely almost entirely melted by 45 ka BP, Wohlfarth 2010. Subsequent glacial advance off and retreat from the coast of western Norway dates around, respectively, 41 and 38-34 ka BP, Hughes et al. 2016, Mangerud et al. 2010. IRD flux to the West of Scotland indicates that the British/Irish *palaeo*-Ice Sheet (BIIS) was large enough to produce icebergs between 50-30 ka BP, Hibbert et al. 2010, although its extent likely remained limited until 30 ka BP, Hughes et al. 2016. The Late Weichselian glaciation is the most recent major glaciation of the EIS before its disintegration; the evolution of the EIS during the LGM and throughout the subsequent deglaciation is carefully described in the next section.

1.3 Eurasian palaeo-Ice Sheet in the last 25,000 years

1.3.1 Reconstructions based on empirical data

To test and validate numerical models results against *palaeo*-observations and proxy records is essential to improve *palaeo*-ice sheets reconstructions. Concerning the EIS, a comprehensive and up-to-date collection of available *palaeo*-observations of the ice sheet extent during the last 25 ka is the first version of the Database of the Eurasian Deglaciation (DATED-1, Hughes et al. 2016). DATED-1, which provides the EIS extent evolution every 1000 years from 25 to 10 ka BP, is based on a Geographical Information System (GIS) database of published dates constraining ice sheet margin timing and geomorphological/geological evidence from the existing literature. In order to clearly quantify the error, for each time slice uncertainties are estimated into a most-credible ice margin line, with bounding maximum/minimum limits based on the existing data. The DATED-1 database has a census date of 1 January 2013.

This study largely relies on DATED-1 dataset, by comparing simulated and DATED-1 EIS extent and total area evolution from 21 to 10 ka BP. In this subsection the EIS evolution in the last 21 ka based on DATED-1 reconstruction is summarised. Unless differently specified, this subsection refers to Hughes et al. 2016 and references therein. The DATED-1 time-slice reconstructions of the EIS extent between 21 and 10 ka BP are shown in Figures 1.8, 1.9, 1.10 (1000 years time slices). The EIS at its LGM extent comprised the SIS, SBKSIS, and BIIS, covering a total area of 5.5 Mkm^2 and reaching an ice volume comprised between 22 (Peltier 2004) and 24 (Hughes et al. 2016) m Sea Level Equivalent (SLE). Looking at EIS total area evolution in the last 21 ka, SIS area loss is relatively constant between 19-14 ka BP, whilst SBKSIS area loss is relatively

faster between 19-18 ka BP, slower between 18-17 ka BP and constant until 14 ka BP (see Figure 1.7a). Although SIS area loss slows down between 14-12 ka BP, there does not appear to have been a net total ice sheet area growth during the Younger Dryas (YD, 12.7-11.5 ka BP), although local and regional data register SIS ice margin advance during this time, Andersen et al. 1995. Also SBKSIS area loss slows down between 14-12 ka BP; however, the SBKSIS after 15 ka BP already contained less than 1 m SLE of ice (see Figure 1.7b), according to the ice sheet area/volume relationship derived from a logarithmic linear regression of the area and volume of the six largest present-day ice sheets and ice caps, Paterson 1994. Conversely, the SIS at the end of the YD contained 4 m SLE of ice, which is a volume size comparable to present-day estimates for the GIS.

Figure 1.6: After Hughes et al. 2016; map of northern Eurasia, illustrating maximum EIS extent during the last glacial period according to Svendsen et al. 2004. SBKSIS = Svalbard-Barents-Kara Sea Ice Sheet; SIS = Scandinavian Ice Sheet; BIIS = British/Irish Ice Sheet. Topography and bathymetry from the GEBCO Digital Atlas published by the British Oceanographic Data Centre on behalf of IOC and IHO (2003).

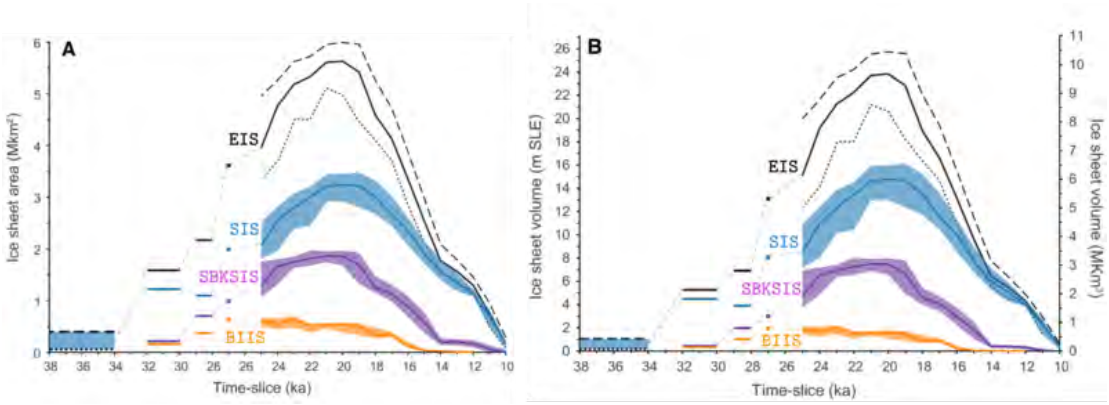

Figure 1.7: After Hughes et al. 2016; evolution of the EIS Area (A) and volume (B) evolution of the EIS from 25 to 10 ka BP (continuous lines).

EIS maximum extent (25-21 ka BP) – BIIS and SBKSIS reached their maximum extent before 25 and 24-20 ka BP, respectively and mantained approximatively the same size for several thousand years. Conversely, the SIS was at its maximum extent relatively late (around 21-20 ka BP), when the ice margin reached the SIS eastern terrestrial limit. The continental shelf edge plays an important role in limiting the EIS growth. In fact, SIS and SBKSIS expansion is restricted on the western margin. Moreover, SBKSIS growth is also limited along the western, northern and north-eastern margin and BIIS can increase its extent only southward, see map in Figure 1.6.

20 ka BP – BIIS surface lowered and a retreat of almost all its margins followed. Retreat of the SIS from the Main Stationary Line (MSL, Denmark) commenced, whilst it remains uncertain whether a retreat from the Pomeranian limit (PL, Poland/Germany) occurred by this time, see map in Figure 1.6 for the MSL and PL positions. It is also not clear whether the SIS retreated from the Norwegian continental shelf to mid-shelf. Analysis of sediment from the North Sea Fan suggests that the calving front of the Norwegian Channel Ice Stream retreated from the channel mouth only after 18.5 ka BP, although in a recent study by Svendsen et al. 2015 the retreat dates around 20 ka BP.

19 ka BP – Minor retreats from the ultimate terrestrial limit are registered in sectors of the southern SIS margin, whereas an ice re-advance over southern Denmark is observed. The SBKSIS started to retreat from the western Barents Sea shelf edge.

18 ka BP – The SIS and BIIS were likely fully separated, whilst the SIS eastern limit advanced showing a thin, highly lobate margin. Although the timing of deglaciation on Novaya Zemlya is uncertain, two radiocarbon dates from the south-western coast suggest that the deglaciation took place before 18 ka BP. The SBKSIS likely retreated from Novaya Zemlya by this age, notwithstanding that the retreat pattern of the SBKSIS eastern Barents Sea margin is poorly constrained. Ice thinning in western Svalbard after 18.5 ka BP is suggested by exposure ages.

17 ka BP – The BIIS extended over Ireland and Scotland only and the SIS appeared to be retreating from the maximum eastern limit across the Russian and eastern European plains. On the Norwegian shelf, the western SIS margin fluctuated during its retreat. According to mapped ice flow directions from the western Barents Sea, the SIS and SBKSIS remained connected by this age; separation between these two ice sheets likely occurred between 17-15 ka BP. Around Svalbard and in the southern Barents

Sea several active ice streams likely caused the ice margin to re-advance multiple times during the retreat and separation of the SIS and SBKSIS. The position of the SBKSIS eastern margin remains speculative by this time.

16 ka BP – The western margin of the SIS continued to oscillate during retreat from the Norwegian shelf, whilst the south-western SIS margin retreated onshore in south-western Norway. The SIS and SBKSIS are separated only in the minimum reconstruction, due to the poorly constrained timing of separation; however, seabed geomorphology suggests that the separation of the two ice sheets occurred consequently to Bjørnøyrenna ice stream retreat and was associated with ice stream activity along the northern Norwegian coast. Retreat pattern from the eastern Barents Sea is still undefined except for indication of ice flow close to Barents Sea central bank.

15 ka BP – The SIS western margin retreated within the Norwegian coastline. The SIS and SBKSIS finally separated in all the three (most credible, minimum, maximum) reconstructions. The northern SBKSIS margin retreated towards the central Barents Sea, Svalbard and Franz Josef Land. According to the minimum reconstruction, Bjørnøya was deglaciated by that age. The ice margin in Svalbard and Franz Josef Land was close to the western coastline.

14 ka BP – The SIS western margin completed its retreat from the entire western coast, whilst on the eastern margin the rate of retreat is poorly constrained and local/regional re-advances might have taken place. By this age the SBKSIS covered Svalbard and Franz Josef Land separately and the Barents Sea is depicted as deglaciated, although constraining dates are scarce.

YD time-slices 13-12 ka BP – YD moraines across Norway document a re-advance of the SIS margin. The ice front position over the Baltic Sea is not well known, although all the Baltic States were likely ice-free before 13.3 ka BP. The SIS eastern margin was closed to the present-day Finnish-Russian border. By 13 ka BP, the SBKSIS margin almost reached the coast in southern Svalbard. In Scotland, ice re-advanced during this period. The BIIS covered the western Highlands in Scotland and likely several small ice caps and glaciers formed in the southern Uplands and Scottish Islands and in Ireland, Wales and northern England. In the 12 ka BP time-slice the ice margin at the end of the YD is shown. By 12 ka BP, much of the Franz Josef Land southern islands and Svalbard outer fjords were likely ice-free.

Post-YD time-slices 11-10 ka BP – The SIS ice margin split into lobes and valley/fjord glaciers after 12 ka BP, not shown in detail in Figure 1.10. Meltwater channels, which can only form below the glacier Equilibrium Line Altitude (ELA), have been found almost on the summits of the Norway and Sweden highest mountains (1500-2000 m a.s.l.). This proves that likely after the YD/Holocene transition the ELA was located above the highest Scandinavian summits, which implies that the ice sheet had no accumulation area and the ice flow was driven by surface slope only. The timing of the final deglaciation of the SIS from the Scandinavian Mountains is not well constrained; according to the available dates SIS deglaciation started shortly after around 10 ka BP and was likely complete by 9 ka BP, or slightly earlier. The BIIS rapidly deglaciated after the YD and Svalbard, Franz Josef Land and Novaya Zemlya were possibly fully deglaciated at this time, with any remaining ice restricted within the present-day coastlines.

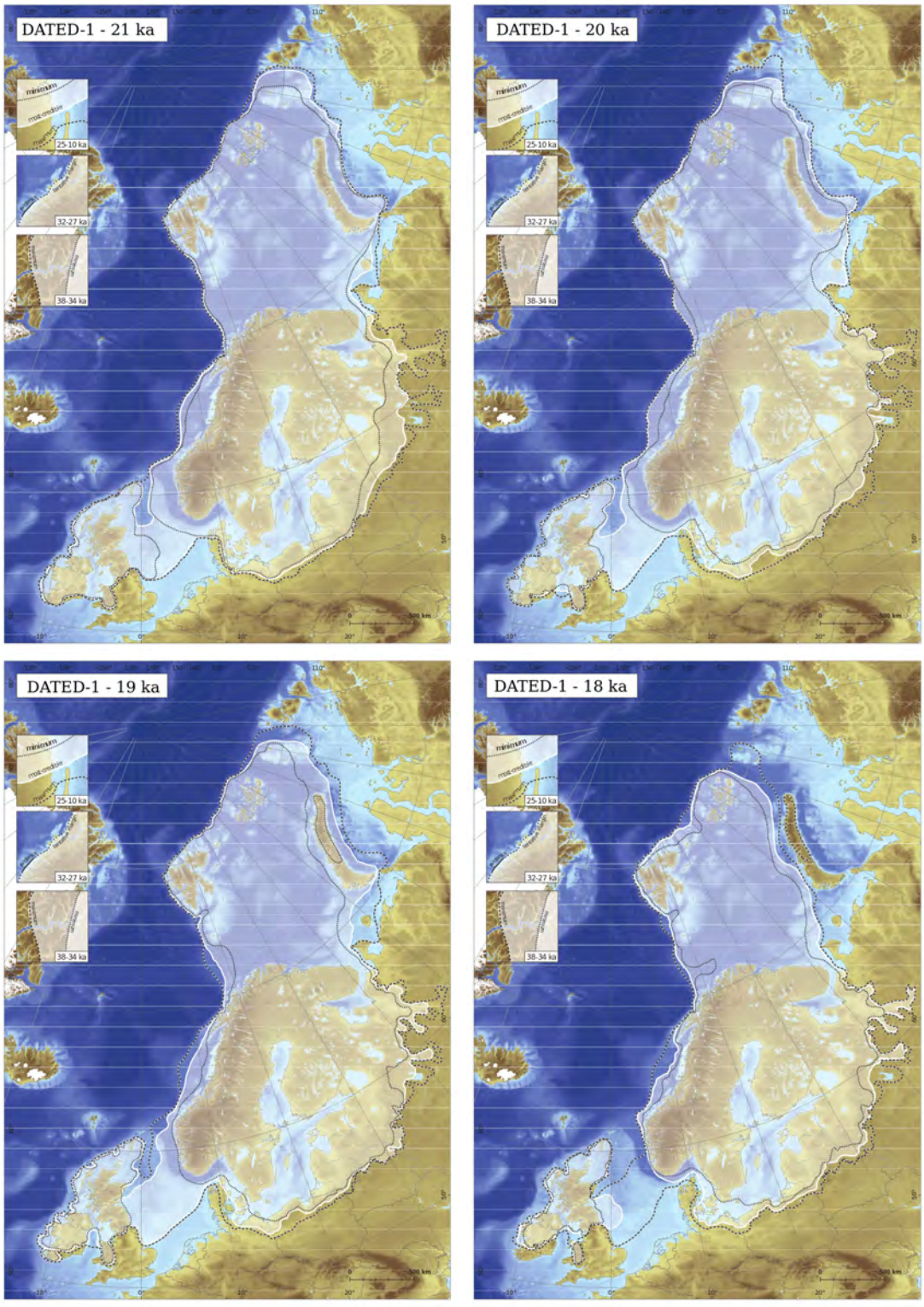

Figure 1.8: After Hughes et al. 2016: 21-18 ka BP DATED-1 time-slice reconstruction of the EIS extent evolution. Most credible (solid white lines), maximum (black dashed lines) and minimum (black dotted lines) ice margin are shown. In the three inlay figures, legends for the ice margin lines between 25-10 ka BP (*top*), 32-27 ka BP (*middle*), 38-34 ka BP (*bottom*) are shown.

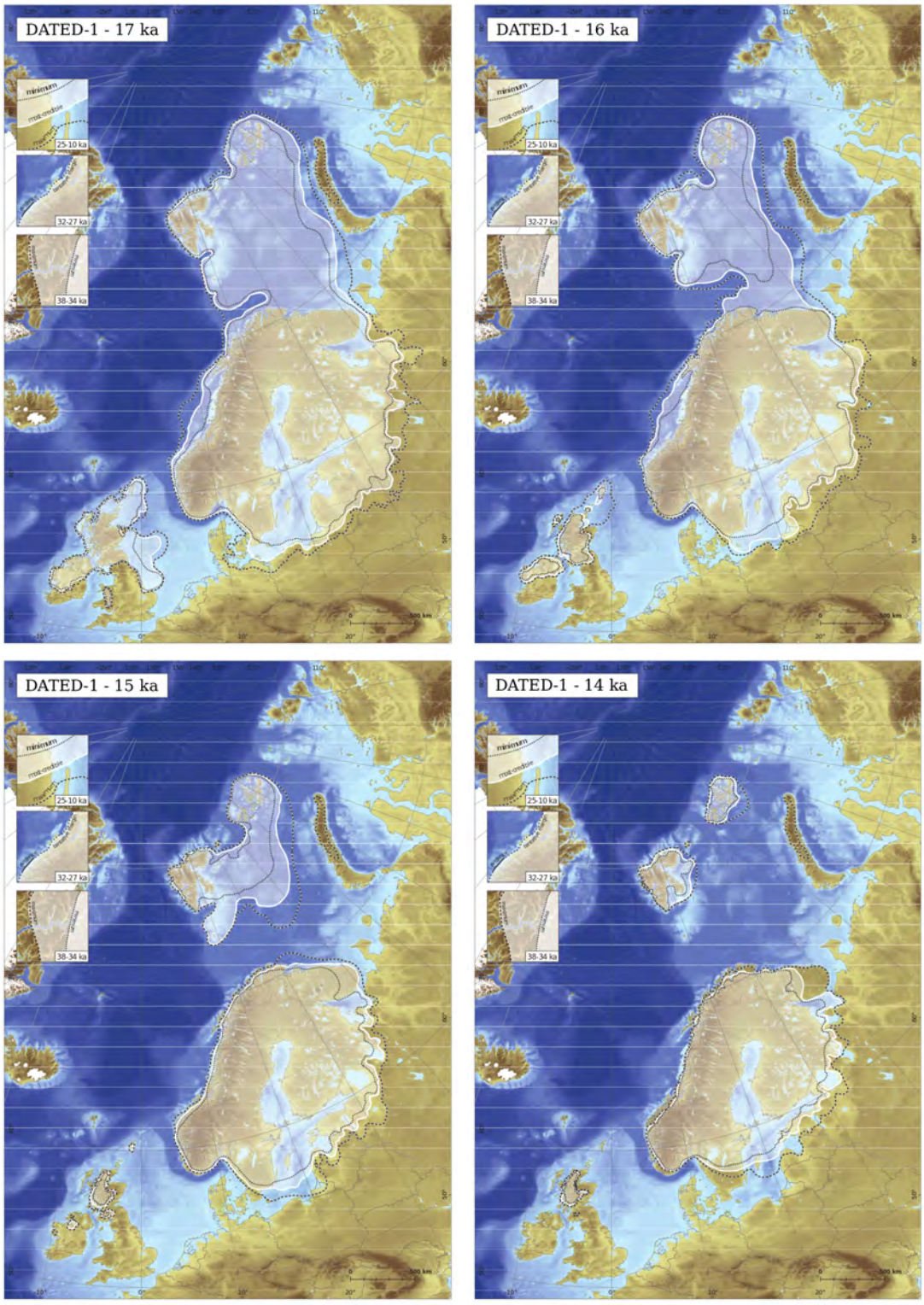

Figure 1.9: After Hughes et al. 2016: 17-14 ka BP DATED-1 time-slice reconstruction of the EIS extent evolution. Most credible (solid white), maximum (black dashed) and minimum (black dotted) ice margin are shown. In the three inlay figures, legends for the ice margin lines between 25-10 ka BP (*top*), 32-27 ka BP (*middle*), 38-34 ka BP (*bottom*) are shown.

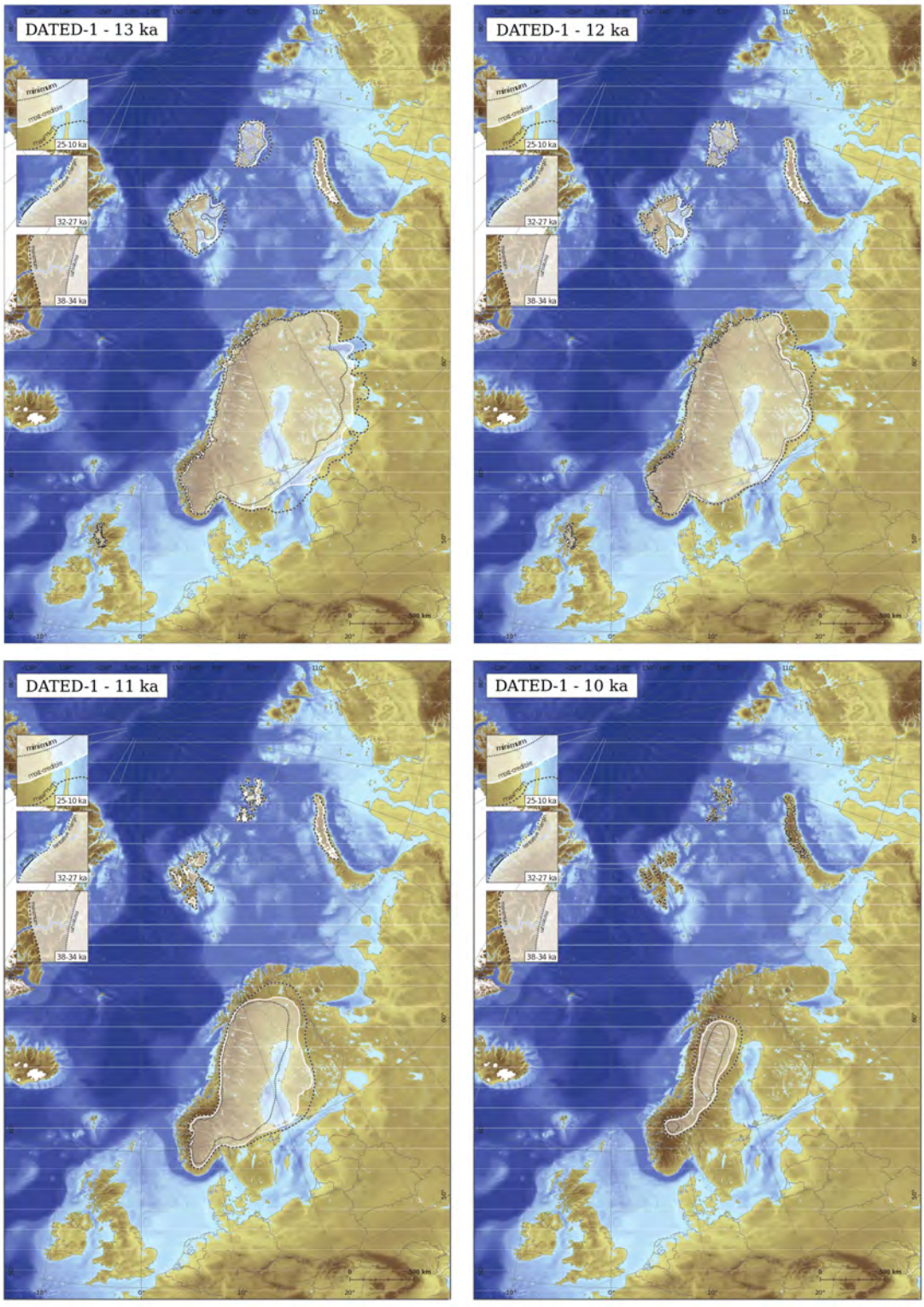

Figure 1.10: After Hughes et al. 2016: 13-10 ka BP DATED-1 time-slice reconstruction of the EIS extent evolution. Most credible (solid white), maximum (black dashed) and minimum (black dotted) ice margin are shown. In the three inlay figures, legends for the ice margin lines between 25-10 ka BP (*top*), 32-27 ka BP (*middle*), 38-34 ka BP (*bottom*) are shown.

1.3.2 Reconstructions based on numerical models

Over the last two decades several earth rheology and ice sheet numerical modelling studies have been dedicated to the reconstruction of the EIS evolution during the last glacial/interglacial cycle. In an early work by Denton & Hughes 1981, steady-state ice mechanical equations have been applied to reconstruct Earth's ice sheets at the LGM, providing ice thickness distribution given the ice sheet margin locations. Such reconstruction, based on the assumption that ice sheets at the LGM were in a state of dynamical equilibrium, largely overestimates the thickness and extent of the EIS, *e.g.* Peltier et al. 1994. A numerical ice sheet model including simplified mass balance, stress balance, heat flow equations and an empirical relationship accounting for isostatic rebound has been employed in Lindstrom & MacAyeal 1989, Lindstrom 1990 to simulate the EIS dynamics during the last deglaciation in response to CO_2 variations. The simulated EIS coverage at the LGM includes the shallow continental shelves of the Barents, Kara, Laptev and East Siberian Seas, whilst the North Sea and Great Britain remains ice-free. A 1 km thick ice shelf forms over the Arctic Ocean and Greenland and Norwegian Seas, and a maximum ice thickness of about 3.5 km over the SIS is registered. The EIS deglaciation in response to CO_2 concentration higher than 250 parts per million (ppm) is predicted to be complete within 9 ka BP. Peltier et al. 1994 employed the global glacial isostatic adjustment model ICE-4G to assess NH ice sheets thickness at the LGM and during the subsequent deglaciation from Relative Sea Level (RSL) data. According to this reconstruction, at the LGM the EIS is suggested to extend over the majority of the Eurasian Arctic, including the Taimyr and Yamal Peninsula, with a maximum ice thickness over the SIS of about 3 km. Moreover, grounded ice entirely covers Great Britain, although the SIS and BIIS remains disconnected. The deglaciation of the SBKSIS is suggested to be complete by 14 ka BP, while the deglaciation of the EIS occurs around 9 ka BP. In opposition to reconstructions where the Eurasian Arctic region was assumed to be continuosly covered by ice, Siegert & Dowdeswell 1995 simulated the SBKSIS alone over the last 30 ka BP with a numerical ISM based on the continuity equation (Mahaffy 1976) and on a steady-state thermal regime assumption. The simulated SBKSIS reaches its maximum extent by 20 ka BP, covering Svalbard, Storfjorden Trough and Spitzbergen Banken in the north-western Barents Sea. The simulated SBKSIS main ice dome is located around eastern Svalbard, with a maximum thickness of 1.2 km. According to this study, SBKSIS decay was complete between 12 and 10 ka BP, depending on the rate of iceberg calving. Similarly, the evolution of the SIS alone has been simulated by Holmlund & Fastook 1995 with a numerical ISM based on the continuity equation (Mahaffy 1976). The simulated SIS reaches its maximum extent around 20 ka BP, whereas the deglaciation takes place between 14.5 and 8 ka BP. The reason for the lack of agreement between such early modelling studies was caused not only by the limitations resulting from the very simplified numerical models employed. In fact, at that time geological observation about EIS thickness, extent and timing were relatively sparse, in particular across the Kara Sea and the coast of Russia, Siegert & Dowdeswell 2004. Therefore, at that time numerical modelers lacked the use of proper *palaeo*-data as boundary conditions and to verify/constrain model results. The terrestrial and marine geological data collected in the QUEEN programme consistently improved the understanding of the dimension and chronology of the EIS during the last

glacial cycles, thus providing reliable sources to constrain numerical ISMs investigations, Svendsen et al. 1999. QUEEN field studies showed that very likely at LGM the EIS did not extend continuously between the Kara and Laptev Sea, Polyak et al. 2002. Moreover, from permafrost profiles and sediment sequences in modern High Arctic lakes it has been inferred that the lowlands of the Taimyr Peninsula were ice-free during LGM, Svendsen et al. 1999. The former numerical ice sheet reconstructions showing a continuous grounded ice cover over Scandinavia, Svalbard and Barents, Kara and Laptev Sea were in clear contrast with such findings (*e.g.*, Denton & Hughes 1981, Peltier 2004, Lindstrom & MacAyeal 1989, Lindstrom 1990). Dowdeswell & Siegert 1999 simulated the EIS evolution over the last 30 ka by employing a numerical ISM based on the continuity equation (Mahaffy 1976) and incorporating a parametrization for sediment deformation and transport beneath ice streams. Numerical simulations from this study indicate that ice streams within bathymetric troughs activate around 25 ka BP. Simulated ice thickness over 1.4 km and not exceeding 1.2 km are found in Barents and Kara Sea respectively, while the simulated SIS thickness exceeds 2.4 km. The simulated SBKSIS margin at its maximum extension reaches the shelf break along the western Barents Sea margin and the Arctic Ocean margin north of the Barents and Kara Seas. The marine portion of the SBKSIS deglaciation starts after 15 ka BP, whilst northern terrestrial ice masses over Svalbard and Franz Josef land decay takes place after 13 ka BP. Storfjorden and Bjørnøya ice streams velocities reach peaks of around 500 and 1000 $\mathrm{m/yr}^{-1}$ respectively. Associated with ice streams activity, simulated delivery of around 4600 and 900 km^3 of sediment at the continental margin of the Storfjorden and Barents Troughs respectively is in good agreement with geophysical observations. The evolution of the EIS through the Weichselian glacial cycle has been simulated in Siegert et al. 2001 by forcing the same ISM as in Dowdeswell & Siegert 1999 with changes in global eustatic sea level and solar insolation. At the LGM the maximum simulated SIS and SBKSIS thickness reaches 2 and 0.75 km. In the Kara Sea the simulated ice thickness does not exceed 250 m, whilst the Taimyr Peninsula remains ice-free. The simulated EIS deglaciation appears to be primarily driven by iceberg calving, leading the marine portion of the SBKSIS to decay first, whereas by 10 ka BP the EIS deglaciation was complete. Peltier 2004 proposed a refined version of the global glacial isostatic adjustment model ICE-4G (Peltier et al. 1994) denoted by ICE-5G. The LGM EIS limits and chronologies provided by QUEEN programme, not available at the time of ICE-4G development, required significant changes with respect to ICE-4G reconstruction. The new QUEEN ice-free topography over most of the Kara Sea and over all of the near coastal region of northern Eurasia results in dramatic differences between ICE-4G and ICE-5G models and provides an excellent agreement between ICE-5G model and RSL data from Novaya Zemlya and south of Novaya Zemlya. The existence of an ice bridge at LGM between the BIIS and the SIS, not known at the time of ICE-4G development, results in reduced BIIS ice thickness. Siegert & Dowdeswell 2004 simulated the evolution of the EIS over the last 30 ka with the same ISM as in Dowdeswell & Siegert 1999, Siegert et al. 2001 by adopting an inverse approach where simulated EIS limits were matched with geological observations. The LGM maximum thickness of the simulated SIS and SBKSIS is 2.7 and 1 km respectively. Similarly to Dowdeswell & Siegert 1999, enhanced iceberg calving in the Barents Sea drives the deglaciation of the SBKSIS from its beginning, 15 ka BP, to its almost complete decay around 12 ka BP, when grounded ice is limited to relatively

shallow seas and archipelagos. Surface melting causes the SIS southern margin to retreat northwards, and by 10 ka BP the EIS deglaciation is almost complete, except for a small ice cap over Scandinavia and few other ice remnants across Svalbard, Novaya Zemlya and Franz Josef Land. In a more recent work, Colleoni et al. 2016 simulated the EIS at the LGM and its evolution throughout the last deglaciation with GRISLI numerical ISM (Ritz et al. 2001), forced with the outputs from six different climate models. The EIS thickness and extent at the LGM vary consistently depending on the climate forcing employed, whilst throughout the deglaciation the eastern part of the EIS is not affected by the choice of the climate forcing. Conversely, the western part of the EIS is more sensitive to surface melt and, as a consequence, to the climatology used to force the ISM. Both in the LGM and in the deglaciation simulation, simulated ice streams within the EIS are well identified and mantain nearly the same location. In the central part of the SIS simulated ice streams are not detected, while in the southern, western and south-western part of the EIS GRISLI simulates large ice streams, independently from the climate forcing. Patton et al. 2016 employed a a first-order thermomechanical ISM to perform transient simulations of the EIS throughout its build-up from 37 ka BP to 19 ka BP. The model is forced with the North Greenland Ice Core Project (NGRIP) $\delta 18\mathrm{O}$ record and empirical evidence such as marginal moraines, exposure ages and relative sea level history is used to constrain the ISM. The study suggests a rapid ice sheet growth. In particular, the western EIS margin expands along much of the western Eurasian shelf break by 29 ka BP. The BIIS, SIS and SBKSIS continue to expand southward and eastward in response to a further temperature cooling, reaching a peak in ice sheet extent ($5 \cdot 10^6$ km^2) and volume (18.1 m SLE) around 22.7 ka BP.

1.3.3 The Storfjorden glacial system (north-western Barents Sea)

Ice streams are acknowledged to play a primary role in ice sheet decay, Margold et al. 2015. Present-day ice streams discharge $\sim$90% of ice in Antarctica (Bamber et al. 2000) and $\sim$50% of ice in Greenland (van den Broeke et al. 2009). In the marine-based WAIS, ice streams might affect the entire ice sheet stability, according to the Marine Ice Sheet Instability (MISI) hypothesis, Weertman 1974. However, observations of present-day ice streams in Antarctica and Greenland are restricted to recent decades and cannot provide insights on ice streams behaviour throughout a whole ice sheet decay cycle. Consequently, reconstructing the location, timing and behaviour of *palaeo*-ice streams can potentially lead to significant improvements in our understanding of the dynamic processes driving present-day and *palaeo*-ice sheets retreat. Insights into the dynamic processes during ice stream flow and retreat are provided by assemblages of submarine landforms exposed by *palaeo*-ice stream retreat across high-latitude continental shelves and fjords, Rebesco et al. 2011 and references therein. In fact, past ice stream activity is associated with characteristic features in the sedimentological and geomorphological record, Stokes & Clark 2001. A very common feature of past ice streaming across transverse troughs on glaciated continental shelves is the developement of Trough Mouth Fans (TMFs), a series of stacked debris flows forming a prograding sediment wedge at the mouth of a cross-shelf trough. On the North-West European glaciated continental margin, many TMFs have been identified, Vorren & Laberg 1997. To analyze and date sediment cores from glacial troughs and associated TMFs to understand the depositional

mechanisms is important in reconstructing past ice sheet dynamics and to decipher palaeoclimate and palaeoenvironment during key periods, such as glacial maxima and deglaciation periods, Lucchi et al. 2013. With geophysical mapping tools, it is possible to study the seafloor morphology and its 3D-structure with higher resolution. Features acknowledged to be indicative of fast-flowing ice are the Mega Scale Glacial Lineations (MSGLs), elongated landforms that are found typically in soft sediments. They can measure 10 to 100 km in length and their length-width ratio is usually larger than 10, Clark 1993. MSGLs provide precious insights into the ice flow pathways. Associated with areas of rapid ice-streaming it is common to find iceberg ploughmarks, features forming in response to the erosive action of drifting-iceberg that grounded and ploughed the sediments, Dowdeswell & Ottesen 2013. 2D seismic-reflection profiles across the continental shelves allow the identification of Grounding Zone Wedges (GZWs). GZWs formation is caused by decades-to-centuries long still-stands during ice sheet retreat across polar shelves; still-stands allow sediment buildup at the Grounding Zone (GZ) through delivery of deforming basal debris from fast-flowing ice streams, Batchelor & Dowdeswell 2015. Typical GZWs are approximately 5 to 20 km long and 50 to 100 m thick, with a lateral width of several tens of kilometers. Their dimension are controlled by sediment flux, still-stand duration and ice stream width. Based on study of *palaeo* and present-day ice streams in Antarctica, estimates of the deforming basal debris delivery flux at the Grounding Zone range between 100 and 800 m^3/yr per m of ice stream width (see Batchelor & Dowdeswell 2015 and references therein).

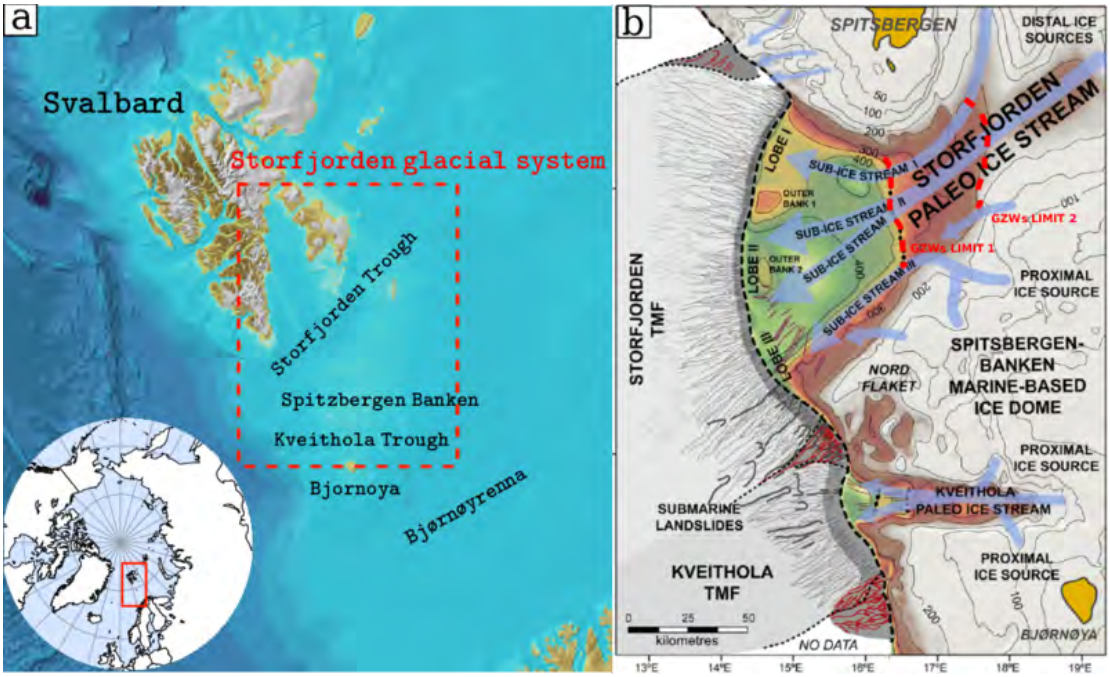

Figure 1.11: (a) Location map of Storfjorden study area, based on IBCAO grid (Jakobsson et al. 2012). Key locations are mentioned in the text. The Storfjorden glacial system is highlighted by the dashed red box. (b) After Pedrosa et al. 2011: Map of Storfjorden study area, with inferred main *palaeo*-ice stream directions during the LGM in Storfjorden and Kveithola Troughs and GZWs limit in Storfjorden Trough.

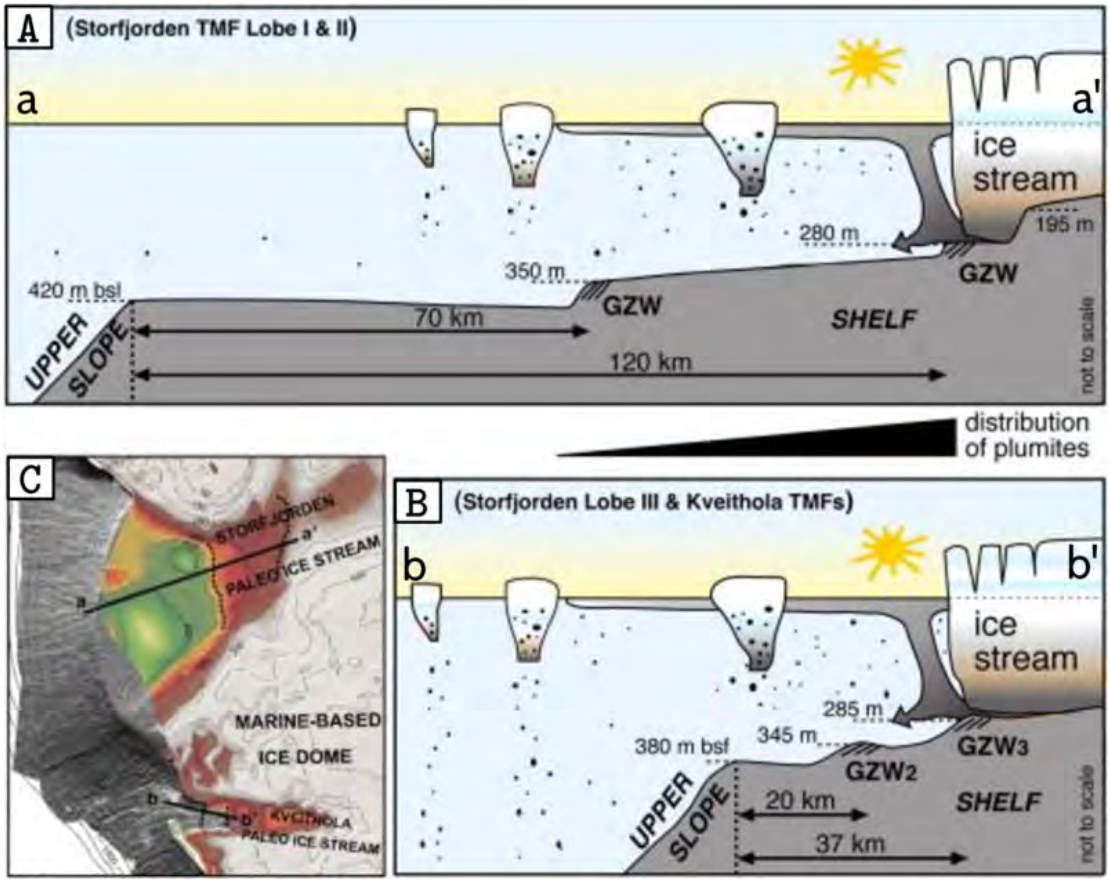

Figure 1.12: After Lucchi et al. 2013: conceptual scheme of the ice stream retreat from the Storfjorden (A) and Kveithola (B) troughs. (C) Bathymetric map as in Figure 1.11b, indicating the location of the two cross sections of figures (A) and (B) and the location of the GZWs formed during the ice streams retreat.

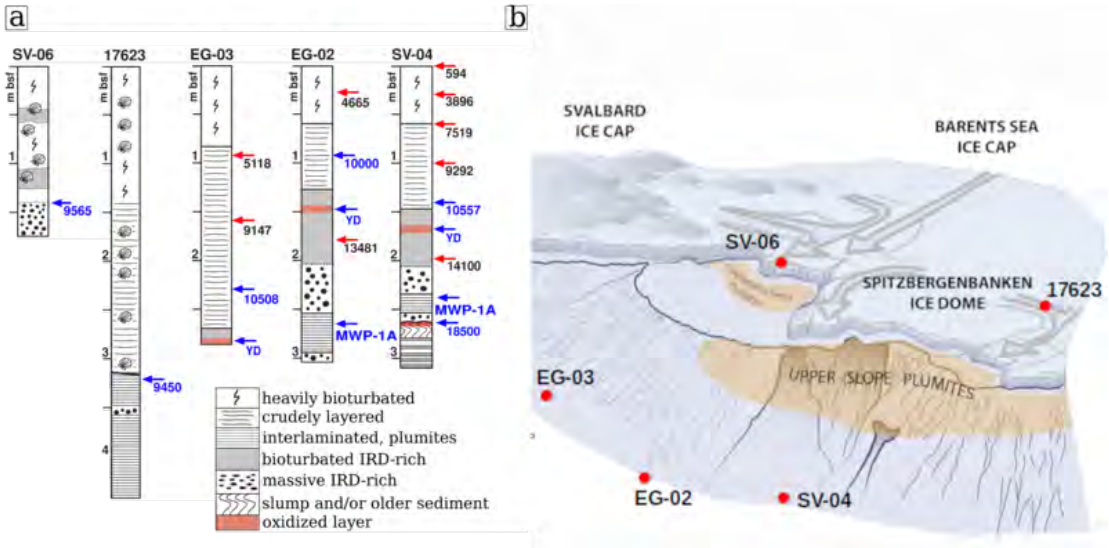

Figure 1.13: From Lucchi R., *personal communication*: (a) synthesis of the main sedimentary facies identified in the SVAIS (SV-04, SV-06), EGLACOM (EG-02, EG-03), CORIBAR (17623) sediment cores with associated timing of deposition according to AMS ^{14}C dating (cal. a BP). In blue the timing of deposition relevant for this study is highlighted; (b) sediment cores position in Storfjorden and Kveithola troughs and TMFs.

In order to reconstruct the *palaeo*-ice streams dynamics history across polar continental shelves it is worthwhile studying the sensitivity of the ice sheet/stream/shelf system to environmental changes such as surface air temperature, precipitation, sea level and ocean temperature and salinity. Glacial systems with small-scale cathment areas and ice reservoirs (*e.g.*, Antarctic Peninsula) show a high sensitivity to frequent climatic changes and thus permit detailed reconstructions of the glacial processes involved during *palaeo*-ice stream advances/retreats. In this sense, the Storfjorden glacial system in the north-western Barents Sea (Figure 1.11a) represents an excellent study area. Storfjorden glacial system is in fact relatively small and it is associated to a relatively small catchment area ($\sim$82,500 km^2), with local provenance from Svalbard and the Spitsbergenbanken, Elverhøi et al. 1998, Mangerud et al. 1998. The catchment area was drained by the Storfjorden ice stream in the North and by the Kveithola ice stream in the South (Figure 1.11b). Due to the short distance between the ice source and calving areas, the ice had relatively short residence times in the ice streams compared to major glacial systems such as Bjørnøyrenna or the Norwegian channel. Multi-beam bathymetry data, sub-bottom seismic profiles and sediment cores (Rebesco et al. 2011, Pedrosa et al. 2011, Lucchi et al. 2013) from Storfjorden and Kveithola troughs and TMFs have been collected during three cruises, SVAIS (Bio Hesperides, July-August 2007), EGLACOM (R/V OGS-Explora, July-August 2008) and CORIBAR (R/V Maria S. Merian, July-August 2013). The aim of the three expeditions was to determine the extent of the SBKSIS in the north-western Barents Sea during glacial periods, to better capture Storfjorden and Kveithola ice streams dynamics and the associated mechanisms of sediment delivery to the ocean and to reconstruct the *palaeo*-environmental conditions in the study area during deglaciation periods, Pedrosa et al. 2011. The presence of MSGLs on the sea floor records typical ice streams flow during the LGM in Storfjorden and Kveithola troughs; both Storfjorden and Kveithola *palaeo*-ice streams reached the shelf edge during the LGM and drained the Storfjorden glacial system, Rebesco et al. 2011. As shown in Pedrosa et al. 2011, Storfjorden *palaeo*-ice stream was actually composed of three sub-ice streams flowing within the same Storfjorden Trough and discharging ice from different ice source areas within the Storfjorden glacial system (see Figure 1.11b for the sub-ice streams flow pathways). Storfjorden sub-ice streams I and II, located in the central and northern part of Storfjorden Trough respectively, discharged the large and distal ice source area of Spitsbergen-Brentsø-Edgeøya and Hopenbanken, respectively. These two sub-ice streams became separated by an area of relatively thinner and slower ice over Outer Bank 1 (Figure 1.11b) on the outer continental shelf. Conversely, Storfjorden sub-ice stream III and Kveithola ice stream drained a local, smaller ice source area in the south-western Spitsbergenbanken. Two outer shelf banks separated the ice flow between Storfjorden sub-ice stream II and III and within Kveithola ice stream respectively, Pedrosa et al. 2011. In both Storfjorden and Kveithola Trough subsequent sediment ridges transverse to ice flow have been interpreted as GZWs formed during still-stands of hundreds of years, Rebesco et al. 2011. According to GZWs location, in Storfjorden Trough the GL retreated first by about 70-80 km from the continental slope, whilst the second GZW is located more inland, about 120 km from the continental slope, as shown in Figure 1.12A. In Kveithola Trough, GZWs were deposited about 20 and 37 km apart from the continental slope (Figure 1.12B), Rebesco et al. 2011. Lucchi et al. 2013 analyzed the sedimentary facies of several SVAIS, EGLACOM and CORIBAR sed-

iment cores in order to identify depositional mechanisms related to palaeoenvironmental conditions in Storfjorden and Kveithola troughs and TMFs. In particular the analysis of five sediment cores (SV-04 and SV-06 from SVAIS cruise, EG-02 and EG-03 from EGLACOM cruise, 17623 from CORIBAR cruise) is particularly relevant for our study, as it provides insights on the Storfjorden and Kveithola ice streams dynamics history during the last deglaciation. The location of the sediment cores SV-04, SV-06, EG-02, EG-03 and 17623 is shown in Figure 1.13b, while a synthesis of their main sedimentary facies is illustrated in Figure 1.13a. The presence of red oxidized sediment in the lower part of core SV-04 has been associated with the release of cold oxygenated waters and is thought to mark the inception of the last deglaciation between 19 and 18 ka BP. The presence in cores EG-02 and SV-04 of a layer containing interlaminated sediments and thick plumite sequences, typically associated with rapid ice stream melting and retreat, is thought to represent the high-latitude marine record of the Meltwater Pulse 1A (MWP-1A). MWP-1A is a dramatic sea level rise event occurring between 14.7 and 13.5 ka BP during which the global eustatic sea level rose about 20 metres within a few hundred years, Lucchi et al. 2013 and references therein. In both EG-02 and SV-04 cores, such interlaminated and plumite-rich layers are preceded and followed by IRD-rich sediment associated with warm climate and enhanced calving rate. Another red oxidized sediment layer is found in the middle part of SV-04, EG-02 and in the lower part of EG-03 sediment cores; in this case Lucchi et al. 2013 intepret this layer as a record of the YD climatic interval. Cores from Storfjorden and Kveithola middle slope (EG-02, EG-03, SV-04) show a gradual change from IRD-rich to crudely layered lithofacies right after YD cold event. Such lithological change, which is accompanied by a first evidence of weak bioturbation and indicates ameliorated climatic/environmental conditions more favorable to biological productivity, dates back to 11-10.5 ka BP. The bioturbations progressively increase and become pervasive in the uppermost part of the three sediment cores, Lucchi et al. 2013. The change from IRD-rich to crudely layered weakely bioturbated sedimentary lithofacies is much more abrupt in sediment cores SV-06 and 17623, which have been collected from Storfjorden and Kveithola inner troughs respectively. The lithological change timing, which dates back to around 9.5 ka BP, is delayed with respect to the sediment cores from Storfjorden and Kveithola TMFs, suggesting that the final retreat of Storfjorden and Kveithola troughs might have taken place in the time frame 11-9 ka BP.

CHAPTER 2

Methods

In this chapter, the methodology adopted in this study is illustrated. First of all, the approach followed to address the main scientific questions posed in this research will be explained. The second section is dedicated to the description of the numerical Ice Sheet Models that have been employed (GRISLI and PSU), with a particular focus on the numerical Ice Sheet Models analogies/differences. The set-up of the simulations performed is illustrated in the second section. The Ice Sheet Models inputs, climate forcing and ocean basal melting parametrizations are shown. It follows a description of the statistical approach that has been adopted in order to deal with poorly constrained parameters in GRISLI numerical model. A method developed to constrain ice streams location in GRISLI numerical model is shown at the end of the section.

2.1 Approach of the study

In order to address the scientific questions motivating this research (see Subsection 1.1), the numerical simulations of the last deglaciation of the EIS need to be analyzed from different points of view. In particular, three different approaches are followed:

- in order to get insights on the ice stream and grounding line dynamics, simulations with two numerical ISMs (GRISLI and PSU) employing different ice stream and grounding line treatment are compared;
- different ocean basal melting parametrizations are tested with both numerical ISMs in order to evaluate the impact of ocean basal melting on the EIS deglaciation;
- simulation results are validated by model-data comparison. Several geological and geophysical reconstructions of EIS evolution and Stofjorden ice stream dynamics history throughout the deglaciation are considered and critically discussed.

The first three scientific questions that are posed in this study aim at understanding what are the components of the climate-ice sheets system which primarily drive the simulated EIS decay and, in particular, the Storfjorden ice stream retreat during the last deglaciation, see Figure 2.1a. Three different basal melting parametrizations are tested (see Subsection 2.3.4) and to what extent the use of different basal melting parametrizations affects the marine-based portion of the EIS is analyzed. The role played by the ice dynamics is investigated through the numerical ISMs intercomparison. In fact, the main discrepancies between the two ISMs employed consists in the different treatment of ice streams and the GL (see Subsection 2.2.2). The other scientific questions posed in this study concern the comparison between simulations and *palaeo*-observations. In this study, a model-data comparison for the last deglaciation of the EIS is proposed on two different scales: first, simulations and *palaeo*-observations are compared on a "global" scale, *i.e.*, by evaluating the evolution of the EIS as a whole, see Figure 2.1b and 2.1c. Model-data comparison is then proposed on a "local" scale by focusing on the Storfjorden glacial system and, in particular, on the Storfjorden ice stream dynamics history, see Figure 2.1c.

Figure 2.1: Schematic representation of the approach adopted to address the scientific questions posed in this study.

As concerns the EIS evolution throughout the last deglaciation, the model-data comparison is performed following different steps:

- for each GRISLI simulation, the simulated total EIS ice volume evolution curves are compared with ICE-5G total EIS ice volume evolution curve and with eustatic SLR data. Best fit simulations with ICE-5G curve and eustatic sea level data are identified;

- model parameter values from GRISLI best fit simulations are used in PSU simulations. Output of PSU simulations are then compared back with ICE-5G total EIS ice volume evolution curve and eustatic sea level data;
- the simulated ice sheet extent in GRISLI best fit simulations with ICE-5G curve and in the corresponding PSU simulations is compared with the DATED-1 EIS reconstruction by Hughes et al. 2016.

The simulated dynamics history of the Storfjorden ice stream throughout the deglaciation is compared with *palaeo*-data from Storfjorden and Kveithola TMFs and troughs as follows:

- for all the GRISLI and PSU simulations, the timing of Storfjorden ice stream retreat from the inner trough is compared with the timing of the onset of interglacial conditions inferred from sediment cores (Lucchi et al. 2013);
- GL dynamics is analyzed during MWP-1A event for the GRISLI best fit simulations with ICE-5G curve and the corresponding PSU simulations. In fact, during such meltwater pulse sedimentary facies associated with rapid ice stream melting and retreat is retrieved in sediment cores (Lucchi et al. 2013);
- by assuming sediment flux of deforming subglacial sediments at the GL of $200\,m^3/yr$ per m of ice stream width is assumed (Dowdeswell et al. 2004, Engelhardt & Kamb 1997), the GZWs formation in Storfjorden trough during the simulated ice stream retreat is estimated. The location of the simulated GZWs in the GRISLI best fit simulations with ICE-5G curve and the corresponding PSU simulations is compared with the GZWs location in Storfjorden trough, according to Rebesco et al. 2011, Lucchi et al. 2013.

2.2 Ice Sheet Models description

Over the last few decades, several ice sheet modelling studies were undertaken and many different types of approaches were followed concerning the complexity of the numerical ISMs equations and boundary conditions, Le Meur et al. 2004. Early numerical ISMs studies employed the Shallow Ice Approximation (SIA, Hutter 1983), which considerably reduces the complexity of the model equations and boundary conditions (*e.g.*, Mahaffy 1976). In the SIA, the ice velocities at the surface are taken proportional to the ice surface gradient and the ice thickness. Such approximation is computationally cheap, and so particularly useful for long-term continental-scale ice sheet simulations, and is able to adequately simulates the ice flow in the interior of ice sheets. However, with the SIA the ice streams can hardly be modeled, as shown by Kirchner et al. 2011. Therefore, in order to simulate fast flowing ice stream and floating ice shelves a proper set of scaled equations has been introduced , namely the Shallow Shelf Approximation (SSA, MacAyeal 1989). In the SSA the longitudinal stresses dominate and the velocities are depth-averaged. Therefore, the use of the SSA is arguable in regions where vertical variations in speed are not negligible, such as across grounding lines, Larour et al. 2012. Moreover, ice stream flow can result both from vertical shear and horizontal stretching. However, a number of hybrid ISMs using heuristic superpositions of the SIA and SSA equations have been developed (see for instance Pollard & DeConto 2012

and references therein). Although such hybrid SIA/SSA models are not rigorous, their computational cost is feasible for long-term continental-scale ice sheet simulations and the SIA/SSA stress balance combination allows high ice velocities to be simulated. In contrast, models with more rigorous (*i.e.*, less approximated) formulations of the ice dynamical equations are computationally too expensive and are not currently feasible for long-term continental-scale simulations, Pollard & DeConto 2012. Since this study aims at simulationg the evolution of the EIS over tha last 21 kyrs, two hybrid SIA/SSA numerical models are employed.

2.2.1 GRISLI Ice Sheet Model

The first numerical ISM that is used in this research is the 3D-thermo-mechanical model GRISLI (GRenoble Ice Shelf and Land Ice model, Ritz et al. 2001). GRISLI has been validated over Antarctica (Ritz et al. 2001) and successfully applied to simulate the inception of the EIS growth during the Early Weichselian period (Peyaud et al. 2007). GRISLI is able to simulate both grounded and floating ice. In the grounded part, a distinction is made between inner-ice sheet flow and ice stream flow. In fact, in the inner-ice sheet grid nodes the SIA is employed, whereas in the ice stream grid nodes GRISLI uses the SSA. The SSA is also used in GRISLI to simulate the flow of floating ice shelves. Here follows a thorough description of GRISLI numerical ISM, based on Ritz et al. 2001, Colleoni et al. 2014 and Greve & Blatter 2009. GRISLI main features are illustrated in Figure 2.2, while in Table 2.1 a list of model symbols and physical constants is included.

Definition of ice flow regions. GRISLI identifies three different regions of ice flow, namely inner-ice sheet zones, ice streams and ice shelves. During a GRISLI simulation, the location of these different regions is determined in every time step. In each region the flow regime is different, in particular:

- the inner-ice sheet regions are grounded-ice areas characterized by the so-called simple-shear flow, Greve & Blatter 2009. Relatively slow ice velocities less than 50 m/yr are typical of these regions. Simple-shear flow results from internal deformation and the stress regime is dominated by the horizontal shear stresses τ_{xz} and τ_{yz}. In addition, some basal sliding might occur if the ice at the base is at the pressure-melting point. In these regions the SIA applies;

- ice streams are regions of grounded fast-flowing ice, with typical velocities around 800 m/yr. Ice streams are characterized by the so-called plug flow regime, dominated by the horizontal longitudinal stresses τ_{xx}, τ_{xy} and τ_{yy}, Greve & Blatter 2009. In reality, ice streams are glaciological features with typical widths of few kilometers. Due to high computational costs, GRISLI horizontal resolution over large domains (such as Eurasia) cannot exceed $20\,\mathrm{km} \times 20\,\mathrm{km}$. Therefore, rather than resolving individual ice streams, GRISLI identifies areas that have the large-scale characteristics of ice streams *i.e.*, narrow valleys, thick sediment layers saturated by meltwater, and areas with low effective basal pressure. In these regions, GRISLI calculates vertically-averaged horizontal ice velocities by following the SSA. The basal drag resisting the ice flow is described by a friction law, Colleoni et al. 2014;

- ice shelves are large floating platforms of ice, typically of few hundreds of meters thick. They are fed by grounded inland ice, and the transition line where the ice starts to float is called Grounding Line (GL). In GRISLI all the ice shelf grid nodes must satisfy a flotation criterion. In these regions the ice flow regime is the same as in ice streams region, except that there is no basal drag. Therefore, GRISLI applies in these regions the SSA to calculate the vertically-averaged horizontal ice velocities and the basal drag is set to zero, Colleoni et al. 2014.

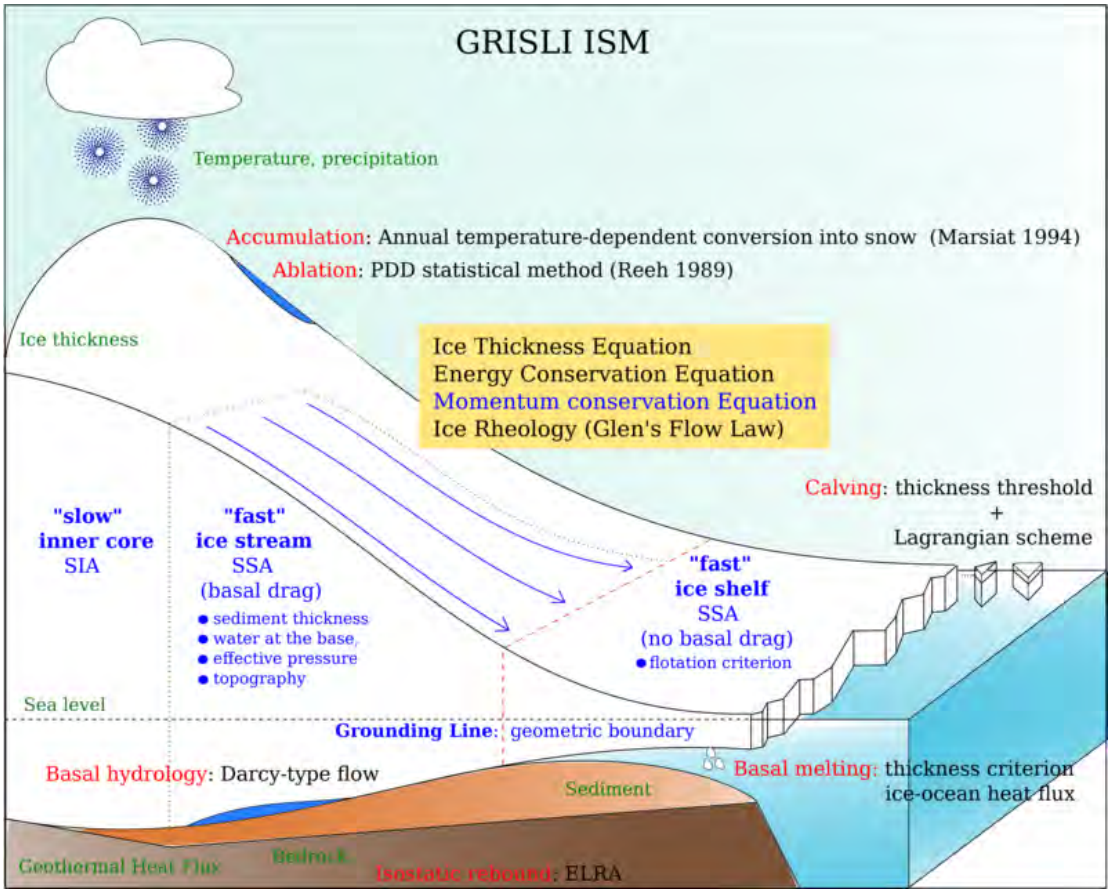

Figure 2.2: GRISLI ISM main features. The model inputs are shown in green, whilst the processes acting at the geometric boundaries of the ice sheet that are parametrized in GRISLI are shown in red. GRISLI governing equations are resumed inside the yellow box; the features related to the ice dynamics (*i.e.*, inner ice sheet/ice stream/ice shelf area and GL treating) are showed in blue.

Fundamental equations. GRISLI governing equations are based on the conservation of mass, momentum and energy equations,

$$\frac{\partial \rho}{\partial t} + \nabla \cdot (\rho \mathbf{u}) = 0\,, \tag{2.1}$$

$$\rho \frac{\partial \mathbf{u}}{\partial t} = \nabla \cdot \tau + \rho \mathbf{g}\,, \tag{2.2}$$

$$\rho c \left(\frac{\partial T}{\partial t} + \mathbf{u} \cdot \nabla T \right) = \nabla \left(\kappa \nabla T \right) + Q_i\,, \tag{2.3}$$

where ρ is the ice density, $\mathbf{u}$ the ice velocity, τ the stress tensor, $\mathbf{g}$ the gravitational acceleration, c the heat capacity of ice, T the ice temperature, κ the thermal conductivity

of ice and Q_i the deformational heat, Colleoni et al. 2014.

Since ice is considered as an incompressible fluid with constant density, the mass conservation equation 2.1 simplifies to

$$\nabla \cdot \mathbf{u} = \frac{\partial u}{\partial x} + \frac{\partial v}{\partial y} + \frac{\partial w}{\partial z} = 0\,, \tag{2.4}$$

where u, v and w are respectively the x,y and z-components of the ice velocity vector $\mathbf{u}$. Equation 2.4 can be vertically integrated from the base to the surface of the ice sheet, denoted with b and s, respectively. Defined the ice thickness h as the surface elevation minus the ice sheet base elevation ($s - b$), the vertically integrated equation 2.4 is transformed into the Ice Thickness Equation (ITE),

$$\frac{\partial h}{\partial t} + \frac{\partial (h\,u)}{\partial x} + \frac{\partial (h\,v)}{\partial y} = \mathsf{SMB} - \mathrm{b}_m\,, \tag{2.5}$$

where SMB and b_m are the surface mass balance and the basal melting rate respectively, Greve & Blatter 2009. In GRISLI the surface mass balance SMB (*i.e.*, accumulation minus ablation) depends on the climate forcing (near-surface air temperature and precipitation, see Subsection 2.3.2). In grounded-ice grid nodes (*i.e.*, inner-ice sheet areas and ice streams), the basal melting rate b_m depends on the ice temperature at the base of the ice sheet and on the geothermal heat flux, whilst under the ice shelves the ice is melted by the ocean heat flux (see Subsection 2.3.4), Colleoni et al. 2014 Moreover, if an ice shelf grid node is located at the ice shelf front (*i.e.*, it is adjacent to a grid point located in the ocean domain with zero ice thickness) calving may occur, depending on a thickness criterion that will be explained later in this subsection.

Considering typical values for ice sheets horizontal and vertical extent, it results that the ratio of ice acceleration and pressure gradient assumes values around 10^{-15}, Greve & Blatter 2009. This leads to the following simplified version of the momentum conservation equation 2.2,

$$\frac{\partial \tau_{xx}}{\partial x} + \frac{\partial \tau_{xy}}{\partial y} + \frac{\partial \tau_{xz}}{\partial z} = 0\,, \tag{2.6}$$

$$\frac{\partial \tau_{yx}}{\partial x} + \frac{\partial \tau_{yy}}{\partial y} + \frac{\partial \tau_{yz}}{\partial z} = 0\,, \tag{2.7}$$

$$\frac{\partial \tau_{zx}}{\partial x} + \frac{\partial \tau_{zy}}{\partial y} + \frac{\partial \tau_{zz}}{\partial z} = \rho g\,. \tag{2.8}$$

Similar scaling considerations as for the momentum conservation equation allows to cancel out horizontal heat conduction terms from the energy conservation equation 2.3, which is thus simplified to

$$\rho c \left(\frac{\partial T}{\partial t} + \mathbf{u} \cdot \nabla T \right) = \frac{\partial T}{\partial z} \left(\kappa \frac{\partial T}{\partial z} \right) + Q_i\,. \tag{2.9}$$

Ice rheology. Since ice is considered as an incompressible fluid with constant density, the pressure p results to be a free field. As a consequence, the ice rheological flow law relates the strain-rate tensor D and the stress deviator tensor τ^{D}, Greve & Blatter 2009. The stress deviator τ^{D} is related to the stress tensor and the pressure by the following relationship,

$$\tau = \tau^{\mathrm{D}} - p\,\mathsf{I} = \tau^{\mathrm{D}} - \frac{1}{3}\mathrm{tr}\tau\,\mathsf{I}\,, \tag{2.10}$$

where I is the unit tensor of order two. As a consequence, $\tau_{ij} = \tau_{ij}^{D}$ if $i \neq j$, $i, j = 1, 2, 3$. The general rheological flow law reads

$$\mathsf{D} = \frac{1}{2\eta\left(T',\, \tau_{\star}\right)} \tau^{\mathrm{D}} \,. \tag{2.11}$$

where η denotes the shear viscosity, T' the temperature relative to the pressure-melting point and $\tau_{\star}$ is the effective stress. The temperature relative to the pressure-melting point T_{mp} is defined as the absolute temperature corrected for the dependence of the melting point on pressure, that is

$$T' = T + T_{\mathrm{mp}} = T + 9.76 \cdot 10^{-8} \rho g \left(s - z\right) \,. \tag{2.12}$$

The effective stress is given by

$$\tau_{\star} = \sqrt{\frac{1}{2}\mathrm{tr}\left(\tau^{\mathrm{D}}\right)^{2}} = \sqrt{\frac{1}{2}\left(\left(\tau_{xx}^{\mathrm{D}}\right)^{2} + \left(\tau_{yy}^{\mathrm{D}}\right)^{2} + \left(\tau_{zz}^{\mathrm{D}}\right)^{2}\right) + \tau_{xy}^{2} + \tau_{xz}^{2} + \tau_{yz}^{2}} \,. \tag{2.13}$$

The inverse of the viscosity (*i.e.*, the so-called fluidity) in Equation 2.11 is a function of the temperature T, the pressure p and the effective stress $\tau_{\star}$,

$$\frac{1}{\eta\left(T',\, \tau_{\star}\right)} = 2\mathsf{E}A\left(T'\right)\tau_{\star}^{n-1} \,. \tag{2.14}$$

$A\left(T'\right)$ is called rate-factor and is expressed in the form of an Arrhenius law,

$$A\left(T'\right) = A_0 \exp\left(-\frac{Q}{RT'}\right) \,, \tag{2.15}$$

where A_0 is a pre-exponential constant, Q is the activation energy and R is the universal gas constant. The term denoted with E in Equation 2.14 is the so-called enhancement factor. The enhancement factor value depends on the type of flow regime. In fact, under condition of simple-shear flow the SIA-enhancement factor ($\mathsf{E}_{\mathrm{SIA}}$) is taken larger than one, in order to account for the anisotropy of ice, Ma et al. 2010. In contrast, under conditions of plug flow the SSA-enhancement factor ($\mathsf{E}_{\mathrm{SSA}}$) is taken less than or equal to one, as the ice does not display fabric anisotropy, Ma et al. 2010. Usually the ratio $\mathsf{E}_{\mathrm{SIA}}/\mathsf{E}_{\mathrm{SSA}}$ ranges between 3 and 10. In large-scale ice sheet modeling studies the SIA-enhancement factor has been set to values ranging from 1 to 5.6, see Colleoni et al. 2016 and reference therein. In this study such range for $\mathsf{E}_{\mathrm{SIA}}$ is explored, whereas the $\mathsf{E}_{\mathrm{SSA}}$ is kept constant and equal to 1 (see Subsection 2.3.5). In GRISLI, the value assumed by the exponent n in Equation 2.14 (*i.e.*, the so-called stress exponent) depends on the region of the ice sheet that is considered, Greve & Blatter 2009. In fact, in those grid nodes where the SIA applies $n = 3$, whereas in those regions where the SSA is adopted $n = 1$. By putting together Equations 2.11, 2.14 and 2.15 the Glen's rheological flow law is obtained,

$$\mathsf{D} = \mathsf{E}A\left(T'\right)\tau_{\star}^{n-1}\tau^{\mathrm{D}} \,. \tag{2.16}$$

Inner-ice sheet dynamics: the SIA. Under simple-shear flow conditions, the only relevant components of the stress deviator τ^{D} are the shear stresses acting on the horizontal plane τ_{xz} and τ_{yz}. Therefore, the normal stress deviators τ_{xx}^{D}, τ_{yy}^{D}, τ_{zz}^{D} and the shear stress acting on the vertical plane τ_{xy} are negligible, Greve & Blatter 2009.

These assumptions allow the momentum conservation equations 2.6, 2.7 and 2.8 to be further simplified, following the SIA. First, it is assumed that all normal stresses are equal to the negative pressure,

$$\tau_{xx} = \tau_{yy} = \tau_{zz} = -p\,. \tag{2.17}$$

By vertically integrating Equation 2.8, the hydrostatic pressure distribution over the ice column is obtained,

$$p = \rho g\,(h - z)\ , \tag{2.18}$$

Since τ^{D}_{xx}, τ^{D}_{yy}, τ^{D}_{zz} and τ_{xy} are negligible, by combining Equations 2.17 and 2.18 it is possible to simplify and to vertically integrate Equations 2.6 and 2.7, which turn into

$$\tau_{xz} = -\rho g\,(s - z)\,\frac{\partial s}{\partial x} \tag{2.19}$$

$$\tau_{yz} = -\rho g\,(s - z)\,\frac{\partial s}{\partial y}\,. \tag{2.20}$$

Moreover, the effective stress can be easily calculated if the geometry of the ice sheet is known,

$$\begin{aligned}\tau_\star &= \sqrt{\tau_{xz}^2 + \tau_{yz}^2} \\ &= \rho g\,(s - z)\left(\left(\frac{\partial s}{\partial x}\right)^2 + \left(\frac{\partial s}{\partial y}\right)^2\right)^{\frac{1}{2}} = \rho g\,(s - z)\mid \nabla s \mid\ .\end{aligned} \tag{2.21}$$

The combination of Glen's flow law (2.16) with Equations 2.19, 2.20, 2.21 along with scaling considerations yields

$$\frac{\partial u}{\partial z} = -2\mathsf{E}_{\mathrm{SIA}} A\left(T'\right)\left(\rho g\,(s - z)\right)^n \mid \nabla s \mid^{n-1} \frac{\partial s}{\partial x}\,, \tag{2.22}$$

$$\frac{\partial v}{\partial z} = -2\mathsf{E}_{\mathrm{SIA}} A\left(T'\right)\left(\rho g\,(s - z)\right)^n \mid \nabla s \mid^{n-1} \frac{\partial s}{\partial y}\,, \tag{2.23}$$

Equations 2.22, 2.23 can be vertically integrated from the ice base b to an arbitrary position z, in order to compute the horizontal velocities troughout the ice column as follows

$$u = u_b - 2\,(\rho g)^n \mid \nabla s \mid^{n-1} \frac{\partial s}{\partial x}\,\mathsf{E}_{\mathrm{SIA}} \int_b^z A\left(T'\right)(s - \overline{z})^n\,\mathrm{d}\overline{z}\,, \tag{2.24}$$

$$v = v_b - 2\,(\rho g)^n \mid \nabla s \mid^{n-1} \frac{\partial s}{\partial y}\,\mathsf{E}_{\mathrm{SIA}} \int_b^z A\left(T'\right)(s - \overline{z})^n\,\mathrm{d}\overline{z}\,, \tag{2.25}$$

where u_b and v_b are the x and y-velocities at the ice base. If the basal ice temperature does not reach the pressure-melting point, u_b and v_b are set to zero in Equations 2.24, 2.25 and no sliding occurs. Otherwise, the basal sliding velocities u_b and v_b are computed following a Weertman-type sliding law, Weertman 1957:

$$u_b = \frac{k}{N}\,(\rho g h)^3 \mid \nabla s \mid \frac{\partial s}{\partial x}\,, \tag{2.26}$$

$$v_b = \frac{k}{N}\,(\rho g h)^3 \mid \nabla s \mid \frac{\partial s}{\partial y}\,, \tag{2.27}$$

where k is an adjustable model parameter which is set to $5 \cdot 10^{-11}$ in GRISLI. The effective pressure N is given by

$$N = \rho g h - P_w \,, \tag{2.28}$$

where P_w is the subglacial water pressure, Colleoni et al. 2014. Subglacial water pressure depends on the basal hydrology, which will be described later in this subsection.

Fast-flowing regions dynamics: the SSA. Ice shelves and ice streams are characterized by fast flow and low surface slopes, Ritz et al. 2001. Consequently, the regime of simple-shear flow found in the inner-ice sheet regions, expressed by Equations 2.24, 2.25, 2.26 and 2.27, no longer applies in such fast-flowing regions. The flow regime dominating ice streams and ice shelves flow is the so-called plug flow, whereby the horizontal velocities are constant over the ice column (Greve & Blatter 2009), *i.e.*

$$\frac{\partial u}{\partial z} \approx 0, \ \frac{\partial v}{\partial z} \approx 0 \,. \tag{2.29}$$

This assumption, along with an hydrostatic approximation and proper scaling considerations, leads to the simplified version of the momentum conservation equations 2.6, 2.7 and 2.8 known as SSA.

The hydrostatic approximation is based on the consideration that in all parts of an ice sheet the shear stresses τ_{xz} and τ_{yz} are several orders of magnitude smaller than the vertical normal stress τ_{zz}, Greve & Blatter 2009. Consequently, the vertical momentum conservation equation 2.8 can be simplified and vertically integrated,

$$\tau_{zz} = -\rho g (s - z) \,. \tag{2.30}$$

This, combined with Equation 2.10, allows to express the horizontal normal stresses τ_{xx} and τ_{yy} so that the horizontal momentum conservation equations 2.6 and 2.7 read

$$2\frac{\partial \tau^{\mathrm{D}}_{xx}}{\partial x} + \frac{\partial \tau^{\mathrm{D}}_{yy}}{\partial x} + \frac{\partial \tau_{xy}}{\partial y} + \frac{\partial \tau_{xz}}{\partial z} = \rho g \frac{\partial s}{\partial x} \,, \tag{2.31}$$

$$2\frac{\partial \tau^{\mathrm{D}}_{yy}}{\partial y} + \frac{\partial \tau^{\mathrm{D}}_{xx}}{\partial y} + \frac{\partial \tau_{xy}}{\partial x} + \frac{\partial \tau_{yz}}{\partial z} = \rho g \frac{\partial s}{\partial y} \,. \tag{2.32}$$

$$\tag{2.33}$$

Equations 2.31 and 2.32 are vertically integrated over the ice column and the vertically integrated deviatoric stress N is introduced,

$$\mathsf{N} = \int_b^h \tau^{\mathrm{D}} \mathrm{d}z \,. \tag{2.34}$$

After other mathematical manipulations, Equations 2.31 and 2.32 are transformed into

$$2\frac{\partial \mathsf{N}_{xx}}{\partial x} + \frac{\partial \mathsf{N}_{yy}}{\partial x} + \frac{\partial \mathsf{N}_{xy}}{\partial y} = \rho g h \frac{\partial s}{\partial x} \,, \tag{2.35}$$

$$2\frac{\partial \mathsf{N}_{yy}}{\partial y} + \frac{\partial \mathsf{N}_{xx}}{\partial y} + \frac{\partial \mathsf{N}_{xy}}{\partial x} = \rho g h \frac{\partial s}{\partial y} \,. \tag{2.36}$$

The inverse form of the Glen's flow law 2.16 is vertically integrated and the vertically integrated viscosity $\overline{\eta}$ is introduced, Greve & Blatter 2009. After introducing Glen's

flow law in Equations 2.35 and 2.36, the horizontal momentum conservation equations finally reads

$$4\frac{\partial}{\partial x}\left(\overline{\eta}\frac{\partial u}{\partial x}\right)+2\frac{\partial}{\partial x}\left(\overline{\eta}\frac{\partial v}{\partial y}\right)+\frac{\partial}{\partial y}\left(\overline{\eta}\left(\frac{\partial u}{\partial y}+\frac{\partial v}{\partial x}\right)\right)=\rho g h\frac{\partial s}{\partial x}-\tau_b^x\,, \tag{2.37}$$

$$4\frac{\partial}{\partial y}\left(\overline{\eta}\frac{\partial v}{\partial y}\right)+2\frac{\partial}{\partial y}\left(\overline{\eta}\frac{\partial u}{\partial x}\right)+\frac{\partial}{\partial x}\left(\overline{\eta}\left(\frac{\partial u}{\partial y}+\frac{\partial v}{\partial x}\right)\right)=\rho g h\frac{\partial s}{\partial y}-\tau_b^y\,, \tag{2.38}$$

which is a system of non-linear elliptical differential equations for the ice horizontal velocities u and v, Greve & Blatter 2009. τ_b^x and τ_b^y denote the x and y-component of the basal drag.

Ice streams. GRISLI identifies ice stream grid nodes according to the following three criteria:

(IS1) the grid node is located in a narrow valley;

(IS2) the grid node has at its base a sediment layer h_s which is thicker than 150 meters and saturated by meltwater (*i.e.*, the hydraulic head h_w exceeds 250 meters, see the basal hydrology description). Moreover, the effective pressure N is lower than $3.5\cdot10^7$ Pascal;

(IS3) the grid node has ice thickness h and surface slope ∇s that are sufficiently low to satisfy $\rho g h\nabla s\leq 7\cdot10^6$ Pascal.

As pointed out for instance by Colleoni et al. 2014, the threshold for sediment thickness in criterion IS2 is ad-hoc and there is no direct evidence providing a constraint for this quantity. The sediment thickness needs to be prescribed as a model input over the model domain, see Subsection 2.3.1. The basal drag term in Equations 2.37 and 2.38 is described by a friction law,

$$\tau_b^x=c_f N u\,, \tag{2.39}$$

$$\tau_b^y=c_f N v\,, \tag{2.40}$$

where c_f is the dimensionless so-called basal drag coefficient, Colleoni et al. 2014. In early works with GRISLI the basal drag coefficient has been set for instance to $1\cdot10^{-5}$ in Eurasia *palaeo*-simulations (Peyaud et al. 2007), to $9\cdot10^{-5}$ in present-day Antarctica simulations (Dumas 2002) and from $10\cdot10^{-5}$ to $100\cdot10^{-5}$ for northern Hemisphere *palaeo*-simulations (Álvarez Solás et al. 2011). In this study several basal drag coefficient values within the range $1\cdot10^{-5}$-$10\cdot10^{-5}$ are tested, following Colleoni et al. 2016 (see Subsection 2.3.5).

Ice shelves. GRISLI determines ice shelf grid nodes position according to a flotation criterion based on Archimede's principle of floating bodies,

$$\rho H=\rho_w\left(\mathsf{SL}-b\right)\,, \tag{2.41}$$

where ρ_w is the ocean water density and SL stands for the sea level. Since the ocean water does not offer any resistance to the ice shelves flow, at the base of ice shelves the basal drag terms τ_b^x and τ_b^y in Equations 2.37 and 2.38 are set to zero, Colleoni et al. 2014.

Coupling the different regions and GL migration. The three different regions (inner-ice sheet, ice streams, ice shelves) are coupled in GRISLI at each time step as

follows. First the ITE 2.5 is solved for the whole domain, in order to determine the ice geometry. Ice thickness and bedrock elevation are computed and the status of each node is determined. If at a specific node the flotation criterion holds, the grid node will be assigned to the ice shelf domain. If conversely at a specific grid node the ice is grounded and at least one of the three criteria for ice streams identification (IS1), (IS2), (IS3) is fulfilled, the grid node is assigned to the ice stream domain. Otherwise, if the ice is grounded and none of the three conditions is fulfilled the grid node is assigned to the inner-ice sheet domain, Ritz et al. 2001. Once that the status of each node is determined, the SIA is solved first in the inner-ice sheet regions. The inner-ice sheet ice velocities computed with the SIA provides then boundary conditions for the SSA system of equations in ice streams and ice shelves. The buttressing effect of the ice shelf on the inland ice velocity is not parametrized in GRISLI. The ice shelf evolution can have an impact on the inland ice only through changes in ice shelf geometry. For instance, a GL thinning results in increased upstream slope and thus enhances the inland ice flow. The subgrid position of the GL is not computed. Consequently, when the GL migrates it jumps from node to node, Ritz et al. 2001.

Ice temperature. The ice temperature is needed to calculate the rate-factor A (see Equations 2.15 and 2.16), the basal melting rate b_m (see the ITE 2.5) and to determine if basal sliding occurs below grounded ice (only if the basal ice temperature is at the pressure-melting point). The energy conservation equation 2.9 is solved in the entire ice sheet domain and takes into account horizontal/vertical advection and vertical diffusion of heat within the ice. Also the heat production through deformation Q_i is considered, Colleoni et al. 2014. At the ice sheet surface the ice temperature is assumed to be at the near-surface air temperature, which is prescribed in GRISLI (see next paragraph). At the ice-bedrock interface a Geothermal Heat Flux (GHF) is prescribed (see Subsection 2.3.1). If the ice base temperature is lower than the pressure-melting point ($T_b < T_{\mathrm{mp}}$), no sliding and basal melting occur and the GHF is transmitted into the ice by vertical diffusion. If instead the ice base temperature is at the pressure-melting point ($T_b = T_{\mathrm{mp}}$), sliding occurs and the melting rate depends on the heat fluxes at both sides and on the heat generated through deformation during the sliding Q_i. Finally, if the ice base temperature exceeds the pressure-melting point ($T_b > T_{\mathrm{mp}}$), the excess in heat $T_b - T_{\mathrm{mp}}$ contributes to basal melting, whereas the basal temperature is held constant at the pressure-melting point ($T_b = T_{\mathrm{mp}}$), Colleoni et al. 2014. The coupling between ice temperature and velocity fields consists in solving Glen's flow law 2.16 and the energy conservation equation 2.9 alternately, Ritz et al. 2001.

Horizontal grid and initial topography. The simulations performed in this study with GRISLI are run on a $20\,\mathrm{km} \times 20\,\mathrm{km}$ regular rectangular grid covering the Eurasian domain. The grid has 210 points in the x-direction and 270 points in the y-direction. A Lambert Equal Area geographical projection centered on the North Pole (0^{o}, $90^{\mathrm{o}}\,\mathrm{N}$) is used to project the grid, and the coordinates are expressed in native Cartesian distances (km), Colleoni et al. 2014. At the beginning of each simulation initial surface topography s_0, ice thickness h_0, bedrock elevation b_0 and sediment thickness h_s have to be set on the $20\,\mathrm{km} \times 20\,\mathrm{km}$ GRISLI grid domain. In Subsection 2.3.1 the initial topography data employed in this study is illustrated.

Climate forcing. In order to determine the surface mass balance of an ice sheet (see next paragraph), three climatic fields need to be set at each time step: the mean annual

and July near-surface air temperature (T^a and T^j, respectively) and the mean annual total precipitation (P^a). Moreover, the mean annual near-surface air temperature is also needed as a boundary condition for the energy conservation equation 2.9. Such climatic fields represent the so-called climate forcing for the ISM. In this study, near-surface air temperature and precipitation data from independent climate simulations are used to force GRISLI (see Subsection 2.3.2).

Typically, there is a large difference between the resolution of an ISM and a climate model. In this study, GRISLI horizontal grid resolution is $20\,\mathrm{km} \times 20\,\mathrm{km}$, whilst the climate models whose data are used have a horizontal grid resolution ranging between $1.125^\mathrm{o} - 3.75^\mathrm{o} \times 1.125^\mathrm{o} - 1.9^\mathrm{o}$ (*i.e.*, around $125 - 417\,\mathrm{km} \times 125 - 211\,\mathrm{km}$). Consequently, before running a simulation with GRISLI it is necessary to downscale the climate fields to take into account differences in elevation resulting from the resolution difference between the ISM and the climate model, Colleoni et al. 2014. The procedure adopted is the following:

• near-surface air temperature, precipitation and surface topography fields from the climate model (T_{GCM}, P_{GCM} and s_{GCM}) are horizontally interpolated on the higher resolution GRISLI $20\,\mathrm{km} \times 20\,\mathrm{km}$ horizontal grid, obtaining the near-surface air temperature, precipitation and surface topography interpolated fields $T_{\mathsf{GCM}\rightharpoonup\mathsf{ISM}}$, $P_{\mathsf{GCM}\rightharpoonup\mathsf{ISM}}$ and $s_{\mathsf{GCM}\rightharpoonup\mathsf{ISM}}$.

• The interpolated surface topography $s_{\mathsf{GCM}\rightharpoonup\mathsf{ISM}}$ differs from the $20\,\mathrm{km} \times 20\,\mathrm{km}$ surface topography s_0 prescribed in GRISLI as initial condition. Near-surface air temperature and precipitation fields are corrected for these elevation changes by means of a lapse-rate value $\overline{\lambda}$ and a precipitation-correction factor $\overline{\gamma}$ as follows

$$T_{\mathsf{ISM}} = T_{\mathsf{GCM}\rightharpoonup\mathsf{ISM}} + \overline{\lambda}\,(s_{\mathsf{GCM}\rightharpoonup\mathsf{ISM}} - s_0)\ , \tag{2.42}$$

$$P_{\mathsf{ISM}} = P_{\mathsf{GCM}\rightharpoonup\mathsf{ISM}} \cdot \exp\left(\overline{\gamma}\,(T_{\mathsf{ISM}} - T_{\mathsf{GCM}\rightharpoonup\mathsf{ISM}})\right)\ , \tag{2.43}$$

where T_{ISM} and P_{ISM} are the final downscaled near-surface air temperature and precipitation fields, respectively. The lapse-rate value and the precipitation-correction factor account for changes in near-surface air temperature and precipitation resulting from changes in elevation through the lapse-rate and elevation-desert effects, see 1.2.1. Values for the lapse-rate and the precipitation-correction factor used in the downscaling procedure are specified in Subsection 2.3.2.

GRISLI allows to perform both steady-state and transient simulations. Transient simulations consist in interpolating the climate forcing between two (or possibly more) climate snapshots by means of a time-varying climate index. Given an initial and a final climate snapshots (C_i and C_f respectively), the downscaled climatic fields read by GRISLI for each snapshot are the initial and final mean annual near-surface air temperature (T_i^a and T_f^a respectively), the initial and final mean July near-surface air temperature (T_i^j and T_f^j respectively), and the initial and final mean annual precipitation (P_i^a and P_f^a respectively). For each snapshot a $20\,\mathrm{km} \times 20\,\mathrm{km}$ surface topography is used for the downscaling procedure. Initial and final surface topography are denoted with s_i and s_f respectively. In order to perform a transient simulation between such initial and final climate snapshots with GRISLI, one needs first to set a reference climate. If for instance the initial climate snapshot C_i is set as reference climate, the climatic fields from the final climate snapshot C_f are then expressed as anomalies with respect

to the reference climate as follows,

$$\triangle T^a = T_f^a - T_i^a + \lambda\,(s_f - s_i)\ , \tag{2.44}$$

$$\triangle T^j = T_f^j - T_i^j + \lambda\,(s_f - s_i)\ , \tag{2.45}$$

$$\triangle P^a = P_f^a / P_i^a\ , \tag{2.46}$$

where the term $\lambda\,(s_i - s_f)$ accounts for temperature changes resulting from the the elevation difference between the two climate snapshots. At each time step t during the transient simulation the mean annual near-surface air temperature, mean July near-surface air temperature and mean annual precipitation are computed as follows,

$$T^a(t) = T_i^a + \triangle T^a \cdot i(t) - \lambda\,(s(t) - s_i)\ , \tag{2.47}$$

$$T^j(t) = T_i^j + \triangle T^j \cdot i(t) - \lambda\,(s(t) - s_i)\ , \tag{2.48}$$

$$P^a(t) = P_i^a \cdot ((\triangle P^a - 1)\,i(t) + 1) \cdot \exp\left(-\gamma\lambda\,(s(t) - s_i)\right)\ , \tag{2.49}$$

where i is the time-varying climate index, modulating between initial and final snapshots. The climate index must be computed so that $i(t_i) = 1$ and $i(t_f) = 0$, where t_i and t_f are the initial and final simulation time, respectively. In such a way, $T^a(t_i) = T_i^a$, $T^j(t_i) = T_i^j$, $P^a(t_i) = P_i^a$ and $T^a(t_f) = T_f^a$, $T^j(t_f) = T_f^j$, $P^a(t_f) = P_f^a$. As shown in Subsection 1.2.1, changes in the geometry of an ice sheet lead to changes in the near-surface air temperature and precipitation by the lapse-rate and elevation-desert effects. GRISLI takes into account such feedbacks by correcting at each time step during run-time the mean annual and July near-surface air temperature and the mean annual precipitation for changes in the ice sheet elevation. The correction (see the last term in Equations 2.47, 2.48, and 2.49) is performed by means of a lapse-rate value λ and a precipitation-correction factor γ in a similar way as in the downscaling procedure. In this study several lapse-rate and precipitation-correction factor values are tested. Following Colleoni et al. 2016, values ranging between $4 - 8.2\,^{\circ}\mathrm{C/km}$ and $0.03 - 0.1\,^{\circ}\mathrm{C}^{-1}$ are explored for the lapse-rate and the precipitation-correction factor, respectively (see Subsection 2.3.5). Finally, in transient simulations also initial and final sea level (SL_i and SL_f) have to be prescribed. At each simulation time step t during a transient simulation, the eustatic sea level is computed by means of a time-varying sea level index i_{SL}, modulating between initial and final sea level,

$$\mathsf{SL}(t) = i_{\mathrm{SL}}(t) \cdot \mathsf{SL}_i + (1 - i_{\mathrm{SL}}(t)) \cdot \mathsf{SL}_f\,. \tag{2.50}$$

Surface mass balance. The surface mass balance (SMB) in GRISLI takes into account accumulation (ACC) and surface ablation (ABL). At each time step, GRISLI computes the $\mathsf{SMB} = \mathsf{ACC} - \mathsf{ABL}$ in each grid node of the ice sheet/stream/shelf domain. The snow accumulation is computed from the mean annual total precipitation following Marsiat 1994. A linear transition between solid and liquid precipitation depending on the mean annual near-surface air temperature is considered to compute the solid precipitation fraction P_{sf},

$$P_{\mathsf{sf}} = \begin{cases} 1 & \text{if } T \leq -10\,^{\circ}\mathrm{C}\,, \\ (7\,^{\circ}\mathrm{C} - T)\,/17\,^{\circ}\mathrm{C} & \text{if } -10\,^{\circ}\mathrm{C} < T \leq 7\,^{\circ}\mathrm{C}\,, \\ 0 & \text{if } T > 7\,.^{\circ}\mathrm{C} \end{cases} \tag{2.51}$$

The accumulation is then computed from the mean annual total precipitation as follows,

$$\mathsf{ACC} = P^a \cdot P_{\mathsf{sf}} \,. \tag{2.52}$$

The ablation is computed using the Positive-Degree-Days (PDD) semi-empirical method (Reeh 1989). PDD method relates the number of days with positive near-surface air temperature (*i.e.*, PDD) with snow and ice melting rates through observations-based melting coefficients. First of all, the near-surface air temperature is assumed to vary sinusoidally over time. Such an assumption allows to reconstruct the annual near-surface air temperature cycle from the mean annual and July near-surface air temperature,

$$T^m(t) = T^a + \left(T^j - T^a\right) \cos \frac{2\pi t}{A} \,, \tag{2.53}$$

where $A = 1\,\text{year}$. Following Reeh 1989, the number of PDD is then computed from the normal probability distribution around the monthly mean temperatures during the year, *i.e.*,

$$\mathsf{PDD}_\sigma = \frac{1}{\sigma\sqrt{2\pi}} \int_0^A \int_0^\infty T \exp\left(\frac{\left(T - T^m(t)\right)^2}{2\sigma^2}\right) \mathrm{d}T\mathrm{d}t \,, \tag{2.54}$$

where t is the time variable, T (°C) is the near-surface air temperature variable, and σ is the standard deviation of the near-surface air temperature. The latter term plays a crucial role for the PDD calculation as it indicates whether the near-surface air temperature has been positive during a month with negative monthly mean temperature, Fausto et al. 2011. Modeling studies showed that an uniform increase of standard deviation of the near-surface air temperature from 2.58°C to 4.58°C leads to a 33% larger melt area over the GIS. Commonly a single value ranging from 4.5°C to 5.5°C is assigned to σ (see Fausto et al. 2011 and reference therein). However, in this study rather than a single-valued σ it is used the altitude-latitude dependent parametrization for the near-surface air temperature standard deviations proposed by Fausto et al. 2011. Based on near-surface air temperature observations at the automatic weather stations on the GIS, mean annual and July standard deviations (σ^a and σ^j respectively) of the near-surface air temperature are parametrized as follows,

$$\sigma^a = 0.324 + 0.0011 \cdot s + 0.0573 \cdot \phi \tag{2.55}$$

$$\sigma^j = 2.22 + 0.0013 \cdot s - 0.0178 \cdot \phi \,, \tag{2.56}$$

where ϕ is the latitude expressed in °N. In such a way, in each grid point of the Eurasian domain mean annual and July standard deviation of near-surface air temperature are computed depending on the surface elevation and on the latitude. Then, similarly as for the near-surface air temperature (see Equation 2.53), a sinusoidally variation of the near-surface air temperature standard deviation over the year is assumed,

$$\sigma(t) = \sigma^a + \left(\sigma^j - \sigma^a\right) \cos \frac{2\pi t}{A} \,. \tag{2.57}$$

The number of PDD is given by

$$\mathsf{PDD}_{\triangle\sigma} = \int_0^A \int_0^\infty \frac{1}{\sigma(t)\sqrt{2\pi}} T \exp\left(\frac{\left(T - T^m(t)\right)^2}{2\sigma^2(t)}\right) \mathrm{d}T\mathrm{d}t \,. \tag{2.58}$$

Note that the only difference between Equations 2.54 and 2.58 is the time/altitude/latitude dependent σ. In order to distinguish clearly between those two formulations, a different notation for the positive-degree-days is used: PDD_σ indicates that a single-value σ has been used, whilst $\mathsf{PDD}_{\triangle\sigma}$ refers to Equation 2.58 including the near-surface air temperature standard deviation parametrization by Fausto et al. 2011.

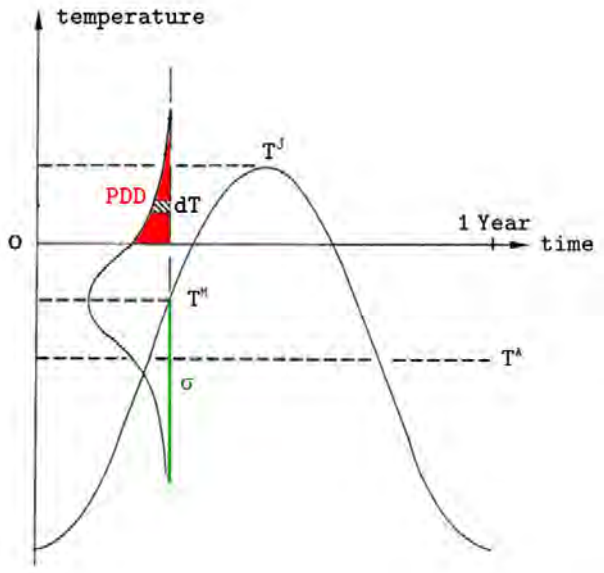

Figure 2.3: After Reeh 1989: scheme illustrating the PDD method.

Once that the number of PDD is calculated, the amount of snow and ice melted is related to the number of PDD by means of the snow and ice melt coefficients (C_s and C_i respectively). In the original PDD method of Reeh 1989 the snow and ice melt coefficients are constant through space and time and assume values of $3\,\mathrm{mm\,d^{-1}\,^oC^{-1}}$ and $8\,\mathrm{mm\,d^{-1}\,^oC^{-1}}$ respectively. However, as revealed by field studies on present-day glaciers and ice caps, such assumption is a crude approximation and does not take into account the high variability of melting coefficients (Colleoni et al. 2016 and reference therein). Tarasov & Peltier 2002 suggested snow and ice melting coefficients depending on the mean annual near-surface air temperature,

$$C_i = \begin{cases} C_i^c & \text{if } T^a < T^c\,, \\ C_i^w + \left(\frac{T^w - T^a}{T^w - T^c}\right)^3 \cdot (C_i^c - C_i^w) & \text{if } T^c \leq T^a < T^w\,, \\ C_i^w & \text{if } T \geq T^w\,, \end{cases} \tag{2.59}$$

$$C_s = \begin{cases} C_s^c & \text{if } T^a < T^c\,, \\ C_s^w + \left(\frac{T^a}{T^w - T^c}\right) \cdot (C_s^c - C_s^w) & \text{if } T^c \leq T^a < T^w\,, \\ C_s^w & \text{if } T \geq T^w\,, \end{cases} \tag{2.60}$$

where $T_c = -1\,^\mathrm{o}\mathrm{C}$, $T_w = 10\,^\mathrm{o}\mathrm{C}$, $C_i^c = 17.22\,\mathrm{mm\,d^{-1}\,^oC}$, $C_i^w = 8.3\,\mathrm{mm\,d^{-1}\,^oC}$, $C_s^c = 2.65\,\mathrm{mm\,d^{-1}\,^oC}$ and $C_s^w = 4.3\,\mathrm{mm\,d^{-1}\,^oC}$. Therefore for the same amount of PDD ice melting is more efficient at low temperatures rather than at high temperatures, whereas the opposite holds for snow. In such a way, snow and ice melting coefficients can vary

spatially and temporally, following the near-surface air temperature distribution. Once that a value for snow and ice melting coefficients is assigned, ablation takes place in three steps:

- fresh snow, if present, is melted first at rate C_s. Meltwater resulting from the melted snow is able to percolate into the snow layer and refreeze as superimposed ice. If the amount of superimposed ice exceeds 60% of the annual snowfall, runoff occurs;
- when all the snow is melted, superimposed ice, if present, is melted at rate C_i;
- when all the snow and the superimposed ice are melted, glacier ice is melted at rate C_i.

Depending on the snow accumulation and on the available melting energy in each time step, not all the steps (or even none of the steps) will be carried out, Colleoni et al. 2014.

Basal hydrology. One of the conditions required in criterion (IS2) to determine the position of ice streams is a large value for the hydraulic head h_{sw}. The hydraulic head is computed by means of a basal hydrology scheme implemented in GRISLI by Peyaud 2006. The basal hydrology under glacier and ice sheets consists in an heterogeneus group of hydrological features, from drainage through a thin water film (< 1 mm) to flow through large networks of cavities and rivers, Colleoni et al. 2014. Present-day studies in Antarctica showed that basal meltwater flows can exert a strong impact on glacial erosion and ice velocity, *e.g.*, Remy & Legresy 2004. However, due to lack of observations, the dynamics of the hydrological processes occurring at the ice sheet base is still poorly understood. As a consequence, the representation of basal hydrology is one of the most arguable features in ISMs, Colleoni et al. 2014.

Basal hydrology in GRISLI follows a Darcy-type flow law. The pressure imposed from the ice on its base is expressed as a potential as follows,

$$\Psi = p_{sw} + \rho_{sw}\, gb + \rho g h + \Psi_0\,. \tag{2.61}$$

where p_{sw} is the subglacial water pressure, ρ_{sw} is the subglacial water density (*i.e.*, the freshwater density) and Ψ_0 is an arbitrary constant. Looking at the right-hand side of Equation 2.61, the second term accounts for the pressure resulting from the altitude of the ice base, whilst the third term represents the pressure deriving from the ice column weight, Colleoni et al. 2014. The pressure Ψ can be expressed as a potential,

$$\nabla\Psi = \nabla p_{sw} + \nabla\left(\rho_{sw}\, gb + \rho g h\right) = \nabla p_{sw} + \rho g\left(\left(\frac{\rho_{sw}}{\rho} - 1\right)\nabla b + \nabla s\right)\,, \tag{2.62}$$

and the meltwater flow follows the gradient of such potential. According to Darcy's law, the flow through a porous medium is proportional to a hydraulic gradient, *i.e.*, the variation of the hydraulic head h_{sw}, Colleoni et al. 2014. The hydraulic head can be expressed as

$$h_{sw} = \frac{\Psi}{\rho_{sw}\, g}\,. \tag{2.63}$$

Therefore, the flow velocity can be expressed as

$$\mathbf{V}_{sw} = -K\nabla h_{sw} = -\frac{K}{\rho_{sw}\, g}\nabla\Psi\,, \tag{2.64}$$

where K represents the so-called hydraulic conductivity. The hydraulic conductivity depends on the soil property, with values ranging from 10^{-9} m/s for the clay to 10^{-5} m/s to the fine sand. However, GRISLI does not account for different soil properties. Therefore, the hydraulic conductivity value is set depending on the ice temperature and on the effective pressure at the base of the ice sheet, Colleoni et al. 2014. If ice basal temperature is below its pressure-melting point T_{mp}, the ground is assumed to be impermeable and the hydraulic conductivity is set to zero. In contrast, if the ice basal temperature exceeds its pressure-melting point T_{mp} a dependence on the effective pressure is added; for high values of the effective pressure the hydraulic conductivity is set to a constant value of $K_0 = 10^{-6}$ m/s, whilst if the effective pressure is low the hydraulic conductivity linearly increases,

$$K = \begin{cases} 0 & \text{if } T < T_{\mathrm{mp}}\,, \\ K_0 & \text{if } T \geq T_{\mathrm{mp}} \ \wedge \ N > 1000 \text{ bar}\,, \\ K_0 \cdot \frac{10^3}{N} & \text{if } T \geq T_{\mathrm{mp}} \ \wedge \ N \leq 1000 \text{ bar}\,. \end{cases} \tag{2.65}$$

The hydraulic head variation is governed by the horizontal variation of the water flux, the basal meltig rate and the infiltration rate into the soil I_{in},

$$\frac{\partial h_{sw}}{\partial t} + \frac{\partial V_{sw}^x}{\partial x} + \frac{\partial V_{sw}^y}{\partial y} = \mathrm{b}_m - I_{\mathrm{in}}\,. \tag{2.66}$$

Calving. If an ice shelf grid node is located at the ice shelf front (*i.e.*, is adjacent to at least one grid point located in the ocean domain with zero ice thickness) calving may occur, following a calving scheme implemented by Peyaud et al. 2007. The calving scheme is based on a thickness criterion. At a certain time step i, if a grid node located at the ice shelf front has ice thickness h_f^i lower than a certain threshold H_c, the status of the ice shelf front grid node is tested, Colleoni et al. 2015. First the upstream ice shelf node is considered, and by means of a Lagrangian scheme its ice thickness variation is computed,

$$\frac{\partial h_u}{\partial t} = \mathsf{SMB} - \mathrm{b}_m - h_u \left(\frac{\partial u}{\partial x} + \frac{\partial v}{\partial y} \right)\,, \tag{2.67}$$

where the ice thickness in the upstream ice shelf node is denoted with h_u. The time needed by the ice to flow from the upstream node to the ice shelf front node can be calculated by

$$\tau_f = \frac{\triangle x}{\triangle u}\,, \tag{2.68}$$

where it has been assumed for semplicity that the ice flow occurs in the x-direction only. The ice thickness of the front node at the time step $i+1$ can be therefore forecasted,

$$h_f^{i+1} = h_u + \tau_f \cdot \frac{\partial h_u}{\partial t}\,. \tag{2.69}$$

If the ice shelf front thickness at the time step $i+1$ is still lower than H_c, calving occurs in the node. If conversely the ice shelf front thickness at the time step $i+1$ is larger than or equal to H_c, there is no calving and the ice shelf front advances. In this study, a constant thickness threshold $H_c = 200\,m$ is employed.

Isostatic rebound. The bedrock reacts to alteration in the surface load according to the so-called isostatic rebound process. In GRISLI, isostatic rebound is described by

the Elastic-Lithosphere/Relaxed-Astenosphere (ELRA) model, Le Meur & Huybrechts 1996. According to ELRA model, the lithosphere reacts to changes in ice load as a thin elastic plate. This allows to take into account a response to surface load variations which is "regional" rather than only "local". In fact, with ELRA model the isostatic rebound affects the bedrock also at some distance from the location where the surface load variation is imposed. The asthenosphere is assumed to respond to a surface load variation with a time lag τ_f, due to its viscous property. Such time lag is the so-called characteristic relaxation time, which is set constant and equal to 3 ka in GRISLI, Colleoni et al. 2014.

Ocean basal melting. The ocean basal melting rates below the ice shelves depends on the ice-ocean heat fluxes. However, in early studies with GRISLI a really simplified approach to the ocean basal melting has been adopted (Ritz et al. 2001, Peyaud et al. 2007, Colleoni et al. 2014, 2015, 2016). In fact, it is assumed that the melting rate depends on the water depth only. A depth threshold z_m is fixed, and two ocean basal melting rate values are prescribed respectively above and below the depth threshold. In this study, a group of transient simulations with such simplified depth-method is run. A constant basal melting rate value of 0.1 m/yr throughout the water column is prescribed. The reason for this choice depends on the SMB over the Barents and Kara Sea with a constat LGM climate forcing. In fact, in these regions only with a low ocean basal melting value of 0.1 m/yr it is possible to have a positive ice shelf mass budget and therefore to develop an extensive ice cover at LGM. Such low ("cold") constant value is prescribed in a group of transient simulations, in order to compare its effect with more sofisticated two-equations basal melting parametrizations taking into account ice-ocean heat fluxes. This single-value "cold" basal melting parametrization will be denoted throughout this work with BCON. The two-equations basal melting parametrizations that have been used and the method applied to force them (in terms of ocean temperature and salinity) are carefully described in Subsection 2.3.4.

Symbol	Description	Units	Value
ρ	Ice density.	kg/m^3	917
$\mathbf{u}$	Ice velocity.	m/yr	-
$\mathbf{u}_b$	Basal ice velocity.	m/yr	-
s	Surface topography.	m	-
b	Bedrock elevation.	m	-
h	Ice thickness.	m	-
s_0	Initial surface topography.	m	-
b_0	Initial bedrock elevation.	m	-
h_0	Initial ice thickness.	m	-
SL	Sea level.	m	-
τ	Stress tensor.	Pa	-
τ^{D}	Stress deviator tensor.	Pa	-
D	Strain rate tensor.	1/s	-
N	Vertically integrated deviatoric stress	Pa	-
η	Ice shear viscosity.	Pa/yr	-
$\overline{\eta}$	Vertically integrated ice viscosity.	Pa/yr	-
τ_b	Basal drag	Pa	-
c_f	Basal drag coefficient.	-	$10^{-5} - 10 \cdot 10^{-5}$
T'	Relative ice temperature	°C	-
$\sigma_\star$	Effective pressure.	Pa	-

Continued on the next page

Continued from previous page

Symbol	Description	Units	Value
T	Ice temperature.	°C	-
T_{mp}	Pressure-melting point.	°C	-
T_b	Basal ice temperature.	°C	-
GHF	Geothermal heat flux.	$\mathrm{W/m^2}$	-
E	Enhancement factor.	-	-
A	Rate factor.	Pa	-
n	Glen's flow law exponent.	-	1-3
Q	Activation energy.	J	-
R	Universal gas constant.	J/mol kg	8.3145
A_0	Pre-exponential coefficient.	Pa	-
c	Ice heat capacity.	J/kg°C	2009
κ	Ice thermal conductivity.	J/m°Cyr	$2.1 \cdot 31557600$
Q_i	Ice deformational heat.	W/°Cm	-
τ_{xz}, τ_{yz}	Horizontal shear stresses.	Pa	-
τ_{xx}, τ_{yy}, τ_{xy}	Horizontal longitudinal stresses.	Pa	-
SMB	Surface mass balance.	m/yr	-
ACC	Accumulation.	m/yr	-
ABL	Ablation.	m/yr	-
b_m	Basal melting rate	m/yr	-
N	Effective pressure.	$\mathrm{kg/m^3}$	-
P_w	Subglacial water pressure.	$\mathrm{kg/m^3}$	-
h_s	Sediment thickness.	m	-
h_w	Hydraulic head.	m	-
ρ_w	Ocean water density.	$\mathrm{kg/m^3}$	1025
λ	Lapse-rate value.	°C/km	4-8.2
γ	Precipitation-correction factor.	1/°C	0.03-0.1
T^a	Mean annual air temperature.	°C	-
T^j	Mean July air temperature.	°C	-
P^a	Mean annual total precipitation.	m/yr	-
P_{sf}	Solid precipitation fraction.	-	-
$\overline{\lambda}$	Lapse-rate value used for downscaling.	°C/km	0.005
$\overline{\gamma}$	Precipitation-correction factor used for downscaling.	1/°C	0.05
PDD	Number of positive-degree-days	°Cd	-
σ	Standard deviation of air temperature.	°C	-
ϕ	Latitude.	°N	-
σ^a	Mean annual standard deviation of air temperature.	°C	-
σ^j	Mean July standard deviation of air temperature.	°C	-
C_i	Ice melting coefficient.	mm/°Cd	-
C_s	Snow melting coefficient.	mm/°Cd	-
C_i^c	"Cold" ice melting coefficient.	mm/°Cd	-
C_s^c	"Cold" melting coefficient.	mm/°Cd	-
C_i^w	"Warm" ice melting coefficient.	mm/°Cd	-
C_s^w	"Warm" melting coefficient.	mm/°Cd	-
Ψ	Pressure potential imposed on the ice base.	Pa	-
P_{sw}	Subglacial water pressure.	Pa	-
ρ_{sw}	Subglacial water density.	$\mathrm{kg/m^3}$	1000
h_{sw}	Hydraulic head.	m	-
$\mathbf{V}_{sw}$	Subglacial water velocity.	m/yr	-
K	Hydraulic conductivity.	m/s	10^{-6}
I_{in}	Infiltration water.	m/yr	-
H_c	Thickness threshold for the calving criterion.	m	200
τ_f	Characteristic relaxation time of the astenosphere.	yr	3000
z_m	Depth threshold for ocean basal melting.	m	450

Table 2.1: List of GRISLI symbols and physical constants.

2.2.2 PSU Ice Sheet Model: analogies/differences with GRISLI

The second numerical ISM model that has been considered in this study is PSU (Pollard & DeConto 2012). PSU is a hybrid SIA/SSA 3D-thermo-mechanical ISM which is able to simulate both grounded and floating ice. Early versions of PSU using the SIA only (*i.e.*, simulating grounded ice only) have been applied to the *palaeo*-AIS and other ice sheets and times. More recent full SIA/SSA versions of PSU have been used to simulate the *palaeo*-AIS, see Pollard & DeConto 2012 and references therein. PSU solves the same set of equations for the ice thickness (ITE), ice temperature, ice rheology and ice dynamics included in GRISLI. However, a first major difference between the two ISMs is represented by the treatment of ice streams. In fact, instead of treating inner-ice sheet regions and ice stream regions as separated regions (as GRISLI does), the grounded ice flow is modulated between 100% SIA and 100% SSA depending on the magnitude of a basal sliding coefficient, which in turn depends on the basal ice temperature, Pollard & DeConto 2012. Another important diffence between GRISLI and PSU is the treatment of the GL migration. In GRISLI the GL is treated as a geometric boundary; its position depends on a flotation criterion only, and when the GL migrates it jumps from node to node. In contrast, in PSU the GL is treated as a dynamic boundary. A parametrization by Schoof 2007 is imposed as a condition on the ice flux across the GL, Pollard & DeConto 2012. In order to apply such internal condition to the ice flux at the GL, at each time step the subgrid position of the GL is computed. A specific aim of this study is to evaluate the impact of the different treatment of ice streams and GL migration on the deglaciation of the SKBSIS and on the Storfjorden ice stream retreat. Therefore, in order to reduce as much as possible other discrepancies between the ISMs, the same SMB and ocean basal melting parametrizations used in GRISLI are included in PSU. However, other minor differences between the two models still remain. Here follows a careful description of the main differences/analogies between PSU and GRISLI. The main discrepancies between the two ISMs are illustrated in Figure 2.4, while in Table 2.2 a list of model symbols and physical constants is included.

Definition of ice flow regions. PSU does not treat inner-ice sheet and ice stream regions as completely separated areas. In fact, the ice flow is then modulated between 100% SIA and 100% SSA depending on the magnitude of a basal sliding coefficient, which in turn depends on the basal ice temperature, Pollard & DeConto 2012. Therefore, three types of flow can exist in the grounded part of an ice sheet, Pollard & DeConto 2012:

- for low values of the basal sliding coefficient ($< 10^{-8}$), almost completely simple-shear flow (100% SIA). Only the SIA velocities are computed;
- for higher values of the basal sliding coefficient ($\geq 10^{-8}$), both SIA and SSA velocities are computed. The flow regime ranges from a combination of simple-shear and plug flows (SIA+SSA) to almost completely plug flow (100% SSA);

Finally, where the ice is floating (*i.e.*, in ice shelf regions) 100% SSA is used, assuming zero basal sliding.

Set of equations. The set of approximated equations solved in PSU are essentially the same included in GRISLI and consists of equations for ice thickness (ITE, Equation

2.5), ice velocities (SIA, Equations 2.24 and 2.25, SSA, Equations 2.37 and 2.38), ice temperature (Equation 2.9) and ice rheology (Glen's flow law, Equation 2.16). However, there are few differences between the two models.

As concerns the ice rheology, in GRISLI the equation for the effective stress 2.21 contains pure SIA or SSA terms only depending on the type of flow. For values of the sliding coefficient larger than or equal to 10^{-8}, PSU computes both SIA and SSA. When this is the case, SIA's vertical shear stresses terms τ_{xz} and τ_{yz} are included in the SSA effective stress formula and SSA's horizontal longitudinal stresses terms τ_{xx}^{D}, τ_{yy}^{D} and τ_{xy} are included in the SIA effective stress formula, Pollard & DeConto 2012. Therefore, the formula for the effective stress is given by

$$\tau_\star = \sqrt{\frac{1}{2}\mathrm{tr}\left(\tau^{\mathrm{D}}\right)^2} = \sqrt{\frac{1}{2}\left(\left(\tau_{xx}^{\mathrm{D}}\right)^2 + \left(\tau_{yy}^{\mathrm{D}}\right)^2\right) + \tau_{xy}^2 + \tau_{xz}^2 + \tau_{yz}^2}\,. \tag{2.70}$$

Moreover, in the Glen's flow law 2.16 PSU considers a nonlinear exponent $n = 3$ in all the ice sheet domain, whereas GRISLI adopts an linear exponent $n = 1$ in the ice stream and ice shelves regions. Another difference between GRISLI and PSU concerns the enhancement factors. In fact, test simulations showed that high values for both $\mathsf{E}_{\mathrm{SIA}} = 10$ and $\mathsf{E}_{\mathrm{SSA}} = 3$ are necessary to match the Hughes et al. 2016 reconstructed ice margin position at LGM in Barents Trough. Such high values are between two to three times higher than the values selected for GRISLI (Colleoni et al. 2016) and ten times higher than the values used with PSU in AIS simulations (Pollard & DeConto 2012).

In the ice dynamics equations, PSU employs a different formulation than GRISLI for the basal velocity. In fact, in all the grounded part of the ice sheet the basal sliding velocity is given by a standard drag law, Pollard & DeConto 2012,

$$u_b = c_\star \mid \tau_b \mid \tau_b^x\,, \tag{2.71}$$

$$v_b = c_\star \mid \tau_b \mid \tau_b^y\,, \tag{2.72}$$

where $c_\star$ is the sliding coefficient (see next paragraph). Since the SSA velocities $\overline{u}$ and $\overline{v}$ are averaged in depth, the SSA basal velocities (denoted here with $\overline{u}_b$ and $\overline{v}_b$) are defined as follows,

$$\overline{u}_b = \overline{u} - \overline{u}_i\,, \overline{v}_b = \overline{v} - \overline{v}_i\,, \tag{2.73}$$

where $\overline{u}_i$ and $\overline{v}_i$ are the depth-averaged SIA velocities. The two basal drag terms in the SSA equations 2.37 and 2.37 are substituted by two basal sliding terms, *i.e.*

$$\frac{f_g}{\sqrt{c_\star} \mid \overline{u}_b^2 + \overline{v}_b^2 \mid}\overline{u}_b\,, \tag{2.74}$$

$$\frac{f_g}{\sqrt{c_\star} \mid \overline{u}_b^2 + \overline{v}_b^2 \mid}\overline{v}_b\,, \tag{2.75}$$

where $f_g = 1$ if the ice is grounded and $f_g = 0$ if the ice is afloat.

Another difference in the ice dynamics between GRISLI and PSU concerns the SIA formulation for those grid nodes where both the SIA and the SSA velocities are computed. In fact, in GRISLI the vertical shear stresses τ_{xz} and τ_{yz} are balanced only by the hydrostatic driving force $\rho g\,(s - z)\,\nabla \mathbf{s}$, which acts on the ice columns above level z

(see Equations 2.22, 2.23). In PSU the effect of the SSA horizontal longitudinal stresses on the ice column above level z are included, Pollard & DeConto 2012. In such a way, Equations 2.22, 2.23 become

$$\tau_{xz} = -\left(\rho g h \frac{\partial s}{\partial x} - \mathsf{LHS}_x\right)\left(\frac{s-z}{h}\right), \tag{2.76}$$

$$\tau_{yz} = -\left(\rho g h \frac{\partial s}{\partial y} - \mathsf{LHS}_y\right)\left(\frac{s-z}{h}\right), \tag{2.77}$$

where LHS_x and LHS_y are the left-hand side of Equations 2.37 and 2.38, respectively.

Basal sliding coefficient. In PSU the sliding coefficient $c_\star$ plays a fundamental role. In fact, it determines not only the sliding velocity in Equations 2.71 and 2.72, but also the ice flow regime. The basal sliding coefficient depends on ice temperature at the ice sheet base, implicitly representing basal hydrology (Pollard & DeConto 2012),

$$\begin{aligned} c_\star &= (1-r)\, c_f + r c_w\,, \\ r &= \max\left\{0\,, \min\left[1\,, \left(T'+3\right)/3\right]\right\}\,, \end{aligned} \tag{2.78}$$

where c_w is the full sliding coefficient and $c_f = 10^{-20}\,\mathrm{m/aPa^2}$ is the "frozen-bed" coefficient, small enough to prevent any sliding. If the ice basal temperature relative to the pressure-melting point is lower than $-3^{\circ}\mathrm{C}$, no sliding occurs. For higher temperatures, the sliding coefficient ramps up linearly to full sliding at the pressure-melting point, Pollard & DeConto 2012. In Pollard & DeConto 2009 the full sliding coefficient c_w was two-valued, representing hard bedrock ($10^{-10}\,\mathrm{m/aPa^2}$) and deformable sediment ($10^{-6}\,\mathrm{m/aPa^2}$). However, in this study a single value for c_w is set and a very poor range of values for this parameter ($10^{-9} - 5\cdot 10^{-8}\,\mathrm{m/aPa^2}$) are explored. In fact, for full sliding coefficient values higher than $5\cdot 10^{-8}$ the ISM presented numerical instabilities preventing any meaningful result.

SIA/SSA coupling. At each time step, in each PSU grid node the basal sliding coefficient $c_\star$ is computed, depending on the ice basal temperature relative to the pressure-melting point. For $c_\star$ values lower than 10^{-8} (including hard bedrock, $\sim 10^{-10}$), ice velocities are computed with the standard SIA dynamics (see Equations 2.24, 2.25). Otherwise, for values of the basal sliding coefficient higher than or equal to 10^{-8}, both SSA and SIA velocities are computed. Ice advection results from internal shear deformation, basal sliding and horizontal stretching, Pollard & DeConto 2012.

Ice shelves. As in GRISLI, ice shelves grid points are identified by the flotation criterion based on Archimede's principle, see Equation 2.41. Under ice shelves the ice basal temperature is set to the ice pressure-melting point. In such a way, in all ice shelves grid points the ice flow is 100% SSA and the basal sliding terms 2.74 and 2.75 are set to zero.

GL migration. In order to better capture GL migration, an analytic constraint on the flux across the GL is applied, Pollard & DeConto 2012. Following Schoof 2007, the flux in parametrized as follows,

$$q_{\mathsf{GL}} = \left(\frac{\overline{A}(T')\,(\rho g)^{n+1}\,(1-\rho/\rho_o)^n}{4^n c_s}\right)^{\frac{1}{m_s+1}} \left(\frac{\tau^{\mathrm{L}}_{ds}}{\tau^{\mathrm{L}}_{sf}}\right)^{\frac{n}{m_s+1}} \left(h_{\mathsf{GL}}^{\frac{m_s+n+3}{m_s+1}}\right), \tag{2.79}$$

where $\overline{A}(T')$ is the averaged rate-factor, ρ_o is the ocean water density, $c_s = 1/\sqrt{c_\star}$ and $m_s = 1/2$, Pollard & DeConto 2012. h_{GL} is the sub-grid ice thickness at the GL,

interpolated in space after estimating the sub-grid GL position between the surrounding floating and grounded grid points. The middle term on the right-hand side in Equation 2.79 takes into account the back stress at the GL due to the ice shelf buttressing effect. $\tau_{\mathrm{ds}}^{\mathrm{L}}$ indicates the longitudinal stretching downstream of the GL, which is calculated from the SSA. The so-called free stress $\tau_{sf}^{\mathrm{L}} = 0.5 \cdot \rho g h_{\mathsf{GL}} (1 - \rho/\rho_w)$ is the same quantity in the absence of any buttressing (see Pollard & DeConto 2012) and reference therein. The vertically averaged velocity at the GL is given by $u_{\mathsf{GL}} = q_{\mathsf{GL}}/h_{\mathsf{GL}}$. Equation 2.79 is imposed in PSU as an internal boundary condition at the GL. Moreover, it is necessary to impose the following additional rule for model resolution larger than 10 km (which is the case in this study);

- if the GL flux q_{GL} is larger than the large-scale SSA flux q_{SSA}, then the GL velocity $u_{\mathsf{GL}} = q_{\mathsf{GL}}/h_{\mathsf{GL}}$ is imposed exactly at the GL grid point;
- if conversely the GL flux q_{GL} is lower than the large-scale SSA flux q_{SSA}, then u_{GL} is imposed at grid point downstream of the GL grid point.

Typically, the former case is associated with GL retreat, whereas the latter indicates GL advance, Pollard & DeConto 2012.

Horizontal grid and initial topography. The simulations performed in this study with PSU are run on a $10' \times 10'$ (*i.e.*, around $18.5\,\mathrm{km} \times 18.5\,\mathrm{km}$) regular rectangular grid covering the Eurasian domain. The Cartesian grid has 870 points in the x-direction and 240 points in the y-direction, and the coordinates are expressed in native Cartesian distances (km), Pollard & DeConto 2012. At the beginning of each simulation initial surface topography s_0, ice thickness h_0 and bedrock elevation b_0 have to be prescribed on the $20\,\mathrm{km} \times 20\,\mathrm{km}$ PSU grid domain. Differently from GRISLI, sediment are not included in the version of PSU used in this study. Therefore, there is no need to prescribe an initial sediment thickness. In Subsection 2.3.1 the initial topography data employed in this study is illustrated.

Climate forcing and surface mass balance. In order to highlight the effect of the ISMs different ice streams and GL treating, the same climate forcing and the same SMB parametrizations used in GRISLI have been included in PSU.

Basal hydrology. Differently from GRISLI, in PSU an explicit scheme for the basal hydrology is absent. Basal hydrology is implicitly represented by the sliding coefficient.

Calving. Calving in PSU is based on the same thickness criterion used in GRISLI, although a constant calving rate is applied in place of the Lagrangian scheme implemented by Peyaud et al. 2007 in GRISLI. If an ice shelf grid node which is located at the ice shelf front has ice thickness h_f^i lower than a certain threshold H_c, then a constant calving rate r_{CAL} is applied. The same threshold $H_c = 200\,\mathrm{m}$ used in GRISLI is used also in PSU. As concerns the calving rate, two values are used in this study. A low "glacial" value of $0.5\,\mathrm{m/yr}$ is used in spin-up simulations in order to develop an extensive ice cover over the Barents and Kara Sea at LGM. In contrast, a much higher value of $60\,\mathrm{m/yr}$ is adopted for transient deglaciation simulations.

Isostatic rebound. The isostatic rebound in PSU is parametrized with the ELRA model (Le Meur & Huybrechts 1996) as in GRISLI. Also in PSU the characteristic relaxation time is set to be equal to 3 ka.

Ocean basal melting. As for the climate forcing and the SMB parametrization, the same ocean basal melting parametrizations tested in GRISLI have been included in PSU.

Therefore, also in PSU the simplified single-value method BCON and the two-equations parametrizations described in Subsection 2.3.4 are compared.

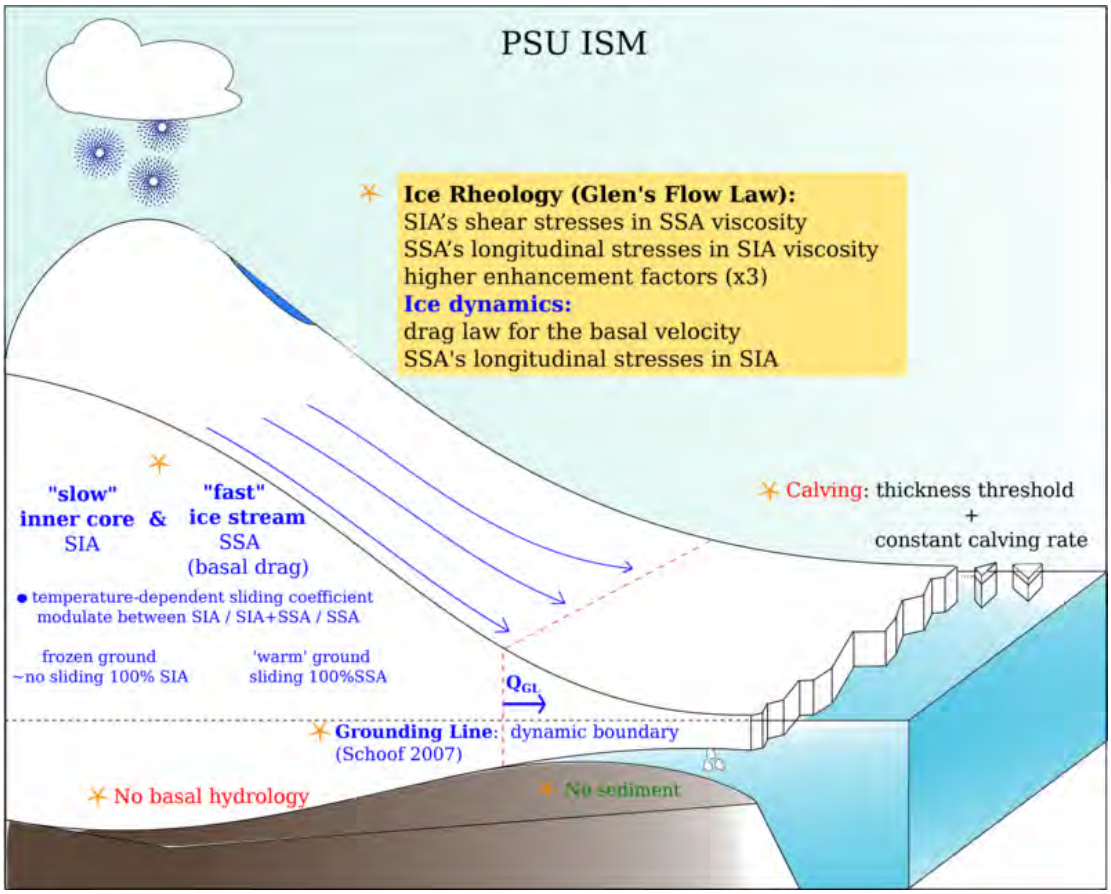

Figure 2.4: Resume of PSU ISM main differences with respect to GRISLI ISM. The model inputs are shown in green, whilst the processes acting at the geometric boundaries of the ice sheet that are parametrized in GRISLI are shown in red. Any feature of PSU ISM not mentioned in this figure is treated in the same way as in GRISLI, see Figure 2.2

.

Symbol	Description	Units	Value
$c_\star$	Basal sliding coefficient.	$\mathrm{m/a\,Pa^2}$	-
c_f	"Frozen-bed" basal sliding coefficient.	$\mathrm{m/a\,Pa^2}$	10^{-20}
c_w	Full basal sliding coefficient.	$\mathrm{m/a\,Pa^2}$	$5 \cdot 10^{-8}$
$\overline{u}$	SSA velocities.	m/yr	-
$\overline{u}_i$	SIA depth-averaged velocities.	m/yr	-
$\overline{u}_b$	SSA basal velocities.	m/yr	-
q_{GL}	Schoof 2007 flux across the GL.	$\mathrm{m^2/a}$	
$\overline{A}$	Depth-integrated rate factor.	Pa	-
h_{GL}	Sub-grid GL thickness.	m	-
$\tau_d^{\mathrm{L}} s$	Longitudinal stretching downstream of the GL.	Pa	-
$\tau_d^{\mathrm{L}} s$	Non-buttressed longitudinal stretching downstream of the GL.	Pa	-
$\mathbf{u}_{\mathsf{GL}}$	Schoof 2007 GL velocity.	m/yr	
r_{CAL}	Calving rate.	m/yr	0.5 - 60

Table 2.2: List of PSU symbols and physical constants.

2.3 Simulations set-up

2.3.1 Ice Sheet Models inputs

As illustrated in Section 2.2, both GRISLI and PSU need as initial conditions surface topography, bedrock elevation and ice thickness. In this study, with both ISMs a first group of so-called spin-up simulations is run, in order to initialize the thermodynamical state of an ice sheet. Such spin-up simulations are transient simulations run between 122 ka BP (MIS5) and LGM. At MIS5, Pre-Industrial (PI, around 1850 a.d.) conditions can be assumed in terms of topography. Therefore, a masked ice-free PI initial surface topography s_0 is prescribed at the beginning of the spin-up simulations (note that, since we assume zero ice thickness over Eurasia at MIS5, h_0 is equal to zero and the bedrock elevation coincides with the surface topography). The PI initial surface topography used is provided by Colleoni (*personal communication*) and is downscaled on GRISLI and PSU grids. In Figure 2.5a, the initial PI surface topography downscaled in GRISLI grid is illustrated. Concerning the climatology, since no fully coupled atmosphere-ocean climate simulations of MIS5 conditions were available, the PI climatology is prescribed at 122 ka BP. During the spin-up simulation, the climatology is progressed from PI to LGM (see Subsections 2.3.2 and 2.3.3) so that at the end of each spin-up the simulated LGM initial surface topography, bedrock elevation and ice thickness are provided.

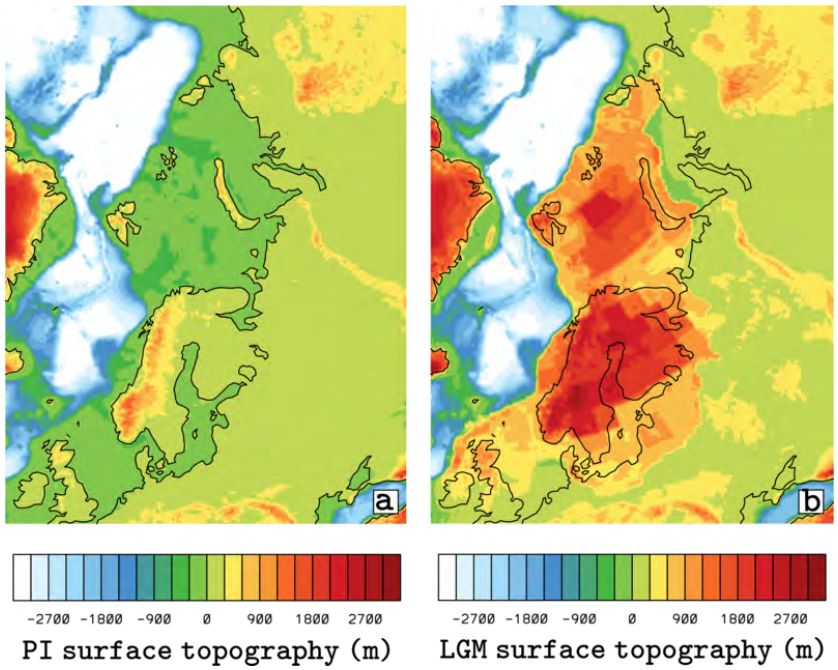

Figure 2.5: (a) PI surface topography from Colleoni (*personal communication*) interpolated on the 20 km × 20 km GRISLI grid. (b) LGM surface topography from ICE-5G data (Peltier 2004) interpolated on the 20 km × 20 km GRISLI grid.

For all the transient LGM-PI simulations with both GRISLI and PSU, the initial topographic fields are provided by the spin-up simulations. A GHF has to be provided for each simulaton with both GRISLI and PSU as a boundary condition for the ice temperature equation 2.9. In GRISLI, a geothermal heat flux map with a resolution of

$1^o \times 1^o$ from Shapiro & Ritzwoller 2004 is interpolated in the $20\,\text{km} \times 20\,\text{km}$ grid (see Figure 2.6a), following for instance Colleoni et al. 2014. In PSU, a constant value of $60\,\text{mW/m}^2$ is used, between the constant values used for the EAIS ($54.6\,\text{mW/m}^2$) and the WAIS ($70\,\text{mW/m}^2$) in Pollard & DeConto 2012. Finally, GRISLI needs also a sediment thickness map, in order to identify ice stream location throughout the simulation (see criterion IS2 in Subsection 2.2.1). So, a sediment thickness map from Laske et al. 1997 is interpolated in the $20\,\text{km} \times 20\,\text{km}$ grid (see Figure 2.6b).

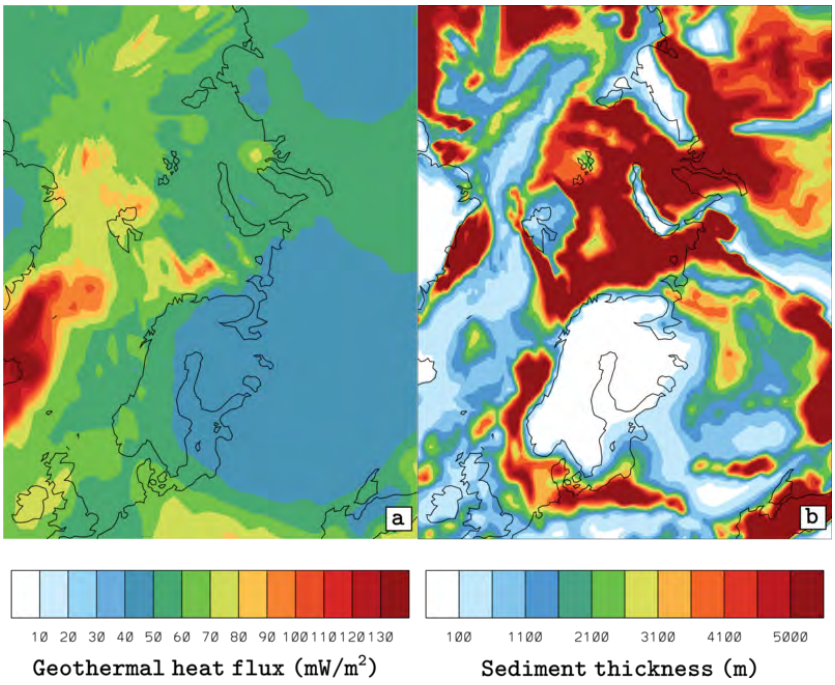

Figure 2.6: (a) Geothermal heat flux map from Shapiro & Ritzwoller 2004 interpolated on the $20\,\text{km} \times 20\,\text{km}$ GRISLI grid. (b) Sediment thickness map from Laske et al. 1997 interpolated on the $20\,\text{km} \times 20\,\text{km}$ GRISLI grid.

2.3.2 Ice Sheet Models Climate forcing: LGM and PI snapshots

In Subsection 2.2.1 it has been shown that in order to perform transient ISMs simulations one needs to prescribe at least two climate shapshots between which climate fields are interpolated in time. For each climate snapshot, mean annual and July near-surface air temperature and total mean annual precipitation are the climatic fields that must be prescribed. In this study both GRISLI and PSU ISMs are forced with climate data generated by means of climate simulations performed with coupled Atmosphere-Ocean General Circulation Models (AOGCMs) participating in the Paleoclimate Modelling Intercomparison Project (PMIP). For more than twenty years, PMIP aims to provide a mechanism for coordinating *palaeo*-climate simulations and model evaluation and intercomparison activities in order to better understand climate change mechanisms and the role of climate feedbacks. *Palaeo*-data synthesis and model-data comparison have been continuously developed to facilitate model evaluation, Braconnot et al. 2012. In particular, modeling groups participating in the PMIP3 project simulated with several AOGCMs the LGM and PI climates by performing steady-state simulations where boundary conditions such as orbital forcing, ice sheets extent/thickness and GHGs con-

centration were kept constant. In a recent work by Colleoni et al. 2016 six AOGCMs for which both LGM and PI simulation outputs were available were selected to force GRISLI ISM in six different 300,000 years long simulations of the EIS with steady-state LGM simulated climate. Compared to ICE-5G reconstruction by Peltier 2004 (based on a global glacial isostasy model) and QUEEN reconstruction by Svendsen et al. 2004 (based on terrestrial and marine geological data), a good agreement in terms of ice sheet size/extent has been obtained with the LGM climate from IPSL-CM5A-LR model (horizontal atmospheric resolution: $3.75^o \times 1.9^o$, Dufresne et al. 2013). In contrast, the use of LGM climate simulated with, respectively, MRI-CGCM3 (horizontal atmospheric resolution of $1.125^o \times 1.125^o$, Yukimoto et al. 2012) and MPI-ESM-P (horizontal atmospheric resolution of $1.9^o \times 1.9^o$, Giorgetta et al. 2013) yielded a largely overestimated and a largely underestimated ice sheet size/extent, respectively. For this reason, LGM and PI climate simulated with IPSL-CM5A-LR model are used for both GRISLI and PSU ISMs simulations. All the climate fields are downscaled from the AOGCMs on the GRISLI and PSU grid by using a lapse-rate factor of 5 ^{o}C/km and a precipitation-correction factor of 0.05 $^o C^{-1}$ (see Section 2.2). The LGM climate fields are downscaled by employing surface topography from ICE-5G reconstruction at the LGM (Peltier 2004) interpolated on GRISLI and PSU grids, see Figure 2.5b. The PI climate fields are downscaled with a PI topography provided by Colleoni (*personal communication*), see Figure 2.5a.

Looking at the PI climatologies, an important control on the northern Eurasia climate is exerted by the poleward atmospheric and oceanic heat transport, which can be both influenced for instance by the topography, bathymetry and surface albedo. In particular, the mean annual and July near-surface air temperature distribution over the Norwegian Sea provides an indication of the strength of the Atlantic Meridional Overturning Circulation (AMOC). MPI-ESM-P model exhibits higher mean annual and July temperatures than MRI-CGCM3 and IPSL-CM5A-LR models over Norwegian Sea, thus suggesting a stronger AMOC with respect to the other two models (Figure 2.7). The mean annual near-surface air temperature over Norwegian Sea is positive for MPI-ESM-P model, whilst for MRI-CGCM3 and IPSL-CM5A-LR models negative temperatures between -6°C and -1°C are registered in the same region (Figure 2.7). A negative mean annual near-surface air temperature over Norwegian Sea implies that the sea ice does not completely disapperar during summer in this area, possibly preventing the North Atlantic warm intermediate water from reaching Barents and Kara Sea. Conversely, a positive mean annual near-surface air temperature necessarily requires open ocean conditions during summer. The three climate models largely agree on the mean annual and July near-surface air temperature distribution over Scandinavia (negative mean annual temperatures, -3°C to -12°C, positive mean July temperatures, 3°C to 15°C) and Siberia/Kara Sea (negative mean annual temperatures, -12°C to -18°C, slightly negative mean July temperatures, -1°C to -5°C). Over the Barents Sea, negative mean annual near-surface air temperatures between -6°C and -15°C are obtained with IPSL-CM5A-LR and MRI-CGCM3 models, whilst MPI-ESM-P model provides warmer temperatures between -6°C and 3°C. A negative July near-surface air temperature down to -3°C is registered with IPSL-CM5A-LR, whilst positive July temperatures between 3°C and 6°C are reached with MRI-CGCM3 and MPI-ESM-P models (Figure 2.7). All the climate models considered in this study show mean annual precipitation maxima up to 1.8 m/yr in the storm tracks area in the North Atlantic.

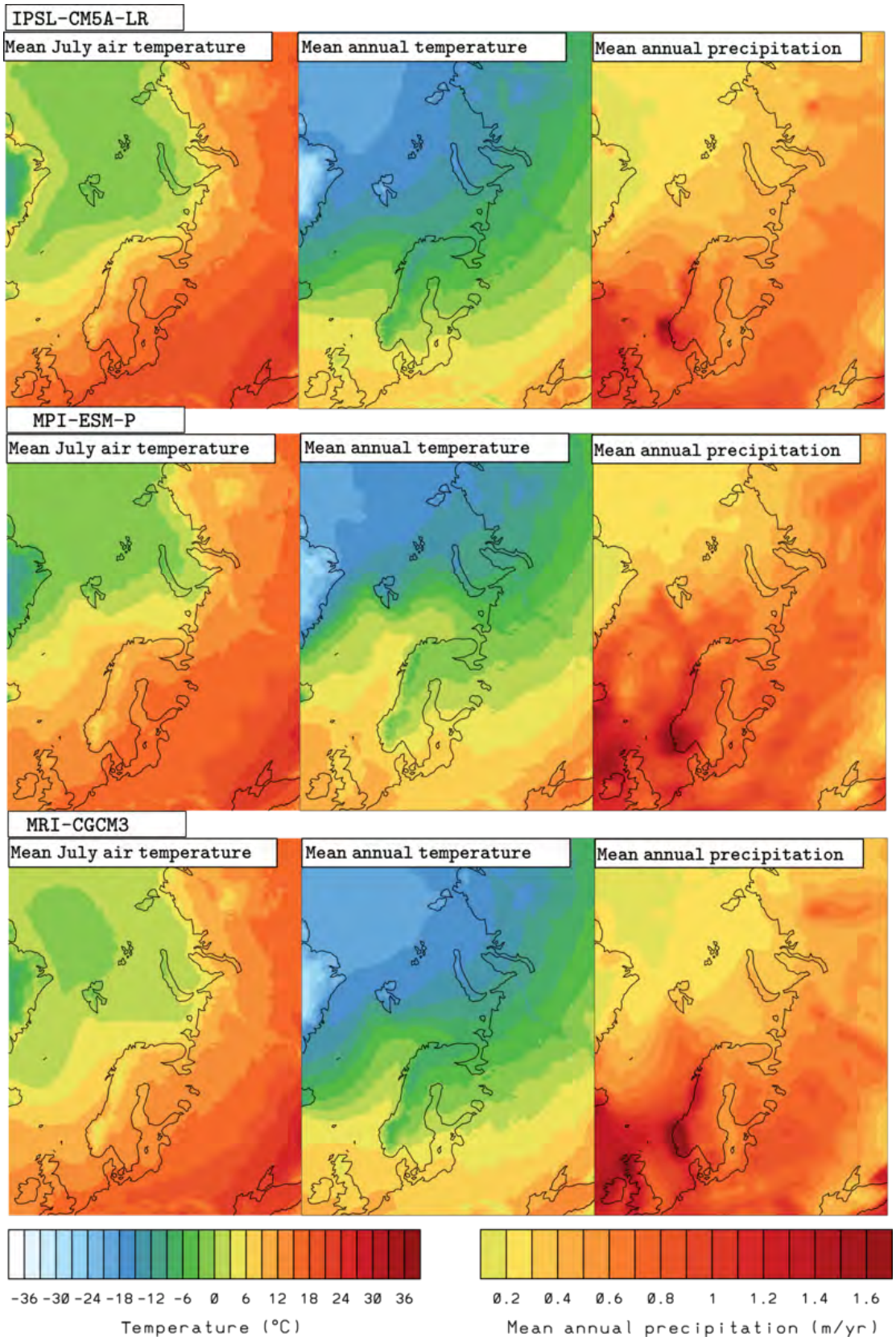

Figure 2.7: IPSL-CM5A-LR, MRI-CGCM3 and MPI-ESM-P Pre-Industrial climate fields (mean annual near-surface air temperature, mean July near-surface air temperature, mean annual precipitation) downscaled on the GRISLI 20 km × 20 km grid.

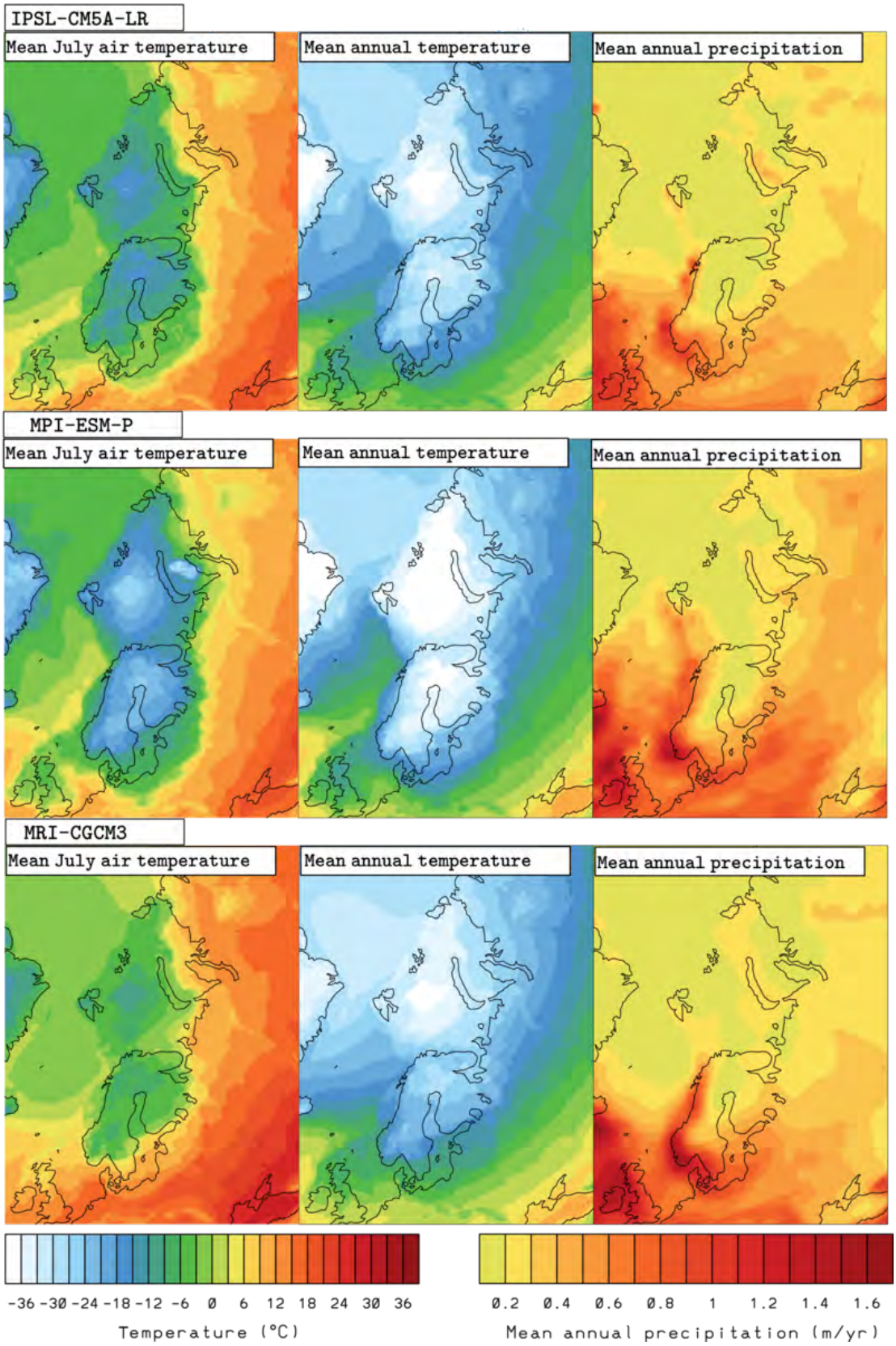

Figure 2.8: IPSL-CM5A-LR, MRI-CGCM3 and MPI-ESM-P Last Glacial Maximum climate fields (mean annual near-surface air temperature, mean July near-surface air temperature, mean annual precipitation) downscaled on the GRISLI 20 km × 20 km.

A higher mean annual precipitation over the Barents Sea is simulated by MPI-ESM-P model in response to the northern expansion of the storm track area, due to the reduced sea ice cover over the Norwegian Sea, Colleoni et al. 2016.

As concerns the LGM climatologies, in all models it is clear the cold imprint of the EIS due to its high elevation and albedo, although the extent of the cooling varies amongst the models. Over the SIS negative mean annual near-surface air temperatures around -12°C along the ice sheet margin and -27°C over the central area are simulated by IPSL-CM5A-LR and MRI-CGCM3 models. In contrast, MPI-ESM-P model register in the same two regions negative temperatures around -18°C and -36°C respectively (Figure 2.8). Negative mean July near-surface air temperature all over the SIS are obtained with IPSL-CM5A-LR and MPI-ESM-P models. However, IPSL-CM5A-LR model simulates weakly negative July temperatures (around 3°C) over a large portion of the SIS in the South, while in the same region MPI-ESM-P the July temperature oscillates between -9°C and -12°C (Figure 2.8). MRI-CGCM3 is the warmer model in this area, showing positive temperatures up to 9°C along the southern SIS margin. According to IPSL-CM5A-LR, MRI-CGCM3 models, over the SBKSIS mean annual near-surface air temperatures vary between -18°C along the ice sheet margin and -36°C over the central dome (Figure 2.8). MPI-ESM-P model simulates an even colder mean annual near-surface air temperature below -36°C over almost the entire SBKSIS. During summer, strong negative air temperatures over the SBKSIS are obtained with IPSL-CM5A-LR and MPI-ESM-P models, while in the same region MRI-CGCM3 model simulates less cold near-surface air temperatures between 0°C and -12°C. It is also worthwhile to notice that during summer IPSL-CM5A-LR and MPI-ESM-P models simulate positive temperatures up to 9°C over the non-glaciated portion of Kara Sea, Yamal Peninsula and Taimyr Peninsula, whilst MRI-CGCM3 fails to reproduce positive temperatures in a large part of these regions (Figure 2.8). For all the climate models, mean annual precipitation slightly decreases along the western margin of the SIS (Figure 2.8). Moreover, over the central part and along the eastern margin of the EIS a precipitation decrease larger than 80% is observed with all the models, in response to (1) the Southward shift of the precipitation caused by the presence of the EIS, acting as a topographic barrier and thus preventing the flow over the ice sheet, (2) the air temperature cooling caused by the EIS (via the lapse-rate effect) which reduces the precipitation through the elevation-desert effect in this area (Figure 2.8). Finally, the presence of the LGM LIS causes a deflection in the path of the extratropical NH westerly winds, leading to slightly increased mean annual precipitation at the south-western margins of the EIS, Colleoni et al. 2016. Finally, as concerns the eustatic sea level, at LGM a value of -135 m with respect to PI is prescribed.

2.3.3 Macro-regional climate indexes from TraCE-21ka simulation

As shown in Section 2.2, in order to perform a transient simulation between two climatic stages (*i.e.*, LGM and PI in the transient simulations of the last deglaciation) climatic indexes representative of the climate evolution in time are needed to interpolate between the two climate snapshots during the simulation. Since GRISLI and PSU ISMs read as climatic input the mean annual and July near-surface air temperature and the mean annual precipitation, it is necessary to provide an index for each climatic field. An

approach widely used in several *palaeo*-ice sheet modeling studies (*e.g.*, Marshall et al. 2000; Marshall 2002, Charbit et al. 2002, Tarasov & Peltier 2004, Zweck & Huybrechts 2005, Clason et al. 2014, Patton et al. 2016) consists in using an index derived from the NGRIP $\delta 18$O record, North Greenland Ice Core Project Members 2007. Such approach based on field data provides the time variability needed to interpolate between initial and final climate snapshots. Nevertheless, by using in this study an index based on the NGRIP δ^{18}O record it would be implicitly assumed that the same climatic oscillations took place in Greenland and Eurasia, which are two regions with remarkably different climatic background, especially in terms of atmospheric and oceanic heat sources and precipitation patterns. Moreover, to use the same NGRIP δ^{18}O-based index for the whole Eurasia relies on the assumption that both air temperature and precipitation varied in Fennoscandina, Svalbard/Barents Sea and Siberia/Kara Sea at the same pace in the last 21 ka, thus neglecting any longitude-latitude variation of the climate fluctuations. Last, but not least, the NGRIP δ^{18}O record approach implies that the same variability for air temperature and precipitation is considered. Although air temperature and precipitation are linked via the elevation-desert feedback, these two climatic components vary in response to different climatic and dynamic processes. In order to include in GRISLI and PSU ISMs a climatic variability depending not only on time but also on latitude/longitude and on the specific climate field that is considered, a different approach is adopted. In fact, climate indexes based on the non-accelerated transient climate simulation of the last 21 ka (TraCE-21ka, Liu et al. 2009) are constructed. The aspects of TraCE-21ka climate simulation which are more relevant for this study are briefly described in the appendix at the end of this section.

TraCE-21ka simulations data are used to construct different indexes for air temperature and precipitation representative of Fennoscandia, Svalbard/Barents Sea and Siberia/Kara Sea macro-regions. For each macro-region, seven different nodes in the TraCE-21ka grid are selected (Figures 2.9g-h-i). In each grid node, mean annual air temperature T_a and mean annual precipitation P_a are computed every 100 years throughout the deglaciation time, that is from LGM to PI (see Figures 2.9a-f). As shown in Section 2.2, both GRISLI and PSU ISMs correct mean annual near-surface air temperature and mean annual precipitation for changes in surface elevation during run-time. Since the same correction is applied in TraCE-21ka simulation, such correction is neglected when computing the climate indexes, in order to not count twice in the ISMs simulations those temperature and precipitation changes resulting from surface elevation variations. Consequently, for each TraCE-21ka grid node that have been selected, at each time step i the temperature variation resulting from the lapse-rate effect is subtracted from the mean annual air temperature as follows

$$T_c^a(i) = T^a(i) - \lambda_T \cdot (S(i) - S(\mathrm{LGM})) \ , \tag{2.80}$$

where $T_c^a(i)$ is TraCE-21ka mean annual air temperature at the time step i corrected from the lapse-rate effect, $S(i)$ is the surface elevation at the time step i, S_{LGM} is the surface elevation at LGM and λ_T is the same lapse-rate of 6.5 $^{\circ}$C/km which have been adopted in TraCE-21ka simulation.

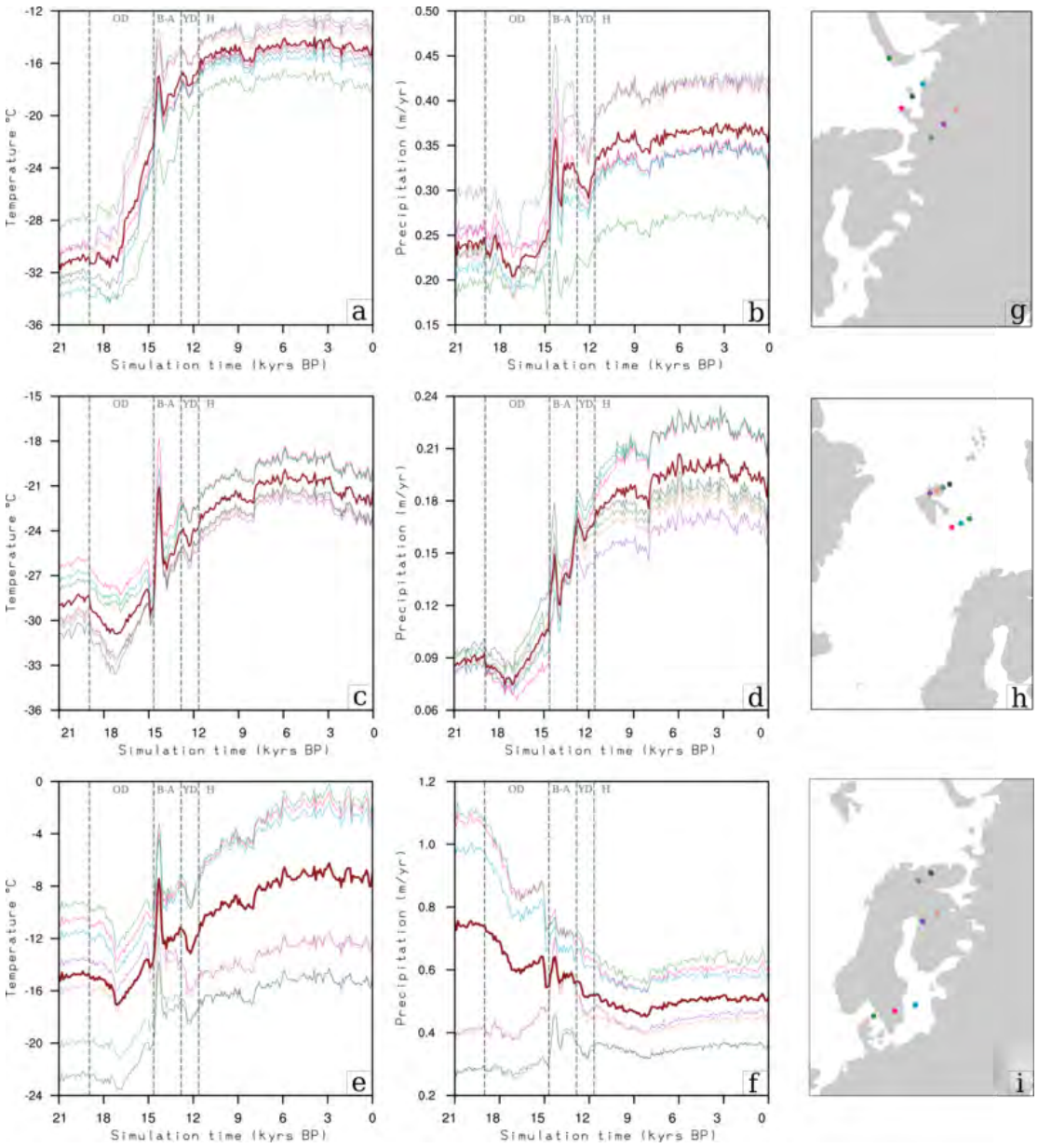

Figure 2.9: Mean annual near-surface air temperature and precipitation evolution at different TraCE-21ka grid points in the three macro-regions Siberia/Kara Sea (a)-(b), Svalbard/Barents Sea (c)-(d) and Fennoscandia (e)-(f). In dark red the average between the different grid points values is shown, whereas the location of the grid points in each macro-region is displayed in panels (g)-(h)-(i).

Similarly, at each time step i those mean annual precipitation changes deriving from changes in elevation are neglected as follows,

$$P_c^a(i) = P^a(i) \cdot \exp\left(-\gamma_T \left(T_c^a(i) - T^a(i)\right)\right) \ , \tag{2.81}$$

where P_c^a is the TraCE-21ka mean annual precipitation at the time step i corrected from elevation differences and γ_T is the precipitation-correction factor, taken equal to 0.05 $^{o}C^{-1}$ following Colleoni et al. 2014.

Corrected mean annual near-surface air temperature and precipitation evolution throughout the deglaciation for each grid node in the three different macro-regions are

shown in Figures 2.9a-f. The grid nodes average for mean annual near-surface air temperature $\overline{T}_c^a$ and precipitation $\overline{P}_c^a$ are considered for each macro-region and at each time step, see the dark red line in Figures 2.9a-f. For each macro-region and at each time step i, the value for temperature and precipiation indexes I_T and I_P respectively is then computed as follows,

$$I_T(i) = \frac{\overline{T}_c^a(i) - \overline{T}_c^a(\text{PI})}{\overline{T}_c^a(\text{LGM}) - \overline{T}_c^a(\text{PI})} , \tag{2.82}$$

$$I_P(i) = \frac{\overline{P}_c^a(i) - \overline{P}_c^a(\text{PI})}{\overline{P}_c^a(\text{LGM}) - \overline{P}_c^a(\text{PI})} , \tag{2.83}$$

so that the all the indexes take value 1 at LGM and 0 at PI.

In Figure 2.10a the TraCE-21ka-based macro-regional mean annual air temperature indexes are shown together with the NGRIP δ^{18}O-based index for comparison. During the first 2 ka a slight warming is registered uniformly in all the three macro-region considered. This is a consequence of the NH increase of insolation during spring and summer driven by the orbital forcing prescribed in TraCE-21ka simulation, see Subsection 2.3.7. The 21-19 ka BP warming predicted by the NGRIP δ^{18}O-based index is much more intense, possibly due to polar amplification effects. Between 19-17 ka BP the mean annual near-surface air temperature in Fennoscandia and Svalbard/Barents Sea regions is affected by the weakening of the AMOC until its near-collapse during H1, see Subsection 2.3.7. In fact, because of the reduced northward heat transport Fennoscandia and Svalbard/Barents Sea regions register a significant cooling and the near-surface air temperature indexes representative of these two macro-regions exceed by up to 20% their LGM value. Siberia/Kara Sea mean annual air temperature does not show significant cooling or warming in the same interval, likely because the weakening of the AMOC does not affect this region in terms of heat transport. The NGRIP δ^{18}O-based index does not display a strong cooling between 19 and 17 ka BP, which can be possibly explained by the lower impact that the AMOC northward heat transport has on the air temperature at the NGRIP core location (inner Greenland). The AMOC resumption after H1 until the end of B-A (see Subsection 2.3.7) results in several abrupt air temperature increases in Fennoscandia and Svalbard/Barents Sea, whilst in Siberia/Kara Sea the warming between H1 and the end of B-A is more gradual. However, the NGRIP δ^{18}O-based index and the TraCE-21ka-based indexes are in good agreement as concerns the magnitude of the warm peak around 14.6 ka BP, with air temperatures close to PI values. The weakening of the AMOC following B-A (see Subsection 2.3.7) results in the YD cold interval both in Fennoscandia and Svalbard/Barents Sea, although NGRIP δ^{18}O values suggest an up to two times stronger cooling. Conversely, in Siberia/Kara Sea the YD cold signal is almost non-existent. After YD, the NGRIP δ^{18}O-based index and the TraCE-21ka-based indexes behaviour is comparable, although the Holocene Climatic Optimum (HCO) starts earlier, *i.e.*, around 9 ka BP according the NGRIP δ^{18}O index.

Concerning the precipitation, in Figure 2.10b the TraCE-21ka-based macro-regional mean annual air temperature indexes are shown along with the NGRIP δ^{18}O index for comparison. Svalbard/Barents Sea and Siberia/Kara Sea precipitation indexes shares similar behaviour, although dry and wet peaks are much more abrupt in Siberia/Kara Sea macro-region. The precipitation pattern in Siberia/Kara Sea and Svalbard/Barents

Sea is closely related to the elevation of the EIS, which acts as a topographic barrier and thus prevents the precipitation over these two macro-regions. Consequently, an increase in precipitation is observed only after 17 ka BP. In Fennoscandia the precipitation index aspect is affected by the strong difference both in pattern and magnitude of mean annual precipitation depending on the latitude of the TraCE-21ka grid nodes (Figure 2.9f). In fact, in the southern part of Scandinavia precipitation at LGM is quite a lot higher than at PI (around +0.4 m/yr); this can be explained with the southward shift of the NH Westerlies, due to the presence of the LIS. Conversely, grid points on the northern part of Fennoscandia register a very weak increase in precipitation between LGM and PI (around +0.1 m/yr). Only after around 13 ka BP, that is after a consistent lowering of the LIS (more than 2 km), all the TraCE-21ka Fennoscandia grid nodes display similar patterns of mean annual precipitation. This results in a Fennoscandia precipitation index which varies quite uniformly, assuming PI values after the beginning of B-A and exceeding by 30% PI values around 14 ka BP. After 14 ka BP, Fennoscandia precipitation index varies within 30% of PI value. Finally, as concerns the eustatic sea level index i_{SL}, the NGRIP δ^{18}O-based index is used to modulate between LGM and PI (see Figure 2.10).

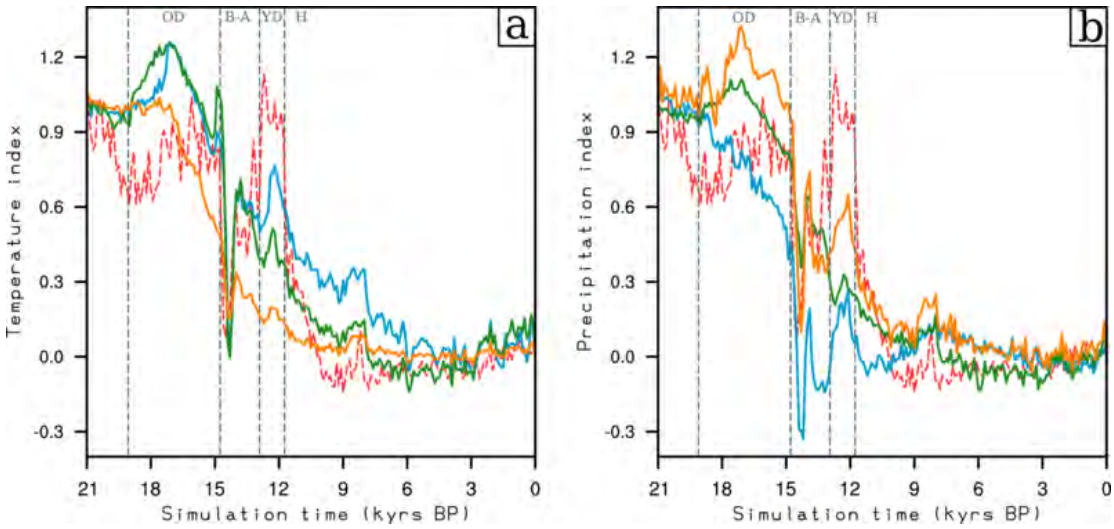

Figure 2.10: (a) Mean annual near-surface air temperature and (b) precipitation macro-regional index representative of Fennoscandia (blue), Svalbard/Barents Sea (green), Siberia/Kara Sea (orange). NGRIP δ^{18}O-based index is shown in dashed red for comparison.

2.3.4 Ocean basal melting parametrizations

As shown by modeling and field studies in present-day Antarctica, large-scale oceanic circulation exerts a strong control on the ocean basal melting below the ice shelves. In fact, warm circumpolar water can override the continental slope front and reach into submerged glacial troughs, thus reaching the GL and causing high basal melting rates under the ice shelves, *e.g.*, Pollard & DeConto 2009, Hellmer et al. 2012, Golledge et al. 2015, Li et al. 2015, Feldmann & Levermann 2015, Alley et al. 2016. Considering the bathymetric similarity between the present-day WAIS and the SBKSIS at the LGM, a similar interplay between ice, ocean currents and continental bathymetry is likely to have occurred. Warm Atlantic water flowing as a subsurface water mass below a layer of

polar surface water could have reached into Barents, Kveithola and Storfjorden trough (*e.g.*, Rasmussen et al. 2007), thus influencing the ice loss at the western Barents Sea margin of the EIS. Therefore, the single-value approach used in the ocean basal melting parametrization BCON (see Subsection 2.2.1) is a crude oversimplification.

In this study, two relatively more sophisticated ocean basal melting parametrizations respectively from Martin et al. 2011 (denoted with BMAR) and Pollard & DeConto 2012 (denoted with BPDC) are tested. Both parametrizations follow Beckmann & Goosse 2003, relating the ocean basal melting rate with the heat flux between ocean and ice at the ice shelf base. The salinity transition occurring in the oceanic mixed layer from the almost fresh ice shelf base water to the salty ocean water is not taken into account in both parametrizations, Pollard & DeConto 2012. Denoted the (positive) ice shelf base depth with z_b and the ocean salinity with S_o, the ice shelf base is assumed to be at the freezing temperature of ocean water T_f at depth z_b, *i.e.*,

$$T_f(z_b) = 0.0939 - 0.057 \cdot S_o(z_b) - 7.64 \cdot 10^{-4} \cdot z_b \,. \tag{2.84}$$

Denoted the ocean temperature with T_o, the ice-ocean heat flux Q_h is then obtained in the parametrization from Martin et al. 2011 as follows,

$$Q_h = \rho_0 c_o \gamma_t F_m \left(T_o(z_b) - T_f(z_b)\right) \,, \tag{2.85}$$

where ρ_0 is the density of the ocean water, c_o the specific heat capacity of the ocean mixed layer, γ_t the thermal exchange velocity and F_m a hand-tuned model parameter with no physical meaning. In Pollard & DeConto 2012 a similar parametrization is proposed, although following Holland et al. 2008 the relationship between the heat flux and the ice-ocean temperature difference is quadratic rather than linear,

$$Q_h = \rho_0 c_o \gamma_t F_m \mid T_o(z_b) - T_f(z_b) \mid \left(T_o(z_b) - T_f(z_b)\right) \,. \tag{2.86}$$

Finally, both parametrizations deduce the ocean basal melting rate b_m from the ice-ocean heat flux as follows,

$$\mathrm{b}_m = \frac{Q_h}{L\rho} \,, \tag{2.87}$$

where L is the latent heat capacity of ice. Both BMAR and BPDC parametrizations have been employed in AIS simulations setting the model parameter $F_m = 0.005$ in Equations 2.85 and 2.86. Such value has been selected by Martin et al. 2011 in order to match the present-day GL position in the WAIS.

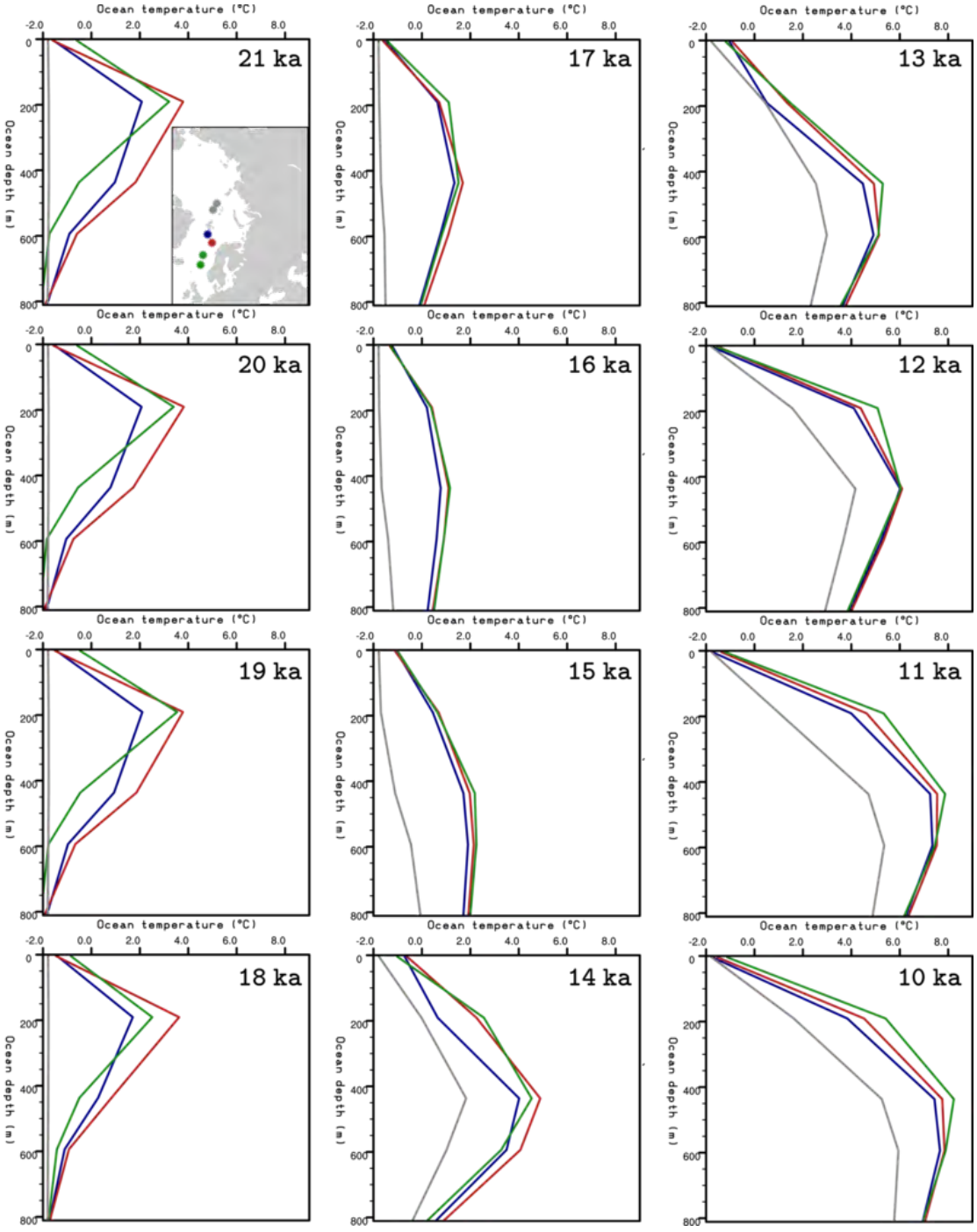

Figure 2.11: Time-slice ocean temperature profiles from Arctic Ocean (grey), Norwegian Sea (green), south-western Barents Sea (red) and north-western Barents Sea (blue) derived from TraCE-21ka climate simulation. The profiles are shown every 1000 years from LGM to 10 ka BP. In the inlay panel, the location of the TraCE-21ka grid nodes that have been used to calculate the vertical profiles is shown with the same color legend.

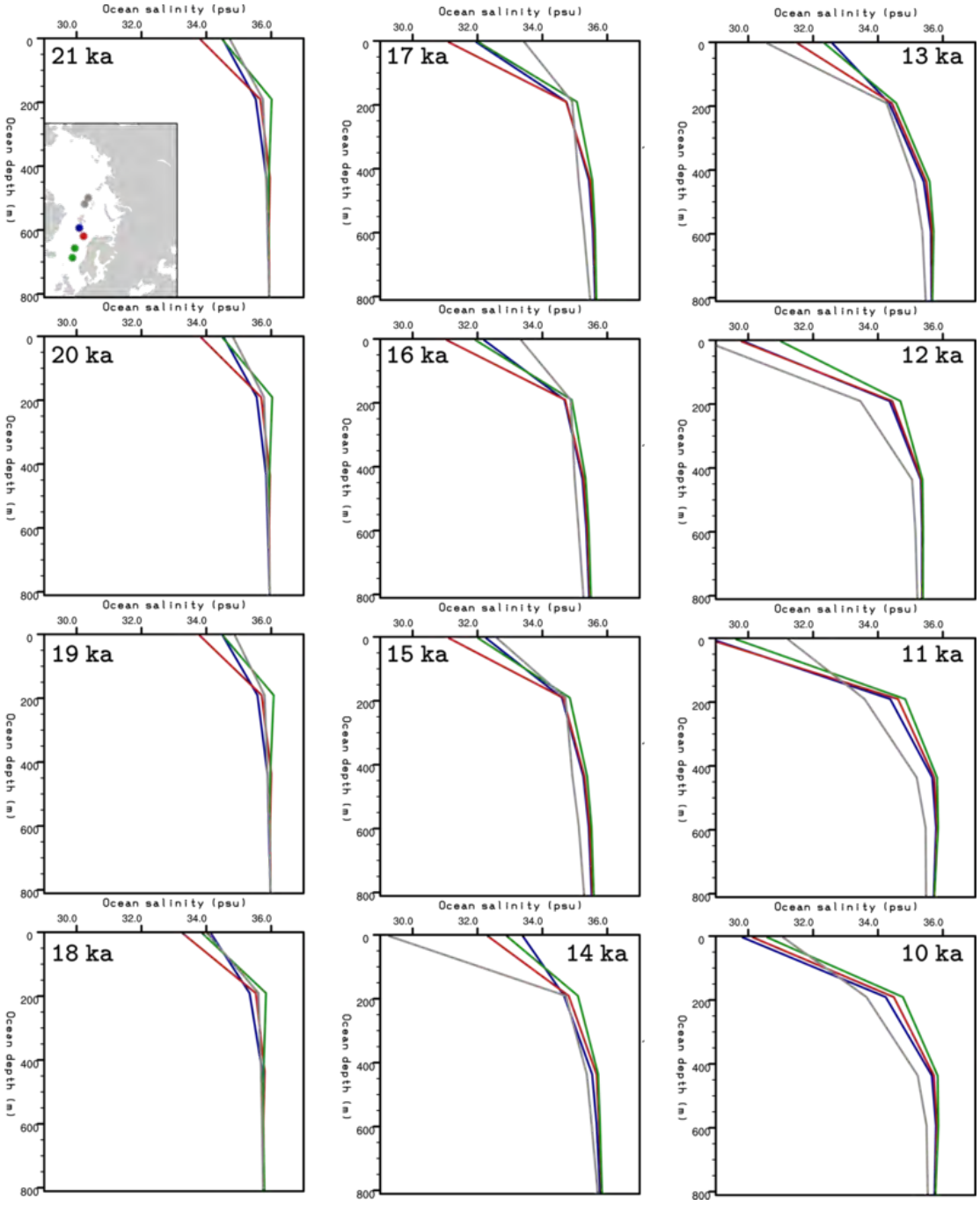

Figure 2.12: Time-slice ocean salinity profiles from Arctic Ocean (grey), Norwegian Sea (green), south-western Barents Sea (red) and north-western Barents Sea (blue) derived from TraCE-21ka climate simulation. The profiles are shown every 1000 years from LGM to 10 ka BP. In the inlay panel, the location of the TraCE-21ka grid nodes that have been used to calculate the vertical profiles is shown with the same color legend.

In particular, the tuning of the model parameter F_m has been performed considering present-day Antarctica ocean temperature and salinity conditions, assuming constant ocean temperature $T_o = -1.7$°C and constant ocean salinity $S_o = 35$. Such oceanic conditions cannot be assumed for this study, as the oceanographic background is completely different in Eurasia than in Antarctica. Therefore, we adopt an approach based on TraCE-21ka climate simulation (Liu et al. 2009) to determine the ocean temperature and salinity values used to force both BMAR and BPDC parametrizations.

TraCE-21ka data are used to determine time/space-varying ocean temperature and salinity in the last 21 ka. In fact, four different time-varying ocean temperature and salinity vertical profiles are computed from TraCE-21ka grid nodes located in the Arctic Ocean, Norwegian Sea, south-western and north-western Barents Sea, respectively (see inlay in Figure 2.11). In both the Arctic Ocean and Norwegian Sea, two grid points in the TraCE-21ka ocean domain are considered (see the inlay Figure 2.11). The vertical profiles representative of these two regions are obtained by taking temperature and salinity averages. In the south-western and north-western Barents Sea only one grid point is selected, as shown in the inlay Figure 2.11. The vertical profiles representative of each macro-region are showed every 1000 years from LGM to PI in Figures 2.11 and 2.12 respectively. The evolution of the profiles is quite similar in the Norwegian Sea, south-western and north-western Barents Sea regions, except for minor differences in the magnitude. The evolution of temperature and salinity profiles in the Arctic Ocean is clearly different, although it is possible to notice a similarity in the evolution pattern after the MWP-1A. However, as in this study we are mainly interested in the evolution of the north-western Barents Sea margin of the EIS, we focus on the oceanographic evolution in the Norwegian Sea, south-western and north-western Barents Sea regions. During the early phase of the deglaciation (21 to 19 ka BP) both salinity and temperature profiles remain essentially unchanged. The profiles show a deep halocline in the first 200 m, whereas below 200 m the salinity is nearly constant throughout the water column. The water temperature reaches its maximum values (between 2 and 4 °C around 200 m depth. During the OD period the salinity decreases (around -2 psu) in the first 400 m, likely due to the NHWM events caused by the melting of the EIS. Between 19 and 17.5 ka BP the water temperature cools down by around 1.5 °C in the first 400 m. Nevertheless, the ocean temperature vertical profile mantains the same pattern. Around 17 ka BP an abrupt change in the temperature profile is observed. In fact, the ocean temperature profile shows a weak temperature rise in the first 400 m and a weak temperature decrease below 400 m. The maximum ocean temperature is reached at 400 m depth and is low (around 2 °C). Such profile pattern remains essentially unchanged until 15 ka BP, except for a slight temperature increase below 400 m. Right after the sudden termination of NHMW after 14.67 ka BP an increase in salinity and another drastic change in the temperature profile pattern is observed. Looking at the ocean temperature vertical profile at 14 ka BP, the ocean temperature increases from the surface to 400 m, reaching a maximum tempeature around 5 °C. We can interprete this abrupt change in pattern as a consequence of the switch from a nearly-collapsed state to a present-day-like state of the AMOC. Between 13 and 12 ka BP the ocean temperature shows an important increase in the first 400 m, whereas after 12 ka BP the ocean temperature increases mostly below 400 m. Finally, a particularly strong halocline is registered at 11 ka BP, likely caused by NHMW events and intermediate warm Atlantic water intrusion.

Ocean temperature and salinity profiles varying every 100 years from LGM to PI and representing each one of the above-mentioned macro-region are obtained from TraCE-21ka. For each macro-region, ocean temperature and salinity profiles are included both in GRISLI and PSU numerical models in the following way:

- first, the LGM and PI ocean temperature and salinity vertical profiles are reconstructed at five selected vertical levels: 0 m, 200 m, 400 m, 600 m, 800 m. At each vertical level, LGM and PI ocean temperature and salinity are obtained from TraCE-21ka simulation and included in GRISLI and PSU. Given a vertical level j, LGM and PI ocean temperature and salinity are denoted with T^j_{LGM}, T^j_{PI}, S^j_{LGM} and S^j_{PI} respectively. The ocean temperature and salinity profiles at LGM and PI are computed during run-time by linearly interpolating between each vertical level. At larger depths than 800 m the ocean temperature and salinity are kept constant.
- at each vertical level j, LGM-PI ocean temperature i^j_T and salinity i^j_S indexes are computed every 100 years from TraCE-21ka data. At a given time t the temperature and salinity indexes are given by,

$$i^j_T = \frac{T^j(t) - T^j_{\mathrm{PI}}}{T^j_{\mathrm{LGM}} - T^j_{\mathrm{PI}}}\,, \tag{2.88}$$

$$i^j_S = \frac{S^j(t) - S^j_{\mathrm{PI}}}{S^j_{\mathrm{LGM}} - S^j_{\mathrm{PI}}}\,, \tag{2.89}$$

$$\tag{2.90}$$

  where j is one of the vertical levels. In such a way all the indexes take value 1 at LGM and 0 at PI. All the ocean temperature and salinity indexes are then included in GRISLI and PSU.

During a GRISLI or PSU simulation, given an ice shelf grid point the ISM identifies first the macro-region in which the point is contained depending on its longitude/latitude. The depth of the ice shelf base $z_b = s - h$ is then computed, and the vertical levels j and $j+1$ such that $j \leq z_b < j+1$ are identified, where $j = 0, 200, 400, 600, 800$. At a given time t, the ocean temperature and salinity at vertical levels j and $j+1$ are computed as follows,

$$T^j(t) = i^j_T(t) \cdot T^j_{\mathrm{LGM}} + \left(1 - i^j_T\right) \cdot T^j_{\mathrm{PI}}\,, \tag{2.91}$$

$$T^{j+1}(t) = i^{j+1}_T(t) \cdot T^{j+1}_{\mathrm{LGM}} + \left(1 - i^{j+1}_T\right) \cdot T^{j+1}_{\mathrm{PI}}\,, \tag{2.92}$$

$$S^j(t) = i^j_S(t) \cdot S^j_{\mathrm{LGM}} + \left(1 - i^j_S\right) \cdot S^j_{\mathrm{PI}}\,, \tag{2.93}$$

$$S^{j+1}(t) = i^{j+1}_S(t) \cdot S^{j+1}_{\mathrm{LGM}} + \left(1 - i^{j+1}_S\right) \cdot S^{j+1}_{\mathrm{PI}}\,. \tag{2.94}$$

$$\tag{2.95}$$

By linearly interpolating between $T^j(t)$, $S^j(t)$ and $T^{j+1}(t)$, $S^{j+1}(t)$ the ocean temperature and salinity at depth z_b are respectively computed and used to force the ocean basal melting parametrizations in Equations 2.85, 2.86 and 2.84. In such a way the ocean basal melting is forced with ocean temperature and salinity varying in time and space

(vertically and horizontally in the sense of macro-regions) throughout each GRISLI and PSU simulation.

Once that an adequate oceanic forcing is set for the ocean basal melting parametrizations BMAR and BPDC, a new strategy to tune the model parameter F_m is needed. In fact, the oceanic conditions under which Martin et al. 2011 tuned the model parameter F_m are drastically different from the oceanic conditions derived from TraCE-21ka (see Figures 2.11 and 2.12). An a-priori analysis of the oceanic forcing used in this study is performed, in order to identify a range of values for F_m to be explored. First of all, a typical GL depth of 400 m in the north-western Barents Sea is considered. Looking at TraCE-21ka simulation, between LGM and 10 ka BP at such depth the warmer water temperature (around 7.5 °C, see Figure 2.11) is reached around 10 ka BP in the South western and north-western Barents Sea. A water salinity of around 35.5 psu is reached at the same depth and time frame in the South western and north-western Barents Sea. By inserting such "warm" ocean conditions in Equations 2.85, 2.86 and 2.84 we obtain the maximum LGM-10 ka BP ocean basal melting rate $\mathrm{b}_{\mathsf{max}}$ as a function of the model parameter F_m only, *i.e.*,

$$\mathrm{b}_{\mathsf{max}} = \begin{cases} 41.97 \cdot F_m^{\mathsf{BMAR}} \cdot 9,73\,, & (\mathsf{BMAR}) \\ 41,97 \cdot F_m^{\mathsf{BPDC}} \cdot (9.73)^2\,. & (\mathsf{BPDC}) \end{cases} \tag{2.96}$$

In such a way for both parametrizations it is possible to identify a range of values for the model parameter F_m so that b_{max} matches the ocean basal melting values observed under the present-day Antarctica ice shelves. Estimates for the annual basal mass-loss rates of Antarctic ice shelves from Depoorter et al. 2013 and Rignot et al. 2013 range between $0.1 - 22\,\mathrm{m/yr}$. However, the averaged annual basal mass-loss rate of ice shelves in the West Antarctica Peninsula take lower values between $0.8 - 1.0\,\mathrm{m/yr}$, Depoorter et al. 2013. Therefore, we decided to set a range for b_{max} between $0.1 - 6\,\mathrm{m/yr}$. In such a way, the ranges identified for the model parameter F_m with BMAR and BPDC parametrizations are, respectively,

$$\begin{aligned} 0.000244 \leq & F_m^{\mathsf{BMAR}} \leq 0.0146\,, \\ 0.0000252 \leq & F_m^{\mathsf{BPDC}} \leq 0.00156\,. \end{aligned}$$

In Subsection 2.3.5 the approach adopted to explore such ranges for the model parameter F_m is carefully explained.

2.3.5 GRISLI Latin Hypercube sampling of model parameters

ISMs typically present a large number of model parameters with a wide range of values. In this sense GRISLI and PSU make no exception, as already shown and discussed in Subsections 2.2.1 and 2.2.2. Due to ISMs computational cost, it is not possible to systematically explore all the possible combinations of model parameter values. Statistical approaches such as the Monte-Carlo sampling is often used in geosciences for many applications, see Colleoni et al. 2016 and reference therein. In a Monte-Carlo sampling a preset number of parameters combinations n is generated through a random exploration of each parameter range. However, since the exploration of the the various ranges of values is random, it is necessary to consider a large number of experiments to explore

the whole range for the different parameters. If the number of experiments n is too low, the tails of the range of each parameter could remain unexplored, Colleoni et al. 2016. This represents a strong limitation in this study, since the lower and the upper values of each parameter range are assumed to be equiprobable. Following Colleoni et al. 2016, a refinement of the standard Monte-Carlo sampling is performed in this study. The so-called Latin Hypercube Sampling (LHS) is constructed so that for each parameter the whole range is systematically explored. In the LHS one has first to define the k variables selected for the analysis and their associated ranges of values. Once that the number of experiments for the analysis n is set, each variable range is equally divided into n bins. The sampled parameters values are generated by means of a random uniform permutation of the n bins for each one of the k variables.

In this study five GRISLI model parameters (*i.e.*, $k = 5$) are considered for the LHS. In Table 2.3 the different parameters, their associated range and their reference values are listed as a summary. The GRISLI model parameters considered for the LHS are:

- the topographic lapse-rate λ, which represents an approximation of how much the near-surface air temperature changes in response to a change in elevation (see Subsections 1.2.1 and 2.2.1). This parameter is poorly constrained in large-scale ice sheet modelling studies, ranging from 6 to $8\,^{\circ}\mathrm{C/km}$, whereas topographic lapse-rate values computed from climate simulations range from 4.1 to $10\,^{\circ}\mathrm{C/km}$ (see Colleoni et al. 2016 and reference therein). Following Stone et al. 2010 and Colleoni et al. 2016, in this study the range 4 to $8.2\,^{\circ}\mathrm{C/km}$ is explored, whereas the value $5\,^{\circ}\mathrm{C/km}$ is taken as reference value;

- the precipitation-correction factor γ, which accounts for changes in precipitation resulting from variations in elevation through the elevation-desert effect (see Subsections 1.2.1 and 2.2.1). In large-scale ice sheet modelling studies this parameter ranges between 0.03 and $0.078\,^{\circ}\mathrm{C}^{-1}$ (*e.g.*, Charbit et al. 2002, although climate modelling studies suggests that γ has higher variability and assumes higher values up to $0.11\,^{\circ}\mathrm{C}^{-1}$. Following Colleoni et al. 2016, in this study the range $0.03 - 0.1\,^{\circ}\mathrm{C}^{-1}$ is explored, whereas the value $0.05\,^{\circ}\mathrm{C}^{-1}$ is taken as reference value ;

- the SIA-enhancement factor $\mathsf{E}_{\mathrm{SIA}}$, accounting for the anisotropy of polycristalline ice under condition of simple-shear flow, Ma et al. 2010 (see Subsections 2.2.1). In large-scale ice sheet modelling studies this parameter is set to values ranging from 1 to 5 (see Colleoni et al. 2016 and reference therein). However, an higher value of 5.6 is suggested by Ma et al. 2010 in a study where it is used an anistropic full-Stokes model explicitly accounting for grain orientation (fabric). Therefore, in accord with Colleoni et al. 2016 the range $1 - 5.6$ is explored, whereas the value 3 is taken as reference value;

- the basal drag coefficient c_f, which modulates the resistive force acting at the base of the ice sheet in ice stream regions treated with the SSA (see 2.2.1, Equations 2.39 and 2.40). In Colleoni et al. 2014 the strong impact of this parameter on the GRISLI-simulated ice thickness is showed. This parameter is set in early works with GRISLI to $1 \cdot 10^{-5}$ in Peyaud et al. 2007, to $9 \cdot 10^{-5}$ in Dumas 2002 and between $10 \cdot 10^{-5} - 100 \cdot 10^{-5}$ in Álvarez Solás et al. 2011. Also in this case

following Colleoni et al. 2016, the range $1 \cdot 10^{-5}$-$10 \cdot 10^{-5}$ is explored, whereas the value $2 \cdot 10^{-5}$ is taken as reference value;

- the ocean basal melting parameter F_m in BMAR and BPDC parametrizations (see Subsection 2.3.4, Equations 2.85, 2.86). In Subsection 2.3.4 a range for this parameter is set, considering the oceanic conditions used to force the ocean basal melting parametrizations and the present-day basal melting rates observed in Antarctica. The range explored in this study is $0.000244 - 0.0146$ for BMAR parametrization (Martin et al. 2011) and $0.0000252 - 0.00156$ for BPDC parametrization (Pollard & DeConto 2012). As reference values for F_m in BMAR and BPDC parametrizations two different values are taken, namely 0.00652 and 0.000751 respectively.

Since in this study the single-valued ocean basal melting parametrization BCON and the two more refined ocean basal melting parametrizations BMAR and BPDC are tested, the LHS of GRISLI model parameters is performed as follows:

- a first group of $n = 80$ simulations is performed by using the single-valued ocean basal melting parametrization BCON. Since the parameter F_m is not involved, a LHS of the four GRISLI parameters λ, γ, $\mathsf{E}_{\mathrm{SIA}}$ and c_f is performed ($k = 4$). Such first ensemble of simulations is denoted with GInd.

- a second group of $n = 100$ simulatons is performed by using the ocean basal melting parametrization BMAR. Therefore, a LHS of the five GRISLI parameters λ, γ, $\mathsf{E}_{\mathrm{SIA}}$, c_f and F_m is performed ($k = 5$), where the range of values for F_m is $0.000244 - 0.0146$. Such ensemble of simulations is denoted with GMar.

- a third group of $n = 100$ simulations is performed by using the ocean basal melting parametrization BPDC. Therefore, a LHS of the five GRISLI parameters λ, γ, $\mathsf{E}_{\mathrm{SIA}}$, c_f and F_m is performed ($k = 5$), where the range of values for F_m is $0.0000252 - 0.00156$. Such ensemble of simulations is denoted with GPDC.

Due to its large computational costs, it is not possible to perform with PSU the same LHS method as in GRISLI. However, GRISLI and PSU have in common four of the five model parameters that are explored with GRISLI LHS, namely λ, γ, $\mathsf{E}_{\mathrm{SIA}}$ and F_m. As concerns the SIA-enhancement factor $\mathsf{E}_{\mathrm{SIA}}$, in PSU an high value of $\mathsf{E}_{\mathrm{SIA}} = 10$ is necessary to match the Hughes et al. 2016 reconstructed GL position at LGM in Barents Trough. Such high value is out of the range explored with the LHS with GRISLI. In contrast, GRISLI optimal values for λ, γ, F_m are employed in PSU simulations.

Parameters	**Symbol**	**Units**	**Min.**	**Max.**	**Ref.**
Lapse-rate value	λ	$^{o}\mathrm{km}^{-1}$	4	8.2	5
Precipitation-correction factor	γ	$^{o}\mathrm{C}^{-1}$	0.03	0.1	0.05
SIA-enhancement factor	$\mathsf{E}_{\mathrm{SIA}}$	-	1	5.6	3
Basal drag coefficient	c_f	-	$1 \cdot 10^{-5}$	$10 \cdot 10^{-5}$	$2 \cdot 10^{-5}$
BMAR model parameter	F_m^{BMAR}	-	0.000244	0.0146	0.00652
BPDC model parameter	F_m^{BPDC}	-	0.0000252	0.00156	0.000751

Table 2.3: Parameters included in the Latin Hypercube Sampling. The minimum, maximum and reference values of each different parameter is shown.

2.3.6 GRISLI topography-based ice stream mask

As shown in Subsection 2.2.1, GRISLI identifies ice streams mainly depending on the bathymetry (*e.g.*, in narrow valleys, criterion IS1) and on a sediment thickness threshold combined with hydraulic head and effective pressure thresholds (criterion IS2). However, when applied to the EIS the sediment threshold in criterion IS2 is not really restrictive. In fact, according to the sediment thickness map by Laske et al. 1997 included in GRISLI (Figure 2.6b) the whole Eurasian grid domain, except for the continental Scandinavia, is covered by a thick sediment layer exceeding the sediment thickness threshold prescribed in condition IS2. Therefore, condition IS2 depends on the hydraulic head and the low effective pressure only to be satisfied. However, both the hydraulic head and the effective pressure mainly depend on the amount of meltwater at the ice sheet base. A strong control on the amount of meltwater at the ice sheet base in GRISLI is exerted by the near-surface air temperature, which controls the amount of surface ablation. As a result, ice stream formation in GRISLI has a strong dependence on the near-surface air temperature, as clearly shown in Figure 2.13b. In fact, ice streams extent is largely overestimated in the western and southern part of the EIS. Such regions, due to its position relative to the North Atlantic storm tracks (Colleoni et al. 2016) present a more temperate climate (see Figure 2.8), thus facilitating ice streams formation in response to an higher basal melting. In particular, the width of Bjørnøyrenna ice stream is largely overestimated with respect to the observations especially in the inner Barents trough (*e.g.*, Piasecka et al. 2016). Also in the BIIS and in the southern SIS the ice streams location and extent are unrealistic compared to reconstructions based on geological evidence (*e.g.*, Stokes & Clark 2001). In contrast, in the northern and eastern part of the EIS ice streams are more narrow and sparse, in response to a more cold and arid climate, see Figure 2.8. In order to reduce such temperature-dependent ice stream overestimation in the southern and western EIS, in Colleoni et al. 2016 an ice stream map restraining the SSA ice flow in GRISLI to the large-scale valleys is tested. Colleoni et al. 2016 identify large-scale valleys in the Eurasian domain by computing the large-scale topographic curvature on a present-day topography map with a resolution of $1'$.

In this study a similar but simpler approach is followed. In fact, large-scale depressions are identified in the present-day topography from Colleoni (*personal communication*, see Figure 2.5b) interpolated on the $20\,\text{km} \times 20\,\text{km}$ GRISLI grid, coarser than the $1'$ resolution topography map used in Colleoni et al. 2016. Moreover, large-scale depressions are identified in the present-day topography map depending on elevation differences only and the topographic curvature is not taken into account. However, such simple method does not fail to catch the major bathymetric lows where *palaeo*-ice streams likely evolved at LGM and during the subsequent deglaciation, as shown in Figure 2.13a. In particular Figure 2.13a shows Norwegian Channel and Storfjorden, Barents, St. Anna, Franz Victoria and Voronin trough are reasonably well represented in the map. Therefore, when such ice stream mask is applied, GRISLI identifies ice streams according to criteria IS1, IS2 and IS3 only inside the red areas in Figure 2.13a. The map of the active ice streams at the LGM in GRISLI simulations for which the ice stream mask is applied is shown in Figure 2.13. After the application of the ice stream mask, the width of the Bjørnøyrenna ice stream is reduced and is more in agreement with

the observations (Piasecka et al. 2016). Also in the southern part of the SIS and (to a less extent) in BIIS the ice streams extent is reduced. Nevertheless, regions treated with the SSA with no corresponding observed ice streams are still present in the southern SIS and in the BIIS. A continuous ice stream in the Norwegian Channel cannot form due to the mask-free ice streams location identified by GRISLI, see Figure 2.13b. Overall, the masked ice streams configuration is more in agreement with the observations and the impact of such ice stream mask on the evolution of the EIS troughout the deglaciation is analyzed. Two new GRISLI ensembles of 100 simulations, denoted with GMARS and GPDCS, are performed by including the ice stream mask method and by keeping the same ocean basal melting parametrizations and model parameter values as in the ensembles GMar and GPDC, respectively (see Subsection 2.3.5).

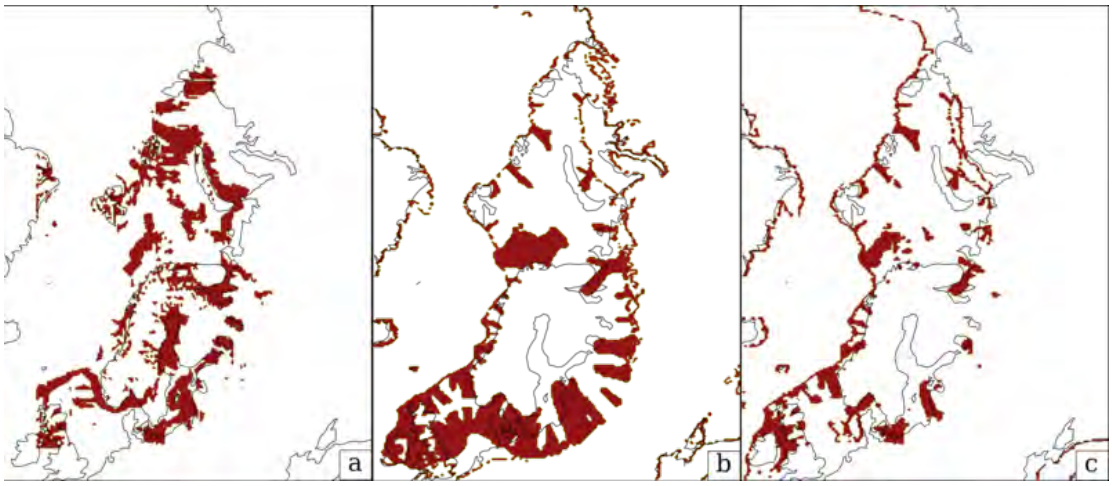

Figure 2.13: (a) Ice stream mask based on present-day topography. Regions where ice streams are allowed to form (according to GRISLI criteria IS1, IS2 and IS3) are indicated in red. The present-day topography used to generate this mask is the same shown in Figure 2.5a. (b) Map of the active ice streams (shown in red) at the LGM in GRISLI simulations for which the ice stream mask shown in (a) is not applied. (c) Map of the active ice streams (shown in red) at the LGM in GRISLI simulations for which the ice stream mask shown in (a) is applied.

2.3.7 Appendix I: TraCE-21ka simulation description

TraCE-21ka simulation have been carried out with the synchronously coupled AOGCM CCSM3 (Collins et al. 2006). Variations in the Earth's orbital parameters, GHGs, ice sheets thickness/extent and meltwater discharge to the ocean are used to force the AOGCM. Changes in the Earth's eccentricity, precession and axial tilt (see Figure 2.15) modulate the annual, seasonal, and latitudinal distributions and magnitudes of incoming solar radiation. As GHGs forcings, CO_2, Methane (CH_4) and Nitrous Dioxide (N_2O) transient concentrations from Joos & Spahni 2008 are adopted (see Figure 2.14). Continental ice sheets thickness and extent are modified approximatively every 500 years, according to ICE-5G reconstruction (see Figures 2.19, 2.16). Finally, meltwater from the continental ice sheets is added to the ocean model according to geological records. A brief description of those TraCE-21ka results that are relevant in this study follows.

During the onset of the last deglaciation (22-19 ka BP), the prescribed change in the GHGs concentration is minimal (see Figure 2.14) and the continental ice sheets orography and extent are kept at LGM condition (see Figures 2.16A-B); as a result, the simulated climate evolution during these 3 ka is dominated by the orbital forcing, He 2011 (see Figure 2.15). In the NH, the increase of insolation during spring and summer results in a mean annual air temperature increase between 22-19 ka BP (see Figure 2.17A), which likely caused the early retreat of the SIS (Clark et al. 2009) thus providing one of the first NH meltwater pulses (NHMWs) at the onset of the last deglaciation, He 2011. In order to represent such early NHMWs, meltwater is added to the ocean model around 19 ka BP, causing an initial decrease in the Atlantic Meridional Overturning Circulation (AMOC), Liu et al. 2009. Prolonged NHMWs after 19 ka BP were caused by the retreat of the NH ice sheets (Dyke 2004), and the corresponding meltwater inputs prescribed in the AOGCM results in the near-collapse of the AMOC in correspondence to the cold Heinrich Event 1 (H1) around 17 ka BP (Figure 2.17C). From H1 to the onset of Bølling-Allerød warm events (B-A) between 14-12.9 ka BP the NHMWs flux decreases and suddenly terminates around 14.6 ka BP. This leads in TraCE-21ka simulation to AMOC resumption, Liu et al. 2009 (see Figure 2.17D). A subsequent increase in NHMWs weakens again the AMOC, resulting in the Younger Dryas cold interval (YD) between 12.9-11.7 ka BP (Figure 2.17E). Following the YD, continued NH ice sheets melting prevents AMOC from reaching the late Holocene level, He 2011 (see Figure 2.17F). As concern the simulated annual snowfall pattern, in the NH the main control is exerted by the continental ice sheets via topographic lowering in a twofold sense (see Figures 2.18A-F, 2.16A-F). In fact, air temperatures increase as the elevation of the EIS and the LIS is reduced because of the lapse-rate effect (a lapse-rate of 6.5 ^{o}C/km is adopted in TraCE-21ka simulation); this causes in turn an increase in precipitation, due to the positive, roughly exponentially relationship between the air temperature and the saturation pressure of water vapour in the atmosphere, He 2011. Moreover, as the LIS topographic barrier lowers/disappears the atmospheric jet shifts northwards and affects temperatures, sea ice and snow cover patterns (see Figures 2.18D-E-F), Ullman et al. 2014.

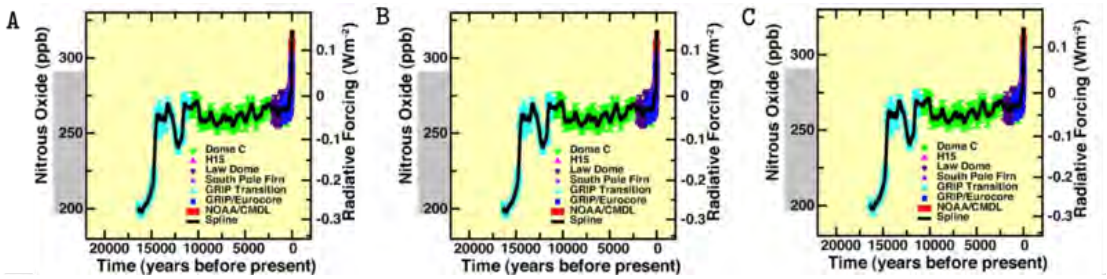

Figure 2.14: After Joos & Spahni 2008. (A) CO_2, (B) CH_4 and (C) N_2O transient concentrations in the last 20,000 years employed as forcing for TraCE-21ka simulation.

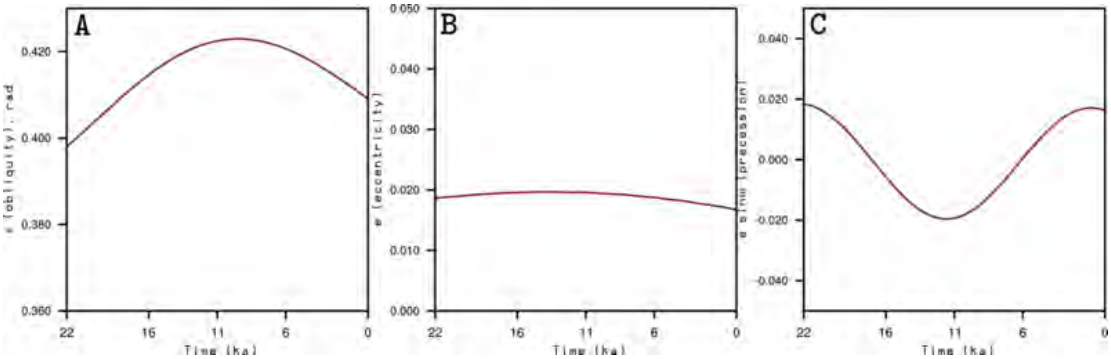

Figure 2.15: Variability of the Earth's orbital parameters (A) obliquity, (B) eccentricity and (C) precession in the last 22,000 years, computed following Laskar et al. 2004.

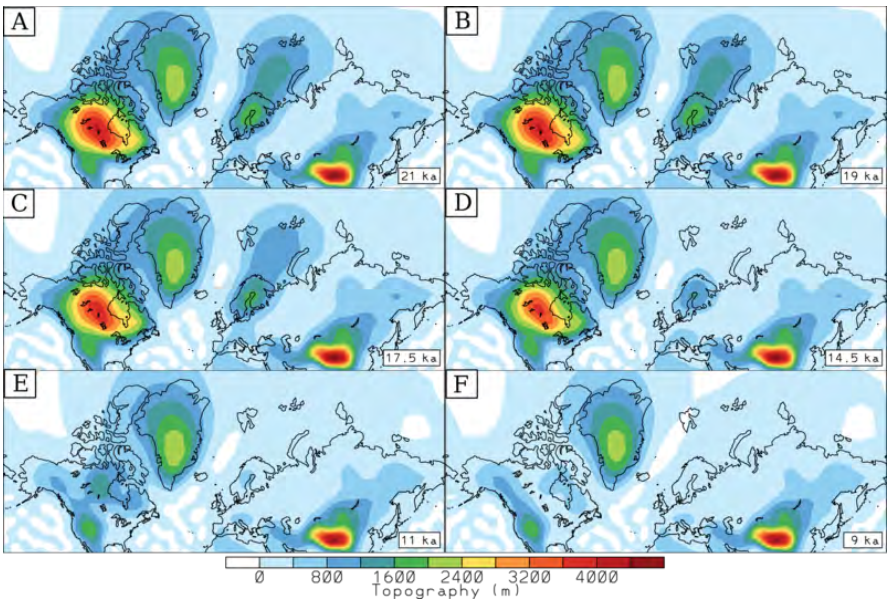

Figure 2.16: Surface topography at six different time slices for TraCE21-ka simulation.

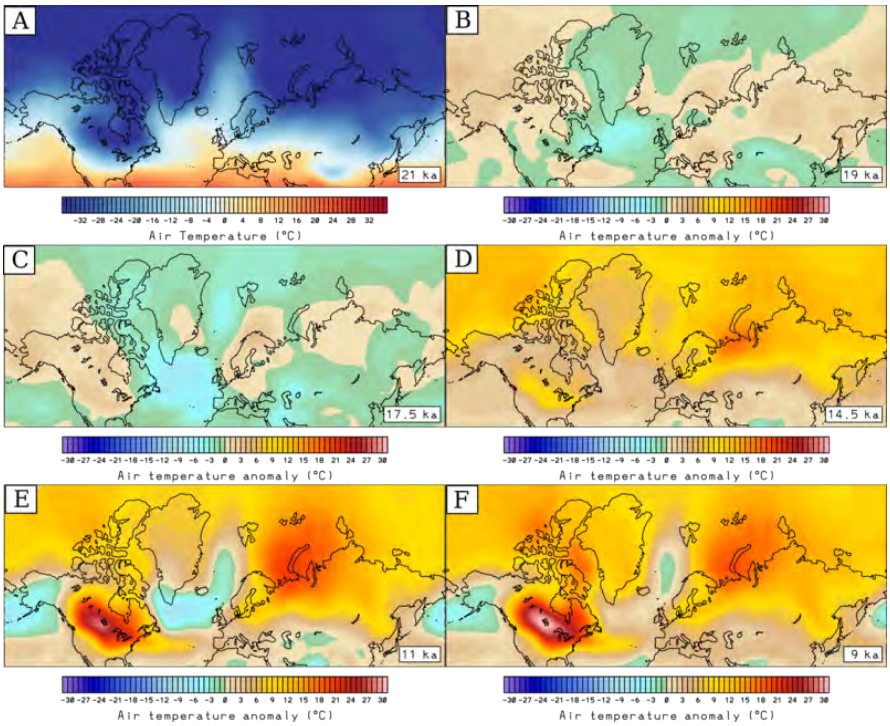

Figure 2.17: (A) TraCE-21ka mean annual near-surface air temperature at LGM and (B), (C), (D), (E), (F) TraCE-21ka mean annual near-surface air temperature anomaly with respect to LGM at different time slices.

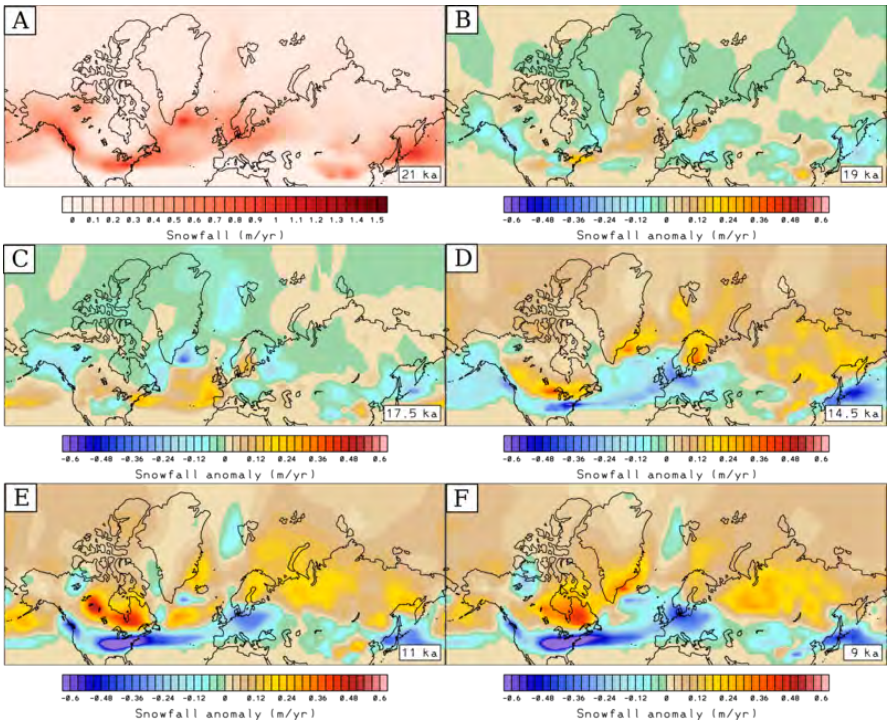

Figure 2.18: (A) TraCE-21ka mean annual snowfall at LGM and (B), (C), (D), (E), (F) TraCE21ka mean annual snowfall anomaly with respect to LGM at different time slices. The conversion from TraCE-21ka total precipitation to snow follows Marsiat 1994.

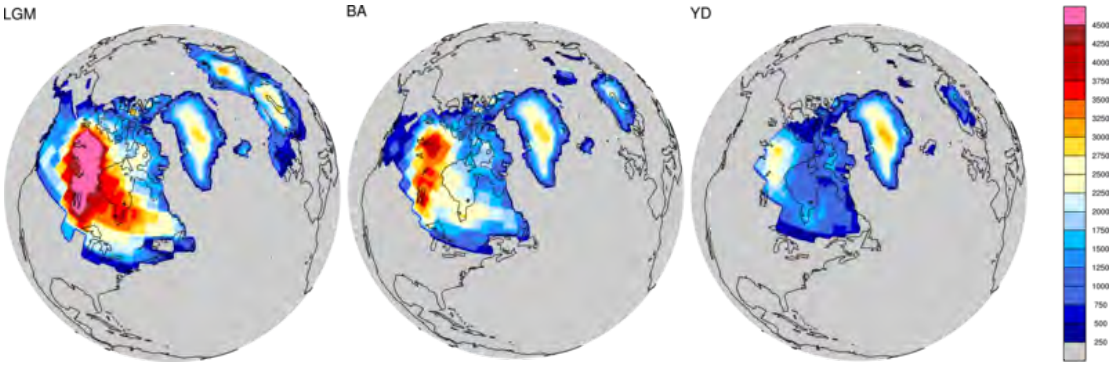

Figure 2.19: After `http://www.cgd.ucar.edu/ccr/TraCE`. ICE-5G reconstruction of northern Hemisphere ice sheet extent and thickness at different time slices, Peltier 2004.

RESULTS

In this chapter, the results obtained in this study are illustrated. The first section is dedicated to the MIS5-LGM spin-up simulations performed with GRISLI and PSU, needed to initialize the thermodynamics in the Ice Sheet Models. The Eurasian *palaeo*-Ice Sheet simulated ice volume and extent at the end of the spin-up simulations are compared with ICE-5G reconstruction and field observations. In the second section, different GRISLI reference simulations are compared in terms of ice volume, extent and velocity evolution throughout the deglaciation, in order to analyze the impact of the different parametrizations used. It follows a description of all the Latin Hypercube Sampling ensembles of simulation carried out with GRISLI. Best fit simulations with ICE-5G reconstruction in terms of ice volume evolution are identified for each GRISLI ensemble. For each best fit simulation, the extent of the EIS throughout the deglaciation is compared with field observations. In the last section, PSU simulations are analyzed. PSU-simulated ice volume and extent evolution throughout the deglaciation are compared with GRISLI simulations, ICE-5G reconstruction and field observations. At the end of this chapter, the simulations analyzed are summarized in a list.

3.1 Spin-up simulations

Large-scale ice sheets thermomechanics responds to oscillations in climate conditions on a long time scale ($10^3 - 10^5$ yrs). Therefore, in order to simulate with an ISM the evolution of an ice sheet during a given period, it is necessary first to spin-up the ISM. In such a way, a realistic representation of the ice thermomechanics is reached at the beginning of the ISM simulation, Colleoni et al. 2014. In order to spin-up an ISM, a commonly used approach consists in performing a transient simulation forced with paleoclimate reconstructions of temperature and precipitation through time. Alternatively, steady-state simulations forced with constant climate conditions through time are used, Rogozhina et al. 2011. In both cases, the spin-up simulation is run over one or two glacial cycles, *i.e.* 100 to 200 ka, Colleoni et al. 2014.

In this study, both GRISLI and PSU are initialized by performing 100 ka long transient simulations between MIS5 and LGM. As already specified in Subsection 2.3.1, at MIS5 PI-like conditions are assumed in terms of topography and climatology. Therefore, PI surface topography and climatology are prescribed at the beginning of the spin-up simulations. In particular, the PI climatology, which is prescribed is simulated with the IPSL-CM5A-LR climate model. As a final climate snapshot, the LGM climatology simulated with the same IPSL-CM5A-LR climate model is prescribed. The interpolation between PI and LGM climatology is performed by means of a climate index based on the NGRIP $\delta 18\mathrm{O}$ record in the last 122 ka, see Figure 3.1. At the end of the spin-up simulations (*i.e.*, at LGM), the ICE-5G total ice volume (22 m SLE) and the DATED-1 ice sheet extent at 21 ka BP are taken as a benchmark for the simulated EIS.

With GRISLI, two different formulations for the PDD method (see Equations 2.54 and 2.58) are tested. The parametrizations, denoted with PDD_σ and $\mathsf{PDD}_{\triangle\sigma}$ respectively, are described in Subsection 2.2.1. Following Colleoni et al. 2016, the constant near-surface air temperature standard deviation σ is set equal to five in PDD_σ formulation, whereas in $\mathsf{PDD}_{\triangle\sigma}$ formulation σ depends on time/altitude/latitude following

Fausto et al. 2011. The GRISLI spin-up simulations employing $\mathsf{PDD}_{\triangle\sigma}$ and PDD_{σ} formulations are denoted, respectively, with $\mathsf{GSpin}\triangle\sigma$ and $\mathsf{GSpin}\sigma$. GRISLI model parameters involved in the LHS method (see Subsection 2.3.5) are set to their reference values, see Table 2.3. As shown in Figure 3.1, in simulation $\mathsf{GSpin}\triangle\sigma$ the total EIS ice volume at LGM is overestimated by almost 30% with respect to ICE-5G reconstruction (around 29 m SLE). Such overestimation is reduced to 15% in simulation $\mathsf{GSpin}\sigma$ (around 25 m SLE), see Figure 3.1. In Figure 3.2, the (a) simulated ice thickness at LGM for simulation $\mathsf{GSpin}\sigma$ and (b) the ice thickness anomaly with respect to simulation $\mathsf{GSpin}\sigma$ for simulation $\mathsf{GSpin}\triangle\sigma$ are shown. Simulation $\mathsf{GSpin}\triangle\sigma$ regularly overestimates ice thickness in the eastern flank of the EIS, with peaks up to 20% in the south-eastern flank of the SBKSIS. This likely results from a combination of the colder climate in the eastern part of the EIS with the elevation-dependence of the near-surface air temperature standard deviation σ on altitude in the parametrization by Fausto et al. 2011. In fact, at the low-altitude margins of the ice sheets the near-surface air temperature standard deviation σ is lower, according to Fausto et al. 2011. A lower near-surface air temperature standard deviation particularly reduces ablation in regions where the monthly mean temperatures are negative, see the PDD method description in Subsection 2.2.1. Therefore, lower values for σ results in lower ablation in the eastern part of the EIS, whereas in the warmer western flank of the EIS the same ice thickness overestimation is not registered. However, also in the southern part of the region connecting the SIS and the BIIS the ice thickness in simulation $\mathsf{GSpin}\triangle\sigma$ is overestimated up to 20% with respect to simulation $\mathsf{GSpin}\sigma$. The extent of the simulated EIS at LGM is essentially unchanged in $\mathsf{GSpin}\triangle\sigma$ and $\mathsf{GSpin}\sigma$ simulations and largely agrees with the DATED-1 reconstruction.

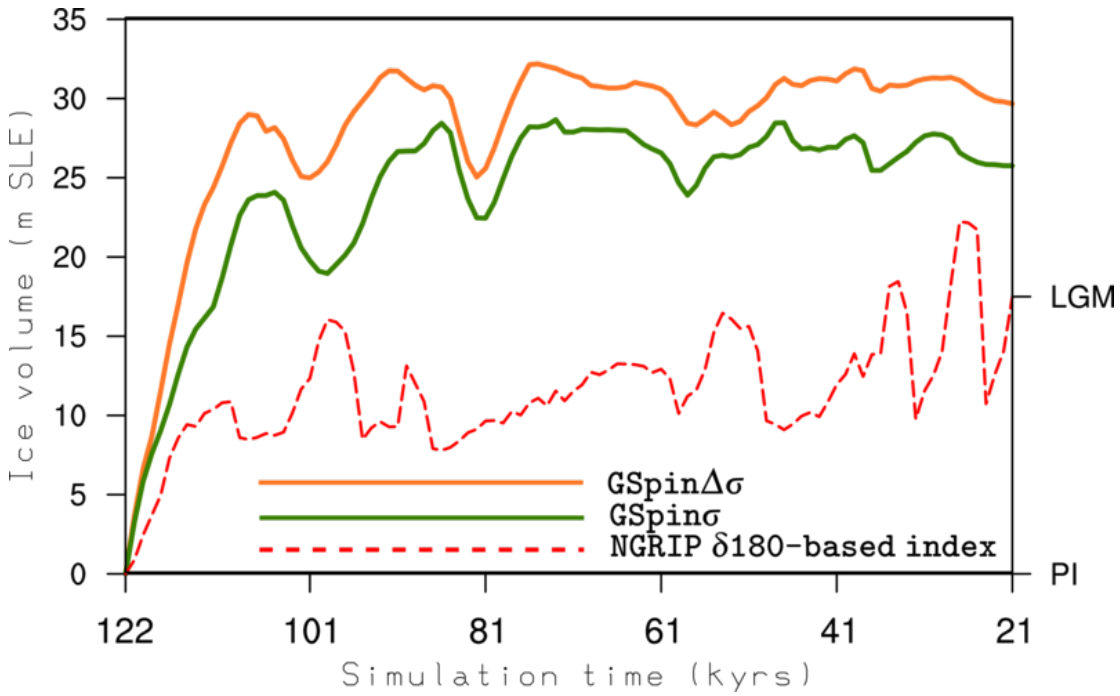

Figure 3.1: Ice volume evolution of the EIS in spin-up simulations $\mathsf{GSpin}\sigma$ (solid green) and $\mathsf{GSpin}\triangle\sigma$ (solid orange) respectively. In dashed red, the NGRIP δ18O-based index used to interpolate between PI and LGM climate snapshots is shown.

The only significant discrepancy between GRISLI and DATED-1 ice sheet extent at LGM is an excess of ice cover in Severnaya Zemlya and Taimyr Peninsula, see Figure 3.2. However, such data-model discrepancy can be addressed to the ICE-5G topography used to downscale the LGM climate fields, see Subsection 2.2.1. In fact, as shown in Figure 2.5b, also in ICE-5G reconstruction the same region is covered by ice up to 1 km thick. After the downscaling procedure, the cold imprint of the ICE-5G LGM topography via the lapse-rate and elevation-desert effects (see Figure 2.8) results in the excess of ice showed in Figure 3.2. Minor discrepancies between GRISLI and DATED-1 are observed at the marine-based western and northern margins of the SBKSIS, where the grounded-ice does not reach the continental slope.

With PSU, only the PDD_σ formulation with $\sigma = 5$ is used. The PSU spin-up simulation adopting GRISLI reference values for the model parameters λ, γ, E_{SIA} and $\mathsf{E}_S SA$ is denoted with $\mathsf{PSpin}\sigma$. As shown in Figure 3.3, in such simulation the total EIS ice volume at LGM is overestimated by 20% with respect to ICE-5G reconstruction (around 26.5 m SLE). Moreover, there is a large discrepancy between $\mathsf{PSpin}\sigma$ and DATED-1 ice sheet extent in the major Barents Sea bathymetric troughs, as shown in Figure 3.4a.

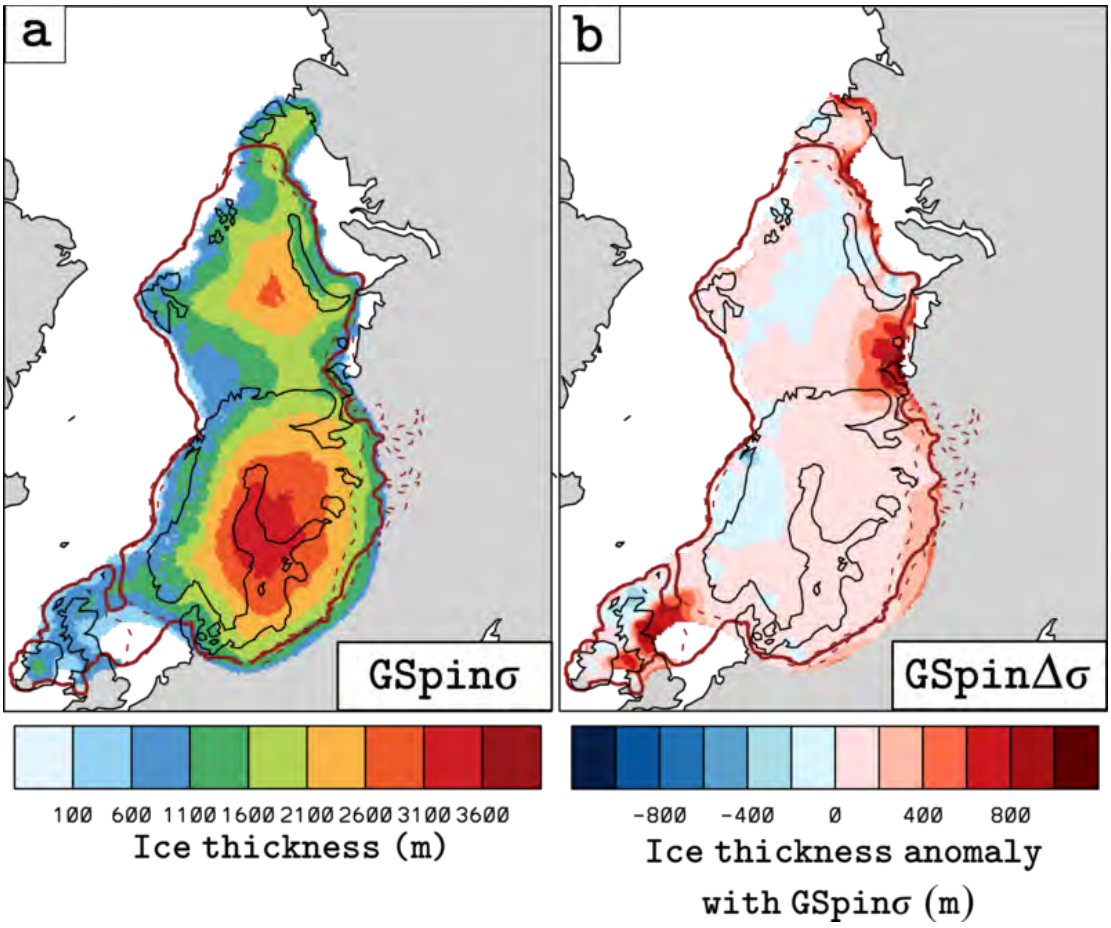

Figure 3.2: Contours of (a) grounded-ice thickness for the EIS at LGM for simulation $\mathsf{GSpin}\sigma$, (b) grounded-ice thickness anomaly with respect to simulation $\mathsf{GSpin}\sigma$ for simulation $\mathsf{GSpin}\Delta\sigma$. DATED-1 extent of the EIS at LGM is shown in solid red (most credible reconstruction) and dashed red (minimum-maximum reconstructions).

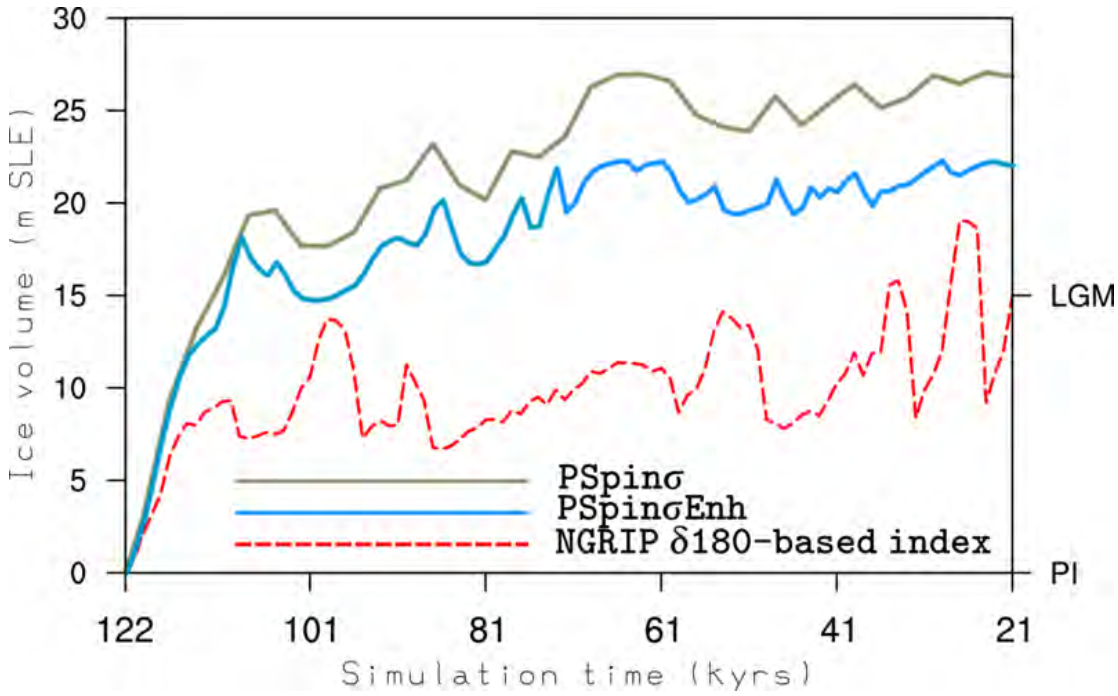

Figure 3.3: Ice volume evolution of the EIS in spin-up simulations PSpinσ (solid grey) and PSpinσEnh (solid light blue) respectively. In dashed red, the NGRIP δ18O-based index used to interpolate between PI and LGM climate snapshots is shown.

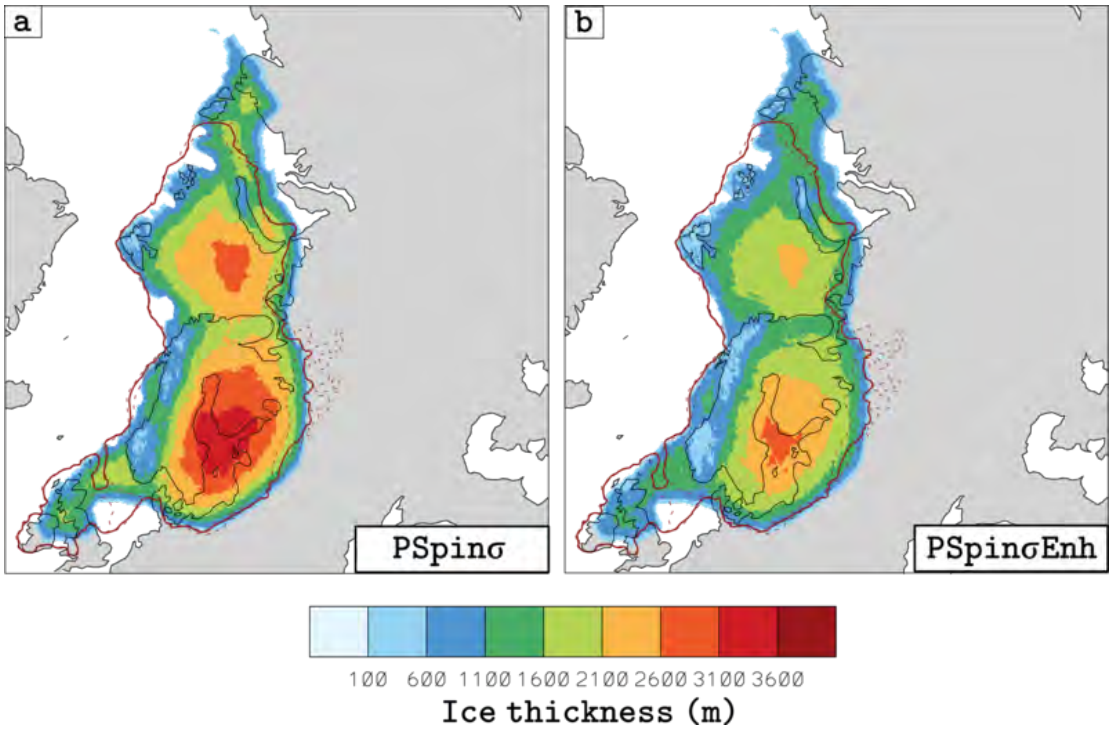

Figure 3.4: Contours of grounded-ice thickness for the EIS at LGM for simulation (a) PSpinσ, (b) PSpinσEnh. DATED-1 extent of the EIS at LGM is shown in solid red (most credible reconstruction) and dashed red (minimum-maximum reconstructions).

Since GRISLI GSpinσ and PSU PSpinσ spin-up simulations are forced with the same climatology and they both adopt the same SMB and ocean basal melting parametrizations, we can address the GRISLI-PSU discrepancy in the LGM ice sheet extent to the different ice stream and GL dynamics. In PSpinσ simulation the ice margin fails to advance inside bathymetric troughs. The same regions are treated as ice stream regions in GSpinσ simulation (see 2.13b). PSpinσ ice velocities are low in the major Barents Sea bathymetric troughs compared with that in GSpinσ, thus preventing the grounded-ice to advance. Due to numerical instabilities, it is not possible to use an higher value for the full sliding coefficient c_w with PSU (see Subsection 2.2.2). Therefore, in order to increase the ice velocities in PSU simulations, higher enhancement factors values ($\mathsf{E}_{\mathrm{SIA}} = 10$ and $\mathsf{E}_{\mathrm{SSA}} = 10$) are adopted in simulation GSpinσEnh. This results in a 15% decrease of the total EIS ice volume at LGM (22 m SLE), thus providing a perfect match with ICE-5G reconstruction (see Figure 3.3b). Moreover, as shown in Figure 3.4b, GSpinσEnh simulated ice extent at LGM is in a better agreement between DATED-1 reconstruction, in particular at the south-western Barents Sea EIS margin. The ice sheet extent is overestimated in Severnaya Zemlya and Taimyr Peninsula as in GRISLI spin-up simulations, due to the ICE-5G topography employed in the downscaling procedure.

Compared to GRISLI GSpinσ simulation, PSU PSpinσEnh simulation shows a lower LGM ice thickness all over the EIS, except for the BIIS and the western SBKSIS (see Figures 3.2a and 3.4b). In particular, in the western SBKSIS the ice thickness is more uniform for PSpinσEnh simulation, whereas GSpinσ simulation shows a lower ice thickness in correspondance to the Barents Trough (see Figures 3.2a and 3.4b). The more uniform ice thickness distribution over the Barents trough displayed by simulation PSpinσEnh can be addressed to the high SIA-enhancement factor adopted. The ice thickness difference reaches values up to 1.5 km in the central dome of the SIS. Moreover, both the SIS and SBKSIS central domes are shifted southward in PSpinσEnh with respect to GSpinσ simulation (see Figures 3.2a and 3.4b).

3.2 GRISLI reference simulations

In order to test with GRISLI to what extent the use of different basal melting parametrizations (see Subsection 2.3.4) and the application of an ice stream mask (see Subsection 2.3.6) could affect the simulated deglaciation of the EIS, several LGM-PI GRISLI reference simulations are compared. In GRISLI reference simulations the model parameters involved in the LHS analysis (see Subsection 2.3.5) are set to their reference values (see Table 2.3). Reference simulations using the basal melting parametrizations BCON, BMAR and BPDC are labeled, respectively, with GIndRef, GMarRef and GPDCRef. Reference simulations employing basal melting parametrizations BMAR and BPDC for which the ice stream mask is included are labeled with GMarSRef and GPDCSRef.

As shown in Figure 3.5, the use of basal melting parametrizations BMAR and BPDC has a strong impact on the ice volume evolution of the EIS throughout the deglaciation with respect to the single-valued parametrization BCON. In particular, the decay of the marine-based SBKSIS appears to be completely dominated by ocean basal melting, as Figure 3.6 clearly shows. Since the SIS is connected with the SBKSIS in its northern flank, it is also affected by the ocean basal melting-driven decay of the SBKSIS

(see Figure 3.7). However, the SIS decay appears to be driven more by the climatic forcing, as shown by its rapid decay around 14 ka BP, after the B-A warm peaks (see Figures 3.7 and 2.10). The difference between BMAR and BPDC ocean basal melting parametrization in terms of total ice volume is visible only after 18 ka BP and the maximum discrepancy between simulations GMarSRef, GPDCSRef does not exceed 3 m SLE. In particular, BMAR parametrization appears to be more effective than BPDC between 18 and 14 ka BP, whereas the converse holds between 14 and 10 ka BP (Figures 3.5 and 3.7). Looking at the TraCE-21ka ocean temperature profile evolution used to force the basal melting parametrizations (see Figure 2.11), it is interesting to notice that between 18 and 14 ka BP ocean temperatures does not exceed 2°C. In contrast, from 14 to 10 ka BP ocean temperatures between 4 and 8°C are reached at typical GL depths in the Barents Sea (300-500 m). Therefore, BMAR parametrization is more effective than BPDC parametrization under "mild" ocean conditions, whereas the opposite is true under "warm" ocean conditions. This can be explained by the linear *vs* quadratic relationship relating the basal melting rate and the ice-ocean heat flux in BMAR and BPDC parametrizations, respectively (see Equations 2.85, 2.86). Ocean basal melting values in Storfjorden Trough during the ice stream retreat in simulations GMarRef and GPDCRef clearly confirm this hypothesis (see Figure 3.9). In fact, higher basal melting values are obtained with GMarRef parametrization between LGM and 14 ka BP.

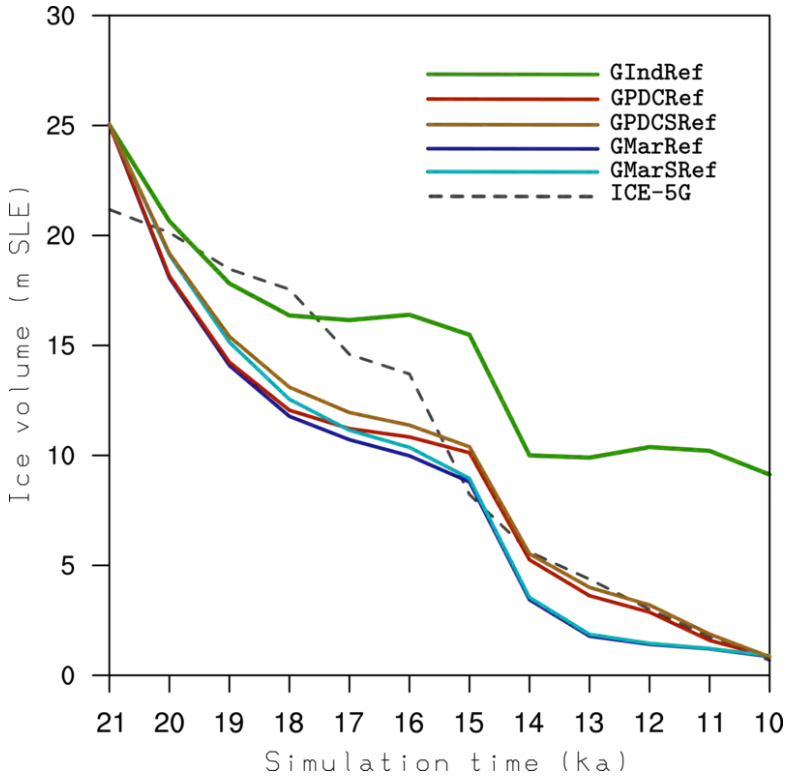

Figure 3.5: Ice volume evolution of the EIS in transient simulations GIndRef (solid green), GMarRef (solid red), GPDCRef (solid light brown), GMarSRef (solid blue) and GPDCSRef (solid light blue). In dashed grey, the ICE-5G ice volume curve is shown for comparison.

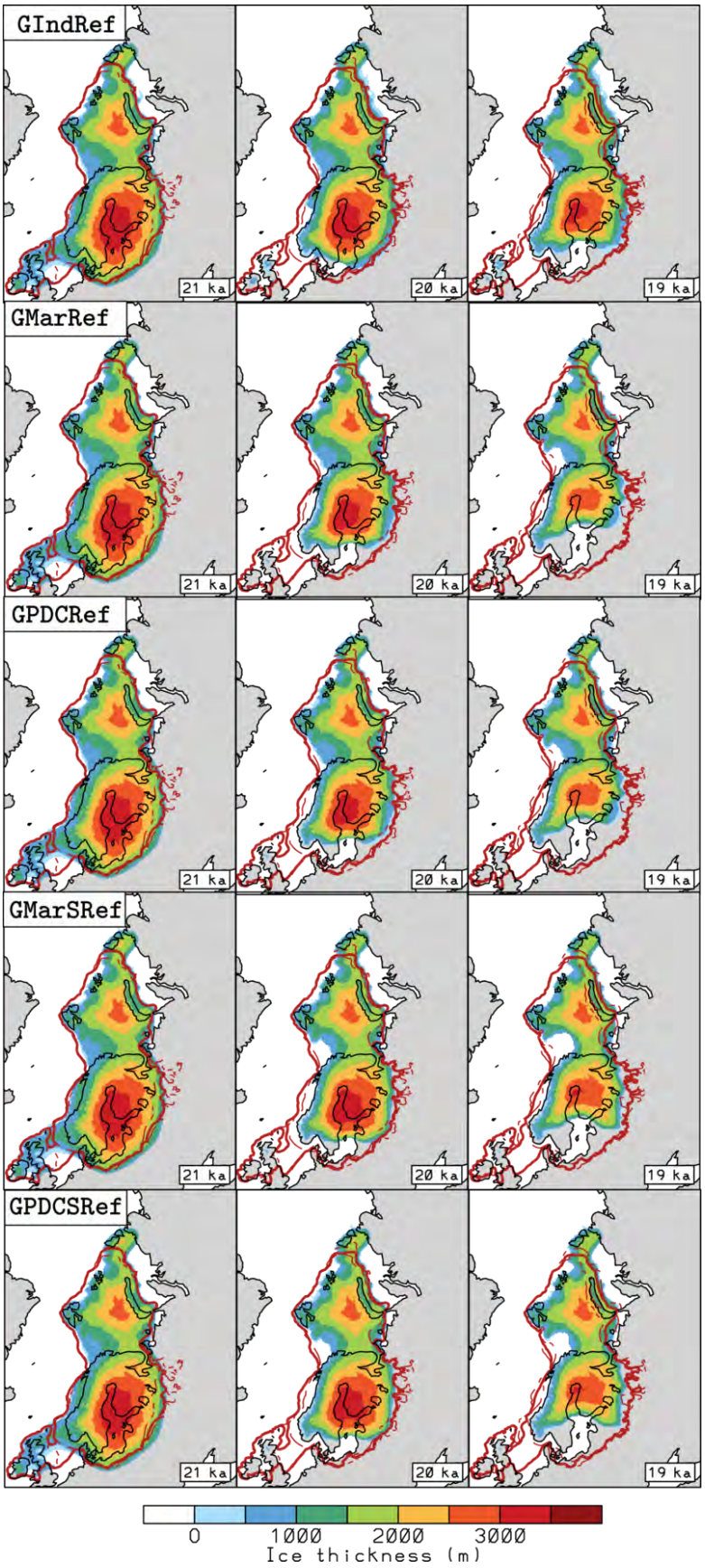

Figure 3.6: EIS ice thickness contour at three selected time slices (21, 20 and 19 ka BP) for simulations GIndRef (top row), GMarRef (second row), GPDCRef (third row), GMarSRef (fourth row) and GPDCSRef (bottom row). DATED-1 extent of the EIS at each time slice is shown in solid red (most credible reconstruction) and dashed red (minimum-maximum reconstructions).

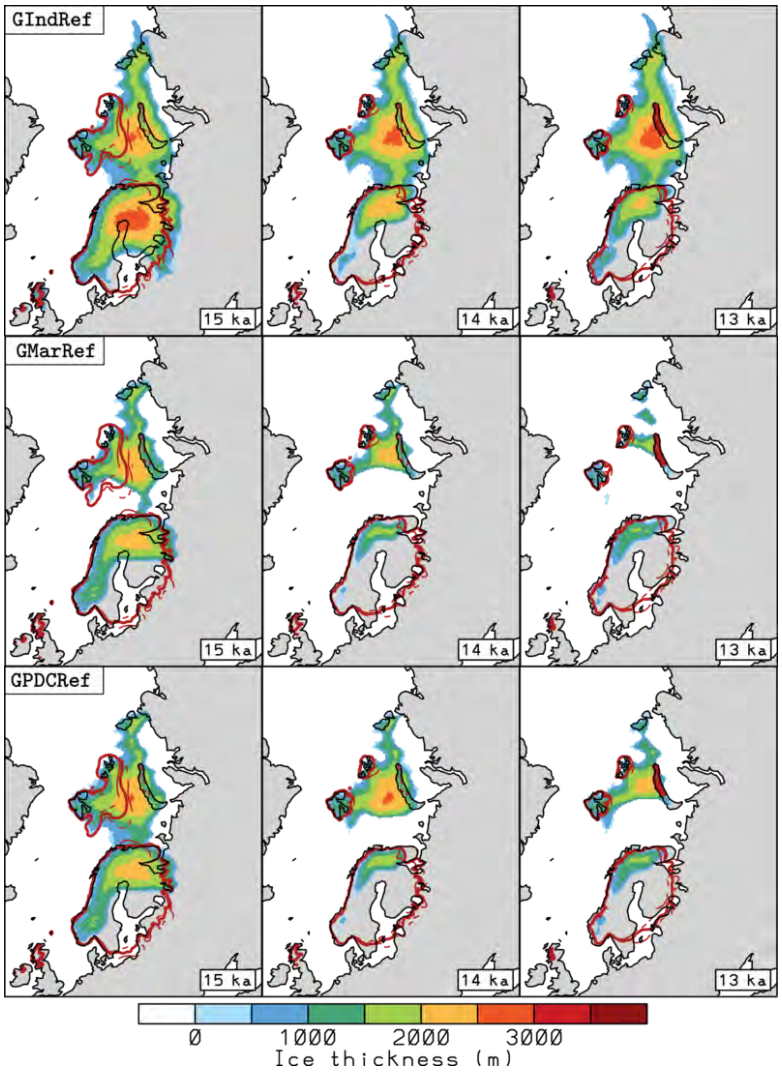

Figure 3.7: EIS ice thickness contour at three selected time slices (15, 14 and 13 ka BP) for simulations GIndRef (top row), GMarRef (middle row), GPDCRef (bottom row). DATED-1 extent of the EIS at each time slice is shown in solid red (most credible reconstruction) and dashed red (minimum-maximum reconstructions).

Reference simulations GMarRef and GPDCRef show an abrupt ice volume loss in the first 2 ka compared with ICE-5G curve (-11 m SLE, Figure 3.5). This initial ice volume loss is more gradual in simulation GIndRef (-7 m SLE at 19 ka BP), although the ice volume curve remains steeper than ICE-5G in the first 2 ka, as shown in Figure 3.5. Therefore, part of the initial melting in simulations GMarRef and GPDCRef can be addressed to the ocean basal melting. However, the largest ice loss in the first 2 ka is registered in the BIIS and in the southern part of the SIS, as shown inf Figure 3.6. The ice loss in these regions can be addressed to a combination of increased air temperatures (see Figure 2.10) and overestimated ice stream extent (see Figure 2.13b). The former enhances surface ablation, whereas the latter facilitates the transport of ice to warmer low latitudes at the southern SIS margin (see Figure 3.8). The effect of the ice stream mask applied in simulations GMarSRef and GPDCSRef is to reduce the southward ice transport in the SIS, leading to a slightly thicker and wider SIS at 19 ka BP (see Figure 3.8).

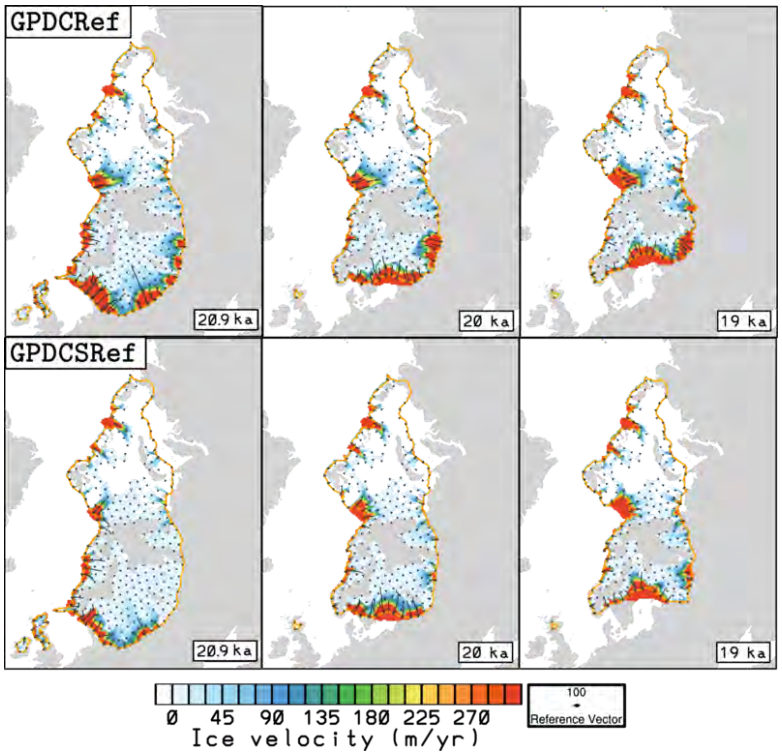

Figure 3.8: EIS horizontal ice velocity contour at three selected time slices (20.9, 20 and 19 ka BP) for simulations GPDCRef (top row) and GPDCSRef (top row). Arrows indicate the grounded-ice velocity direction, whereas the grounded-ice limit is shown in yellow.

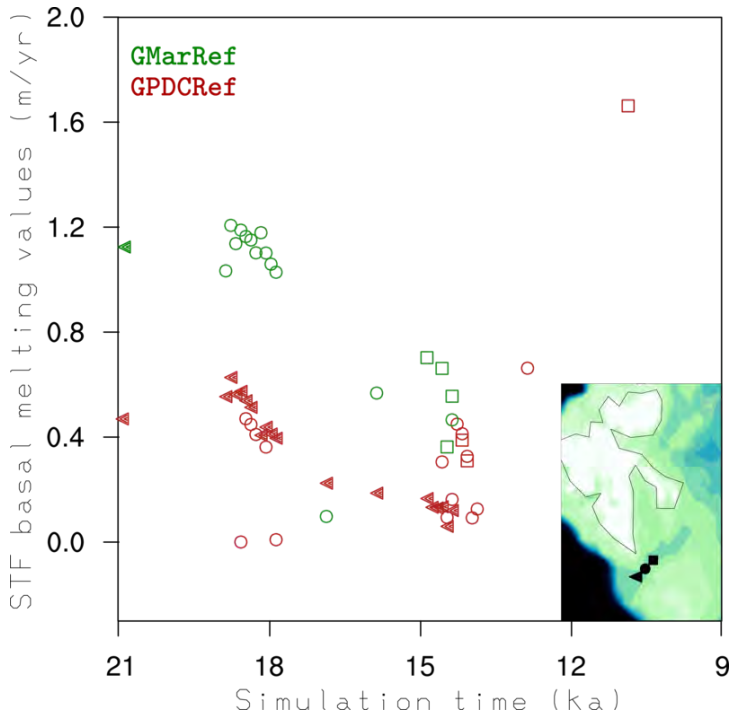

Figure 3.9: Scatter plot of basal melting values in Storfjorden trough during the ice stream retreat in simulations GMarRef (green) and GPDCRef (red). The different symbols used to mark the basal melting values (triangles, circles and squares) indicate the GRISLI grid node under which basal melting is occurring, see map in the inlay figure.

It is also interesting to notice that the application of the ice stream mask in simulations GMarSRef and GPDCSRef enhances the ocean basal melting effect in the Barents trough at the western margin of the SBKSIS (see Figure 3.6). This can be explained by the reduced width of the masked-Bjørnøyrenna ice stream, which leads to a less efficient ice transport from the inner part of the SBKSIS to its western margin (see Figure 3.8). This in turn reduces the ice thickness at the western marine margin and consequently enhances the effect of the ocean basal melting. Despite the larger ice volume loss in the Barents Sea Trough, the application of the ice stream mask in simulations GMarSRef and GPDCSRef reduces the total EIS volume loss by 2-3 m SLE in the first 2 ka with respect to simulations GMarRef and GPDCRef.

3.3 GRISLI Latin Hypercube Sampling ensembles

As illustrated in Subsection 2.3.5, in this study a LHS of five poorly constrained GRISLI parameters is performed. The five ensembles of simulations generated are denoted with GInd (80 simulations), GMar (100 simulations), GPDC (100 simulations), GMarS (100 simulations) and GPDCS (100 simulations). In the simulations from the ensembles GInd, GMar and GPDC, the ocean basal melting parametrizations BCON, BMAR and BPDC are employed, respectively. The simulations ensembles GMARS and GPDCS are performed by including the ice stream mask method and by keeping the same ocean basal melting parametrizations and model parameter values as in the ensembles GMar and GPDC, respectively. In all the simulations from each ensemble, the total ice volume evolution throughout the deglaciation is analyzed. In particular, for each ensemble the simulations showing the best match with ICE-5G ice volume curve and the maximum/minimum ice volume evolution are identified (see Figures 3.10, 3.11, 3.12, 3.13 and 3.14) and denoted with

- GIndBvol, GIndMAXvol, GIndMINvol,
- GMarBvol, GMarMAXvol, GMarMINvol,
- GPDCBvol, GPDCMAXvol, GPDCMINvol,
- GMarSBvol, GMarSMAXvol, GMarSMINvol,
- GPDCSBvol, GPDCSMAXvol, GPDCSMINvol,

respectively. A thorough analysis of each GRISLI ensemble in terms of LHS parameter values, total ice volume and ice sheet extent is hereafter provided. In the LHS ensemble GInd, the single-valued ocean basal melting parametrization BCON is used. Therefore, in this ensemble the parameters involved in the LHS affect the climate forcing (λ, γ) and the ice dynamics ($\mathsf{E}_{\mathrm{SIA}}$, c_f) only. Looking at the parameters values for the simulations GIndBvol, GIndMINvol and GIndMAXvol it emerges clearly that the SIA-enhancement factor value has the strongest control on the EIS ice volume evolution throughout the deglaciation. In fact, the minimum and maximum volume evolution is obtained for $\mathsf{E}_{\mathrm{SIA}} = 1.4$ and $\mathsf{E}_{\mathrm{SIA}} = 5.5$, respectively (see Table 3.1). In contrast, the lapse-rate factor has similar values in the minimum and maximum volume evolution simulations ($\lambda = 4.76$ and $\lambda = 4.75$ respectively, see Table 3.1). Therefore, its impact on the ice volume decay of the EIS is less important to those of the SIA-enhancement factor. Similarly, the precipitation-correction factor apparently does not

play any role in modulating the ice volume loss of the EIS. The basal drag coefficient c_f is lower ($4.6 \cdot 10^{-5}$) for the minimum volume simulation than for the maximum volume simulation ($8 \cdot 10^{-5}$), suggesting that the drag under ice streams might play an important role in the deglaciation of the EIS. However, in simulation GIndBvol the basal drag coefficient value is lower than in both GIndMINvol and GIndMAXvol simulations ($c_f = 3.75 \cdot 10^{-5}$), whereas $\mathsf{E}_{\mathrm{SIA}}$ value ($\mathsf{E}_{\mathrm{SIA}} = 2.52$) lays between the values assumed in simulations GIndMINvol and GIndMAXvol, see Table 3.1. This proves that the SIA-enhancement factor exerts the strongest control on the EIS ice volume evolution amongst the model parameters tested in the ensemble GInd. In ensembles GMarBvol, GPDCBvol, GMarSBvol and GPDCSBvol the ocean basal melting parameter F_m is included in the LHS procedure. F_m controls the magnitude of the maximum ocean basal melting rate during a simulation (from 0.1 up to 6 m/yr, see Subsection 2.3.4), thus affecting the EIS mass balance in its marine-based portion. In all minimum volume simulations GMarMINvol, GPDCMINvol, GMarSMINvol and GPDCSMINvol the SIA-enhancement factor value is larger than 5.4, whereas in all maximum volume simulations GMarMAXvol, GPDCMAXvol, GMarSMAXvol and GPDCSMAXvol $\mathsf{E}_{\mathrm{SIA}}$ is lower than 1.4, see Table 3.1. In contrast, the ocean basal melting parameter F_m is similar in both minimum and maximum simulations from all the ensembles, see Table 3.1. Therefore, also in GMarBvol, GPDCBvol, GMarSBvol and GPDCSBvol ensembles the strongest control on the EIS ice volume evolution is exerted by the SIA-enhancemente factor value rather than the ocean basal melting parameter F_m. However, this is not entirely surprising as the terrestrial SIS contains most of the EIS ice volume. As a consequence, changes in the marine-based SBKSIS ice volume evolution have a lower impact on the overall EIS evolution. Compared to ICE-5G ice volume curve, ice volume curves in best fit simulations GIndBvol, GMarBvol, GPDCBvol, GMarSBvol and GPDCSBvol show a much more rapid ice volume loss in the first 2 ka (see Figures 3.10-3.14). The largest ice volume loss (between 7.5-8 m SLE) occur in simulations GIndBvol, GPDCBvol and GPDCSBvol, whereas in simulations GMarBvol and GMarSBvol the first 2 ka ice volume loss is slightly reduced (between 7-7.5 m SLE). However, in all best fit simulations this initial ice volume loss largely exceeds those predicted by ICE-5G (around 3 m SLE). Also in the subsequent 1 ka an ice volume loss around 2.5 m SLE is registered in all best fit simulations, whilst in the same time interval (19-18 ka BP) an ice volume loss of around 1 m SLE occur according to ICE-5G reconstruction (see Figures 3.10-3.14). Also between 18-17 ka BP best fit simulations and ICE-5G ice volume curves are quite different. In fact, ICE-5G curve shows an ice volume decrease of 3 m SLE, whereas in simulations GIndBvol, GPDCBvol, GPDCSBvol, GMarBvol and GMarSBvol the ice volume loss does not exceed 1 m SLE, as shown in Figures 3.10-3.14. However, at 17 ka BP the ICE-5G total EIS ice volume (around 15 m SLE) is close to those predicted by simulations GPDCSBvol, GMarBvol and GMarSBvol (around 14, 15 and 14 m SLE respectively, see Figures 3.11, 3.14 and 3.13). A larger ice volume difference around 2 m SLE with respect to ICE-5G is registered in simulations GIndBvol and GPDCBvol (see Figures 3.10 and 3.11). Between 17 and 16 ka BP the ice volume decrease predicted by ICE-5G and by GIndBvol, GPDCBvol, GPDCSBvol, GMarBvol and GMarSBvol simulations is almost identically low (between 0.5-1 m SLE, see Figures 3.10-3.14). Between 16 and 15 ka BP the ICE-5G ice volume decrease abruptly by around 6 m SLE, whereas between 15 and 14 ka BP a lower decrease around 2.5 m SLE is registered. At 14 ka

BP, the ICE-5G total EIS volume is estimated to be around 5.6 m SLE. In contrast, in all best fit simulations the abrupt ice volume decrease is shifted by 1 ka (see Figures 3.10-3.14). In fact, between 16-15 ka BP the ice volume loss is low (around 1 m SLE) in GIndBvol, GPDCBvol, GPDCSBvol, GMarBvol and GMarSBvol simulations. Between 15-14 ka BP, GMarBvol, GPDCSBvol and GMarSBvol simulations predict an ice volume loss between 6-7 m SLE, whereas in GIndBvol and GPDCBvol simulations a lower ice volume decrease between 4.5 and 5 is registered. The 1 ka delay between GRISLI best fit simulations and ICE-5G can be easily explained by looking at the TraCE-21ka-based air temperature indexes used to modulate between LGM and PI climate snapshots, see Figure 2.10. In fact, according to such climate indexes the B-A warm peaks occur after 15 ka BP. Moreover, high meltwater discharge from the EIS between 15-14 ka BP is in agreement with MWP-1A. However, at 14 ka BP the ICE-5G reconstruction and simulations GPDCBvol, GPDCSBvol, GMarBvol and GMarSBvol are in good agreement in terms of total EIS ice volume, as shown in Figures 3.11-3.14. In simulation GIndBvol the EIS ice volume at 14 ka BP is slightly overestimated (around 7 m SLE) with respect to ICE-5G, as shown in 3.10. This can be explained by the low constant ocean basal melting rate prescribed in BCON parametrization, which leads to a SBKSIS at 14 ka BP larger than in simulations GPDCBvol, GPDCSBvol, GMarBvol and GMarSBvol (see Figures 3.15-3.19). After 14 ka BP, the EIS ice volume evolution is similar in ICE-5G reconstruction and simulations GIndBvol, GPDCBvol, GPDCSBvol, GMarBvol and GMarSBvol, with an overall ice loss around 4 m SLE.

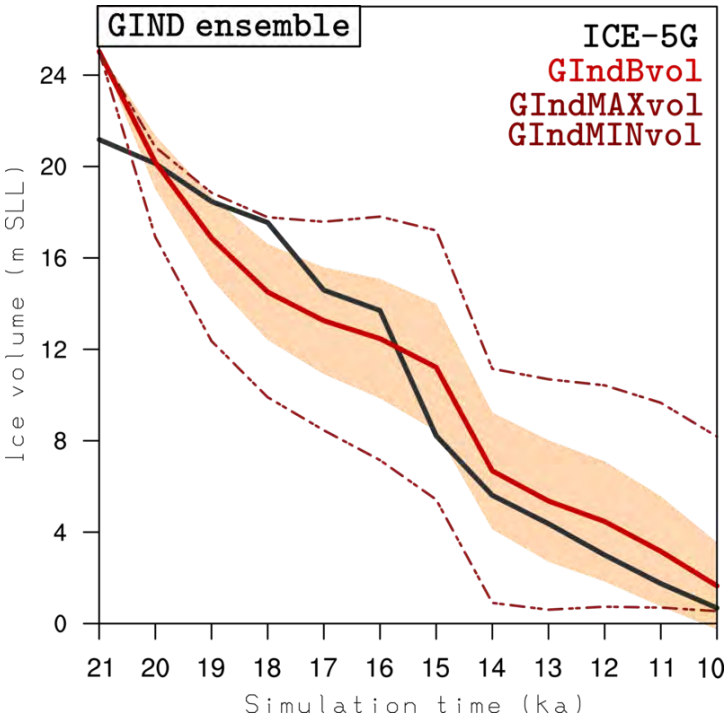

Figure 3.10: Ice volume evolution of the EIS in transient simulations GIndBvol (solid red), GIndMAXvol and GIndMINvol (dashed red) from the GRISLI LHS ensemble GInd. In shaded red the uncertainty, expressed with the ensemble standard deviation σ is shown. In solid black, the ICE-5G ice volume curve is shown for comparison.

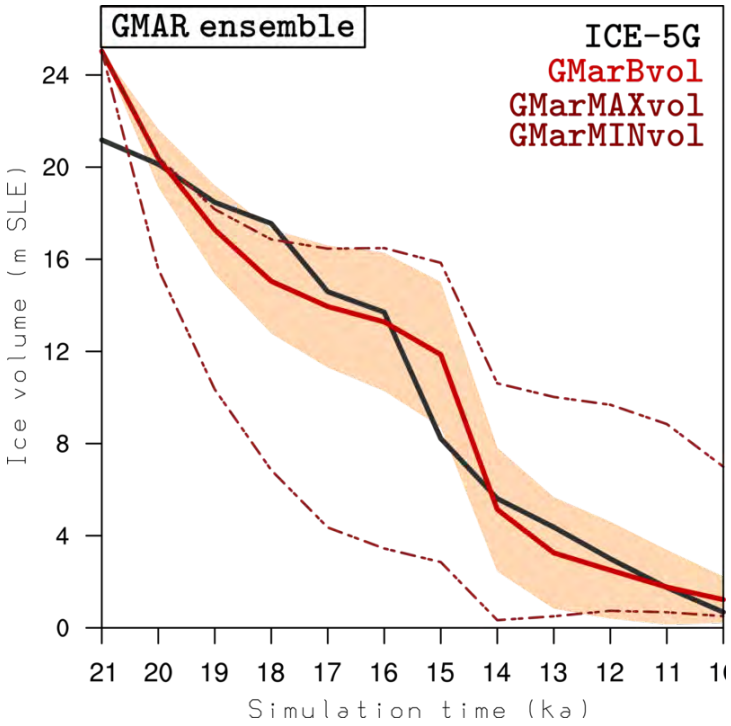

Figure 3.11: Ice volume evolution of the EIS in transient simulations GMarBvol (solid red), GMarMAXvol and GMarMINvol (dashed red) from the GRISLI LHS ensemble GMar. In shaded red the uncertainty, expressed with the ensemble standard deviation σ is shown. In solid black, the ICE-5G ice volume curve is shown for comparison.

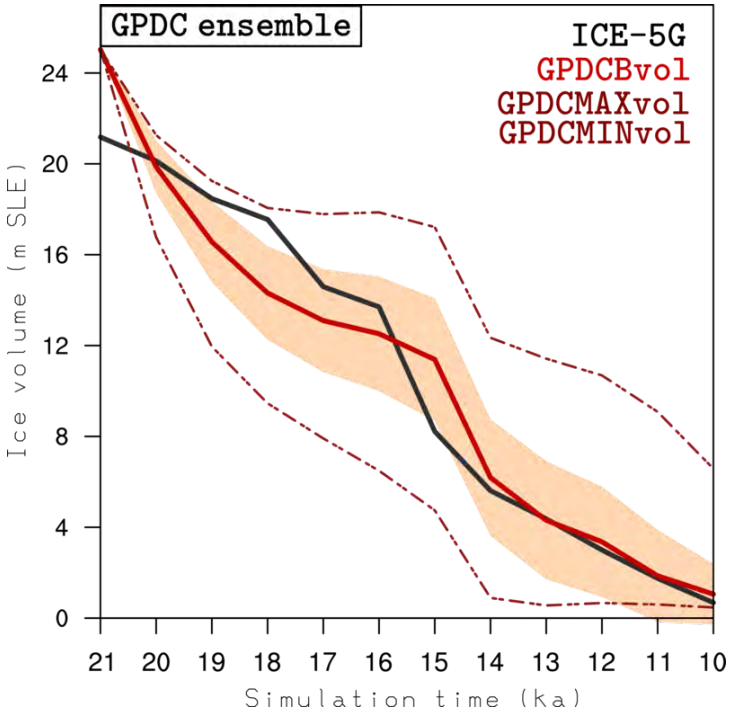

Figure 3.12: Ice volume evolution of the EIS in transient simulations GPDCBvol (solid red), GPDCMAXvol and GPDCMINvol (dashed red) from the GRISLI LHS ensemble GPDC. In shaded red the uncertainty, expressed with the ensemble standard deviation σ is shown. In solid black, the ICE-5G ice volume curve is shown for comparison.

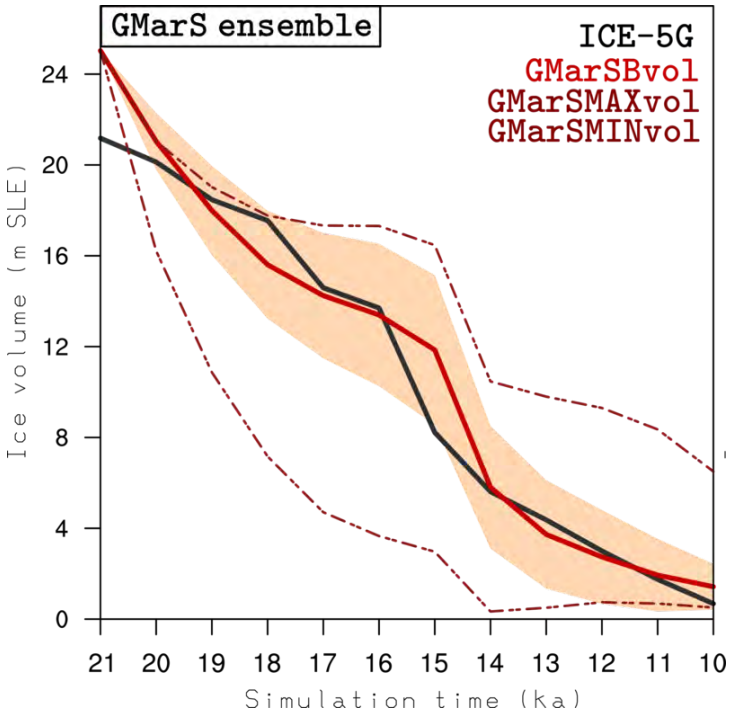

Figure 3.13: Ice volume evolution of the EIS in transient simulations GMarSBvol (solid red), GMarSMAXvol and GMarSMINvol (dashed red) from the GRISLI LHS ensemble GMarS. In shaded red the uncertainty, expressed with the ensemble standard deviation σ is shown. In solid black, the ICE-5G ice volume curve is shown for comparison.

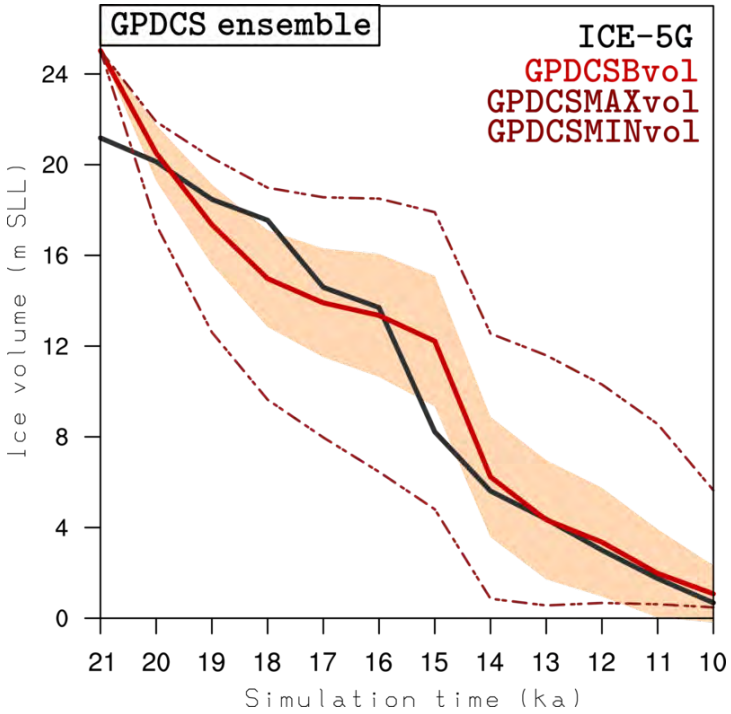

Figure 3.14: Ice volume evolution of the EIS in transient simulations GPDCSBvol (solid red), GPDCSMAXvol and GPDCSMINvol (dashed red) from the GRISLI LHS ensemble GPDCS. In shaded red the uncertainty, expressed with the ensemble standard deviation σ is shown. In solid black, the ICE-5G ice volume curve is shown for comparison.

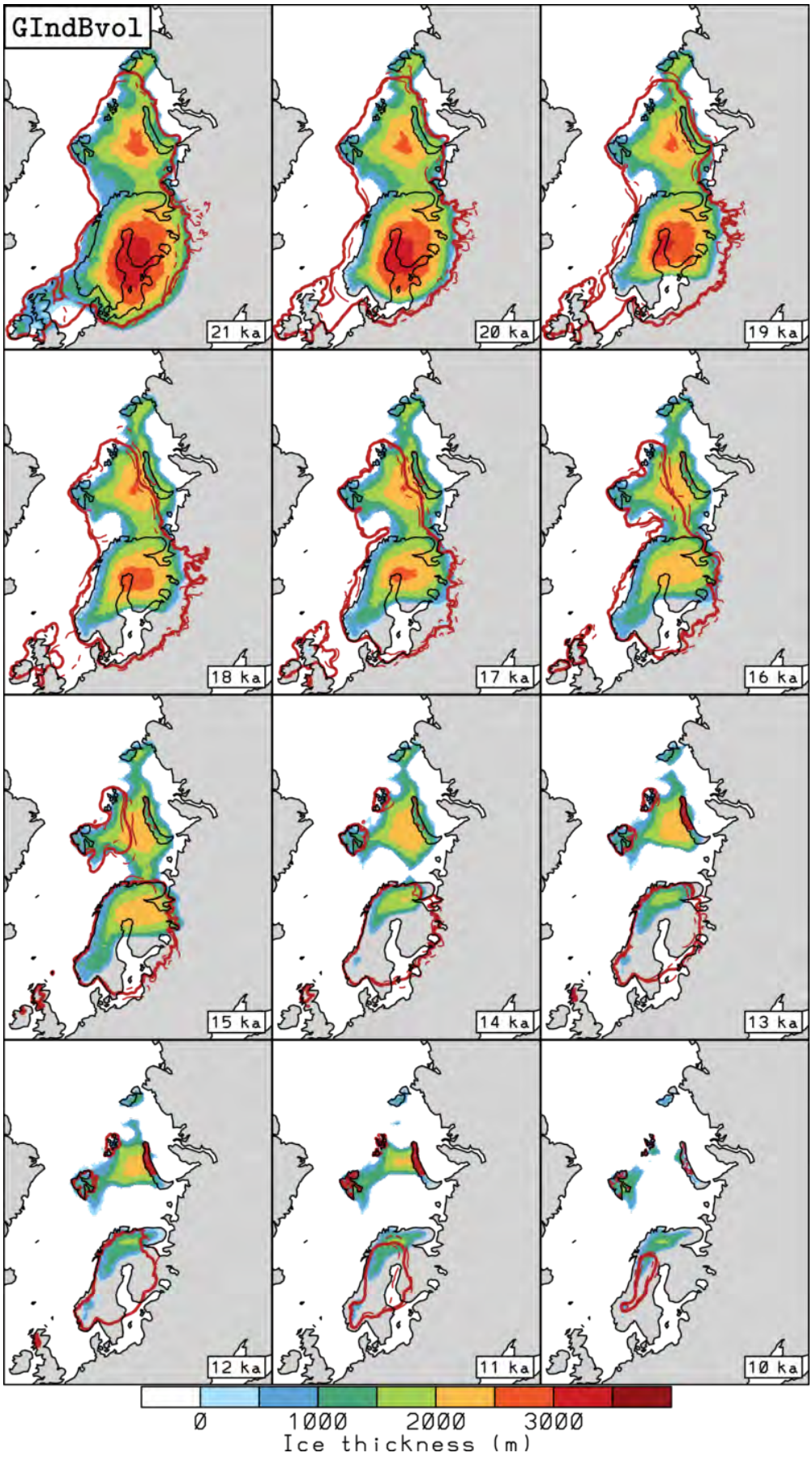

Figure 3.15: Time-slice EIS ice thickness contour every 1000 years between 21 and 10 ka BP for simulation GIndBvol. DATED-1 extent of the EIS at each time slice is shown in solid red (most credible reconstruction) and dashed red (minimum-maximum reconstructions).

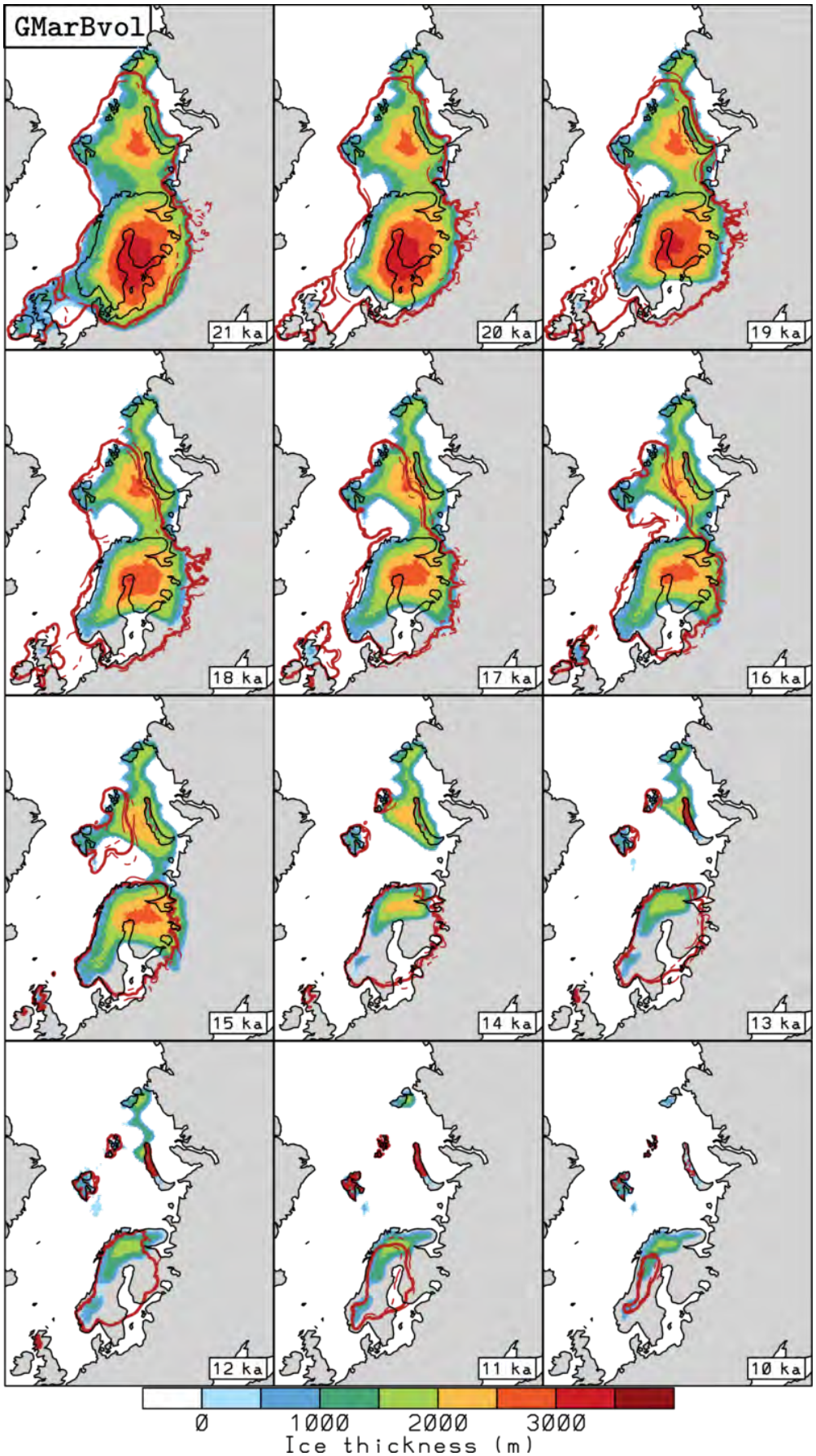

Figure 3.16: Time-slice EIS ice thickness contour every 1000 years between 21 and 10 ka BP for simulation GMarBvol. DATED-1 extent of the EIS at each time slice is shown in solid red (most credible reconstruction) and dashed red (minimum-maximum reconstructions).

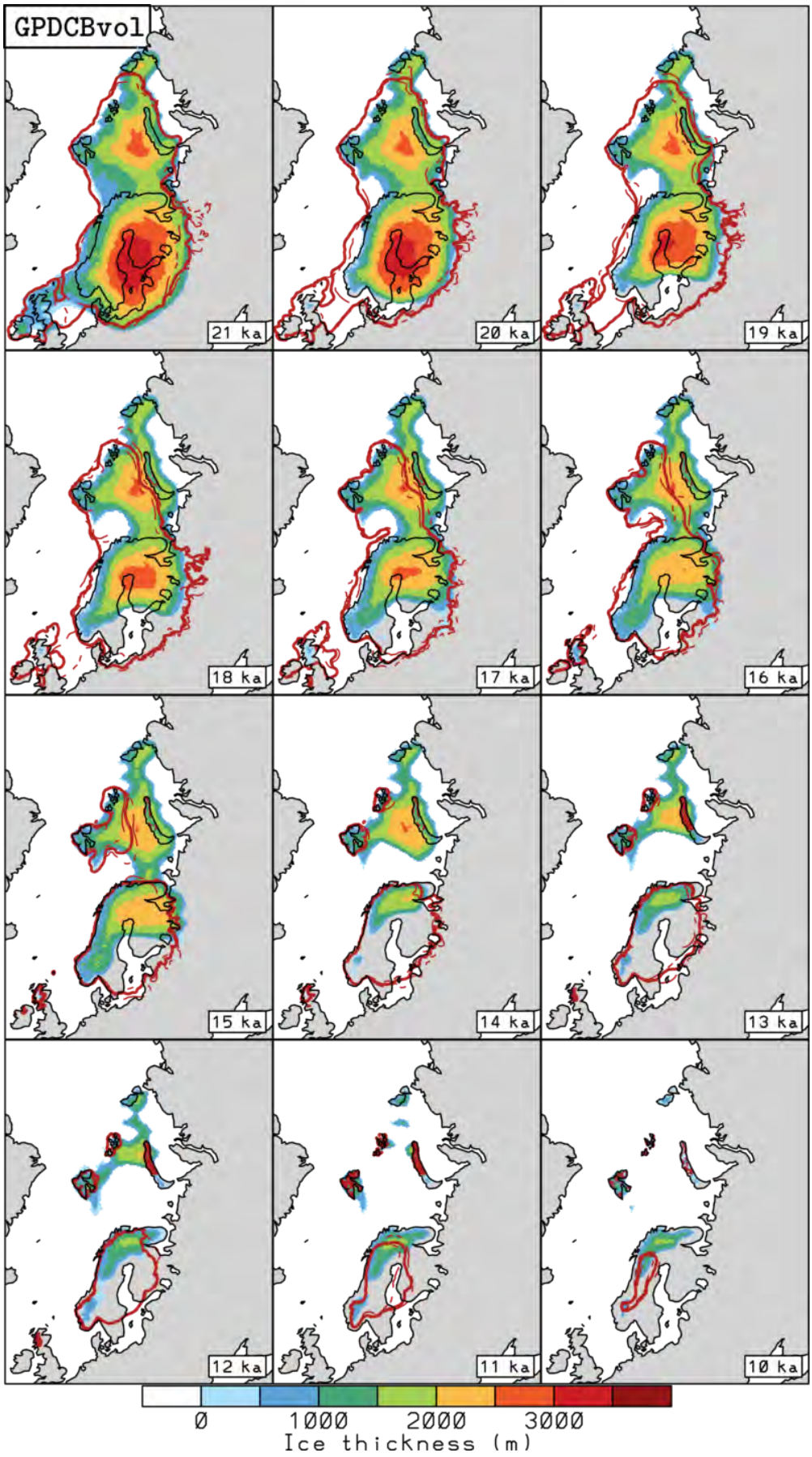

Figure 3.17: Time-slice EIS ice thickness contour every 1000 years between 21 and 10 ka BP for simulation GPDCBvol. DATED-1 extent of the EIS at each time slice is shown in solid red (most credible reconstruction) and dashed red (minimum-maximum reconstructions).

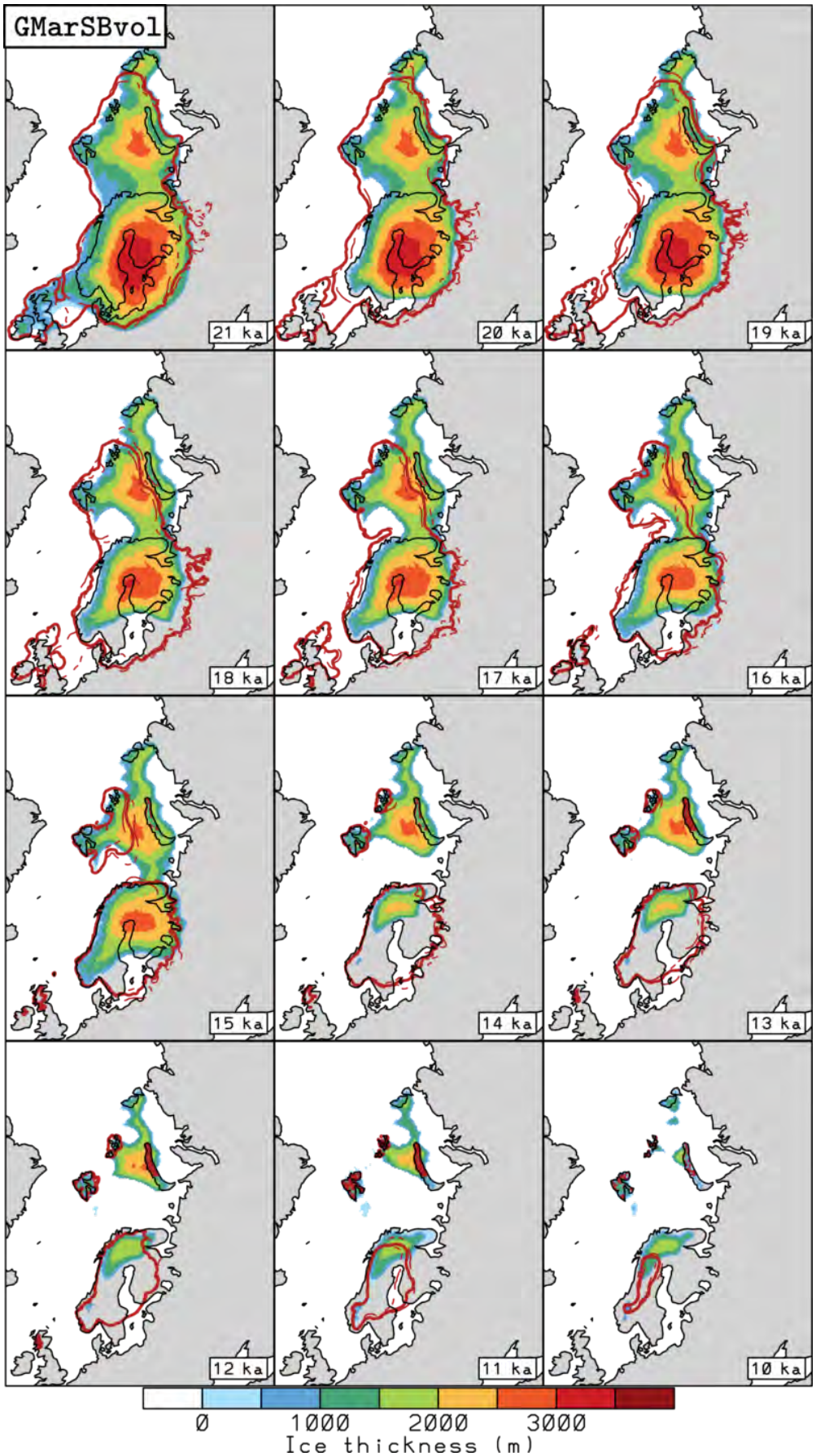

Figure 3.18: Time-slice EIS ice thickness contour every 1000 years between 21 and 10 ka BP for simulation GMarSBvol. DATED-1 extent of the EIS at each time slice is shown in solid red (most credible reconstruction) and dashed red (minimum-maximum reconstructions).

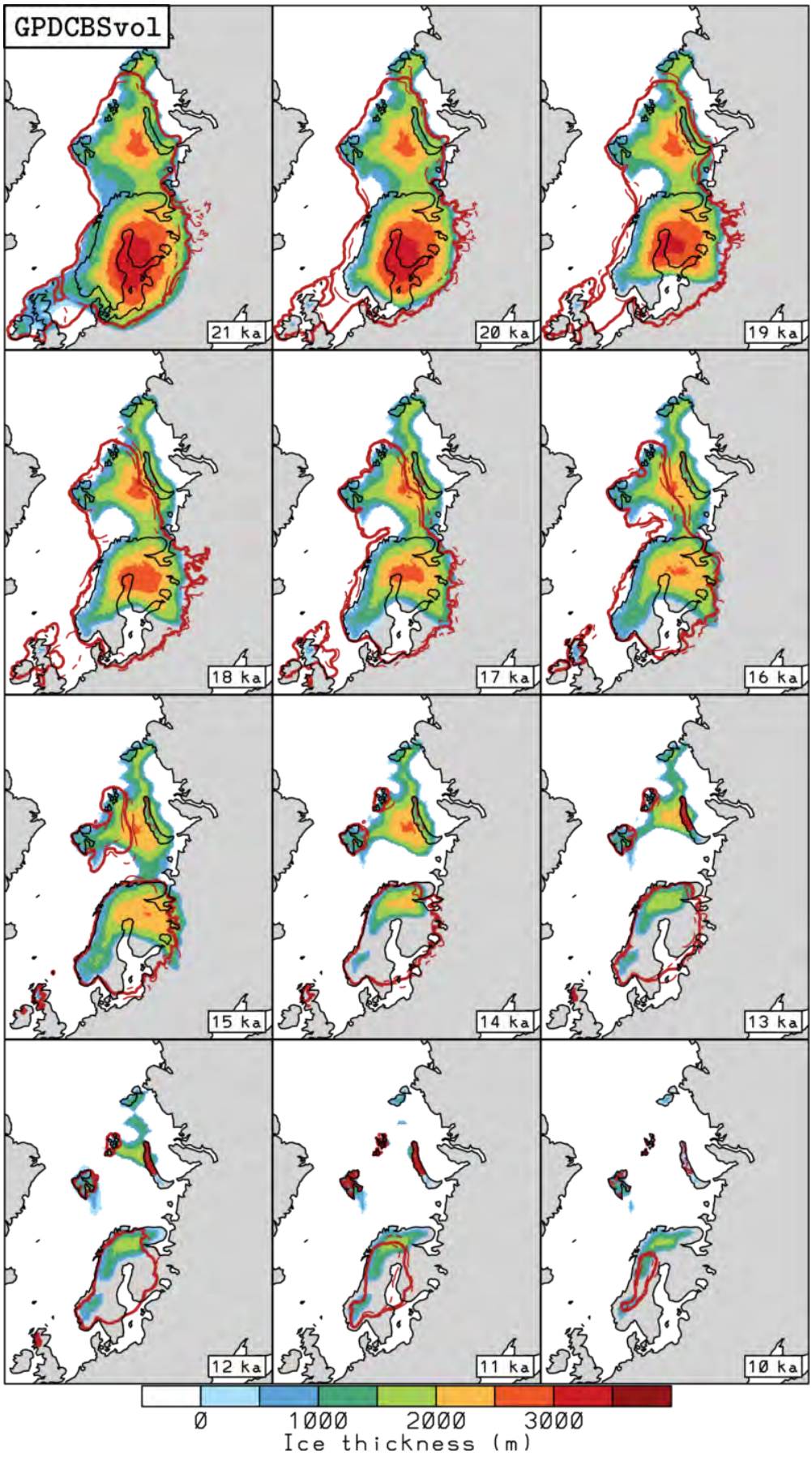

Figure 3.19: Time-slice EIS ice thickness contour every 1000 years between 21 and 10 ka BP for simulation GPDCSBvol. DATED-1 extent of the EIS at each time slice is shown in solid red (most credible reconstruction) and dashed red (minimum-maximum reconstructions).

The EIS extent evolution throughout the deglaciation is similar in all best fit simulations. By 20 ka BP, the BIIS is completely deglaciated in all the best fit simulations (see Figures 3.15-3.19). In contrast, according to DATED-1 most credible reconstruction the BIIS is disconnected from the SIS by 18 ka BP and is almost entirely deglaciated by 16-15 ka BP. In all best fit simulations the southern SIS and the south-western SBKSIS margins show a significant retreat between 21-19 ka BP (see Figures 3.15-3.19), due to the combination of increased air temperatures (see Figure 2.10) and ice stream dynamics (see Figure 2.13b) as already discussed in Subsection 3.2. This is not in agreement with DATED-1 reconstruction, which shows only minor (or nonexistent) retreats in these regions in the 21-19 ka BP time frame. Minor retreats are also registrated in GIndBvol, GMarBvol, GPDCBvol, GMarSBvol and GPDCSBvol simulations at the northern SBKSIS and western SIS margins (see Figures 3.15-3.19). The western SIS margin retreat by 19 ka BP is shown only in the minimum DATED-1 reconstruction, whereas the SBKSIS northern margin starts to retreat only after 19 ka BP in DATED-1 reconstruction. Between 19 and 18 ka BP, further retreat of the south-western SBKSIS and southern SIS margins occurs all best fit simulations (see Figures 3.15-3.19). In contrast, according to DATED-1 reconstruction during this time frame the eastern margin of the SBKSIS retreats across Novaya Zemlya. The eastern margin of the SBKSIS represents one of the most critical regions in terms of model-data agreement for all the best fit simulations GIndBvol, GMarBvol, GPDCBvol, GMarSBvol and GPDCSBvol. In fact, the simulated eastern SBKSIS margin does not show the westward migration depicted in DATED-1 reconstruction throughout the deglaciation. As a consequence, a thick SBKSIS central dome in the north-eastern Barents Sea persists until the ice sheet decay (see Figures 3.15-3.19). This is in clear contradiction with respect to DATED-1 reconstruction, predicting a large-scale retreat of both the western and eastern SBKSIS margins. The reason of such a highly static eastern SBKSIS margin in GRISLI simulations could be related to the cold LGM and PI mean annual air temperatures simulated by IPSL-CM5A-LR model in the eastern Barents Sea and Kara Sea (see Figures 2.8 and 2.7). In fact, cold air temperatures reduces the surface ablation and the amount of meltwater at the ice sheet base, due to the temperature diffusion. Reduced amount of meltwater at the ice sheet base prevents the formation of ice stream regions in GRISLI (see criteria IS2 in Subsection 2.2.1). Between 18-15 ka BP the EIS extent remains mostly unchanged in all best fit simulations, except for minor ice margin retreats in the south-western Barents Sea (see Figures 3.15-3.19). By 15 ka BP, the SIS and the SBKSIS remain connected in all best fit simulations, whereas in DATED-1 reconstruction the ice sheets are disconnected also in the maximum reconstruction, see Figures 3.15-3.19. Between 15-14 ka BP, in GIndBvol, GMarBvol, GPDCBvol, GMarSBvol and GPDCSBvol simulations the SIS and the SBKSIS are finally disconnected and the SIS extent is restricted to northern Scandinavia (see Figures 3.15-3.19). The central ice dome in the eastern Barents Sea remains connected to Svalbard ice complex in simulations GIndBvol, GPDCBvol, GMarSBvol and GPDCSBvol, whereas the two regions are disconnected in simulation GMarBvol, see Figures 3.15-3.19. According to DATED-1 reconstruction, the decay of the SIS occurs between 11-10 ka BP, whereas in all best fit simulations after 13 ka BP the SIS is restricted to a narrow area in northern Scandinavia. As concerns the SBKSIS, according to DATED-1 reconstruction the ice sheet decay occurs between 15-14 ka BP. In contrast, SBKSIS decay occurs between 11-10 ka BP in GIndBvol and GMarSBvol sim-

ulations, between 12-11 ka BP in GPDCBvol and GPDCSBvol simulations and between 13-12 ka BP in GMarBvol simulation, see Figures 3.15-3.19.

3.4 PSU simulations

As already explained in Subsection 2.3.5, due to large computational costs it is not possible to perform with PSU the large number of simulations performed with GRISLI. Therefore, a restricted number of simulations are run with PSU by using model parameter values from the GRISLI best fit simulations. PSU simulation employing BMAR ocean basal melting parametrization and the same model parameter values as in GRISLI best fit simulation GMarBvol is denoted with $\mathsf{PMarBvol_b}$, see Table 3.1. The total EIS ice volume evolution between 21-10 ka BP in simulation $\mathsf{PMarBvol_b}$ is shown in Figure 3.21. Compared to ICE-5G ice volume curve, $\mathsf{PMarBvol_b}$ largely overestimates the total EIS ice volume throughout the deglaciation. In particular, simulation $\mathsf{PMarBvol_b}$ predicts that at 15 ka BP the total EIS ice volume is the same as at LGM, which is in clear contradiction both with ICE-5G ice volume curve and DATED-1 reconstruction. By looking at the ice thickness and velocity evolution between 21-16 ka BP, it emerges that the ice volume overestimation results from a combination of climatic and dynamic factors. In fact, in PSU the different ice stream treatment results in simulated ice stream regions and ice velocities considerably lower with respect to GRISLI simulations (see Figures 3.8 and 3.22). As a consequence, the simulated ice sheet/stream dynamics plays a secondary role in PSU. In simulation $\mathsf{PMarBvol_b}$ the only portions of the EIS which are dynamically active between 21-15 ka BP are the western and northern marine margins of the SBKSIS (see Figure 3.23), which are governed by ocean basal melting, calving and GL migration.

In contrast, the terrestrial SIS and eastern SBKSIS margins position remains unchanged in the first 6 ka in simulation $\mathsf{PMarBvol_b}$, see Figure 3.23. Moreover, between 21-15 ka BP the central SBKSIS dome shows a very little thinning and the ice thickness in the central SIS dome even increases. This behaviour can be explained by looking at the climate indexes used to force PSU, see Figure 2.10. In fact, under such low simulated ice sheet/stream dynamics, the first control on the ice sheet evolution is exerted by the SMB, which in turn depends on the climate forcing. In both Fennoscandia and Svalbard/Barents Sea macro-regions, near-surface air temperature indexes remain close to its LGM value until 15 ka BP, as shown in Figure 2.10a. In contrast, total precipitation index representative of Fennoscandia reaches its PI value few hundreds of years after 15 ka BP, see Figure 2.10b. This explain why ice thinning is low in the central SBKSIS dome and ice thickening occurs in the central SIS dome.

In order to obtain a simulated total EIS ice volume evolution closer to ICE-5G reconstruction, the PDD_σ method is used in place of the $\mathsf{PDD}_{\triangle\sigma}$ method (see Subsection 2.2.1). After preliminary test simulations, the standard deviation of near-surface air temperature σ is set to a value of 6.5 °C, which is the upper bound from the parametrization by Fausto et al. 2011. PSU simulation employing PDD_σ method and using ocean basal melting parametrization and model parameter values as in simulation $\mathsf{PMarBvol_b}$ is denoted with $\mathsf{PMarBvol_a}$. As shown in Figure 3.21, the use of PDD_σ in simulation $\mathsf{PMarBvol_a}$ has a strong impact on the total EIS ice volume evolution. In the time frame 21-18 ka BP there is an excellent agreement between simulation $\mathsf{PMarBvol_a}$ and ICE-5G

reconstruction, although the total EIS ice volume remains slightly overestimated after 18 ka BP. Such ice volume overestimation can be addressed to the combination of cold near-surface air temperature and increased precipitation prescribed by TraCE-21ka index over Fennoscandia, as shown in Figure 2.10. In fact, the EIS ice thickness evolution clearly shows that the SIS central dome thickness remains unchanged between 21-16 ka BP (see Figure 3.20). In contrast, in the same time frame the SBKSIS central dome thickness decreases by around 20% with respect to LGM, as shown in Figure 3.20.

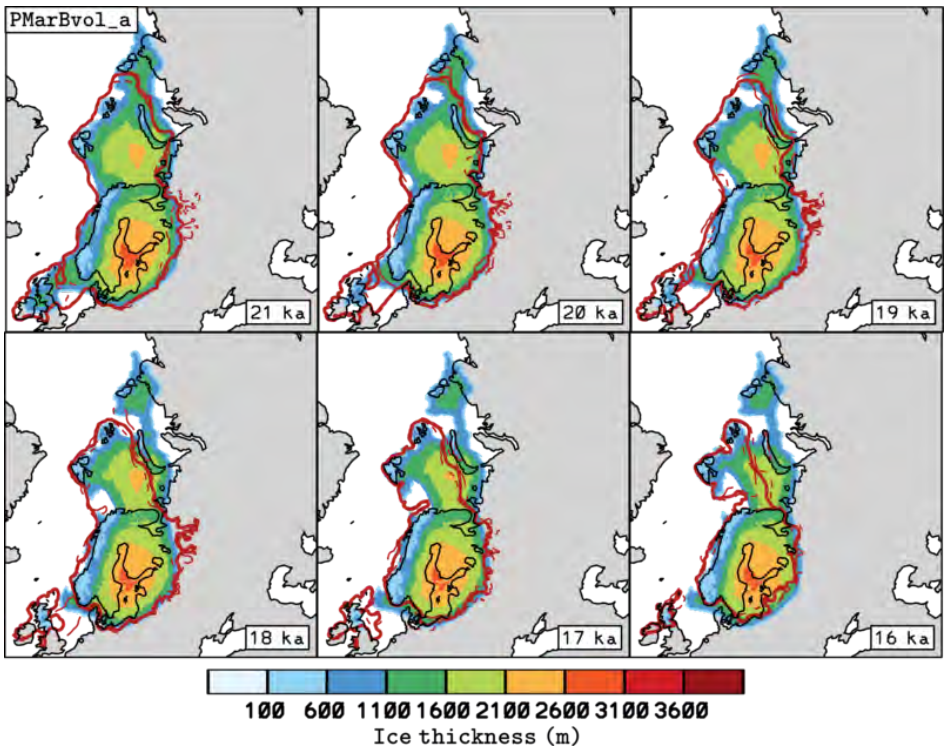

Figure 3.20: Time-slice EIS ice thickness contour every 1000 years between 21 and 16 ka BP for simulation $\mathsf{PMarBvol_a}$. DATED-1 extent of the EIS at each time slice is shown in solid red (most credible reconstruction) and dashed red (minimum-maximum reconstructions).

Therefore, in order to further reduce the total EIS ice volume overestimation after 18 ka BP, the same precipitation index representative of Svalbard/Barents Sea is employed also in Fennoscandia macro-region. PSU simulation employing such corrected Fennoscandia precipitation index, PDD_σ method and using ocean basal melting parametrization and model parameter values as in simulation $\mathsf{PMarBvol_a}$ is denoted with PMarBvol. As shown in Figure 3.21, in simulation PMarBvol the total EIS ice volume curve after 18 ka BP is closer to ICE-5G ice volume curve with respect to simulation $\mathsf{PMarBvol_a}$. Therefore, in all PSU simulations presented hereafter the corrected Fennoscandia precipitation index and the PDD_σ method with $\sigma = 6.5\,^{\circ}\mathrm{C}$ are employed. In particular, PSU simulations employing BCON and BPDC ocean basal melting parametrizations, respectively and model parameter values as in GRISLI best fit simulations GIndBvol and GPDCBvol, respectively are denoted with PIndBvol and PPDCBvol, respectively. Similarly, PSU simulations employing BMAR, BCON and BPDC ocean basal melting parametrizations, respectively and model parameter values as in GRISLI reference simulations are denoted with PIndRef, PMarRef and PPDCRef, respectively.

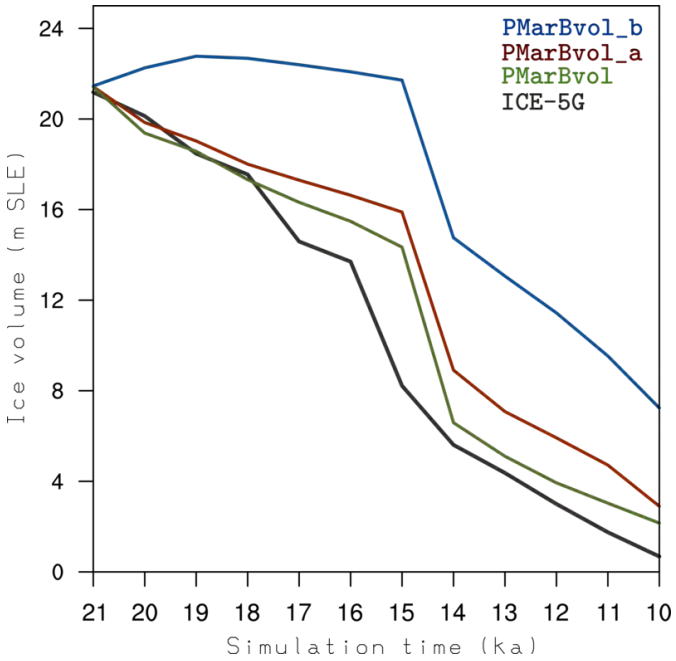

Figure 3.21: Ice volume evolution of the EIS in transient simulations $\mathsf{PMarBvol}_b$ (solid blue), $\mathsf{PMarBvol}_a$ (solid red) and PMarBvol (solid green) In solid black, the ICE-5G ice volume curve is shown for comparison.

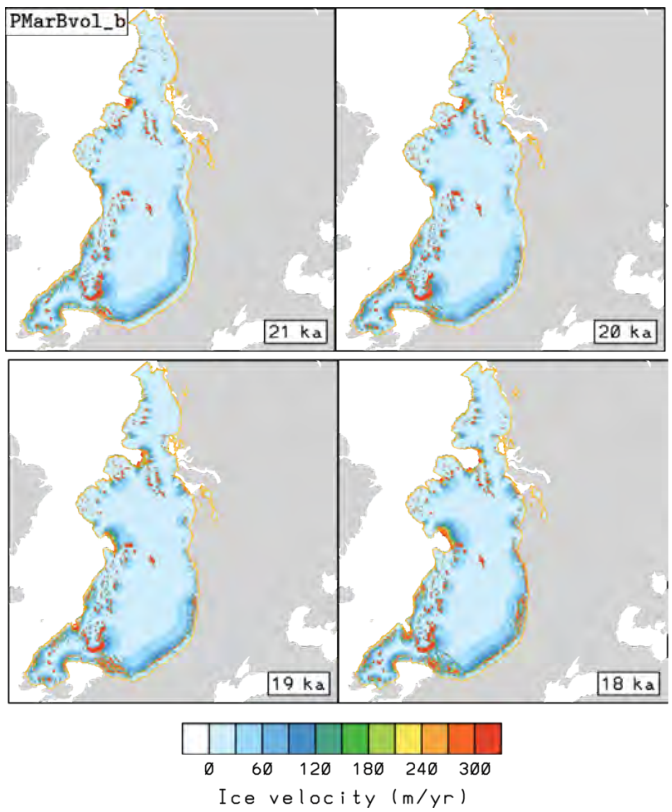

Figure 3.22: EIS horizontal ice velocity contour at four selected time slices (21, 20, 19 and 18 ka BP) for PSU simulation PMarBvol. At each time slice, the grounded-ice limit is shown in orange.

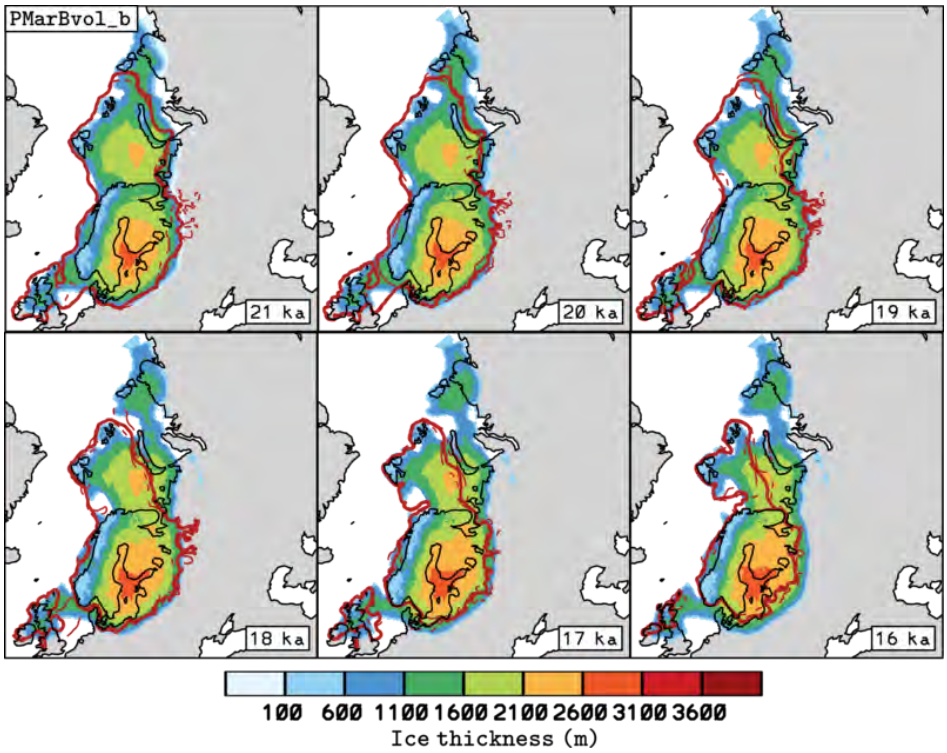

Figure 3.23: Time-slice EIS ice thickness contour every 1000 years between 21 and 16 ka BP for simulation $\mathsf{PMarBvol}_{\mathsf{b}}$. DATED-1 extent of the EIS at each time slice is shown in solid red (most credible reconstruction) and dashed red (minimum-maximum reconstructions).

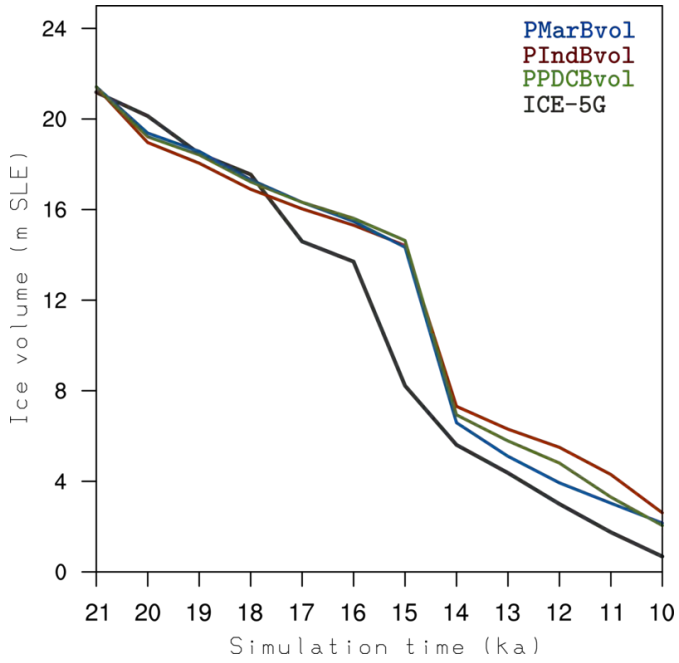

Figure 3.24: Ice volume evolution of the EIS in transient simulations PIndBvol (solid red), PMarBvol (solid blue) and PPDCBvol (solid green) In solid black, the ICE-5G ice volume curve is shown for comparison.

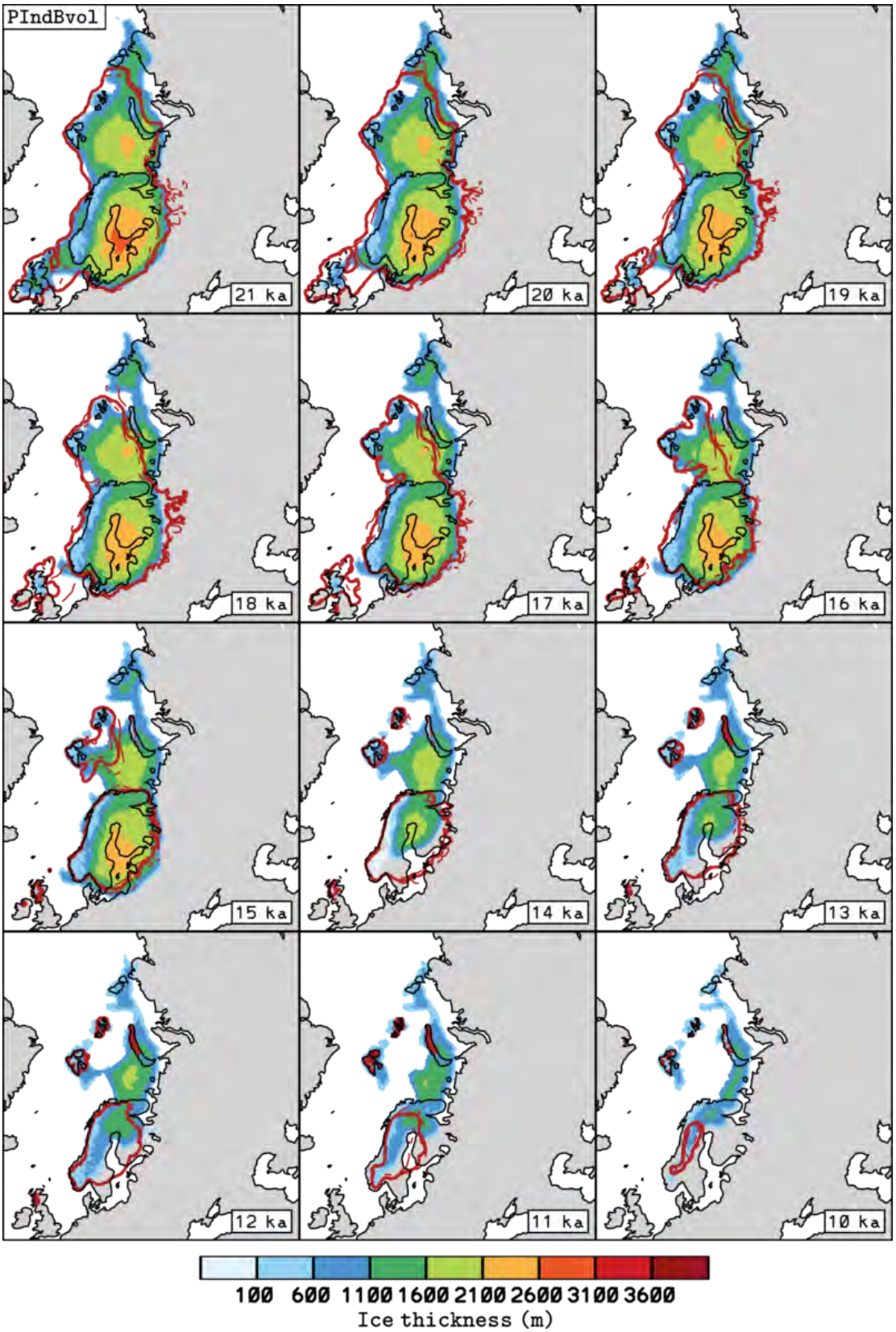

Figure 3.25: Time-slice EIS ice thickness contour every 1000 years between 21 and 10 ka BP for simulation PIndBvol. DATED-1 extent of the EIS at each time slice is shown in solid red (most credible reconstruction) and dashed red (minimum-maximum reconstructions).

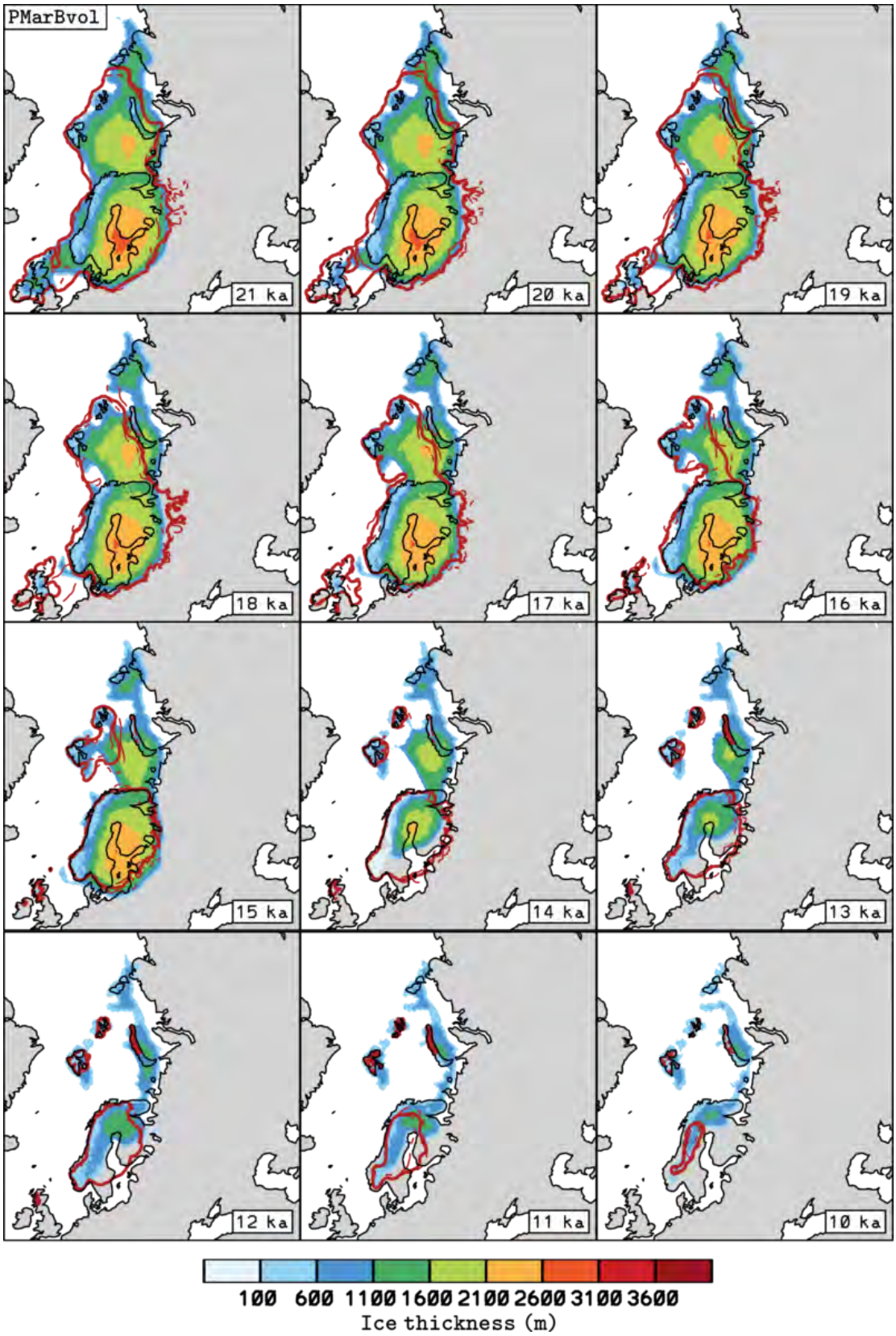

Figure 3.26: Time-slice EIS ice thickness contour every 1000 years between 21 and 10 ka BP for simulation PMarBvol. DATED-1 extent of the EIS at each time slice is shown in solid red (most credible reconstruction) and dashed red (minimum-maximum reconstructions).

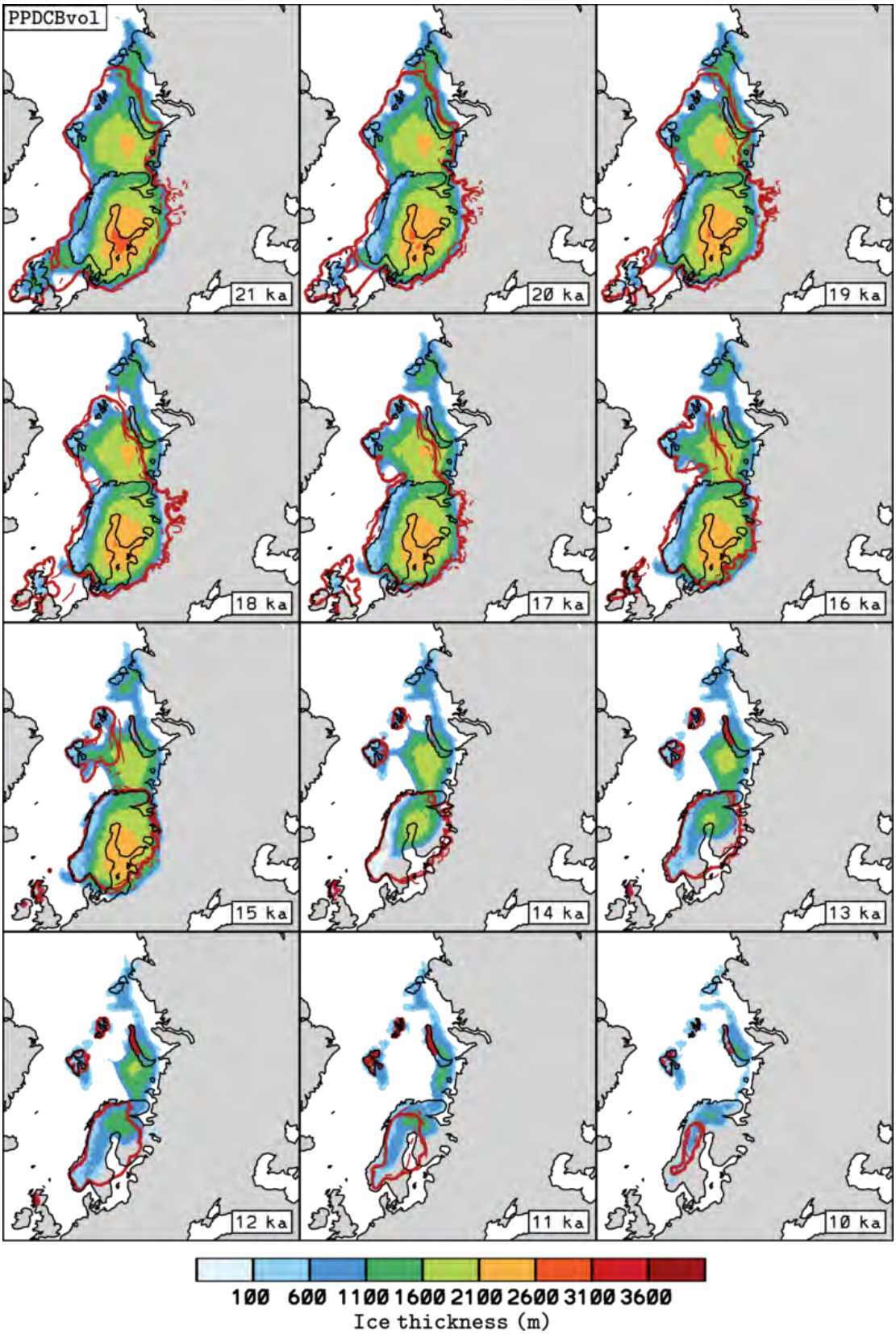

Figure 3.27: Time-slice EIS ice thickness contour every 1000 years between 21 and 10 ka BP for simulation PPDCBvol. DATED-1 extent of the EIS at each time slice is shown in solid red (most credible reconstruction) and dashed red (minimum-maximum reconstructions).

The EIS ice volume evolution throughout the deglaciation is almost identical in PSU simulations PIndBvol, PMarBvol and PPDCBvol, see Figure 3.24. Little discrepancies (less than 1 m SLE) between the three different ice volume curves are shown only after 14 ka BP. Between 21-18 ka BP, total EIS ice volume evolution in simulations PIndBvol, PMarBvol and PPDCBvol is in very good agreement with ICE-5G reconstruction. The large difference between PSU (PIndBvol, PMarBvol and PPDCBvol) and GRISLI (GIndBvol$_b$, GMarBvol and GPDCBvol) total ice volume curves in the first 3 ka can be explained by the completely different ice sheet/streams dynamics in the southern SIS, as shown in Figures 3.8 and 3.22. In fact, in GRISLI simulations ice stream dynamics play a fundamental role in the early (first 2 ka) southern SIS retreat, enhancing transport of ice to warmer low latitudes at the southern SIS margin (see Section 3.2). In PSU, ice streams extent and velocity are considerably lower and therefore such early southern SIS retreat is absent, as shown in Figures 3.25-3.27. Between 18-17 ka BP, ICE-5G curve shows an ice volume decrease of 3 m SLE, whereas in PSU simulations PIndBvol, PMarBvol and PPDCBvol the ice volume decrease is lower (around 1 m SLE). Conversely, between 17 and 16 ka BP ICE-5G and PSU ice volume curves share almost the same slope, predicting a low ice volume loss around 1 m SLE. At 16 ka BP, the total ice volume is overestimated by PSU simulations with respect to ICE-5G reconstruction by around 2 m SLE. PSU (PIndBvol, PMarBvol and PPDCBvol) and GRISLI (GIndBvol$_b$ GMarBvol and GPDCBvol) total ice volume curves share the same slope between 18-14 ka BP (see Figures 3.10-3.14 and 3.24). In fact, in all simulations a low total ice volume loss is predicted between 18-15 ka BP, due to the cold near-surface air temperatures (see TraCE-21ka indexes in Figure 2.10). After 15 ka BP, both GRISLI and PSU simulations predict an abrupt ice volume loss, 1 ka delayed with respect to ICE-5G reconstruction. The ice volume loss in GRISLI best fit simulations ranges between 4.5-7 m SLE, whereas the ice volume loss predicted by PSU PIndBvol, PMarBvol and PPDCBvol simulations is around 8 m SLE (see Figures 3.10-3.14 and 3.24). However, at 14 ka BP the total EIS ice volume predicted by PSU simulations is around 1.5 m SLE higher than in ICE-5G reconstruction and GRISLI best fit simulatiions (see Figures 3.10-3.14 and 3.24). After 14 ka BP, the EIS ice volume evolution is similar in ICE-5G reconstruction, GRISLI best fit simulations and PSU simulations PIndBvol, PMarBvol and PPDCBvol, with an overall ice loss around 4 m SLE. However, between 14-10 ka BP the total EIS ice volume in PSU simulations PIndBvol, PMarBvol and PPDCBvol is overestimated with respect to ICE-5G reconstruction by up to 2 m SLE. By looking at the ice thickness evolution in GRISLI (GIndBvol$_b$ GMarBvol and GPDCBvol, see Figures 3.15-3.17) and PSU (PIndBvol, PMarBvol and PPDCBvol, see Figures 3.25-3.27) simulations, it emerges clearly that the ice volume overestimation is caused by an excess of ice in the south-eastern Barents Sea in PSU simulations. Such ice cover is the remnant of the SBKSIS ice dome and it is not entirely melted at 10 ka BP, see Figures 3.25-3.27. Similarly as in all GRISLI best fit simulations, the simulated eastern SBKSIS margin does not show the westward migration depicted in DATED-1 reconstruction throughout the deglaciation, likely due to insufficient simulated ice sheet/stream dynamics (see Figure 3.22). Therefore, the SBKSIS evolution in terms of ice sheet extent does not show a good agreement with DATED-1 reconstruction. In contrast, there is a good agreement between PSU simulations 3.25-3.27 and DATED-1 reconstruction as concerns the SIS evolution. In fact, PSU simulations predict a SIS retreat from its western, eastern and

southern margins only after 15 ka BP. Although the simulated retreat is more intense than those predicted by DATED-1 reconstruction, the simulated and reconstructed SIS size throughout the deglaciation is comparable, 3.25-3.27. Moreover, in PSU simulations PIndBvol, PMarBvol and PPDCBvol the SIS retreats into the inner Norwegian Channel between 19 and 18 ka BP, which is in agreement with *in-situ* sediment analysis, see Figures 3.25-3.27. By 10 ka BP, the SIS is restricted to a narrow area in northern Scandinavia in simulations PIndBvol, PMarBvol and PPDCBvol, in agreement with DATED-1 reconstructions. As concerns the SBKSIS decay, the western, northern and central parts of Barents Sea remains ice free between 12-10 ka BP, which is in agreement with DATED-1 reconstruction.

As already done for GRISLI ISM in Section 3.2, PSU reference simulations PIndRef, PMarRef and PPDCRef are compared, in order to test to what extent the use of different ocean basal melting parametrizations (see Subsection 2.3.4) affects the simulated EIS deglaciation. In Figure 3.28, the total EIS ice volume evolution in reference simulations PIndRef, PMarRef and PPDCRef is shown. Two considerations emerge by looking at Figure 3.28; first, by changing values of those PSU model parameters which are in common with GRISLI (*i.e.*, lapse-rate factor λ, precipitation-correction factor γ, ocean basal melting parameter F_m, see Table 3.1) the total EIS volume evolution remains essentially unchanged. This is not entirely surprising in light of the GRISLI LHS ensembles analysis carried out in Section 3.3. In fact, model parameter values for minimum/maximum/best fit with ICE-5G GRISLI simulations shows that the SIA-enhancement factor $\mathsf{E}_{\mathrm{SIA}}$, amongst the other model parameters tested, exerts the strongest control on the EIS ice volume evolution. As already explained in Section 3.1, in order to compensate for low ice sheet/stream velocities constant values for both $\mathsf{E}_{\mathrm{SIA}} = 10$ and $\mathsf{E}_{\mathrm{SIA}} = 3$ are adopted in all PSU simulations. Therefore, with PSU it is possible to test only model parameters having a weak control on the total EIS volume evolution. The second consideration is that the use of ocean basal melting parametrizations BMAR and BPDC, which are based on ice-ocean heat fluxes, does not provide significative differences with respect to the single-valued ocean basal melting parametrizations BCON in terms of total EIS ice volume evolution. This is more surprising, in particular considering that the impact of ocean basal melting parametrizations BMAR and BPDC on the total EIS ice volume evolution is high in GRISLI, see Figure 3.5. This implies that in PSU the marine-based portion of the EIS is controlled by another dynamic process rather than ocean basal melting. In order to investigate the role played by calving and GL migration, two additional simulations are run with PSU. Both simulations employs corrected Fennoscandia precipitation index, PDD_σ method with $\sigma = 6.5\,^{\circ}\mathrm{C}$ and ocean basal melting parametrization BMAR. Moreover, in both simulations the same values as in simulation PMarBvol for the parameters λ, γ and F_m are adopted. In a first simulation denoted with $\mathsf{PMarBvol}_{\mathsf{cal}}$ the calving rate is reduced from 60 to 30 m/yr, whereas in a second simulation denoted with $\mathsf{PMarBvol}_{\mathsf{GL}}$ the GL migration parametrization proposed by Schoof 2007 is not used. Figure 3.29 clearly shows that the strongest control on the marine-based portion of the EIS in PSU is exerted by the GL dynamics; in fact, without the Schoof 2007 GL migration parametrization the total EIS ice volume is overestimated up to 4 m SLE after 14 ka BP, see Figure 3.29. Although the role played by simulated calving in regulating the total EIS ice volume evolution is secondary with respect to the GL dynamics, its impact is larger than the ocean basal melting, see Figures 3.28 and 3.29.

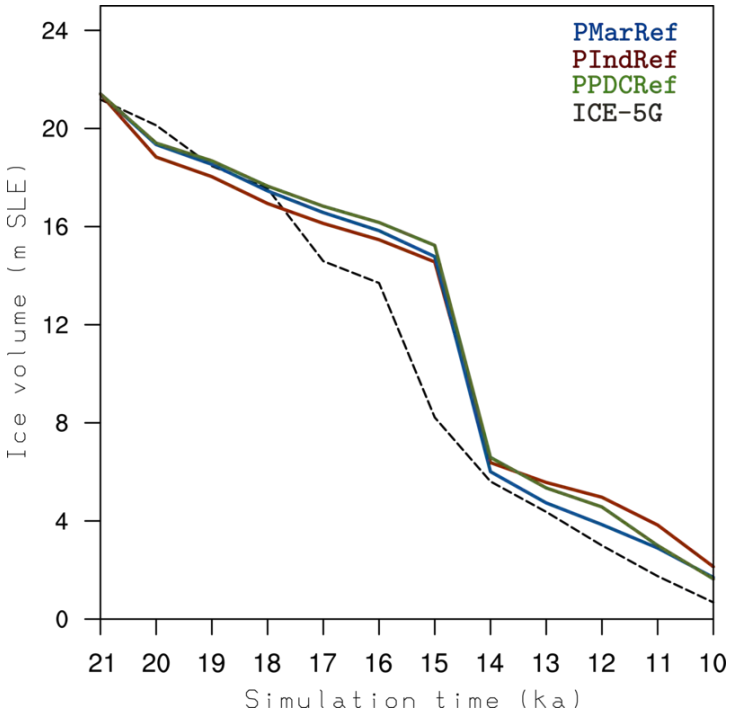

Figure 3.28: Ice volume evolution of the EIS in PSU reference simulations PIndRef (solid red), PMarRef (solid blue) and PPDCRef (solid green). In dashed black, the ICE-5G ice volume curve is shown for comparison.

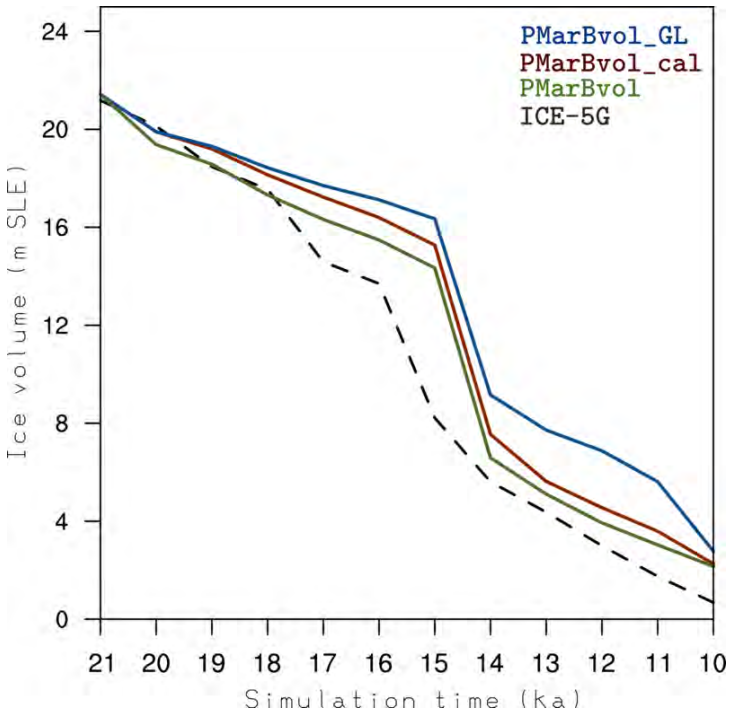

Figure 3.29: Ice volume evolution of the EIS in PSU transient simulations PMarBvol (solid green), $\text{PMarBvol}_{\text{cal}}$ (solid red) and $\text{PMarBvol}_{\text{GL}}$ (solid blue). In dashed black, the ICE-5G ice volume curve is shown for comparison.

Simulation description	ID	Climate forcing			Parametrizations		LHS parameters					Other			
		Initial	Final	Index	PDD	BMELT	λ	γ	c_f	F_m	E_{SIA}	E_{SSA}	σ	b_m	r_{CAL}
GRISLI spin-up.	GSpin$\triangle\sigma$	PI	LGM	δ18O	PDD$_{\triangle\sigma}$	BCON	5.00	0.050	$2.00 \cdot 10^{-5}$	-	3.00	1.00	-	0.1	-
	GSpinσ	PI	LGM	δ18O	PDD$_{\sigma}$	BCON	5.00	0.050	$2.00 \cdot 10^{-5}$	-	3.00	1.00	5	0.1	-
PSU spin-up.	PSpinσ	PI	LGM	δ18O	PDD$_{\sigma}$	BCON	5.00	0.050	-	-	10.00	3.00	5	0.1	0.5
	PSpinσEnh	PI	LGM	δ18O	PDD$_{\sigma}$	BCON	5.00	0.050	-	-	10.00	3.00	5	0.1	0.5
GRISLI reference.	GIndRef	LGM	PI	TraCE-21ka	PDD$_{\triangle\sigma}$	BCON	5.00	0.050	$2.00 \cdot 10^{-5}$	-	3.00	1.00	-	0.1	-
	GMarRef	LGM	PI	TraCE-21ka	PDD$_{\triangle\sigma}$	BMAR	5.00	0.050	$2.00 \cdot 10^{-5}$	0.006520	3.00	1.00	-	-	-
	GPDCRef	LGM	PI	TraCE-21ka	PDD$_{\triangle\sigma}$	BPDC	5.00	0.050	$2.00 \cdot 10^{-5}$	0.000751	3.00	1.00	-	-	-
	GMarSRef	LGM	PI	TraCE-21ka	PDD$_{\triangle\sigma}$	BMAR	5.00	0.050	$2.00 \cdot 10^{-5}$	0.006520	3.00	1.00	-	-	-
	GPDCSRef	LGM	PI	TraCE-21ka	PDD$_{\triangle\sigma}$	BPDC	5.00	0.050	$2.00 \cdot 10^{-5}$	0.000751	3.00	1.00	-	-	-
GRISLI best fit.	GIndBvol	LGM	PI	TraCE-21ka	PDD$_{\triangle\sigma}$	BCON	7.01	0.067	$3.75 \cdot 10^{-5}$	-	2.52	1.00	-	0.1	-
	GMarBvol	LGM	PI	TraCE-21ka	PDD$_{\triangle\sigma}$	BMAR	5.99	0.033	$6.89 \cdot 10^{-5}$	0.011300	4.10	1.00	-	-	-
	GPDCBvol	LGM	PI	TraCE-21ka	PDD$_{\triangle\sigma}$	BPDC	5.99	0.040	$7.07 \cdot 10^{-5}$	0.001080	4.84	1.00	-	-	-
	GMarSBvol	LGM	PI	TraCE-21ka	PDD$_{\triangle\sigma}$	BMAR	5.10	0.070	$7.20 \cdot 10^{-5}$	0.012000	1.25	1.00	-	-	-
	GPDCSBvol	LGM	PI	TraCE-21ka	PDD$_{\triangle\sigma}$	BPDC	7.00	0.040	$2.48 \cdot 10^{-5}$	0.001400	2.86	1.00	-	-	-
GRISLI min. vol.	GIndMINvol	LGM	PI	TraCE-21ka	PDD$_{\triangle\sigma}$	BCON	4.76	0.092	$4.60 \cdot 10^{-5}$	-	5.50	1.00	-	0.1	-
	GMarMINvol	LGM	PI	TraCE-21ka	PDD$_{\triangle\sigma}$	BMAR	4.14	0.071	$1.90 \cdot 10^{-5}$	0.013300	5.48	1.00	-	-	-
	GPDCMINvol	LGM	PI	TraCE-21ka	PDD$_{\triangle\sigma}$	BPDC	5.07	0.090	$3.65 \cdot 10^{-5}$	0.001100	5.43	1.00	-	-	-
	GMarSMINvol	LGM	PI	TraCE-21ka	PDD$_{\triangle\sigma}$	BMAR	4.14	0.071	$1.90 \cdot 10^{-5}$	0.013300	5.48	1.00	-	-	-
	GPDCSMINvol	LGM	PI	TraCE-21ka	PDD$_{\triangle\sigma}$	BPDC	5.07	0.090	$3.65 \cdot 10^{-5}$	0.001100	5.43	1.00	-	-	-
GRISLI max. vol.	GIndMAXvol	LGM	PI	TraCE-21ka	PDD$_{\triangle\sigma}$	BCON	4.65	0.033	$8.00 \cdot 10^{-5}$	-	1.40	1.00	-	0.1	-
	GMarMAXvol	LGM	PI	TraCE-21ka	PDD$_{\triangle\sigma}$	BMAR	5.00	0.040	$5.20 \cdot 10^{-5}$	0.0000600	1.39	1.00	-	-	-
	GPDCMAXvol	LGM	PI	TraCE-21ka	PDD$_{\triangle\sigma}$	BPDC	6.37	0.030	$5.72 \cdot 10^{-5}$	0.001020	1.11	1.00	-	-	-
	GMarSMAXvol	LGM	PI	TraCE-21ka	PDD$_{\triangle\sigma}$	BMAR	4.80	0.040	$8.70 \cdot 10^{-5}$	0.003300	1.00	1.00	-	-	-
	GPDCSMAXvol	LGM	PI	TraCE-21ka	PDD$_{\triangle\sigma}$	BPDC	5.07	0.090	$3.65 \cdot 10^{-5}$	0.001100	5.43	1.00	-	-	-
PSU "best fit".	PMarBvol	LGM	PI	TraCE-21ka(c)	PDD$_{\sigma}$	BMAR	5.10	0.070	-	0.011300	10.00	3.00	6.5	-	60
	PIndBvol	LGM	PI	TraCE-21ka(c)	PDD$_{\sigma}$	BCON	7.01	0.067	-	-	10.00	3.00	6.5	0.1	60
	PPDCBvol	LGM	PI	TraCE-21ka(c)	PDD$_{\sigma}$	BMAR	5.99	0.040	-	0.001080	10.00	3.00	6.5	-	60
	PMarBvol$_b$	LGM	PI	TraCE-21ka	PDD$_{\triangle\sigma}$	BMAR	5.10	0.070	-	0.011300	10.00	3.00	-	-	60
	PMarBvol$_a$	LGM	PI	TraCE-21ka	PDD$_{\sigma}$	BMAR	5.10	0.070	-	0.011300	10.00	3.00	6.5	-	60
PSU reference.	PMarRef	LGM	PI	TraCE-21ka(c)	PDD$_{\sigma}$	BMAR	5.00	0.050	-	0.006520	10.00	3.00	6.5	-	60
	PIndRef	LGM	PI	TraCE-21ka(c)	PDD$_{\sigma}$	BCON	5.00	0.050	-	-	10.00	3.00	6.5	0.1	60
	PPDCRef	LGM	PI	TraCE-21ka(c)	PDD$_{\sigma}$	BMAR	5.00	0.050	-	0.000751	10.00	3.00	6.5	-	60
Half calving.	PMarRef$_{cal}$	LGM	PI	TraCE-21ka(c)	PDD$_{\triangle\sigma}$	BMAR	5.00	0.050	-	0.006520	10.00	3.00	-	-	30
No Schoof GL.	PMarRef$_{GL}$	LGM	PI	TraCE-21ka(c)	PDD$_{\sigma}$	BMAR	5.00	0.050	-	0.006520	10.00	3.00	6.5	-	60

Table 3.1: List of all the GRISLI and PSU simulations analyzed. The notation TraCE-21ka(c) in the "Index" column indicates the corrected TraCE-21ka index, see Section 3.4.

DISCUSSION

In this chapter, the model-data comparison is discussed. In the first section, the post-LGM Global Eustatic Sea Level estimated from Ice Sheet Models simulations is analyzed and compared with coral reef data. In the second section, *palaeo*-observations and simulations are compared in the context of Storfjorden ice stream dynamics history.

4.1 Estimating the post-LGM Global Eustatic Sea Level

In Sections 3.3, 3.4 the EIS total ice volume evolution throughout the deglaciation is compared with ICE-5G ice volume curve in order to identify best fit simulations from LHS ensembles GIND, GMAR, GPDC, GMARS and GPDCS. However, ICE-5G reconstruction is based on a global glacial isostatic adjustment model (Peltier 2004). Therefore, to test GRISLI/PSU simulations against ICE-5G reconstruction cannot be considered as a direct model-data comparison. In this study, a different approach is proposed in order to link GRISLI/PSU simulated ice volume with observational data. In fact, the global Eustatic Sea Level (ESL) throughout the last deglaciation is estimated from GRISLI/PSU-simulated EIS ice volume evolution and compared with those inferred from coral reef data (Peltier & Fairbanks 2006, Fairbanks 1989, Lambeck & Chappell 2001, Fleming et al. 1998 and Spratt & Lisiecki 2016). ESL is estimated from GRISLI/PSU simulations between 21-10 ka BPevery 1 ka as follows;

- at each time slice, the discrepancy between GRISLI/PSU and ICE-5G EIS total volume, denoted with $\triangle$EIS, is computed;
- at each time slice, the EIS discrepancy ($\triangle$EIS) is weighted over the ICE-5G EIS total volume, in order to compute the discrepancy per m SLE between ICE-5G and GRISLI/PSU, denoted with %EIS;
- at each time slice, the discrepancy per m SLE (%EIS) is applied to ICE-5G ice volume reconstructions of the other major ice sheets (obtaining $\mathrm{LIS}_{\mathsf{ISM}}$, $\mathrm{GIS}_{\mathsf{ISM}}$, $\mathrm{AIS}_{\mathsf{ISM}}$) and glaciers/ice caps (obtaining $\mathrm{Other}_{\mathsf{ISM}}$). In such a way, the GRISLI/PSU-based ESL $\mathsf{ESL}_{\mathsf{ISM}}$ is estimated,

$$\mathsf{ESL}_{\mathsf{ISM}} = -\left(\mathrm{LIS}_{\mathsf{ISM}} + \mathrm{GIS}_{\mathsf{ISM}} + \mathrm{AIS}_{\mathsf{ISM}} + \mathrm{EIS}_{\mathsf{ISM}} + \mathrm{Other}_{\mathsf{ISM}}\right) . \tag{4.1}$$

ESL is estimated from GRISLI and PSU simulations GIndBvol, PIndBvol, GMarSBvol, PMarBvol, GPDCSBvol and PPDCBvol (see Figures 4.1-4.3 and 4.4). Moreover, for GRISLI ensembles GIND, GMARS and GPDCS the simulations showing the best match with coral reef ESL data are identified and labeled with GIndBslr, GMarSBslr and GPDCSBslr (see Figures 4.1-4.3).

At LGM, GRISLI-ESL (around -145 m with respect to present-day level) is underestimated with respect to the lowest ESL proxy by slightly more than 20%, see Figures 4.1-4.3. In contrast, PSU-ESL is in good agreement with coral reef data, see Figure 4.4. In all GRISLI best-fit simulations GIndBvol, GMarSBvol, GPDCSBvol, GIndBslr, GMarSBslr and GPDCSBslr the ESL rise between 21-18 ka BPis abrupt with respect to coral reef data, and at 18 ka BPthe ESL is overestimated with respect to the highest ESL proxy (around -130 m with respect to present-day level) by less than 20%, see Figures

4.1-4.3. PSU simulations PIndBvol, PMarBvol and PPDCBvol show a good match with coral reef data both in terms of ESL magnitude at LGM (around -125 m with respect to present-day level) and slope of the sea level curve between 21-18 ka, see Figure 4.4. Between 18-15 ka, all GRISLI best fit simulations GIndBvol, GMarSBvol, GPDCSBvol, GIndBslr, GMarSBslr and GPDCSBslr and all PSU simulations PIndBvol, PMarBvol and PPDCBvol predict an ESL fall around 10 m which is not supported by coral reef data trend. At 15 ka, GRISLI-ESL (around -120 m with respect to present-day level) is underestimated by less than 10% with respect to the lowest ESL proxy, see Figures 4.1-4.3. the same time slice, PSU simulations PIndBvol, PMarBvol and PPDCBvol show a larger ESL underestimation around 15% with respect to the lowest ESL proxy, see Figure 4.4. Between 15-14 ka, an abrupt increase of the ESL is predicted by all GRISLI best fit simulations and PSU simulations, see Figures 4.1-4.4. The ESL rise predicted by GRISLI simulations ranges between 35-40 m, overestimating the ESL rise inferred from coral reef data, see Figures 4.1-4.3. A slightly higher ESL rise around 40-45 m is predicted by all PSU simulations between 15-14 ka, see Figure 4.4. However, the timing of such abrupt ESL rise is in agreement with MWP-1A timing. After 14 ka, there is a good match between GRISLI/PSU-ESL and those inferred from coral reef data, both in terms of ESL magnitude and slope of the sea level curve, see Figures 4.1-4.3. However, a large group of ESL coral reef data predict a lower sea level than those estimated by GRISLI/PSU simulations and ICE-5G reconstruction.

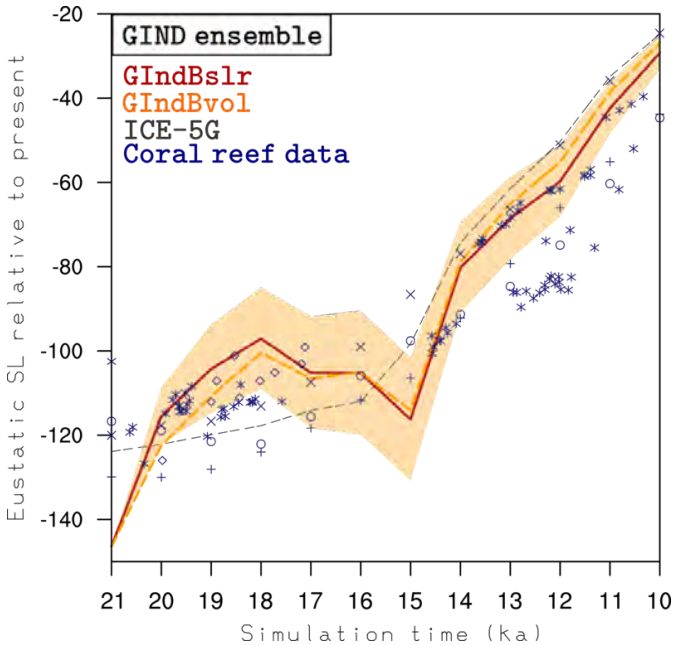

Figure 4.1: Global eustatic sea level with respect to PI between 21-10 ka BPcomputed from simulation GIndBslr (solid red) and GIndBvol (dashed yellow). In shaded red the uncertainty, computed from GIND ensemble standard deviation σ is shown. The dashed grey line is the ICE-5G global eustatic sea level rise curve. For comparison, sea level rise data from coral reef are shown with blue stars (Peltier & Fairbanks 2006), circles (Fairbanks 1989), crosses (Lambeck & Chappell 2001), diamonds (Fleming et al. 1998) and multiplication signs (Spratt & Lisiecki 2016).

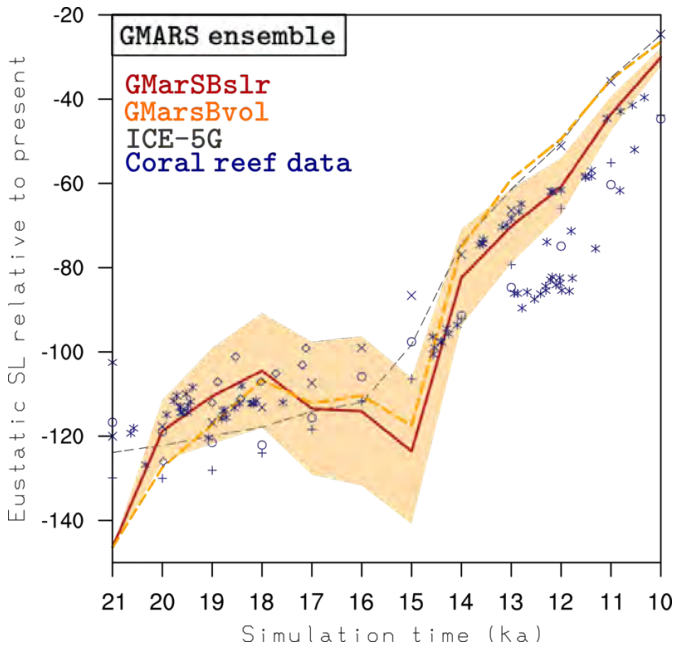

Figure 4.2: Global eustatic sea level with respect to PI between 21-10 ka BPcomputed from simulation GMarSBslr (solid red) and GMarSBvol (dashed yellow). In shaded red the uncertainty, computed from GMARS ensemble standard deviation σ is shown. The dashed grey line is the ICE-5G global eustatic sea level rise curve. For comparison, sea level rise data from coral reef are shown with blue stars (Peltier & Fairbanks 2006), circles (Fairbanks 1989), crosses (Lambeck & Chappell 2001), diamonds (Fleming et al. 1998) and multiplication signs (Spratt & Lisiecki 2016).

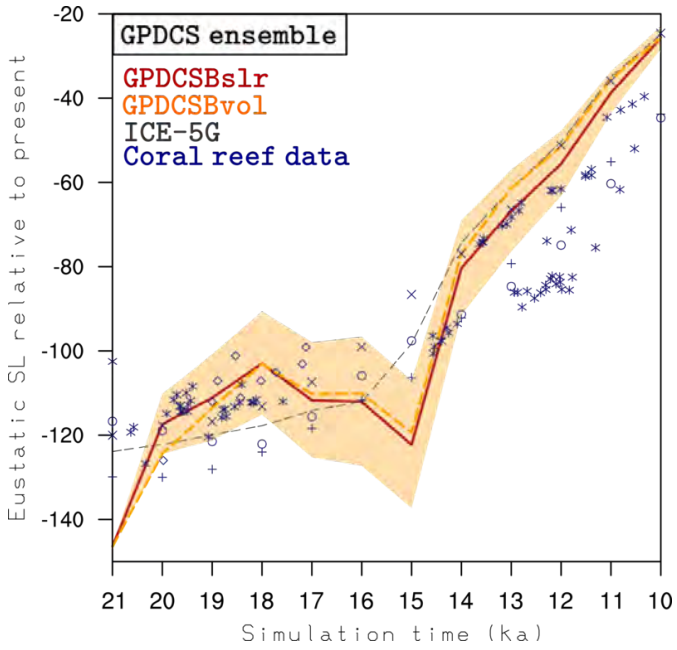

Figure 4.3: Global eustatic sea level with respect to PI between 21-10 ka BPcomputed from simulation GPDCSBslr (solid red) and GPDCSBslr (dashed yellow). In shaded red the uncertainty, computed from GPDCS ensemble standard deviation σ is shown. The dashed grey line is the ICE-5G global eustatic sea level rise curve. For comparison, sea level rise data from coral reef are shown with blue stars (Peltier & Fairbanks 2006), circles (Fairbanks 1989), crosses (Lambeck & Chappell 2001), diamonds (Fleming et al. 1998) and multiplication signs (Spratt & Lisiecki 2016).

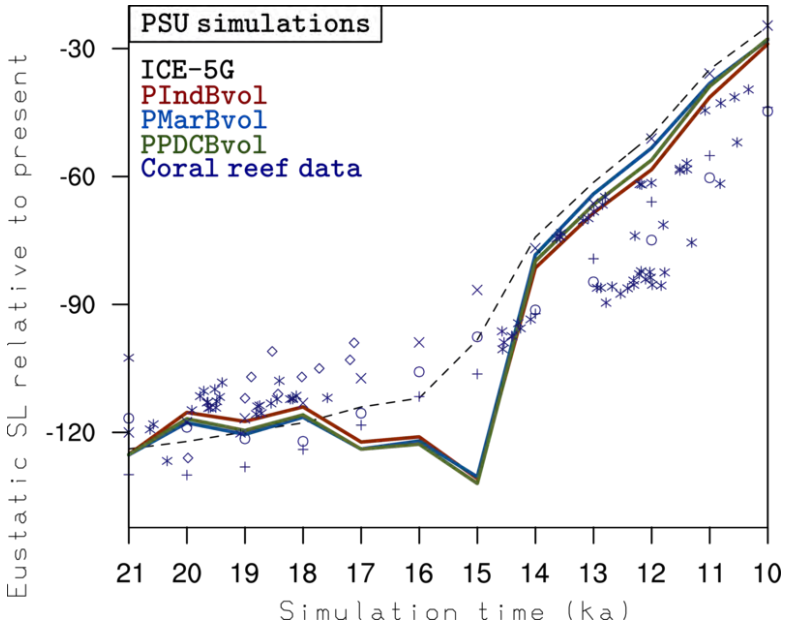

Figure 4.4: Global eustatic sea level with respect to PI between 21-10 ka BPcomputed from simulation PIndBvol (solid red), PMarBvol (solid blue) and PPDCBvol (solid green). The dashed grey line is the ICE-5G global eustatic sea level rise curve. For comparison, sea level rise data from coral reef are shown with blue stars (Peltier & Fairbanks 2006), circles (Fairbanks 1989), crosses (Lambeck & Chappell 2001), diamonds (Fleming et al. 1998) and multiplication signs (Spratt & Lisiecki 2016).

4.2 Dynamics History of Storfjorden *palaeo*-ice stream

As already pointed out in Section 2.1, in this study the simulated Storfjorden ice stream dynamics history throughout the deglaciation is compared with *palaeo*-data available from Storfjorden and Kveithola TMFs and troughs such as sediment cores, MSGLs and GZWs (see Subsection 1.3.3 for the description of *palaeo*-data used in this study).

First of all, the timing of simulated Storfjorden ice stream deglaciation is analyzed. In this analysis, Storfjorden ice stream is considered deglaciated when the simulated GL retreats from GRISLI/PSU grid node corresponding to the inner GZWs Limit according to Pedrosa et al. 2011, namely GZWs Limit 2 (GZWL2) in Figure 1.11b. GZWL2 is located around 120 km inland in Storfjorden Trough with respect to the continental slope, see 1.12a. In Figure 4.5, the GRISLI/PSU grid nodes selected for the analysis of Storfjorden ice stream and the GRISLI/PSU grid node corresponding to GZWL2 are shown. The timing of Storfjorden ice stream deglaciation for GRISLI LHS ensembles GInd, GMar and GPDC and PSU simulations PIndBvol, PMarBvol and PPDCBvol is shown in Figures 4.6, 4.7 and 4.8. The use of different basal melting parametrizations in GRISLI has a strong impact on the timing of the deglaciation of Storfjorden ice stream. In fact, the simulated deglaciation occurs between 11-9 ka BPin 71% of simulations in the ensemble GIND. As concerns the remnant 29% of simulations in the ensemble GIND, Storfjorden ice stream deglaciation occurs after 9 ka BPin all simulations except two simulations for which the deglaciation is dated 11.5 ka. However, for all the simulations in the ensemble GIND the deglaciation occurs after 12 ka BP(see Figure 4.6). GRISLI ensemble GMAR shows a completely different distribution of Storfjorden ice stream deglaciation timing. In fact, only in 25% of simulations in GMAR ensemble the

simulated deglaciation occurs between 11-9 ka. For all simulations except two in the remnant 75% the Storfjorden ice stream deglaciation occurs before 11 ka. More generally, Storfjorden ice stream deglaciation occurs before 14 ka BPin 64% of simulations in GMAR ensemble (see Figure 4.7). Such early deglaciation timing is directly linked to the linear relationship relating the basal melting rate and the ice-ocean heat flux in BMAR parametrization, which allows for a high basal melting rate under the "mild" ocean conditions between 18 and 14 ka. As concerns GPDC ensemble, the distribution of Storfjorden ice stream deglaciation timing is more similar to GIND ensemble. In fact, the simulated Storfjorden ice stream deglaciation occurs between 11-9 ka BPin 72% of simulations in GPDC ensemble. The delayed deglaciation timing with respect to ensemble GMAR can be explained by the quadratic relationship linking the basal melting rate and the ice-ocean heat flux in BPDC parametrization, which allows for a high basal melting rate only under the "warm" ocean conditions after 14 ka. However, the deglaciation timing distribution of the remnant 28% simulations is completely different from those of GIND ensemble. In fact, Storfjorden ice stream deglaciation occurs after 9 and 12 ka BPonly in the 5% and 12% of simulations, respectively. In contrast, in the remaining 16% of simulations in GPDC ensemble the deglaciation occurs before 14 ka BP(see Figure 4.8). Sedimentary facies analysis of sediment cores from Storfjorden and Kveithola TMFs suggests that the deglaciation of Storfjorden ice stream might have taken place in the time frame 11-9 ka, Lucchi et al. 2013. Therefore, GRISLI simulation ensemble employing ocean basal melting parametrization BPDC is in a good agreement with the deglaciation timing suggested by sediment cores analysis see Figure 4.8). Conversely, GRISLI simulation ensemble employing BMar parametrization shows a bad match with *palaeo*-data in terms of deglaciation timing see Figure 4.7). It is interesting to notice that also GRISLI simulation ensemble GIND shows a good agreement with deglaciation timing suggested by sediment cores analysis see Figure 4.6).

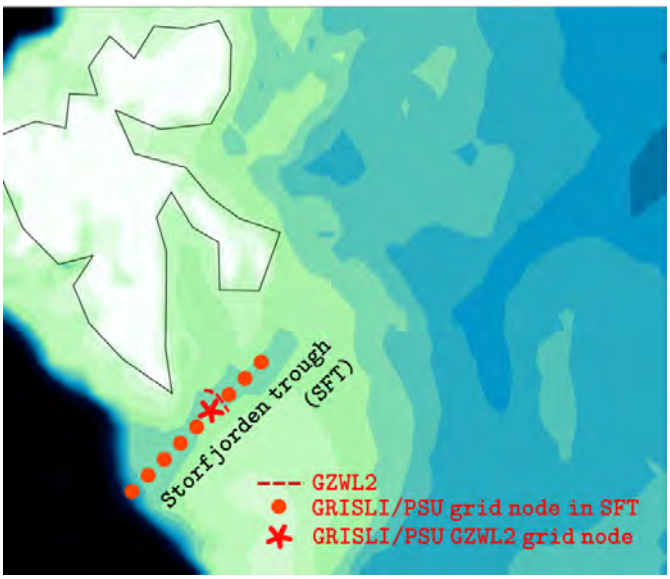

Figure 4.5: 20 km × 20 km bathymetric map of Storfjorden glacial system area. The GRISLI/PSU grid points selected to analyze Storfjorden ice stream dynamics are identified with full circles, whereas the GRISLI/PSU grid node corresponding to the GZWs Limit 2 (GZWL2, see Figure 1.11b, Pedrosa et al. 2011) is marked with a red star. GZWL2 position is shown in dashed red.

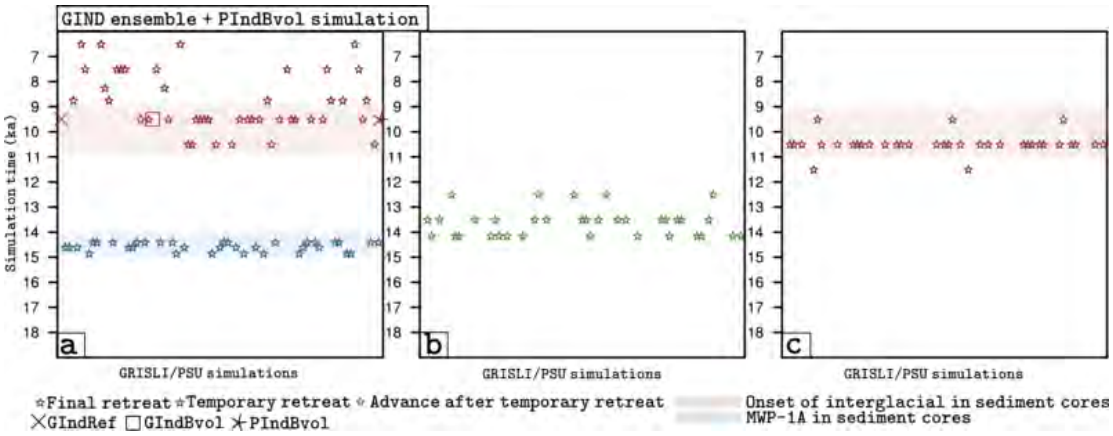

Figure 4.6: (a) Timing of Storfjorden ice stream retreat from GZWL2 (y-axis) for each GRISLI simulation belonging to ensemble GIND and PSU simulation PIndRef (x-axis). If the ice stream retreat is not followed by an advance, the corresponding timing is marked in red, whereas if the ice stream retreat is followed by an advance the corresponding timing is marked in blue. (b) Timing of Storfjorden ice stream re-advance in GZWL2 (y-axis) for GRISLI/PSU simulations showing a temporary retreat from GZWL2 in (a). (c) Timing of final Storfjorden ice stream retreat from GZWL2 (y-axis) GRISLI/PSU simulations showing a temporary retreat from GZWL2 in (a). Simulations GIndRef, GIndBvol and PIndRef are marked with a cross, empty square and star respectively.

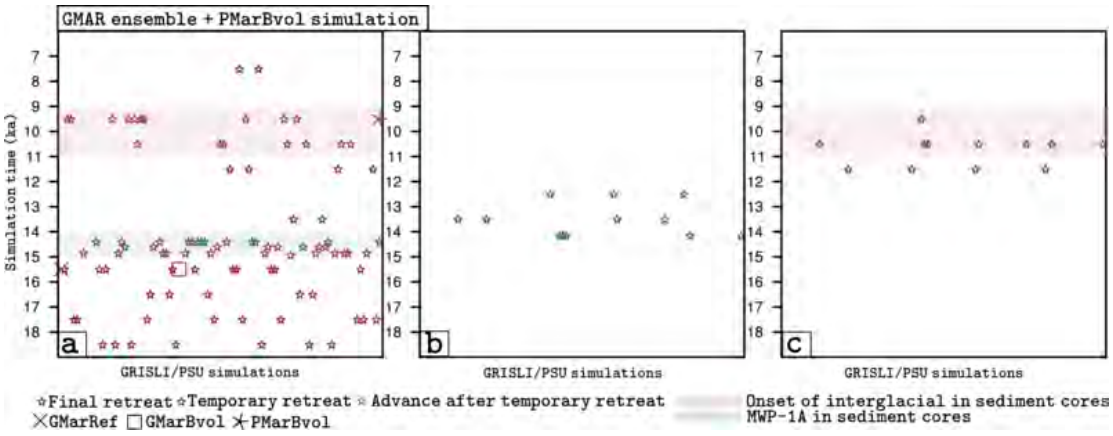

Figure 4.7: (a) Timing of Storfjorden ice stream retreat from GZWL2 (y-axis) for each GRISLI simulation belonging to ensemble GMAR and PSU simulation PMarRef (x-axis). If the ice stream retreat is not followed by an advance, the corresponding timing is marked in red, whereas if the ice stream retreat is followed by an advance the corresponding timing is marked in blue. (b) Timing of Storfjorden ice stream re-advance in GZWL2 (y-axis) for GRISLI/PSU simulations showing a temporary retreat from GZWL2 in (a). (c) Timing of final Storfjorden ice stream retreat from GZWL2 (y-axis) GRISLI/PSU simulations showing a temporary retreat from GZWL2 in (a). Simulations GMarRef, GMarBvol and PMarRef are marked with a cross, empty square and star respectively.

In fact, since ocean basal melting is low for all simulations in GIND ensemble, Storfjorden ice stream deglaciation is driven mainly by atmospheric forcing. The good match with Lucchi et al. 2013 data in terms of deglaciation timing suggests that atmospheric forcing could have played a major role in the Storfjorden ice stream retreat. As concerns PSU simulations PIndBvol, PMarBvol and PPDCBvol, a good agreement with *palaeo*-data is shown in terms of Storfjorden ice stream deglaciation timing. In fact, in simulations PIndBvol, PMarBvol and PPDCBvol the deglaciation occurs between 10-9, 10-9 and 11-10 ka, respectively (see Figures 4.6, 4.7 and 4.8). It is also interesting to notice that several simulations in GRISLI ensembles GInd (44%), GMar (31%) and GPDC (53%) show GL retreat from GZWL2 grid node between 15-14 ka.

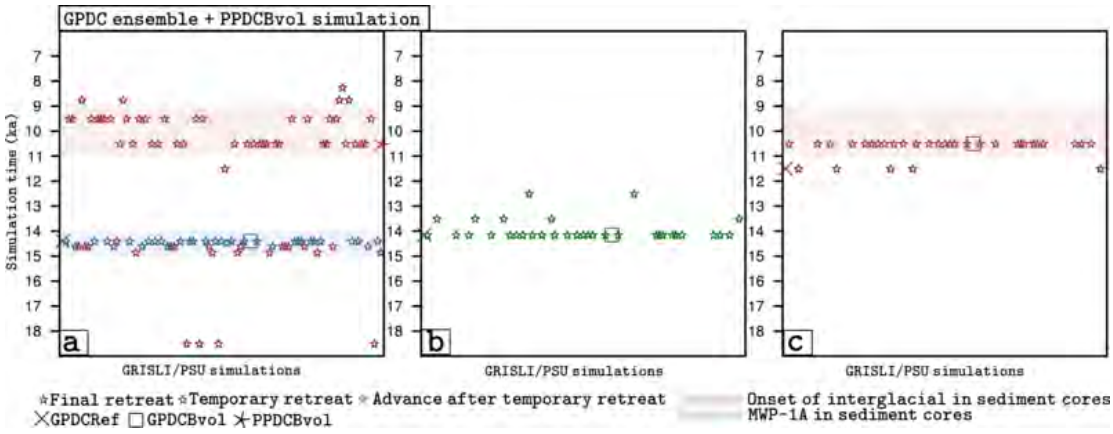

Figure 4.8: (a) Timing of Storfjorden ice stream retreat from GZWL2 (y-axis) for each GRISLI simulation belonging to ensemble GPDC and PSU simulation PPDCRef (x-axis). If the ice stream retreat is not followed by an advance, the corresponding timing is marked in red, whereas if the ice stream retreat is followed by an advance the corresponding timing is marked in blue. (b) Timing of Storfjorden ice stream re-advance in GZWL2 (y-axis) for GRISLI/PSU simulations showing a temporary retreat from GZWL2 in (a). (c) Timing of final Storfjorden ice stream retreat from GZWL2 (y-axis) GRISLI/PSU simulations showing a temporary retreat from GZWL2 in (a). Simulations GPDCRef, GPDCBvol and PPDCRef are marked with a cross, empty square and star respectively.

In some simulations such retreat is only temporary and it is followed by a readvance within 2 ka, which is in turn followed by the ice stream deglaciation within few ka. In particular, in GRISLI ensembles GInd, GMar and GPDC the 15-14 ka BPretreat is followed by a readvance in 100%, 35% and 66% of simulations, respectively. Such simulated GL temporary retreat in simulations from GInd and GPDC ensembles is in agreement with sedimentary facies analysis of sediment cores from Storfjorden and Kveithola TMFs, suggesting that in correspondance of MWP-1A event Storfjorden ice stream experienced rapid melting and retreat (Lucchi et al. 2013). In order to identify the main drivers of Storfjorden ice stream retreat between 15-14 ka, the lateral profile of the ice stream in simulations GIndBvol and GPDCBvol is analyzed in Figures 4.9 and 4.10 respectively. In simulation GIndBvol, the sudden sea level rise at 14.6 ka BPcauses the ice at the GL to start floating, thus leading to GL retreat to GZWL2 grid node. A thin ice shelf forms, likely due to the high, basal drag-free ice shelf velocities. At 14.5 ka BPthe ice shelf extent is reduced, most likely by calving at the front. After 14.5 ka, sea level slowly drops and the Storfjorden ice stream profile remains essentially unchanged, with no further GL retreats or advances. However, such stable ice stream/shelf configuration results from the low ocean basal melting rate set to 0.1 m/yr. In fact, an higher GL dynamics is observed in simulation GPDCBvol. As in simulation GIndBvol, the sudden sea level rise is the trigger for a first GL retreat to GZWL2 grid node. However, ocean basal melting reduces the extent of the ice shelf forming at 14.6 ka BPwith respect to simulation GIndBvol. Further ocean basal melting reduces the ice shelf thickness between 14.5-14.2 ka, causing the ice at the GL to start floating and thus leading to a further GL retreat at 14.2 ka. In contrast, due to the relatively lower sea level at 14.1 ka, the GL advances and the ice returns grounded in GZWL2 grid node. In PSU simulations PIndBvol, PMarBvol and PPDCBvol the GL thickness is two times higher than in GRISLI simulations at 15 ka BP (around 800 m, see Figure 4.11). Therefore, GL stability is not affected by the sea level rise betweeen 15-14 ka, although a GL thinning is observed at 14 ka.

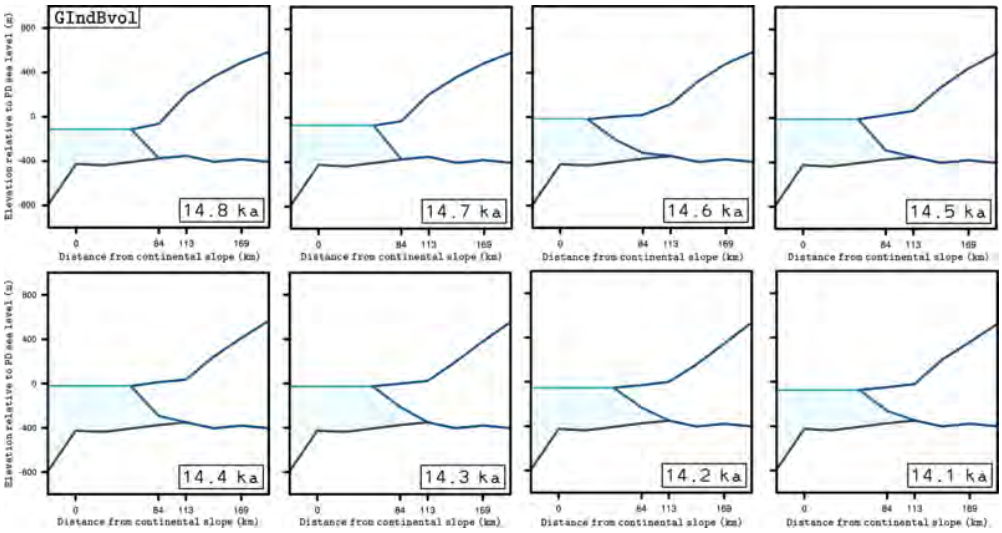

Figure 4.9: Lateral section of Storfjorden ice stream at eight selected time slices (14.8, 14.7, 14.6, 14.5, 14.4, 14.3, 14.2, 14.1 ka) for simulation GIndBvol. The GRISLI grid nodes shown in this profile are the same as in Figure 4.5. Notice that the the sea level is relative to PD.

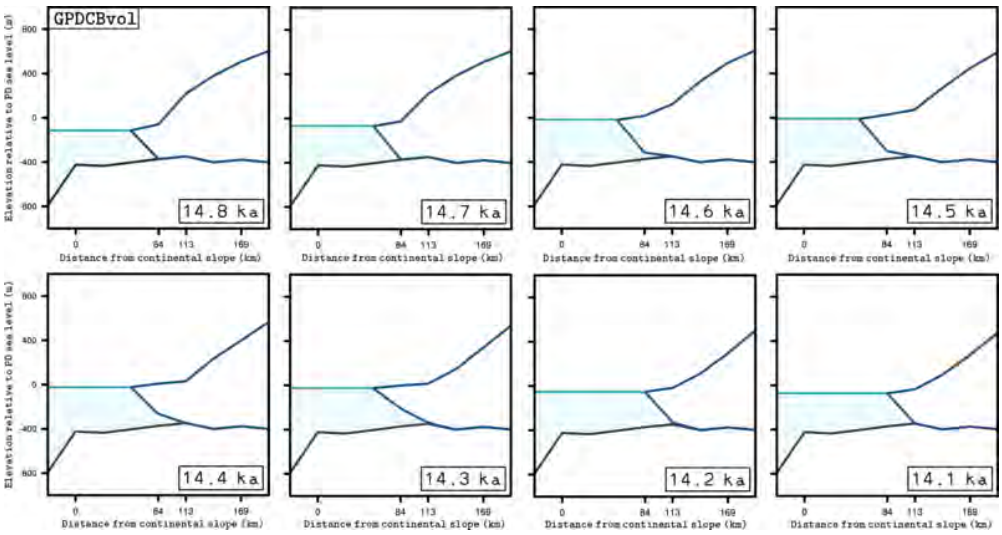

Figure 4.10: Lateral section of Storfjorden ice stream at eight selected time slices (14.8, 14.7, 14.6, 14.5, 14.4, 14.3, 14.2, 14.1 ka) for simulation GPDCBvol. The GRISLI grid nodes shown in this profile are the same as in Figure 4.5. Notice that the the sea level is relative to PD.

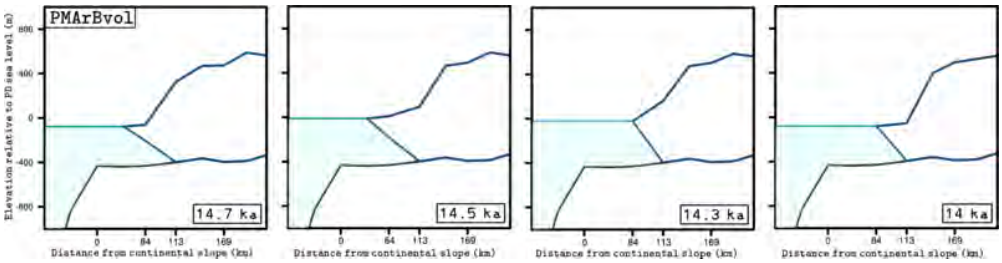

Figure 4.11: Lateral section of Storfjorden ice stream at four selected time slices (14.7, 14.5, 14.3, 14 ka) for simulation PMarBvol. The PSU grid nodes shown in this profile are the closest to GRISLI grid nodes in Figure 4.5. Notice that the the sea level is relative to PD.

In order to estimate the GZWs formation in Storfjorden trough during the ice stream retreat, a sediment flux of deforming subglacial sediments at the GL of 200 m^3/yr per m of ice stream width is assumed (Dowdeswell et al. 2004, Engelhardt & Kamb 1997). In Figures 4.12, 4.13 and 4.14 the estimated GZWs accumulation in Storfjorden trough for GRISLI simulations GIndBvol, GMarBvol and GPDCBvol, respectively is shown. The three simulations agree on the GZWs position, located at 84 and 113 km from the continental slope, respectively. This is in excellent agreement with the GZWs Limit 1 and 2 positions, see Figures 1.11b (Pedrosa et al. 2011) and 1.11a (Lucchi et al. 2013). Due to the major residence time of Storfjorden ice stream in Storfjorden trough, larger GZWs thickness (between 100-200 m) is estimated in simulations GIndBvol and GPDCBvol, whereas at the end of simulation GMarBvol the estimated thickness of the GZWs is lower than 100 m. In PSU simulations PIndBvol, PMarBvol and PPDCBvol the GZWs accumulation is concentrated on one single grid node rather than in two grid nodes as for GRISLI best fit simulations. In particular, a 200 m thick GZW accumulates at the PSU grid node corresponding to the GZWs Limit 2 (*i.e.*, 130 km from the continental slope), as shown in Figure 4.15. In contrast, at the end of simulation $\text{PMarBvol}_{\text{GL}}$ (for which the GL migration parametrization by Schoof 2007 is not used) two distinct GZWs form. The GZWs thickness is similar to those in GIndBvol and GPDCBvol simulations, whereas their position is shifted inland by one PSU grid node with respect to GZWs limit 1 and 2. However, the difference in terms of Storfjorden ice stream residence time in the inner trough between PSU simulations PMarBvol and $\text{PMarBvol}_{\text{GL}}$ testifies the strong impact exerted by the Schoof 2007 GL migration parametrization on the ice stream retreat throughout the deglaciation.

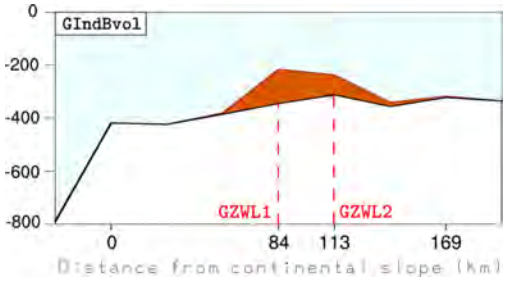

Figure 4.12: GZWs accumulation (brown) in Storfjorden trough at the end of simulation GIndBvol. The GRISLI grid nodes shown in this profile are the same as in Figure 4.5. GZWs Limit 1 and 2 from Pedrosa et al. 2011 (see Figure 1.11c) are marked in red.

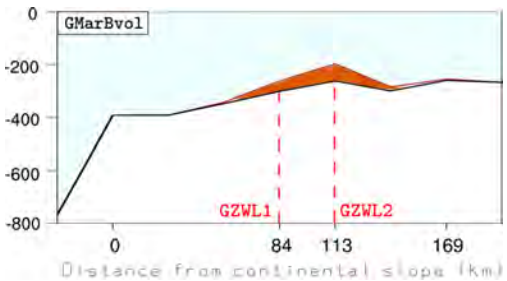

Figure 4.13: GZWs accumulation (brown) in Storfjorden trough at the end of simulation GMarBvol. The GRISLI grid nodes shown in this profile are the same as in Figure 4.5. GZWs Limit 1 and 2 from Pedrosa et al. 2011 (see Figure 1.11c) are marked in red.

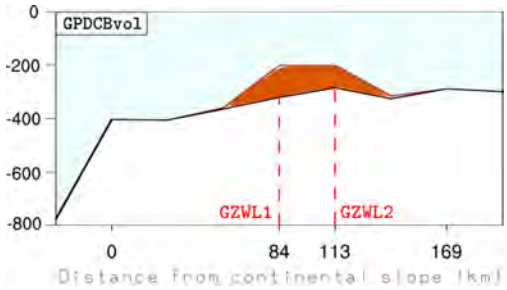

Figure 4.14: GZWs accumulation (brown) in Storfjorden trough at the end of simulation GPDCBvol. The GRISLI grid nodes shown in this profile are the same as in Figure 4.5. GZWs Limit 1 and 2 from Pedrosa et al. 2011 (see Figure 1.11c) are marked in red.

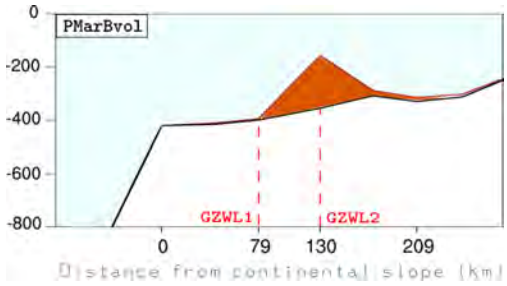

Figure 4.15: GZWs accumulation (brown) in Storfjorden trough at the end of simulation PMarBvol. The PSU grid nodes shown in this profile are the closest to GRISLI grid nodes in Figure 4.5. GZWs Limit 1 and 2 from Pedrosa et al. 2011 (see Figure 1.11c) are marked in red.

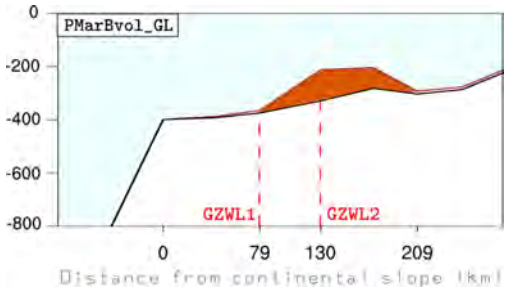

Figure 4.16: GZWs accumulation (brown) in Storfjorden trough at the end of simulation $\mathsf{PMarBvol}_{\mathsf{GL}}$. The PSU grid nodes shown in this profile are the closest to GRISLI grid nodes in Figure 4.5. GZWs Limit 1 and 2 from Pedrosa et al. 2011 (see Figure 1.11c) are marked in red.

Conclusions

In this study, the evolution of the Eurasian *palaeo*-Ice Sheet during the last deglaciation has been reconstructed with GRISLI and PSU numerical Ice Sheet Models. The Ice Sheet Models differ mainly in the ice stream parametrization and in the complexity with which Grounding Line migration is treated. A new approach has been adopted to modulate air temperature and precipitation fields throughout the deglaciation. Macro-regional indexes based on a transient climate simulation of the last 21 ka are used. Two different ocean basal melting parametrizations based on ice-ocean heat fluxes have been tested. Time-varying vertical profiles of ocean temperature and salinity have been employed to force the ocean basal melting parametrizations, in order to provide temporal and spatial variability of the basal melting rate under the ice shelves. A Latin Hypercube Sampling has been performed with GRISLI Ice Sheet Model, in order to explore the values range of five poorly constrained model parameters. Optimal model parameter values have been selected by identifying GRISLI simulations showing the best match with ICE-5G reconstruction in terms of simulated ice volume evolution throughout the deglaciation. With PSU Ice Sheet Model, an inverse-type approach has been adopted in order to match PSU simulations results with ICE-5G reconstruction. Finally, the sensitivity of the PSU Ice Sheet Model to calving rate and Grounding Line migration treating has been tested. The main conclusions resulting from this study are the following:

- **What component of the climate-ice sheet system primarily drives the simulated Eurasian *palaeo*-Ice Sheet last deglaciation both in its marine and terrestrial portion?**

  In GRISLI Ice Sheet Model, a major control on the deglaciation of the terrestrially-based Scandinavian *palaeo*-Ice Sheet is exerted by the ice stream dynamics. In fact, simulated ice streams in GRISLI cover almost all the British/Irish *palaeo*-Ice Sheet and the southern Scandinavian *palaeo*-Ice Sheet, thus enhancing the transport of ice to ice sheet margins. This leads to rapid decay of the British-Irish *palaeo*-Ice Sheet and to significant retreat of the southern Scandinavian *palaeo*-Ice Sheet in the first simulated 2 ka, despite the climate forcing is close to Last Glacial Maximum conditions. Ocean basal melting and ice stream dynamics in GRISLI Ice Sheet Model have a strong control on the decay of marine-based Svalbard/Barents/Kara Sea Ice Sheet. The simulated Bjørnøyrenna ice stream plays a crucial role in discharging ice from the inner part of the ice sheet. Moreover, the use of ocean basal melting parametrizations based on ice-ocean heat fluxes has a strong impact the ice sheet decay. Amongst all the GRISLI parameter tested with the Latin Hypercube Sampling, the SIA-enhancement factor has the strongest control on the Eurasian *palaeo*-ice sheets deglaciation. As concerns PSU Ice Sheet Model, the Scandinavian *palaeo*-Ice Sheet decay is mainly controlled by the climate forcing rather than by the ice stream dynamics as in GRISLI. In fact, simulated ice streams in PSU are restricted to the margin of the ice sheet. Also in the marine-based Svalbard/Barents/Kara Sea *palaeo*-Ice Sheet the ice stream dynamics play a minor role in PSU than in GRISLI. Moreover, the strongest control on the Svalbard/Barents/Kara Sea *palaeo*-Ice Sheet decay is exerted by Grounding Line migration rather than by ocean basal melting.

- **To what extent do the different parametrization of ice stream dynamics and Grounding Line migration in the Ice Sheet Models impacts the simulated deglaciation of the Eurasian *palaeo*-Ice Sheet?**

  The different treatment of ice stream and Grounding Line migration dynamics in PSU Ice Sheet Model with respect to GRISLI Ice Sheet Model has a profound effect on the simulated deglaciation of the Eurasian *palaeo*-Ice Sheet. In fact, the extent of simulated ice streams in PSU is considerably reduced with respect to GRISLI, leading to lower ice sheet velocities and consequently to less ice discharge via fast-flowing areas. Under such condition of reduced ice dynamics in PSU the climate forcing plays a major role in modulating the deglaciation of the Eurasian *palaeo*-Ice Sheet, in particular in its terrestrial-based portion. The use in PSU Ice Sheet Model of a more advanced Grounding Line migration parametrization has a strong effect on the marine-based Svalbard/Barents/Kara Sea *palaeo*-Ice Sheet decay. In fact, in PSU the Grounding Line dynamics plays a primary role with respect to ocean basal melting, whereas in GRISLI ocean basal melting exerted the strongest control on the marine-based portion of the Eurasian *palaeo*-Ice Sheet. As concerns the Storfjorden ice stream, the reduced ice stream dynamics in PSU results in higher Grounding Line thickness. As a consequence, the sudden sea level rise during the Meltwater Pulse-1A does not trigger the rapid ice stream retreat observed in GRISLI simulations.

- **To what extent do the use of different ocean basal melting parametrizations in the Ice Sheet Models impacts the simulated deglaciation of the marine-based Svalbard/Barents/Kara Sea *palaeo*-Ice Sheet and the Storfjorden ice stream retreat?**

  In the GRISLI Ice Sheet Model, the use of ocean basal melting parametrizations based on ice-ocean heat fluxes and forced with time-varying vertical profiles of ocean temperature and salinity has a strong impact on the deglaciation of the Svalbard/Barents/Kara Sea *palaeo*-Ice Sheet and on the Storfjorden ice stream retreat. Compared to a simple single-valued and constant in time ocean basal melting rate, the use of ice-ocean heat fluxes parametrizations results in a more rapid Svalbard/Barents/Kara Sea *palaeo*-Ice Sheet decay and therefore in a more rapid total Eurasian *palaeo*-Ice Sheet ice volume loss throughout the deglaciation. Also the retreat of Storfjorden ice stream is much more rapid in GRISLI simulations employing ocean basal melting parametrizations based on ice-ocean heat fluxes than in those using the single-valued and constant in time ocean basal melting rate. Differently from GRISLI, in PSU Ice Sheet Model the use of different ocean basal parametrizations does not affect neither the Eurasian *palaeo*-Ice Sheet decay, nor the Storfjorden ice stream retreat, due to the major role exerted by Grounding Line migration and calving in regulating the decay of the marine-based portion of the ice sheet.

- **Is the simulated Eurasian *palaeo*-Ice Sheet evolution during the last deglaciation in agreement with the observations in terms of ice sheet volume and extent through time?**

  GRISLI simulations are in good agreement with the ICE-5G reconstruction in

terms of total Eurasian *palaeo*-Ice Sheet ice volume evolution throughout the deglaciation, although in the first 3 ka the ice volume loss simulated with GRISLI is higher than those predicted by ICE-5G reconstruction. However, after 18 ka BP GRISLI and ICE-5G total Eurasian *palaeo*-Ice Sheet ice volume curves are comparable in terms of slope and magnitude. In GRISLI simulations a peak in ice volume loss occurs between 15 and 14 ka BP in response to the Bølling-Allerød warm period, whereas in ICE-5G reconstruction the ice volume loss peak occurs earlier between 16 and 15 ka BP. PSU simulations are in good agreement with ICE-5G reconstruction in terms of total Eurasian *palaeo*-Ice Sheet ice volume evolution throughout the deglaciation, in particular between 21 and 18 ka BP. As in GRISLI simulations, the peak in total ice volume loss occurs in PSU simulations between 15 and 14 ka BP. Although the slope of PSU and ICE-5G total Eurasian *palaeo*-Ice Sheet ice volume curves are comparable after 14 ka BP, the total ice sheet volume is constantly overestimated in PSU simulations with respect to ICE-5G reconstruction. In terms of ice sheet extent evolution throughout the deglaciation, there are large discrepancies between GRISLI simulations and DATED-1 reconstruction, in particular in the southern Scandinavian *palaeo*-Ice Sheet and in the eastern Svalbard/Barents/Kara Sea *palaeo*-Ice Sheet. In the southern Scandinavian *palaeo*-Ice Sheet, the overestimation of the ice stream extent leads the British/Irish *palaeo*-Ice Sheet to decay and the southern Scandinavian *palaeo*-Ice Sheet to retreat earlier than in DATED-1 reconstruction. The simulated decay of the Scandinavian *palaeo*-Ice Sheet occurs in GRISLI simulations around 13-12 ka BP, 2 ka earlier than in DATED-1 reconstruction. Moreover, due to the combination of modest ice velocities and cold air temperatures, the eastern margin of the Svalbard/Barents/Kara Sea *palaeo*-Ice Sheet does not show the westward migration throughout the deglaciation depicted in DATED-1 reconstruction. As a consequence, the decay of the Svalbard/Barents/Kara Sea *palaeo*-Ice Sheet in GRISLI simulations is delayed by few thousand years with respect to DATED-1 reconstruction. Also in PSU simulations the eastern margin of the Svalbard/Barents/Kara Sea *palaeo*-Ice Sheet does not migrate westward as in DATED-1 reconstruction, leading to an excess of ice cover in the south-eastern Barents Sea which is not entirely melted at 10 ka BP. However, the western, northern and central parts of Barents Sea are ice free between 12-10 ka BP, in agreement with DATED-1 reconstruction. There is also good agreement between PSU simulations and DATED-1 reconstruction as concerns the Scandinavian *palaeo*-Ice Sheet evolution and decay. Finally, global Eustatic Sea Level estimates based on GRISLI and PSU simulations show a good agreement with coral reef data after 15 ka BP. Between 15-14 ka BP an abrupt global Eustatic Sea Level Rise around 35-45 m is estimated, whereas between 14 and 10 ka BP a more gradual global Eustatic Sea Level Rise around 50-55 m is observed.

- **Is the simulated Storfjorden ice stream deglaciation in agreement with the field observations in terms of deglaciation timing and dynamics?**

  A large number (70%) of GRISLI simulations employing, respectively, the single-valued basal melting rate and the ice-ocean heat fluxes basal melting parametrization by Pollard & DeConto 2012 date the Storfjorden ice stream deglaciation be-

tween 11 and 9 ka BP, which is in excellent agreement with the timing of the onset of interglacial conditions inferred from sediment cores (Lucchi et al. 2013). In contrast, in a large number (64%) of GRISLI simulations employing the ice-ocean heat fluxes basal melting parametrization by Martin et al. 2011 the Storfjorden ice stream is deglaciated before 14 ka BP, which is not supported by any *palaeo*-data. Also PSU simulations are in agreement with sediment cores (Lucchi et al. 2013) in terms of Storfjorden ice stream deglaciation timing. Between 15 and 14 ka BP GRISLI simulations show Grounding Line retreat, initially triggered by a sudden sea level rise around 14.6 ka BP. This is in excellent agreement with sedimentary facies retrieved in sediment cores from Storfjorden and Kveithola Trough Mouth Fans and trough (Lucchi et al. 2013). In fact, during Meltwater Pulse-1A sedimentary facies associated with rapid ice stream melting and retreat is retrieved in several cores. Due to larger ice thickness at the Grounding Line, in PSU simulations the sudden sea level rise around 14.6 ka BP does not cause ice stream retreat. Finally, estimated position and thickness of Grounding Zone Wedges forming during Storfjorden ice stream retreat in GRISLI simulations are in excellent agreement with geophysical observations (Rebesco et al. 2011). Conversely, Grounding Zone Wedges forming during Storfjorden ice stream retreat in PSU simulations simulations do not show the same match with geophysical observations.

Future perspectives of this study

In this study, a new approach is undertaken to modulate the oscillation of atmospheric fields employed to force the Ice Sheet Models. Distinct macro-regional indexes for air temperature and precipitation derived from the transient climate simulation TraCE-21ka are used instead of the more common NGRIP δ18O-based index. Such TraCE-21ka-based indexes allow for a climatic variability depending not only on time but also on the macro-region and the specific climate field that is considered. However, number and location of the TraCE-21ka grid points selected to compute the atmospheric indexes are somehow arbitrary. A refinement of this method could allow for a better representation of the climate oscillation in the Eurasian region. However, TraCE-21ka transient simulation is performed with a global, coupled ocean-atmosphere-sea ice-land surface climate model. Therefore, this method could be adopted in other ice sheet simulatons during the last 21,000 years.

Two ocean basal melting parametrizations taken from the literature are tested with both the Ice Sheet Models employed in this study. Since both parametrizations are based on ice-ocean heat fluxes, ocean temperature and salinity need to be prescribed to compute the basal melting rate under the ice shelves. In this research, a new approach is proposed to force the ocean basal melting parametrizations with vertical profiles of ocean temperature and salinity varying in time and space (in the macro-regional sense as for the atmospheric indexes). The ocean temperature and salinity vertical profiles are computed from TraCE-21ka climate simulation, in a similar way as for the atmospheric indexes. Moreover, a new approach is followed to tune a poorly constrained model parameter which is included in both ocean basal melting parametrizations. The approach is based on present-day basal melting observations in Antarctica and on the TraCE-21ka ocean conditions used to force the parametrization. Also in this case the methodology presents aspects that could be refined, in order to obtain a more realistic distribution of the ocean basal melting rates over time and space. However, similarly as for the atmospheric indexes this method could be employed in other marine-based ice sheet simulatons of the last 21,000 years.

Another crucial aspect of this research is the model-data comparison, which is proposed both on a "global" scale (*i.e.*, by looking at the Eurasian *palaeo*-Ice Sheet as a whole) and on a "local" scale (*i.e.*, by looking at the Storfjorden ice stream retreat throughout the deglaciation). A new method to estimate the global Eustatic Sea Level evolution from the numerical Ice Sheet Models simulations is proposed. Although the method strongly depends on ICE-5G reconstruction of the ice sheets evolution in the last 21,000 years, it allows for a direct comparison between numerical reconstructions (*i.e.*, Ice Sheet Models simulations and ICE-5G reconstruction) and coral reef data in terms of global Eustatic Sea Level rise. In terms of ice sheet extent, a more direct comparison between Ice Sheet Models simulations and DATED-1 reconstruction is proposed.

As concerns Storfjorden ice stream, simulations and observations are compared in order to reconstruct the ice stream dynamics history throughout the deglaciation. The timing of simulated dynamic events such as the Storfjorden ice stream deglaciation and ice stream rapid retreat and melting during the Meltwater Pulse-1A are compared to the timing inferred from sediment cores from Storfjorden and Kveithola Trough Mouth Fans and troughs. The accumulation of Grounding Zone Wedges is estimated for Ice

Sheet Models simulations, based on the residence time of Storfjorden ice stream in Storfjorden trough. Position and thickness of the estimated Grounding Zone Wedges are then compared to geophysical reconstructions in Storfjorden trough. The model-data comparison that is proposed in this study could represent an important task to reconstruct the dynamics history in similar marine-based *palaeo*-ice streams. Nevertheless, in this study a *caveat* of such methodology is represented by the coarse resolution (around $20\,\mathrm{km} \times 20\,\mathrm{km}$) of the Ice Sheet Models that are employed. In fact, Storfjorden trough is 254 km long and 40 km wide in the inner continental shelf. Therefore, the use of Ice Sheet Models allowing for higher resolution is needed to provide a more realistic reconstruction of the dynamics history of Storfjorden and, possibly, Kveithola ice streams.

Moreover, this study highlights that the identification of ice stream areas is one of the most critical aspects in both Ice Sheet Models. A simple method to constrain ice streams position based on present-day topography is proposed in this work. Nevertheless, the use of Ice Sheet Models including a more realistic treating of ice streams can considerably improve the reliability of the numerical reconstructions. Other possible future developments of this research concern the parametrization in the Ice Sheet Models of processes acting at the geometric boundaries of the ice sheets. For instance, the use of more refined calving parametrizations, relating calving rates with ice shelves stress and velocity could have an important impact on the marine-based portion of the Eurasian *palaeo*-Ice Sheet. Another important task to carry out in future research is the inclusion in the Ice Sheet Models of a module accounting for sediment transport and deformation beneath the ice sheets.

Bibliography

Alley, K. E., Scambos, T. A., Siegfried, M. R., & Fricker, H. A. (2016). Impacts of warm water on Antarctic ice shelf stability through basal channel formation. *Nature Geoscience*, 9(4), 290–293.

Alvarez-Solas, J., Charbit, S., Ritz, C., Paillard, D., Ramstein, G., & Dumas, C. (2010). Links between ocean temperature and iceberg discharge during Heinrich events. *Nature Geoscience*, 3(2), 122–126.

Álvarez Solás, J., Montoya, M., Ritz, C., Ramstein, G., Charbit, S., Dumas, C., Nisancioglu, K., Dokken, T., & Ganopolski, A. (2011). Heinrich event 1: an example of dynamical ice-sheet reaction to oceanic changes. *Climate of the Past*, 7(4), 1297–1306.

Andersen, B. G., Lundqvist, J., & Saarnisto, M. (1995). The Younger Dryas margin of the Scandinavian ice sheet—an introduction. *Quaternary International*, 28, 145–146.

Bamber, J. L., Vaughan, D. G., & Joughin, I. (2000). Widespread complex flow in the interior of the Antarctic ice sheet. *Science*, 287(5456), 1248–1250.

Batchelor, C. & Dowdeswell, J. (2015). Ice-sheet grounding-zone wedges (GZWs) on high-latitude continental margins. *Marine Geology*, 363, 65–92.

Beckmann, A. & Goosse, H. (2003). A parameterization of ice shelf–ocean interaction for climate models. *Ocean modelling*, 5(2), 157–170.

Berger, A., Li, X., & Loutre, M.-F. (1999). Modelling northern hemisphere ice volume over the last 3Ma. *Quaternary Science Reviews*, 18(1), 1–11.

Birchfield, G., Weertman, J., & Lunde, A. T. (1981). A paleoclimate model of northern hemisphere ice sheets. *Quaternary Research*, 15(2), 126–142.

Bonelli, S., Charbit, S., Kageyama, M., Woillez, M.-N., Ramstein, G., Dumas, C., & Quiquet, A. (2009). Investigating the evolution of major Northern Hemisphere ice sheets during the last glacial-interglacial cycle. *Climate of the Past*, 5(3), 329–345.

Born, A., Kageyama, M., & Nisancioglu, K. (2010). Warm Nordic Seas delayed glacial inception in Scandinavia. *Climate of the Past*, 6(6), 817.

Braconnot, P., Harrison, S. P., Kageyama, M., Bartlein, P. J., Masson-Delmotte, V., Abe-Ouchi, A., Otto-Bliesner, B., & Zhao, Y. (2012). Evaluation of climate models using palaeoclimatic data. *Nature Climate Change*, 2(6), 417–424.

Cane, M. A. & Molnar, P. (2001). Closing of the Indonesian seaway as a precursor to east African aridification around 3–4 million years ago. *Nature*, 411(6834), 157–162.

Charbit, S., Ritz, C., Philippon, G., Peyaud, V., & Kageyama, M. (2007). Numerical reconstructions of the Northern Hemisphere ice sheets through the last glacial-interglacial cycle. *Climate of the Past*, 3(1), 15–37.

Charbit, S., Ritz, C., & Ramstein, G. (2002). Simulations of Northern Hemisphere ice-sheet retreat:: sensitivity to physical mechanisms involved during the Last Deglaciation. *Quaternary Science Reviews*, 21(1), 243–265.

Clark, C. D. (1993). Mega-scale glacial lineations and cross-cutting ice-flow landforms. *Earth surface processes and landforms*, 18(1), 1–29.

Clark, P., Dyke, A., Shakun, J., Carlson, A., Clark, J., W. B., Mitrovica, J., Hostetler, S., & McCabe, M. (2009). The last Glacial Maximum. *Science*, 325(5941), 710–714.

Clason, C. C., Applegate, P., & Holmlund, P. (2014). Modelling Late Weichselian evolution of the Eurasian ice sheets forced by surface meltwater-enhanced basal sliding. *Journal of Glaciology*, 60(219), 29–40.

Claussen, M. (2009). Late Quaternary vegetation-climate feedbacks. *Climate of the Past*, 5, 203–216.

Colleoni, F. et al. (2015). GRenoble Ice-Shelf and Land-Ice model: a practical user guide. *CMCC Research Paper*, (RP0249).

Colleoni, F., Quiquet, A., & Masina, S. (2016). *Long-term safety of a planned geological repository for spent nuclear fuel in Forsmark – Phase 2: Impact of ice sheet dynamics, climat forcing and multi-variate sensitivity analysis on maximum ice sheet thickness*. Technical Report SKB TR-14-21, Swedish Nuclear Fuel and Waste Management Co, Stockholm, Sweden.

Colleoni, F., Wekerle, C., & Masina, S. (2014). *Long-term safety of a planned geological repository for spent nuclear fuel in Forsmark – Phase 1: Estimate of maximum ice sheet thicknesses*. Technical Report SKB TR-14-21, Swedish Nuclear Fuel and Waste Management Co, Stockholm, Sweden.

Collins, W., Bitz, M., a. B. M. a. B. G., Bretherton, C., Carton, J., Chang, P., Doney, S., Hack, J., Henderson, T., Kiehl, J., Large, W., McKenna, D., Santer, B., & Smith, R. (2006). The Community Climate System Model Version 3 (CCSM3). *Journal of Climate*, 19(11), 2122–2143.

Cook, K. H. & Held, I. M. (1988). Stationary waves of the ice age climate. *Journal of climate*, 1(8), 807–819.

de Boer, B., Dolan, A., Bernales, J., Gasson, E., Golledge, N., Sutter, J., Huybrechts, P., Lohmann, G., Rogozhina, I., Abe-Ouchi, A., et al. (2015). Simulating the Antarctic ice sheet in the late-Pliocene warm period: PLISMIP-ANT, an ice-sheet model intercomparison project. *The Cryosphere*, 9, 881–903.

Denton, G. H. & Hughes, T. J. (1981). The Arctic ice sheet: an outrageous hypothesis. *The Last Great Ice Sheets. Wiley, New York*, (pp. 437–467).

Depoorter, M., Bamber, J., Griggs, J., Lenaerts, J., Ligtenberg, S., Van den Broeke, M., & Moholdt, G. (2013). Calving fluxes and basal melt rates of Antarctic ice shelves. *Nature*, 502(7469), 89–92.

Deser, C., Walsh, J. E., & Timlin, M. S. (2000). Arctic Sea Ice Variability in the Context of Recent Atmospheric Circulation Trends. *Journal of Climate*, 13(3), 617–633.

Dowdeswell, J., Cofaigh, C. Ó., & Pudsey, C. (2004). Continental slope morphology and sedimentary processes at the mouth of an Antarctic palaeo-ice stream. *Marine Geology*, 204(1), 203–214.

Dowdeswell, J. & Ottesen, D. (2013). Buried iceberg ploughmarks in the early Quaternary sediments of the central North Sea: a two-million year record of glacial influence from 3D seismic data. *Marine Geology*, 344, 1–9.

Dowdeswell, J. A. & Siegert, M. J. (1999). Ice-sheet numerical modeling and marine geophysical measurements of glacier-derived sedimentation on the Eurasian Arctic continental margins. *Geological Society of America Bulletin*, 111(7), 1080–1097.

Dufresne, J.-L., Foujols, M.-A., Denvil, S., Caubel, A., Marti, O., Aumont, O., Balkanski, Y., Bekki, S., Bellenger, H., Benshila, R., et al. (2013). Climate change projections using the IPSL-CM5 Earth System Model: from CMIP3 to CMIP5. *Climate Dynamics*, 40(9-10), 2123–2165.

Dumas, C. (2002). *Modélisation de l'évolution de l'Antarctique depuis le dernier cycle glaciaire-interglaciaire jusqu'au futur: importance relative des différents processus physiques et rôle des données d'entrée*. PhD thesis, Université Joseph-Fourier-Grenoble I.

Dyke, A. (2004). An outline of North American deglaciation with emphasis on central and northern Canada. *Developments in Quaternary Sciences*, 2, 373–424.

Eldrett, J. S., Harding, I. C., Wilson, P. A., Butler, E., & Roberts, A. P. (2007). Continental ice in Greenland during the Eocene and Oligocene. *Nature*, 446(7132), 176–179.

Elverhøi, A., Hooke, R. L., & Solheim, A. (1998). Lateo Cenozoic erosion and sediment yield from the Svalbard–Barents Sea region: Implications for understanding erosion of glacierized basins. *Quaternary Science Reviews*, 17(1), 209–241.

Engelhardt, H. & Kamb, B. (1997). Basal hydraulic system of a West Antarctic ice stream: constraints from borehole observations. *Journal of Glaciology*, 43(144), 207–230.

Epstein, S. & Mayeda, T. (1953). Variation of O18 content of waters from natural sources. *Geochimica et cosmochimica acta*, 4(5), 213–224.

Fairbanks, R. G. (1989). A 17, 000-year glacio-eustatic sea level record: influence of glacial melting rates on the Younger Dryas event and deep-ocean circulation. *Nature*, 342(6250), 637–642.

Fausto, R. S., Ahlstrøm, A. P., van As, D., & Steffen, K. (2011). Present-day temperature standard deviation parameterization for Greenland. *Journal of Glaciology*, 57(206), 1181–1183.

Feldmann, J. & Levermann, A. (2015). Collapse of the West Antarctic Ice Sheet after local destabilization of the Amundsen Basin. *Proceedings of the National Academy of Sciences*, 112(46), 14191–14196.

Fleming, K., Johnston, P., Zwartz, D., Yokoyama, Y., Lambeck, K., & Chappell, J. (1998). Refining the eustatic sea-level curve since the Last Glacial Maximum using far- and intermediate-field sites. *Earth and Planetary Science Letters*, 163(1–4), 327 – 342.

Francis, J., Ashworth, A., Cantrill, D., Crame, J., Howe, J., Stephens, R., Tosolini, A., Thorn, V., Cooper, A., Barrett, P., et al. (2008). Antarctica: A keystone in a changing world. In *Proceedings of the 10th International Symposium on Antarctic Earth Sciences* (pp. 19–27).

Ganopolski, A., Calov, R., & Claussen, M. (2010). Simulation of the last glacial cycle with a coupled climate ice-sheet model of intermediate complexity. *Climate of the Past*, 6(2), 229–244.

Giorgetta, M. A., Jungclaus, J., Reick, C. H., Legutke, S., Bader, J., Böttinger, M., Brovkin, V., Crueger, T., Esch, M., Fieg, K., et al. (2013). Climate and carbon cycle changes from 1850 to 2100 in MPI-ESM simulations for the Coupled Model Intercomparison Project phase 5. *Journal of Advances in Modeling Earth Systems*, 5(3), 572–597.

Golledge, N. R., Fogwill, C. J., Mackintosh, A. N., & Buckley, K. M. (2012). Dynamics of the last glacial maximum Antarctic ice-sheet and its response to ocean forcing. *Proceedings of the National Academy of Sciences*, 109(40), 16052–16056.

Golledge, N. R., Kowalewski, D. E., Naish, T. R., Levy, R. H., Fogwill, C. J., & Gasson, E. G. (2015). The multi-millennial Antarctic commitment to future sea-level rise. *Nature*, 526(7573), 421–425.

Greve, R. & Blatter, H. (2009). *Dynamics of ice sheets and glaciers*. Springer Science & Business Media.

He, F. (2011). Simulating transient climate evolution of the last deglaciation with CCSM3. *PhD thesis*.

Heinemann, M., Timmermann, A., Elison Timm, O., Saito, F., & Abe-Ouchi, A. (2014). Deglacial ice sheet meltdown: orbital pacemaking and CO 2 effects. *Climate of the Past*, 10(4), 1567–1579.

Hellmer, H. H., Kauker, F., Timmermann, R., Determann, J., & Rae, J. (2012). Twenty-first-century warming of a large Antarctic ice-shelf cavity by a redirected coastal current. *Nature*, 485(7397), 225–228.

Hibbert, F. D., Austin, W. E., Leng, M. J., & Gatliff, R. W. (2010). British Ice Sheet dynamics inferred from North Atlantic ice-rafted debris records spanning the last 175 000 years. *Journal of Quaternary Science*, 25(4), 461–482.

Holland, P., Jenkins, A., & Holland, D. (2008). The response of ice shelf basal melting to variations in ocean temperature. *Journal of Climate*, 21(11), 2558–2572.

Holmlund, P. & Fastook, J. (1995). A time dependent glaciological model of the Weichselian ice sheet. *Quaternary International*, 27, 53–58.

Hughes, A., Gyllencreutz, R., Lohne, O., Mangerud, J., & Svendsen, J. I. (2016). The last Eurasian ice sheets – a chronological database and time-slice reconstruction, DATED-1. *Boreas*, 45(1), 1–45.

Hutter, K. (1983). *Theoretical glaciology: material science of ice and the mechanics of glaciers and ice sheets*, volume 1. Springer.

ICAO, I. C. A. O. (2002). *Manual of the ICAO standard atmosphere [: extended to 80 kilometres (262 500 feet)*. ICAO.

Ingólfsson, Ó. & Landvik, J. Y. (2013). The Svalbard–Barents Sea ice-sheet – Historical, current and future perspectives. *Quaternary Science Reviews*, 64, 33–60.

Jakobsson, M., Mayer, L., Coakley, B., Dowdeswell, J. A., Forbes, S., Fridman, B., Hodnesdal, H., Noormets, R., Pedersen, R., Rebesco, M., et al. (2012). The international bathymetric chart of the Arctic Ocean (IBCAO) version 3.0. *Geophysical Research Letters*, 39(12).

Joos, F. & Spahni, R. (2008). Rates of change in natural and anthropogenic radiative forcing over the past 20,000 years. 105(5), 1425–1430.

Joughin, I. & Alley, R. B. (2011). Stability of the West Antarctic ice sheet in a warming world. *Nature Geoscience*, 4(8), 506–513.

Kageyama, M., Laîné, A., Abe-Ouchi, A., Braconnot, P., Cortijo, E., Crucifix, M., De Vernal, A., Guiot, J., Hewitt, C., Kitoh, A., et al. (2006). Last Glacial Maximum temperatures over the North Atlantic, Europe and western Siberia: a comparison between PMIP models, MARGO sea–surface temperatures and pollen-based reconstructions. *Quaternary Science Reviews*, 25(17), 2082–2102.

Keigwin, L. (1982). Isotopic paleoceanography of the Caribbean and East Pacific: role of Panama uplift in late Neogene time. *Science*, 217(4557), 350–353.

Kirchner, N., Hutter, K., Jakobsson, M., & Gyllencreutz, R. (2011). Capabilities and limitations of numerical ice sheet models: A discussion for Earth-scientists and modelers. *Quaternary Science Reviews*, 30(25-26), 3691–3704.

Kitamura, A. & Kawagoe, T. (2006). Eustatic sea-level change at the Mid-Pleistocene climate transition: new evidence from the shallow-marine sediment record of Japan. *Quaternary Science Reviews*, 25(3), 323–335.

Knies, J., Matthiessen, J., Vogt, C., Laberg, J. S., Hjelstuen, B. O., Smelror, M., Larsen, E., Andreassen, K., Eidvin, T., & Vorren, T. O. (2009). The Plio-Pleistocene glaciation of the Barents Sea–Svalbard region: a new model based on revised chronostratigraphy. *Quaternary Science Reviews*, 28(9), 812–829.

Kürschner, W. M., Kvaček, Z., & Dilcher, D. L. (2008). The impact of Miocene atmospheric carbon dioxide fluctuations on climate and the evolution of terrestrial ecosystems. *Proceedings of the National Academy of Sciences*, 105(2), 449–453.

Lambeck, K. & Chappell, J. (2001). Sea level change through the last glacial cycle. *Science*, 292(5517), 679–686.

Lambeck, K., Yokoyama, Y., & Purcell, T. (2002). Into and out of the Last Glacial Maximum: sea-level change during Oxygen Isotope Stages 3 and 2. *Quaternary Science Reviews*, 21(1), 343–360.

Larour, E., Seroussi, H., Morlighem, M., & Rignot, E. (2012). Continental scale, high order, high spatial resolution, ice sheet modeling using the Ice Sheet System Model (ISSM). *Journal of Geophysical Research: Earth Surface*, 117(F1).

Laskar, J., Robutel, P., Joutel, F., Gastineau, M., Correia, A., & Levrard, B. (2004). A long-term numerical solution for the insolation quantities of the Earth. *Astronomy & Astrophysics*, 428(1), 261–285.

Laske, G., Masters, G., et al. (1997). A global digital map of sediment thickness. *Eos Trans. AGU*, 78(78), F483.

Le Meur, E., Gagliardini, O., Zwinger, T., & Ruokolainen, J. (2004). Glacier flow modelling: a comparison of the Shallow Ice Approximation and the full-Stokes solution. *Comptes Rendus Physique*, 5(7), 709–722.

Le Meur, E. & Huybrechts, P. (1996). A comparison of different ways of dealing with isostasy: examples from modelling the Antarctic ice sheet during the last glacial cycle. *Annals of Glaciology*, 23(1), 309–317.

Li, X., Rignot, E., Morlighem, M., Mouginot, J., & Scheuchl, B. (2015). Grounding line retreat of Totten Glacier, East Antarctica, 1996 to 2013. *Geophysical Research Letters*, 42(19), 8049–8056.

Lindstrom, D. & MacAyeal, D. (1989). Scandinavian, Siberian, and Arctic Ocean glaciation: effect of Holocene atmospheric CO2 variations. *Science*, 245(4918), 628–631.

Lindstrom, D. R. (1990). The Eurasian ice sheet formation and collapse resulting from natural atmospheric CO2 concentration variations. *Paleoceanography*, 5(2), 207–227.

Liu, Z., Otto-Bliesner, B. L., He, F., Brady, E. C., Tomas, R., Clark, P. U., Carlson, A. E., Lynch-Stieglitz, J., Curry, W., Brook, E., Erickson, D., Jacob, R., Kutzbach, J., & Cheng, J. (2009). Transient Simulation of Last Deglaciation with a New Mechanism for Bølling-Allerød Warming. *Science*, 325(5938), 310–314.

Lucchi, R. G., Camerlenghi, A., Rebesco, M., Colmenero-Hidalgo, E., Sierro, F., Sagnotti, L., Urgeles, R., Melis, R., Morigi, C., Bárcena, M., & et al. (2013). Postglacial sedimentary processes on the Storfjorden and Kveithola trough mouth fans: Significance of extreme glacimarine sedimentation. *Global and planetary change*, 111, 309–326.

Ma, Y., Gagliardini, O., Ritz, C., Gillet-Chaulet, F., Durand, G., & Montagnat, M. (2010). Enhancement factors for grounded ice and ice shelves inferred from an anisotropic ice-flow model. *Journal of Glaciology*, 56(199), 805–812(8).

MacAyeal, D. R. (1989). Large-scale ice flow over a viscous basal sediment: Theory and application to ice stream B, Antarctica. *Journal of Geophysical Research: Solid Earth*, 94(B4), 4071–4087.

Mahaffy, M. (1976). A three-dimensional numerical model of ice sheets: Tests on the Barnes Ice Cap, Northwest Territories. *Journal of Geophysical Research*, 81(6), 1059–1066.

Mangerud, J., Astakhov, V. I., Murray, A., & Svendsen, J. I. (2001). The chronology of a large ice-dammed lake and the Barents–Kara Ice Sheet advances, Northern Russia. *Global and Planetary Change*, 31(1), 321–336.

Mangerud, J., Dokken, T., Hebbeln, D., Heggen, B., Ingolfsson, O., Landvik, J. Y., Mejdahl, V., Svendsen, J. I., & Vorren, T. O. (1998). Fluctuations of the Svalbard–Barents Sea Ice Sheet during the last 150 000 years. *Quaternary Science Reviews*, 17(1), 11–42.

Mangerud, J., Gulliksen, S., & Larsen, E. (2010). 14C-dated fluctuations of the western flank of the Scandinavian Ice Sheet 45–25 kyr BP compared with Bølling–Younger Dryas fluctuations and Dansgaard–Oeschger events in Greenland. *Boreas*, 39(2), 328–342.

Margold, M., Stokes, C. R., & Clark, C. D. (2015). Ice streams in the Laurentide Ice Sheet: Identification, characteristics and comparison to modern ice sheets. *Earth-Science Reviews*, 143, 117–146.

Marshall, S. J. (2002). Modelled nucleation centres of the Pleistocene ice sheets from an ice sheet model with subgrid topographic and glaciologic parameterizations. *Quaternary International*, 95, 125–137.

Marshall, S. J., Tarasov, L., Clarke, G. K., & Peltier, W. R. (2000). Glaciological reconstruction of the Laurentide Ice Sheet: physical processes and modelling challenges. *Canadian Journal of Earth Sciences*, 37(5), 769–793.

Marsiat, I. (1994). Simulation of the northern hemisphere continental ice sheets over the last glacial-interglacial cycle: experiments with a latitude-longitude vertically integrated ice sheet model coupled to zonally averaged climate model. *Paleoclimates*, 1, 59–98.

Martin, M., Winkelmann, R., Haseloff, M., Albrecht, T., Bueler, E., Khroulev, C., & Levermann, A. (2011). The Potsdam Parallel Ice Sheet Model (PISM-PIK)–Part 2: Dynamic equilibrium simulation of the Antarctic ice sheet. *The Cryosphere*, 5(3), 727–740.

Masson-Delmotte, V., Kageyama, M., Braconnot, P., Charbit, S., Krinner, G., Ritz, C., Guilyardi, E., Jouzel, J., Abe-Ouchi, A., Crucifix, M., et al. (2006). Past and future polar amplification of climate change: climate model intercomparisons and ice-core constraints. *Climate Dynamics*, 26(5), 513–529.

Matthiessen, J., Knies, J., Vogt, C., & Stein, R. (2009). Pliocene palaeoceanography of the Arctic Ocean and subarctic seas. *Philosophical Transactions of the Royal Society of London A: Mathematical, Physical and Engineering Sciences*, 367(1886), 21–48.

Mercer, J. (1970). A former ice sheet in the Arctic Ocean? *Palaeogeography, Palaeoclimatology, Palaeoecology*, 8(1), 19 – 27.

Milanković, M. (1941). *Kanon der Erdbestrahlung und seine Anwendung auf das Eiszeitenproblem*. na.

Mudelsee, M. & Raymo, M. E. (2005). Slow dynamics of the Northern Hemisphere glaciation. *Paleoceanography*, 20(4).

Mudelsee, M. & Stattegger, K. (1997). Exploring the structure of the mid-Pleistocene revolution with advanced methods of time-series analysis. *Geologische Rundschau*, 86(2), 499–511.

Naish, T., Powell, R., Levy, R., Wilson, G., Scherer, R., Talarico, F., Krissek, L., Niessen, F., Pompilio, M., Wilson, T., et al. (2009). Obliquity-paced Pliocene West Antarctic ice sheet oscillations. *Nature*, 458(7236), 322–328.

North Greenland Ice Core Project Members (2007). 50 year means of oxygen isotope data from ice core NGRIP. Supplement to: North Greenland Ice Core Project Members (2004): High-resolution record of Northern Hemisphere climate extending into the last interglacial period. Nature, 431, 147-151, doi:10.1038/nature02805.

Oerlemans, J. (1980). Model experiments on the 100,000-yr glacial cycle. *Nature*, 287(5781), 430–432.

Paterson, W. (1994). *The physics of glaciers*. Butterworth-Heinemann.

Patton, H., Hubbard, A., Andreassen, K., Winsborrow, M., & Stroeven, A. P. (2016). The build-up, configuration, and dynamical sensitivity of the Eurasian ice-sheet complex to Late Weichselian climatic and oceanic forcing. *Quaternary Science Reviews*, 153, 97–121.

Pedrosa, M. T., Camerlenghi, A., De Mol, B., Urgeles, R., Rebesco, M., & Lucchi, R. G. (2011). Seabed morphology and shallow sedimentary structure of the Storfjorden and Kveithola Trough-Mouth Fans (North West Barents Sea). *Marine Geology*, 286(1-4), 65–81.

Pekar, S. F. & DeConto, R. M. (2006). High-resolution ice-volume estimates for the early Miocene: Evidence for a dynamic ice sheet in Antarctica. *Palaeogeography, Palaeoclimatology, Palaeoecology*, 231(1), 101–109.

Peltier, W. (2004). Global glacial isostasy and the surface of the ice-age earth: the ICE-5G (VM2) model and GRACE. *Annual Review of Earth and Planetary Sciences*, 32(1), 111–149.

Peltier, W. & Fairbanks, R. G. (2006). Global glacial ice volume and Last Glacial Maximum duration from an extended Barbados sea level record. *Quaternary Science Reviews*, 25(23), 3322–3337.

Peltier, W. R. et al. (1994). Ice age paleotopography. *SCIENCE-NEW YORK THEN WASHINGTON-*, (pp. 195–195).

Perovich, D. K., Light, B., Eicken, H., Jones, K. F., Runciman, K., & Nghiem, S. V. (2007). Increasing solar heating of the Arctic Ocean and adjacent seas, 1979–2005: Attribution and role in the ice-albedo feedback. *Geophysical Research Letters*, 34(19).

Peyaud, V. (2006). *Rôle de la dynamique des calottes glaciaires dans les grands changements climatiques des périodes glaciaires-interglaciaires.* PhD thesis, Université Joseph-Fourier-Grenoble I.

Peyaud, V., Ritz, C., & Krinner, G. (2007). Modelling the Early Weichselian Eurasian Ice Sheets: role of ice shelves and influence of ice-dammed lakes. *Climate of the Past Discussions*, 3(1), 221–247.

Piasecka, E. D., Winsborrow, M. C., Andreassen, K., & Stokes, C. R. (2016). Reconstructing the retreat dynamics of the Bjørnøyrenna Ice Stream based on new 3D seismic data from the central Barents Sea. *Quaternary Science Reviews*, 151, 212–227.

Pollard, D. & De Conto, M. (2003). A coupled climate–ice sheet modeling approach to the Early Cenozoic history of the Antarctic ice sheet. *Palaeogeography, Palaeoclimatology, Palaeoecology*, 198(1 - 2), 39 – 52. Antarctic Cenozoic palaeoenvironments: geologic record and models.

Pollard, D. & DeConto, R. M. (2009). Modelling West Antarctic ice sheet growth and collapse through the past five million years. *Nature*, 458(7236), 329–332.

Pollard, D. & DeConto, R. M. (2012). Description of a hybrid ice sheet-shelf model, and application to Antarctica. *Geoscience Model Development*, 5, 1273–1295.

Polyak, L., Gataullin, V., Gainanov, V., Gladysh, V., & Goremykin, Y. (2002). Kara Sea expedition yields insight into extent of LGM ice sheet. *Eos, Transactions American Geophysical Union*, 83(46), 525–529.

Pritchard, H., Ligtenberg, S., Fricker, H., Vaughan, D., Van den Broeke, M., & Padman, L. (2012). Antarctic ice-sheet loss driven by basal melting of ice shelves. *Nature*, 484(7395), 502–505.

Rasmussen, T. L., Thomsen, E., Ślubowska, M. A., Jessen, S., Solheim, A., & Koç, N. (2007). Paleoceanographic evolution of the SW Svalbard margin (76 N) since 20,000 14 C yr BP. *Quaternary Research*, 67(1), 100–114.

Raymo, M. E., Ruddiman, W. F., & Froelich, P. N. (1988). Influence of late Cenozoic mountain building on ocean geochemical cycles. *Geology*, 16(7), 649–653.

Rebesco, M., Laberg, J., Pedrosa, M., Camerlenghi, A., Lucchi, R., Zgur, F., & Wardell, N. (2013). Onset and growth of Trough-Mouth Fans on the North-Western Barents Sea margin e implications for the evolution of the Barents Sea/Svalbard Ice Sheet. *Quaternary Science Reviews*, 30, 1e8.

Rebesco, M., Liu, Y., Camerlenghi, A., Winsborrow, M., Laberg, J. S., Caburlotto, A., Diviacco, P., Accettella, D., Sauli, C., Wardell, N., et al. (2011). Deglaciation of the western margin of the Barents Sea Ice Sheet—a swath bathymetric and sub-bottom seismic study from the Kveithola Trough. *Marine Geology*, 279(1), 141–147.

Reeh, N. (1989). Parameterization of melt rate and surface temperature on the Greenland ice sheet. *Polarforschung*, 59(3), 113–128.

Remy, F. & Legresy, B. (2004). Subglacial hydrological networks in Antarctica and their impact on ice flow. *Annals of Glaciology*, 39(1), 67–72.

Rignot, E., Jacobs, S., Mouginot, J., & Scheuchl, B. (2013). Ice-shelf melting around Antarctica. *Science*, 341(6143), 266–270.

Ritz, C., Rommelaere, V., & Dumas, C. (2001). Modeling the evolution of Antarctic ice sheet over the last 420,000 years: Implications for altitude changes in the Vostok region. *Journal of Geophysical Research: Atmospheres*, 106(D23), 31943–31964.

Roe, G. H. & Lindzen, R. S. (2001). The mutual interaction between continental-scale ice sheets and atmospheric stationary waves. *Journal of Climate*, 14(7), 1450–1465.

Rogozhina, I., Martinec, Z., Hagedoorn, J., Thomas, M., & Fleming, K. (2011). On the long-term memory of the Greenland Ice Sheet. *Journal of Geophysical Research: Earth Surface*, 116(F1).

Ruddiman, W. F. (2001). *Earth's Climate: past and future*. Macmillan.

Sato, T. & Greve, R. (2012). Sensitivity experiments for the Antarctic ice sheet with varied sub-ice-shelf melting rates. *Annals of Glaciology*, 53(60), 221–228.

Schoof, C. (2007). Ice sheet grounding line dynamics: Steady states, stability, and hysteresis. *Journal of Geophysical Research: Earth Surface*, 112.

Schoof, C. (2012). Marine ice sheet stability. *Journal of Fluid Mechanics*, 698, 62–72.

Shapiro, N. M. & Ritzwoller, M. H. (2004). Inferring surface heat flux distributions guided by a global seismic model: particular application to Antarctica. *Earth and Planetary Science Letters*, 223(1), 213–224.

Siegert, M. J. & Dowdeswell, J. A. (1995). Numerical modeling of the late Weichselian Svalbard-Barents Sea ice sheet. *Quaternary Research*, 43(1), 1–13.

Siegert, M. J. & Dowdeswell, J. A. (2004). Numerical reconstructions of the Eurasian Ice Sheet and climate during the Late Weichselian. *Quaternary Science Reviews*, 23(11), 1273–1283.

Siegert, M. J., Dowdeswell, J. A., Hald, M., & Svendsen, J.-I. (2001). Modelling the Eurasian Ice Sheet through a full (Weichselian) glacial cycle. *Global and Planetary Change*, 31(1–4), 367 – 385. The late Quaternary stratigraphy and environments of northern Eurasia and the adjacent Arctic seas - new contributions from QUEEN.

Siegert, M. J., Dowdeswell, J. A., Svendsen, J.-I., & Elverhøi, A. (2002). The Eurasian Arctic during the last ice age. *American Scientist*, 90(1), 32–39.

Solomon, S., Qin, S., Manning, M., Chen, Z., Marquis, M., Averyt, K., Tignor, M., & Miller, H. (2007). *IPCC, 2007: The Physical Science Basis. Contribution of Working Group I to the Fourth Assessment Report of the Intergovernmental Panel on Climate Change*. Cambridge University Press, Cambridge, United Kingdom and New York, NY, USA.

Spratt, R. M. & Lisiecki, L. E. (2016). A Late Pleistocene sea level stack. *Climate of the Past*, 12(4), 1079.

Stocker, T., Qin, D., Plattner, G.-K., Tignor, M., Allen, S., Boschung, J., Nauels, A., Xia, Y., Bex, V., & Midgley, P. (2013). *IPCC, 2013: Climate Change 2013: The Physical Science Basis. Contribution of Working Group I to the Fifth Assessment Report of the Intergovernmental Panel on Climate Change*. Cambridge University Press, Cambridge, United Kingdom and New York, NY, USA.

Stokes, C. R. & Clark, C. D. (2001). Palaeo-ice streams. *Quaternary Science Reviews*, 20(13), 1437–1457.

Stokes, C. R., Tarasov, L., Blomdin, R., Cronin, T. M., Fisher, T. G., Gyllencreutz, R., Hättestrand, C., Heyman, J., Hindmarsh, R. C., Hughes, A. L., et al. (2015). On the reconstruction of palaeo-ice sheets: recent advances and future challenges. *Quaternary Science Reviews*, 125, 15–49.

Stone, E., Lunt, D., Rutt, I., & Hanna, E. (2010). Investigating the sensitivity of numerical model simulations of the modern state of the Greenland ice-sheet and its future response to climate change. *The Cryosphere*, 4(3), 397.

Straneo, F. & Heimbach, P. (2013). North Atlantic warming and the retreat of Greenland's outlet glaciers. *Nature*, 504(7478), 36–43.

Svendsen, J. I., Alexanderson, H., Astakhov, V. I., Demidov, I., Dowdeswell, J. A., Funder, S., Gataullin, V., Henriksen, M., Hjort, C., Houmark-Nielsen, M., et al. (2004). Late Quaternary ice sheet history of northern Eurasia. *Quaternary Science Reviews*, 23(11), 1229–1271.

Svendsen, J. I., Astakhov, V. I., Bolshyanov, D. Y., Demidov, I., Dowdeswell, J. A., Gataullin, V., Hjort, C., Hubberten, H. W., Larsen, E., Mangerud, J., et al. (1999). Maximum extent of the Eurasian ice sheets in the Barents and Kara Sea region during the Weichselian. *Boreas*, 28(1), 234–242.

Svendsen, J. I., Briner, J. P., Mangerud, J., & Young, N. E. (2015). Early break-up of the norwegian channel ice stream during the last glacial maximum. *Quaternary Science Reviews*, 107, 231–242.

Tarasov, L. & Peltier, W. R. (1999). Impact of thermomechanical ice sheet coupling on a model of the 100 kyr ice age cycle. *Journal of Geophysical Research: Atmospheres*, 104(D8), 9517–9545.

Tarasov, L. & Peltier, W. R. (2002). Greenland glacial history and local geodynamic consequences. *Geophysical Journal International*, 150(1), 198–229.

Tarasov, L. & Peltier, W. R. (2004). A geophysically constrained large ensemble analysis of the deglacial history of the North American ice-sheet complex. *Quaternary Science Reviews*, 23(3), 359–388.

Tripati, A. K., Eagle, R. A., Morton, A., Dowdeswell, J. A., Atkinson, K. L., Bahé, Y., Dawber, C. F., Khadun, E., Shaw, R. M., Shorttle, O., et al. (2008). Evidence for

glaciation in the Northern Hemisphere back to 44 Ma from ice-rafted debris in the Greenland Sea. *Earth and Planetary Science Letters*, 265(1), 112–122.

Ullman, D. J., LeGrande, A. N., Carlson, A. E., Anslow, F. S., & Licciardi, J. M. (2014). Assessing the impact of Laurentide Ice Sheet topography on glacial climate. *Climate of the Past*, 10(2), 487–507.

Van den Berg, J., Van de Wal, R., Milne, G., & Oerlemans, J. (2008). Effect of isostasy on dynamical ice sheet modeling: A case study for Eurasia. *Journal of Geophysical Research: Solid Earth*, 113(B5).

van den Broeke, M., Bamber, J., Ettema, J., Rignot, E., Schrama, E., van de Berg, W. J., van Meijgaard, E., Velicogna, I., & Wouters, B. (2009). Partitioning recent Greenland mass loss. *science*, 326(5955), 984–986.

Vorren, T. O. & Laberg, J. S. (1997). Trough mouth fans—palaeoclimate and ice-sheet monitors. *Quaternary Science Reviews*, 16(8), 865–881.

Weertman, J. (1957). Steady-State Creep through Dislocation Climb. *Journal of Applied Physics*, 28(3), 362–364.

Weertman, J. (1974). Stability of the junction of an ice sheet and an ice shelf. *Journal of Glaciology*, 13(67), 3–11.

Wohlfarth, B. (2010). Ice-free conditions in Sweden during Marine Oxygen Isotope Stage 3? *Boreas*, 39(2), 377–398.

Yamagishi, T., Abe-Ouchi, A., Saito, F., Segawa, T., & Nishimura, T. (2005). Re-evaluation of paleo-accumulation parameterization over Northern Hemisphere ice sheets during the ice age examined with a high-resolution AGCM and a 3-D ice-sheet model. *Annals of Glaciology*, 42(1), 433–440.

Yokoyama, Y., De Deckker, P., Lambeck, K., Johnston, P., & Fifield, L. K. (2001). Sea-level at the Last Glacial Maximum: evidence from northwestern Australia to constrain ice volumes for oxygen isotope stage 2. *Palaeogeography, Palaeoclimatology, Palaeoecology*, 165(3), 281–297.

Yukimoto, S., Adachi, Y., Hosaka, M., Sakami, T., Yoshimura, H., Hirabara, M., Tanaka, T. Y., Shindo, E., Tsujino, H., Deushi, M., et al. (2012). A new global climate model of the Meteorological Research Institute: MRI-CGCM3—model description and basic performance—. *J. Meteorol. Soc. Jpn. Ser II*, 90(0), 23–64.

Zachos, J. C., Dickens, G. R., & Zeebe, R. E. (2008). Age and d18O analysis relating to Cenozoic greenhouse climates. *PANGAEA*.

Zweck, C. & Huybrechts, P. (2005). Modeling of the northern hemisphere ice sheets during the last glacial cycle and glaciological sensitivity. *Journal of Geophysical Research: Atmospheres*, 110(D7).